

**VIBROACOUSTIC RESPONSE DUE TO TURBULENT
BOUNDARY LAYER OVER PLATE STRUCTURES**

Thesis submitted by

BIPLAB RANJAN ADHIKARY

Doctor of Philosophy (Engineering)

**Department of Civil Engineering
Faculty Council of Engineering & Technology
Jadavpur University
Kolkata, India**

2023

JADAVPUR UNIVERSITY
KOLKATA – 700 032, INDIA

INDEX NO. 292/18/E

**1. Title of the thesis: Vibroacoustic response due to turbulent boundary layer over
plate structures**

2. Name, Designation & Institution of the Supervisor/s:

- 1. Dr. Partha Bhattacharya**
Professor
Department of Civil Engineering
Jadavpur University,
Kolkata 700032, India

- 2. Dr. Atanu Sahu**
Assistant Professor
Department of Civil Engineering
National Institute of Technology Silchar,
Silchar 788010, India

3. List of publication:

Journal Publications

- [1] **Adhikary, B. R.**, Majumdar, A., Sahu, A., Bhattacharya, P., (2023), Sensitivity of TBL Wall-Pressure Over the Flat Plate on Numerical Turbulence Model Parameter variations, *CFD Letters* 15, Issue 7, 148-174.
- [2] **Adhikary, B. R.**, Sahu, A., Bhattacharya, P., A FE-BE based coupled vibroacoustic model for non-homogeneous TBL excited composite panels involving Cholesky decomposition, *Journal of Applied Mechanics and Technical Physics*, 64, Issue 6, 1128-1140.
- [3] **Adhikary, B. R.**, Majumdar, A., Sahu, A., Bhattacharya, P., (2023), Finite element modelling of transmission of TBL induced vibrational energy through a stiffened double panel using CFD sensitivity study, *Journal of the Brazilian Society of Mechanical Sciences and Engineering*, 45, article number 595.

4. List of Patents – Nil

5. List of Presentations in National / International Conference:

- [1] **Adhikary, B. R.**, Majumdar, A., Sarkar, S., Bhattacharya, P., (2022), Sensitivity mapping between different TBL wall-pressure spectra and CFD models using OpenFOAM and Fluent solver, *Proceedings of the 9th International and 49th National Conference on Fluid Mechanics and Fluid Power (FMFP)*, December 14-16, 2022, IIT Roorkee, India.
- [2] Majumdar, A., **Adhikary, B. R.**, Bhattacharya, P., (2022), Reduction in turbulence-induced non-linear dynamic vibration using tuned liquid damper (TLD), *Proceedings of the 9th International and 49th National Conference on Fluid Mechanics and Fluid Power (FMFP)*, December 14-16, 2022, IIT Roorkee, India.
- [3] **Adhikary, B. R.**, Sahu, A., Bhattacharya, P., (2022), TBL induced vibroacoustic response of aircraft panels involving CFD with artificial inflow turbulence and FE-RRM approach, *Proceedings of the 28th International Congress on Sound and Vibration (ICSV)*, 24-28 July, 2022, Singapore.
- [4] Sarkar, S., **Adhikary, B. R.**, Sahu, A., Bhattacharya, P., (2019), Parametric study of TBL induced structural vibration of a flat plate using Smol'yakov and Tkachenko model, *7th International Congress on Computational Mechanics and Simulation (ICCMS)*, 11-13 December, 2019, IIT Mandi, Mandi, India.
- [5] **Adhikary, B. R.**, Sahu, A., Bhattacharya, P., (2018), Modelling of sound radiation into the free field due to turbulent boundary layer (TBL) excitation, *13th Western Pacific Acoustics Conference*, 11-15 November, 2018, New Delhi, India.
- [6] Bhattacharya, P., **Adhikary, B. R.**, Sahu, A., (2017), Active structural-acoustic control of sound transmission through a double wall panel based on frequency weighted h_2 – optimal

controller, *Proceedings of the 24th International Congress on Sound and Vibration (ICSV)*, 23-27 July, 2017, London, United Kingdom.

[7] Sarkar, S., **Adhikary, B. R.**, Sahu, A., Bhattacharya, P., (2018), Structural vibration models for TBL last 60 years: a review, *Structural Engineering Convention (SEC)*, Jadavpur University, Kolkata, India, 19-21 December 2018.

[8] **Adhikary, B. R.**, Sahu, A., Bhattacharya, P., (2017), Effect of lamina sequences on sound transmission behaviour through laminated composite panel, *Proceedings of The Nineteenth National Seminar on Aerospace Structures*, VIT, Vellore, India, 23-25 February 2017.

STATEMENT OF ORIGINALITY

I **Shri Biplab Ranjan Adhikary** registered on 31st May, 2018 do hereby declare that this thesis entitled “**Vibroacoustic response due to turbulent boundary layer over plate structures**” contains literature survey and original research work done by the undersigned candidate as part of Doctoral studies.

All information in this thesis been obtained and presented in accordance with existing academic rules and ethical conduct. I declare that, as required by these rules and conduct, I have fully cited and referred all materials and results that are not original to this work.

I also declare that I have checked this thesis as per the “Policy on Anti Plagiarism, Jadavpur University, 2019”, and the level of similarity as checked by iThenticate software is 7 %.

Signature of Candidate:

Biplab Ranjan Adhikary

Date: 20/09/2023

Certified by Supervisor(s):

(Signature with date, seal)

Partha Bhattacharya
20/09/23

Atanu Sahu
20/09/2023

Dr. Partha Bhattacharya
(Professor)
Department of Civil Engineering
Jadavpur University
Kolkata 700032
India

Dr. Atanu Sahu
(Assistant Professor)
Department of Civil Engineering
National Institute of Technology Silchar
Silchar 788010
India

Professor
CIVIL ENGINEERING DEPARTMENT
JADAVPUR UNIVERSITY
KOLKATA-32

Asst. Professor
Department of Civil Engineering
NIT, Silchar

CERTIFICATE FROM THE SUPERVISOR/S

This is to certify that the thesis entitled “**Vibroacoustic response due to turbulent boundary layer over plate structures**”, Index No. 292/18/E, submitted by **Shri Biplab Ranjan Adhikary**, who got his name registered on 31st May, 2018 for the award of Ph.D. (Engg.) degree of Jadavpur University is absolutely based upon his own work under the supervision of **Dr. Partha Bhattacharya and Dr. Atanu Sahu** and that neither his thesis nor any part of the thesis has been submitted for any degree/diploma or any other academic award anywhere before.

(Signature of the supervisor/s
and date with office seal)

Partha Bhattacharya
20/9/23

Atanu Sahu
20/09/2023

Dr. Partha Bhattacharya
(Professor)
Department of Civil Engineering
Jadavpur University
Kolkata 700032
India

Dr. Atanu Sahu
(Assistant Professor)
Department of Civil Engineering
National Institute of Technology Silchar
Silchar 788010
India

Professor
CIVIL ENGINEERING DEPARTMENT
JADAVPUR UNIVERSITY
KOLKATA-32

Asst. Professor
Department of Civil Engineering
NIT, Silchar

**Dedicated
To
My Father**

DECLARATION

This work has not previously been submitted for a degree or diploma in any University. To the best of my knowledge and belief, the thesis contains no material previously published or written by another person except where due reference is made in the thesis itself.

Biplab Ranjan Adhikary

BIPLAB RANJAN ADHIKARY

ACKNOWLEDGEMENTS

The person who upheld me from nowhere and provided me with the opportunity to continue his high-end research legacy, at the same time furnished me the freedom to create my own, the person I will be beyond grateful forever to, is my supervisor Dr. Partha Bhattacharya. Without him, my serious research journey would never have started. He has extended his supervision, mentorship, and unwavering support throughout my doctoral journey, and taught me how to push oneself beyond his comfort zone.

I would like to express my sincere gratitude to my senior turned joint supervisor Dr. Atanu Sahu who exposed me to the fruits of epistemology and has been a continuous mentor to date.

I am indebted for the unconditional support I received from my student-turned-co-researcher Ananya. Her sincere and relentless efforts constitute a significant portion of my research journey.

I wish one day my son Rangeet will read this and will be able to understand what it takes to produce a doctoral thesis. He is six, and I am grateful to him for his mature and sensible support during my research tenure. I would like to remember my late grandmother Smt. Gita Rani Adhikary on this occasion. She was a pillar in the truest sense. I am thankful to my family; mother Smt. Bijali Adhikary, elder sister Smt. Subhra Roy Adhikary, niece Advaita, and beloved ‘poka’ Dr. Suman Roy for his caring guardianship, Shri Bamapada Sinha, Smt. Kalyani Sinha, Shri Subodh Roy, and Smt. Jayita Majumdar for their continuous support.

My sincere regards to Dr. Swarnendu Sen, Dr. Sourav Sarkar, Dr. Aranyak Chakraborty.

My heartfelt acknowledgement to my dearest friends Arpan, and Shyamal, Soumya Da, Atanu Da, and ‘prehistoric students’ Debodyuti, Shreya, Anusua, Tanusree, Dr. Abhirup, Rakesh for their support.

Special gratitude to ‘captain’ Kingshuk, Manmatha, Pankaj Da, and Soumyendra Da.

I would like to thank my batch mates Pritam, Abhishek, Mukul, Abhijit, Sumanta, Gurusaday, Suman, Shibsankar, Rik, Debosmita, Pritha, Rahul, Prashant, Rajesh Da for their loving encouragement. I am grateful to my fellow researchers Sayak, Saptarshi, Atriya, and juniors Tapan, Likhan, Souvik, Sourish, Arkadeb, and especially Saikat, Surajit, and Aritra whom I always found standing just beside me.

I would like to sincerely thank AR&DB (DRDO) and WBDST for their financial support during the tough times, Mr. Bhaskar G. Rajalu, McDermott for his prompt, visionary, and decisive actions.

I thank all the teaching and non-teaching staff members of the Department of Civil Engineering, very special Jadavpur University – my second home.

Last but not least, I thank all my students and the science-technology enthusiasts I have come across, who, through their questions, always inspired me to think in-depth and re-search.

Biplab Ranjan Adhikary

ABSTRACT

“If you want to find the secrets of the universe, think in terms of energy, frequency, and vibration” – Nicola Tesla

The present thesis started in the quest to understand the energy, frequency, and vibration behaviour of the structural panels when subjected to turbulent boundary layer (TBL) excitation, one of the major noise sources. Structural vibration and noise (vibroacoustic) problem is a serious issue encountered by the transportation industry in terms of human health, environmental noise pollution, structural stress, fatigue, etc. Therefore, it is very important to understand the TBL-excited vibroacoustic behaviour of the vehicular panel and the enclosed cabin. Usage of stiffened, tensioned, double wall panels and panels made of orthotropic laminated composites also necessitates a comprehensive TBL-excited vibroacoustic study with a fully coupled system development.

Over the years, the vibroacoustic response of plate structures subjected to a turbulent boundary layer flow has been the subject of numerous studies. This is because the interaction between the flow and the plate can lead to significant changes in the acoustic and vibration characteristics of the panel. The understanding of this interaction is essential in various engineering domains such as aerospace, automobile, marine, high-speed railway, and civil engineering where plate structures are commonly used.

This thesis work focuses on investigating the vibroacoustic response of a plate structure due to the fully developed turbulent boundary layer over it. Besides the analytical and semi-analytical models, the study combines computational fluid dynamics (CFD), Reynolds-averaged Navier-Stokes (RANS) simulations, and large eddy simulations (LES) to investigate/predict the turbulent pressure fluctuations over a plate structure. The aim is to understand vibration, sound radiation, and sound transmission characteristics of several different panel configurations that include single, double, tensioned, and stiffened panels. Different orthotropic laminated panels are also extensively studied in this context. The study also evaluates the influence of the turbulent boundary layer on the panel's overall vibroacoustic response. In-house finite element (FE) codes are developed to couple the TBL loading with the flexible structure and the flexible structure with the adjacent acoustic medium. All the coupling models are developed in the FE environment using in-house MATLAB (ver. R2013b) or cloud-based Python scripts.

Different semi-analytical single-point wall-pressure spectrum models are used to estimate the pressure fluctuations, with prior studies of their prediction accuracy with the wind tunnel experiments and the in-flight test results. All these spectrum models essentially work based on the TBL wall parameters, like boundary layer thickness, displacement thickness, momentum thickness, shear velocity, etc. Therefore, one has to depend upon the experimental feed, which is quite a labour and cost intensive. In order to predict various wall parameters, the computational fluid dynamics (CFD) simulations are carried out using both commercial and open-source flow solvers, ANSYS Fluent (V14.5) and OpenFOAM (v-2012 in Ubuntu 20.04 LTS), respectively. A

detailed sensitivity study is performed to identify the change in wall-pressure fluctuations due to the choice of RANS turbulence model parameters, like turbulence model, solver, normalized wall distance, flow velocity, etc. The best predicting configuration is thus identified and used in further vibroacoustic computations in the energy (power spectral density; PSD) domain.

The wall pressure fluctuations are estimated in the normal frequency domain also. In order to achieve this, two methods are adopted in the present study. A) The wall-pressure spectrum is decomposed using Cholesky's technique. This resulted in the pressure fluctuations magnitude in the frequency domain. B) The large eddy simulation (LES) is employed to simulate the real-time pressure fluctuations over single or multiple points over the plate. The Smagorinsky-Lilly model is used as the sub-grid scale model. Typical LES models have a near-wall eddy-damping issue which is resolved using the artificial inflow turbulence generated using the superposition of the Fourier modes. This continuously perturbs the flow and desired near-wall pressure fluctuations are obtained.

In the present study, the single-point pressure fluctuation is obtained considering the wall beneath the TBL to be rigid. Considering the TBL wall pressure to be random, stationary, and ergodic, the cross-spectrum of the pressure fluctuations over the plate is calculated using Corcos and Mellen's spatial coherence function. This pressure cross-spectrum is further used to estimate the plate vibration.

Once the wall-pressure fluctuation is obtained over the panel, in the next step the TBL-excited plate vibration is estimated using a one-way coupled fluid-structure interaction model. A two-way coupling model is used to couple the excited plate and the adjacent acoustic domain to estimate the radiated sound power in the free field or the sound transmission into the enclosed cavity. The required panel transfer function or the frequency response function (FRF) is developed using the mode shape and frequency data obtained from the FE modal analysis using MATLAB or ANSYS APDL (V14.5). The FE discretization of the panel is performed with the TBL-induced plate bending wave consideration. The coupling between the TBL cross-spectra and the panel transfer function resulted in panel response in terms of displacement and velocity PSD.

In order to simulate the real-life sound radiation and transmission phenomena *four* types of TBL-structure-acoustic coupling models are developed to account for single panel, panel-enclosure, panel-cavity-panel (double wall), and panel-cavity-panel-enclosure (double wall backed by an enclosure) systems. Panels are modelled using 4-node isoparametric plate elements, and the acoustic domain is modelled using 8-noded 3D brick elements. Once the transfer functions of the panel(s) and the acoustic domain(s) are estimated in a fully coupled condition, they are used to calculate the panel-radiated sound power into the free field using the radiation resistance matrix (RRM) technique, where each finite element behaves as an elemental radiator. The TBL-excited panel velocity PSD is coupled with the RRM and the radiated sound power is estimated. In the case of sound transmission into an enclosure, the system transfer functions of each part are directly coupled with the TBL cross PSD, and the panel velocity PSD and the enclosure pressure PSD are obtained.

As observed from the two-fold sensitivity study, $k - \omega$ family of turbulence models are found to be best predicting the TBL wall pressure over a flat plate. Large eddy simulation (LES) powered by the in-house developed user defined functions (UDFs) for artificial inflow turbulence manifests excellent wall pressure fluctuation prediction. Wall pressure fluctuations using Cholesky decomposition coupled with boundary element (BE) technique estimates panel vibration and sound radiation in frequency domain, providing with similar trend to the results obtained in the PSD domain. Orthotropic laminated composite panels with $(45/-45)_n$ sequence, when excited by TBL force, exhibits counter-intuitive vibroacoustic results. The results obtained using FE-RRM technique for free field sound radiation, and fully coupled FE-FE technique for sound transmission in panel-gap-panel-enclosure system are in excellent agreement with the reported analytical results.

In real-life transport vehicles, different type of structural variations is observed, in terms of geometry, material properties and support conditions. In order to capture these variations, the present study uses FE modelling of the orthotropic laminated composite panels, stiffened and tensioned panels with generic boundary conditions and scope of different geometry. This study can thus be useful for any structural or aerodynamic modification of the transport vehicle in the very early design stage.

CONTENT

ABSTRACT	IX
NOMENCLATURE	XV
ABBREVIATION	XVI
LIST OF FIGURES	XVII
LIST OF TABLES	XXII
1 CHAPTER 1: INTRODUCTION	1
1.1 BACKGROUND.....	1
1.2 MOTIVATION FOR THE PRESENT RESEARCH	4
1.3 ORGANIZATION OF THE DISSERTATION	5
2 CHAPTER 2: LITERATURE REVIEW	8
2.1 INTRODUCTION.....	8
2.2 OVERVIEW AND CLASSIFICATION OF PREVIOUS LITERATURE	8
2.3 REVIEW OF PREVIOUS WORKS ON TBL WALL PRESSURE ESTIMATION STUDY.....	9
2.3.1 Analytical and semi-analytical techniques.....	9
2.4 REVIEW OF EARLIER WORKS ON TBL-STRUCTURE INTERACTION MODELLING AND FREE FIELD SOUND RADIATION	20
2.5 REVIEW OF COUPLED TBL-INDUCED VIBROACOUSTIC PROBLEMS IN ENCLOSED FIELD	25
2.6 CRITICAL APPRAISAL OF THE PREVIOUS WORKS.....	26
2.7 THE OBJECTIVE AND THE APPROACH.....	27
3 CHAPTER 3: TBL WALL PRESSURE ESTIMATION	29
3.1 INTRODUCTION.....	29
3.2 MATHEMATICAL DESCRIPTION	29
3.2.1 Semi-analytical models.....	29
3.3 COMPUTATIONAL FLUID DYNAMICS	33
3.3.1 Reynolds-Averaged Navier Stokes (RANS).....	33
3.3.2 Large Eddy Simulation (LES)	43
3.4 NUMERICAL METHODOLOGY	54
3.4.1 Combined Semi-Analytical Model and RANS approach	54
3.4.2 Large Eddy Simulation (LES)	57
3.5 RESULTS AND DISCUSSION	60
3.5.1 Combined Semi-Analytical Model and RANS approach	60

3.5.2	Large Eddy Simulation (LES)	73
3.6	SPATIAL CORRELATION FUNCTION AND PRESSURE CROSS POWER SPECTRAL DENSITY (CPSD)	81
3.7	CONCLUSION	81
3.7.1	Combined RANS-Semi-Analytical Model Approach	81
3.7.2	Large Eddy Simulation (LES) and Artificial Inflow Turbulence	82
4	CHAPTER 4: TBL-EXCITED STRUCTURAL VIBRATION	83
4.1	INTRODUCTION	83
4.2	MATHEMATICAL DESCRIPTION	84
4.2.1	Vibration of Panels; Random Excitation	84
4.2.2	Finite Element Modelling; Structural Panel	88
4.3	NUMERICAL METHODOLOGY	94
4.3.1	Turbulence-Structure Coupling: PSD Domain	94
4.3.2	Turbulence-Structure Coupling: Frequency Domain; Cholesky's Decomposition	95
4.4	RESULTS AND DISCUSSION	97
4.4.1	Validation Study	98
4.4.2	TBL-Induced Vibration of Single Stiffened Panels	103
4.4.3	TBL-Induced Vibration of Orthotropic Panels	104
4.4.4	Vibration Response of Isotropic and Orthotropic Panels in Frequency Domain: New Approach	107
4.5	CONCLUSION	110
4.5.1	PSD analysis: Stiffened panel	111
4.5.2	PSD analysis: Orthotropic panel	111
4.5.3	Frequency analysis (Cholesky decomposition): Orthotropic panel	111
5	CHAPTER 5: TBL-EXCITED STRUCTURAL VIBROACOUSTICS	112
5.1	INTRODUCTION	112
5.2	MATHEMATICAL DESCRIPTION	113
5.2.1	Free Field Sound Radiation	113
5.2.2	Sound Transmission Mechanism into an Enclosed Cavity	117
5.2.3	Structural Modelling: Tensioned Panel	124
5.3	NUMERICAL METHODOLOGY	126
5.3.1	Sound Radiation into the Free Field	126
5.3.2	Sound Transmission into the Enclosed Cavity	127
5.4	RESULTS AND DISCUSSION	128
5.4.1	Sound Radiation into the Free Field	128
5.4.2	TBL-Induced Vibrational Energy Transfer through Stiffened Double Wall Panel	136

5.4.3	Sound Transmission into the Enclosed Cavity	148
5.5	CONCLUSION	151
5.5.1	Sound Radiation into the Free Field	152
5.5.2	TBL-Induced Vibrational Energy Transfer through Stiffened Double Wall Panel 152	
5.5.3	Sound Transmission into the Enclosed Cavity	153
6	CHAPTER 6: CONCLUSIONS	154
6.1	INTRODUCTION.....	154
6.2	WALL PRESSURE ESTIMATION USING CFD	155
6.3	COUPLED VIBROACOUSTIC MODELLING IN ENERGY DOMAIN.....	156
6.4	COUPLED VIBROACOUSTIC MODELLING IN FREQUENCY DOMAIN	157
6.5	CONCLUSIONS.....	157
6.6	SCOPE FOR FUTURE RESEARCH.....	158
6.7	STATEMENT OF CONTRIBUTION.....	159
	APPENDIX A	160
	APPENDIX B	163
	BIBLIOGRAPHY	165
	VITA.....	179

NOMENCLATURE

ξ_1, ξ_3	Separation length between two points along stream-wise and crossflow directions, respectively
ω	Radial frequency
ω_n	Natural frequency
k	Turbulence kinetic energy
ϵ	Turbulence kinetic energy dissipation rate
Φ_p	Single-point wall-pressure spectrum
Φ_{pp}	Cross power spectrum of wall-pressure fluctuations
Γ	Spatial coherence function
U_0/U_0	Free stream velocity
U_c	Convective velocity
$[M_e]$	Element mass matrix
$[K_e]$	Element stiffness matrix
$[\rho]$	Plate inertia matrix
$[M]$	Global structural mass matrix
$[C]$	Global structural damping matrix
$[K]$	Global structural stiffness matrix
E	Modulus of elasticity
G	Modulus of rigidity
ν	Poisson ratio
k_s	Shear correction factor
F_{tbl}	TBL induced force in time domain
$F(\omega)$	TBL induced force in frequency domain
d_s	Structural panel displacement in time domain
\dot{d}_s	Structural panel velocity in time domain
\ddot{d}_s	Structural panel acceleration in time domain
$d_s(\omega)$	Structural panel displacement in frequency domain
$\dot{d}_s(\omega)$	Structural panel velocity in frequency domain
$\ddot{d}_s(\omega)$	Structural panel acceleration in frequency domain
S_{ww}	Panel displacement PSD
S_{vv}	Panel velocity PSD
S_{gg}	Pressure PSD for gap cavity
S_{ee}	Pressure PSD for enclosed cavity
p	Sound pressure radiated by the panel excited by the TBL
g	Free space Green's function
k	Acoustic wave number
q	Structural displacement in modal domain

m	Modal mass
H	Frequency response function
φ	Mode shape
P_{rad}	Radiated sound power
P_{ref}	Reference sound power

ABBREVIATION

BE	Boundary element
CFD	Computational fluid dynamics
FE	Finite element
FRF	Frequency response function
FSI	Fluid-structure interaction
LES	Large eddy simulation
PSD	Power spectral density
RANS	Reynolds-averaged Navier Stokes
RRM	Radiation resistance matrix
RSP	Radiated sound power
SGS	Sub-grid scale
TBL	Turbulent boundary layer
TL	Transmission loss

LIST OF FIGURES

Figure 3.3.1: Prandtl mixing length vs van Driest model mixing length.....	36
Figure 3.3.2: Energy cascading; turbulence dissipation with wave number.....	39
Figure 3.3.3: Blending function between $k - \omega$ and $k - \epsilon$ models.....	41
Figure 3.3.4(a): Calculating velocity scale using vertical line.....	49
Figure 3.3.4(b): Calculating velocity scale using horizontal line.....	49
Figure 3.4.1: Schematic of the domain for flat plate TBL simulation; replication of the experimental set up by Salze <i>et al.</i> , 2014.....	55
Figure 3.4.2(a): Coarse Mesh.....	55
Figure 3.4.2(b): Medium Mesh.....	55
Figure 3.4.2(c): Fine Mesh.....	55
Figure 3.4.3(a): Mesh for $y^+ = 1$ for $U = 30$ m/s.....	57
Figure 3.4.3(b): Mesh for $y^+ = 30$ for $U = 30$ m/s.....	57
Figure 3.4.3(c): Mesh for $y^+ = 100$ for $U = 30$ m/s.....	57
Figure 3.4.4: a) grid clustering near the wall, b) normalized velocity profile; black – universal velocity profile, red – present LES study.....	58
Figure 3.5.1(a): Comparison of wall-spectrum models with Goody-Simpson wind tunnel experiment. Ref. 4×10^{-10} Pa ²	61
Figure 3.5.1(b): Comparison of wall-spectrum models with Rackl and Weston in-flight test data. Ref. 4×10^{-10} Pa ²	61
Figure 3.5.2(a): Point 1; $U_\infty=30$ m/s; Open FOAM.....	63
Figure 3.5.2(b): Point 1; $U_\infty=30$ m/s; ANSYS Fluent.....	63
Figure 3.5.2(c): Point 2; $U_\infty=30$ m/s; Open FOAM.....	63
Figure 3.5.2(d): Point 2; $U_\infty=30$ m/s; ANSYS Fluent.....	63
Figure 3.5.3: Universal velocity plot for $U_\infty=30$ m/s at location 1; OpenFOAM.....	64
Figure 3.5.4: Universal velocity plot for $U_\infty=30$ m/s at location 2; OpenFOAM.....	64
Figure 3.5.5(a): Estimation of error in MSP and turbulent wall parameters at point 1; $U_\infty = 30$ m/s; OpenFOAM, $k - \omega$ turbulence model, Smol'yakov-Tkachenko spectrum model.....	65
Figure 3.5.5(b): Estimation of error in MSP and turbulent wall parameters at point 1; $U_\infty = 30$ m/s; ANSYS Fluent, $k - \omega$ turbulence model, Smol'yakov-Tkachenko spectrum model.....	65
Figure 3.5.5(c): Estimation of error in MSP and turbulent wall parameters at point 1; $U_\infty = 50$ m/s; OpenFOAM, $k - \omega$ turbulence model, Smol'yakov-Tkachenko spectrum model.....	65
Figure 3.5.5(d): Estimation of error in MSP and turbulent wall parameters at point 1; $U_\infty = 50$ m/s; ANSYS Fluent, $k - \omega$ turbulence model, Smol'yakov-Tkachenko spectrum model.....	65
Figure 3.5.6(a): Estimation of error in MSP and turbulent wall parameters at point 1; $U_\infty = 30$ m/s; OpenFOAM, $k - \omega$ turbulence model, Rackl-Weston spectrum model.....	66
Figure 3.5.6(b): Estimation of error in MSP and turbulent wall parameters at point 1; $U_\infty = 30$ m/s; ANSYS Fluent, $k - \omega$ turbulence model, Rackl-Weston spectrum model.....	66

Figure 3.5.6(c): Estimation of error in MSP and turbulent wall parameters at point 1; $U_\infty = 50$ m/s; OpenFOAM, $k-\omega$ turbulence model, Rackl-Weston spectrum model.....	66
Figure 3.5.6(d): Estimation of error in MSP and turbulent wall parameters at point 1; $U_\infty = 30$ m/s; ANSYS Fluent, $k-\omega$ turbulence model, Rackl-Weston spectrum model.....	66
Figure 3.5.7(a): Convergence of of \bar{p}^2 (MSP) with y^+ . Point 1; $U_\infty = 30$ m/s; OpenFOAM, Smol'yakov-Tkachenko spectrum model.....	68
Figure 3.5.7(b): Convergence of of \bar{p}^2 (MSP) with y^+ . Point 1; $U_\infty = 30$ m/s; ANSYS Fluent, Smol'yakov-Tkachenko spectrum model.....	68
Figure 3.5.7(c): Convergence of of \bar{p}^2 (MSP) with y^+ . Point 1; $U_\infty = 50$ m/s; OpenFOAM, Smol'yakov-Tkachenko spectrum model.....	68
Figure 3.5.7(d): Convergence of of \bar{p}^2 (MSP) with y^+ . Point 1; $U_\infty = 50$ m/s; ANSYS Fluent, Smol'yakov-Tkachenko spectrum model.....	68
Figure 3.5.8(a): Convergence of of \bar{p}^2 (MSP) with y^+ . Point 2; $U_\infty = 30$ m/s; OpenFOAM, Smol'yakov-Tkachenko spectrum model.....	69
Figure 3.5.8(b): Convergence of of \bar{p}^2 (MSP) with y^+ . Point 2; $U_\infty = 30$ m/s; ANSYS Fluent, $k-\omega$ model, Smol'yakov-Tkachenko spectrum model.....	69
Figure 3.5.8(c): Convergence of of \bar{p}^2 (MSP) with y^+ . Point 2; $U_\infty = 50$ m/s; OpenFOAM, Smol'yakov-Tkachenko spectrum model.....	69
Figure 3.5.8(d): Convergence of of \bar{p}^2 (MSP) with y^+ . Point 2; $U_\infty = 50$ m/s; ANSYS Fluent, Smol'yakov-Tkachenko spectrum model.....	69
Figure 3.5.9(a): Convergence of of \bar{p}^2 (MSP) with y^+ . Point 1; $U_\infty = 30$ m/s; OpenFOAM, Rackl-Weston spectrum model.....	70
Figure 3.5.9(b): Convergence of of \bar{p}^2 (MSP) with y^+ . Point 1; $U_\infty = 30$ m/s; ANSYS Fluent, $k-\omega$ model, Rackl-Weston spectrum model.....	70
Figure 3.5.9(c): Convergence of of \bar{p}^2 (MSP) with y^+ . Point 1; $U_\infty = 50$ m/s; OpenFOAM, Rackl-Weston spectrum model.....	70
Figure 3.5.9(d): Convergence of of \bar{p}^2 (MSP) with y^+ . Point 1; $U_\infty = 50$ m/s; ANSYS Fluent, Rackl-Weston spectrum model.....	70
Figure 3.5.10(a): Convergence of of \bar{p}^2 (MSP) with y^+ . Point 2; $U_\infty = 30$ m/s; OpenFOAM, Rackl-Weston spectrum model.....	71
Figure 3.5.10(b): Convergence of of \bar{p}^2 (MSP) with y^+ . Point 2; $U_\infty = 30$ m/s; ANSYS Fluent, $k-\omega$ model [20], Rackl-Weston spectrum model.....	71
Figure 3.5.10(c): Convergence of of \bar{p}^2 (MSP) with y^+ . Point 2; $U_\infty = 50$ m/s; OpenFOAM, Rackl-Weston spectrum model.....	71
Figure 3.5.10(d): Convergence of of \bar{p}^2 (MSP) with y^+ . Point 2; $U_\infty = 50$ m/s; ANSYS Fluent, Rackl-Weston spectrum model.....	71
Figure 3.5.11: Effect of change in turbulence intensity on velocity profile.....	73
Figure 3.5.12: Schematic of flow passed 2-D circular cylinder case.....	74

Figure 3.5.13: a) Coefficient of pressure and b) Scaled skin friction coefficient at different θ , θ being the angle of the points over the body, measured from the trailing edge. (Experimental results are as reported by Revell <i>et al.</i> , 1977)	75
Figure 3.5.14: Streamlines at different time steps.....	75
Figure 3.5.15: Pressure contours at different time steps.....	75
Figure 3.5.16: Schematic of turbulent flow over flat plate cases.....	76
Figure 3.5.17: (a) Grid clustering near the wall, (b) Wall values along the stream-wise length, (c) Normalized velocity vs normalized wall distance, the red line represents the present study [Case II].....	79
Figure 3.5.18: (a) Pressure fluctuations over time, (b) Power spectral density (PSD) of wall pressure fluctuations (c) comparison between results obtained through the present study and spectral synthesizer method (Fluent V14.5) [Case I: Free stream velocity 44.7 m/s].....	79
Figure 3.5.19: (a) Pressure fluctuations over time, (b) Power spectral density (PSD) of wall pressure fluctuations [Case II: Free stream velocity 170 m/s].....	80
Figure 3.5.20: Velocity contour of artificial inflow turbulence generated using UDF in ANSYS Fluent; a) y-velocity contour, b) z-velocity contour	80
Figure 4.2.1: Schematic of TBL excited plate placed on an infinite baffle.....	84
Figure 4.2.2: Four-node quadrilateral element in Cartesian co-ordinate and isoparametric element in natural co-ordinate.....	89
Figure 4.2.3: Orthotropic laminated composite ply sequence.....	92
Figure 4.3.1: Flow chart representing TBL induced structural vibration and radiated sound power estimation using Cholesky decomposition and FE-BE coupled solver.....	97
Figure 4.4.1: Effect of homogeneity in turbulence on plate velocity PSD of all side clamped steel plate at (x, y) (0.15m, 0.12m); flow velocity 44.7 m/s.....	100
Figure 4.4.2: Grid convergence study for all side clamped steel plate at (x, y) \equiv (0.15m, 0.12m); flow velocity 44.7 m/s.....	100
Figure 4.4.3: Numerical and experimental point plate velocity PSD of all side clamped steel plate at (x, y) \equiv (0.15m, 0.12m); flow velocity 44.7 m/s.....	101
Figure 4.4.4: Numerical and experimental averaged plate velocity PSD of all side clamped steel plate; flow velocity 44.7 m/s.....	101
Figure 4.4.5: a) Measured and curve fitted structural loss factor, b) Measured and numerically predicted plate velocity spectrum. Free stream velocity 44.7 m/s; LES.....	102
Figure 4.4.6: Schematic of the longitudinally stiffened panel; simply supported 0.5 m \times 0.35 m \times 2 mm aluminium plate; 20 mm \times 2 mm stiffeners throughout.....	103
Figure 4.4.7: Schematic of the transverse stiffened panel; simply supported 0.5 m \times 0.35 m \times 2 mm aluminium plate; 20 mm \times 2 mm stiffeners throughout.....	103
Figure 4.4.8: Averaged plate velocity PSD (in dB) for two stiffener orientations, i) longitudinal and ii) transverse. Simply supported aluminium panel of dimension 0.5 m \times 0.35 m \times 2 mm aluminium plate; 20 mm \times 2 mm throughout. Flow speed 35.8 m/s.....	104

Figure 4.4.9: Averaged plate velocity PSD, all sides simply supported; flow speed 44.7 m/s; a) Case 1, b) Case 2a & 2b, c) Case 3a & 3b, d) Case 4a & 4b.....	106
Figure 4.4.10: Comparison of the averaged plate velocity PSD for different lamina sequences; all sides simply supported; flow speed 44.7 m/s.....	107
Figure 4.4.11: Sensitivity of averaged quadratic velocity $\langle V^2 \rangle$ (in dB) to grid resolution; simply supported Aluminium plate with $L_x = 0.5\text{m}$, $L_y = 0.35\text{m}$, thickness = 2mm; flow velocity of 44.7 m/s.....	108
Figure 4.4.12: Averaged quadratic velocity, $\langle V^2 \rangle$ (in dB) of simply supported plate with $L_x = 0.5\text{m}$, $L_y = 0.35\text{m}$, thickness = 2 mm subjected to a TBL flow with flow velocity of 44.7 m/s (a) Case I; Aluminium (b) Case II & III; orthotropic (0/90) $_n$ (c) Case IV & V; orthotropic (30/-30) $_n$ (d) Case VI & VII; orthotropic (45/-45) $_n$	109
Figure 5.2.1: Geometric Interpretation of Rayleigh Integral.....	116
Figure 5.2.2: Schematic of TBL-induced vibroacoustic problem through double wall panel	118
Figure 5.2.3: Schematic of a double wall panel configuration backed by an enclosed cavity	122
Figure 5.4.1: Sensitivity of average radiated SPL $L_{p,\text{rad}}$ (in dB) to grid resolution; simply supported Aluminium plate with $L_x = 0.5\text{m}$, $L_y = 0.35\text{m}$, thickness = 2mm; flow velocity of 44.7 m/s.....	129
Figure 5.4.2: Average radiated SPL $L_{p,\text{rad}}$ (in dB) of simply supported plate with $L_x = 0.5\text{m}$, $L_y = 0.35\text{m}$, thickness = 2mm subjected to a TBL flow with flow velocity of 44.7 m/s (a) Case 1; Aluminium (b) Case 2a&2b; orthotropic (0/90) $_n$ (c) Case 3a &3b; orthotropic (30/-30) $_n$ (d) Case VI & VII; orthotropic (45/-45) $_n$	131
Figure 5.4.3: Radiated sound power from vibrating panels for flow speed 44.7 m/s, a) Case 1, b) Case 2a & 2b, c) Case 3a & 3b, d) Case 4a & 4b.....	133
Figure 5.4.4: Comparison of first mode radiated sound power from vibrating isotropic and orthotropic laminated panels for flow speed 44.7 m/s.....	134
Figure 5.4.5: RSP from tensioned plate, with structural damping ratio 0.01 and 0.05.....	136
Figure 5.4.6: RSP from non-tensioned plate (SS), with structural damping ratio 0.01.....	136
Figure 5.4.7: Effect of gap thickness on panel 'b' velocity; similar plate thickness; $U_\infty = 35.8\text{ m/s}$ Both panels are simply supported.....	138
Figure 5.4.8: Effect of gap thickness on panel 'b' velocity; different plate thickness; $U_\infty = 35.8\text{ m/s}$ Both panels are simply supported.....	138
Figure 5.4.9: TBL-induced vibration of double wall configuration; similar plate thickness; gap = 0.1 m; $U_\infty = 35.8\text{ m/s}$ Both panels are simply supported.....	139
Figure 5.4.10: TBL-induced vibration of double wall configuration; different plate thickness; gap = 0.1 m; $U_\infty = 35.8\text{ m/s}$ Both panels are simply supported.....	139
Figure 5.4.11: Schematic of the longitudinally stiffened panel.....	140
Figure 5.4.12: Schematic of the transverse stiffened panel.....	140

Figure 5.4.13: Effect of stiffener orientation; gap = 0.075 m	143
Figure 5.4.14: Effect of stiffener orientation; gap = 0.1 m.....	143
Figure 5.4.15: Effect of stiffening on vibration of panel ‘b’; $t_a = t_b = 2$ mm; gap = 0.1 m; $U_\infty = 35.8$ m/s Both panels are simply supported.....	144
Figure 5.4.16: Comparison of vibration of panel ‘a’ and panel ‘b’; panel ‘a’ is longitudinally stiffened; gap = 0.1 m; $U_\infty = 35.8$ m/s Both panels are simply supported.....	144
Figure 5.4.17: Comparison of vibration of panel ‘a’ and panel ‘b’; panel ‘a’ is transversely stiffened; gap = 0.1 m; $U_\infty = 35.8$ m/s Both panels are simply supported.....	145
Figure 5.4.18: Radiated sound power for single and double panel configurations; gap = 0.1 m; $U_\infty = 35.8$ m/s Both panels are simply supported.....	146
Figure 5.4.19: Pressure PSD inside the cavity measured at a point $(L_{x3}, L_{y3}, -2L_{z3})$; double panel configurations with varying source panel thickness; gap = 0.1 m; $U_\infty = 35.8$ m/s Both panels are simply supported.....	146
Figure 5.4.20: Transmission loss through different panel systems; skin panel is stiffened or unstiffened with thickness (t_a) 1 mm or 1.5 mm. Radiating panel is unstiffened with thickness 1 mm.....	148
Figure 5.4.21: Enclosure pressure PSD at $(L_{x3}, L_{y3}, -2L_{z3})$	150
Figure 5.4.22: Pressure PSD at $(L_{x3}, L_{y3}, -2L_{z3})$ for different gap distance.....	150
Figure 5.4.23: Numerical and analytical plate response prediction of a double-wall system.....	151

LIST OF TABLES

Table 2.1: Evolution of the model coefficients of the standard $k - \epsilon$ model.....	16
Table 3.4.1: Three different 2D meshes.....	55
Table 3.4.2: Geometry and meshing information; 2D LES study of TBL over flat plate.....	58
Table 3.4.3: Mesh sensitivity study.....	58
Table 3.5.1: Point 1; $k - \omega$ SST; OpenFOAM; $U_\infty = 30\text{m/s}$	62
Table 3.5.2: Point 1; $k - \omega$ SST; Fluent; $U_\infty = 30\text{m/s}$	62
Table 3.5.3: Point 2; $k - \omega$ SST; OpenFOAM; $U_\infty = 30\text{m/s}$	62
Table 3.5.4: Point 2; $k - \omega$ SST; Fluent; $U_\infty = 30\text{m/s}$	62
Table 3.5.5: y^+ calculation for $U = 30\text{m/s}$	64
Table 3.5.6: y^+ calculation for $U = 50\text{m/s}$	64
Table 3.5.7: Model parameters for estimation of velocity and MSP sensitivity to turbulence intensity.....	72
Table 3.5.8: Change in MSP due to varying turbulence intensity.....	73
Table 3.5.9: Geometry and meshing information for flow over flat plate cases.....	76
Table 3.5.10: Grid sensitivity study based on turbulent boundary layer parameters.....	77
Table 4.4.1: Accuracy of $k - \omega$ model.....	98
Table 4.4.2: Model properties	99
Table 4.4.3: measured structural loss factor (Han <i>et al.</i> , 1999).....	102
Table 4.4.4: Frequency (Hz) and mode numbers for aluminium and different orthotropic laminated composite plates.....	105
Table 4.4.5: TBL-induced plate velocity PSD (dB, ref. $10^{-12} \text{ m}^2/\text{s}^2$) at the first mode; flow velocity 44.7 m/s.....	106
Table 4.4.6: Central deflection ($\times 10^{-4}\text{m}$) of 0.5m x 0.35 m simply supported orthotropic plates subjected to a uniformly distributed load of $5.714\text{N}/\text{m}^2$	110
Table 5.4.1: Three different finite element grid systems for grid sensitivity study.....	128
Table 5.4.2: Frequency (in Hz) and mode numbers for simply supported rectangular panels having dimensions 0.5 m x 0.35 m x 0.002 m.....	130
Table 5.4.3: Average radiated SPL (in dB) from rectangular simply supported 0.5 m x 0.35 m x 0.002 m panels placed in a baffle subjected to a flow velocity of 44.7 m/s.....	130
Table 5.4.4: Model properties for the validation study of TBL-induced sound radiation.....	135
Table 5.4.5: First ten frequencies (Hz) and mode numbers for tensioned and non-tensioned plates.....	136
Table 5.4.6: Flow and structural properties for the double wall energy transmission case.....	137
Table 5.4.7: Uncoupled and coupled frequency (Hz) Uncoupled.....	142
Table 5.4.8: Model properties for the double wall backed acoustic enclosure properties of the external flow.....	149
Table 5.4.9: First eight frequencies (Hz) upto 1000Hz.....	149

Table 3.A.1: Experimental and numerical parameters; Point 1; $U_\infty = 30$ m/s.....	160
Table 3.A.2: Experimental and numerical parameters; Point 1; $U_\infty = 50$ m/s.....	161
Table 3.A.3: Error in \bar{p}^2 estimation (in %); point 1; Smol'yakov-Tkachenko model.....	162
Table 3.A.4: Error in \bar{p}^2 estimation (in %); point 2; Smol'yakov-Tkachenko model.....	162
Table 3.A.5: Error in \bar{p}^2 estimation (in %); point 1; Rackl-Weston Model.....	162
Table 3.A.6: Error in \bar{p}^2 estimation (in %); point 2; Rackl-Weston Model.....	162

CHAPTER 1: INTRODUCTION

1.1 BACKGROUND

Sound and vibration are much older than humanity. The elastic wave generation due to any vibration phenomena is eternal. The big bang was a vibration on the space fabric itself. But human beings exploited sound and vibration to the fullest possible extent to make life easier. The radio and ultrasound are the inventions any species can be proud of. Apart from the usage of the radio wave in the defence and marine sectors, communications, medical tests, and even structural damage detection is possible with the help of non-invasive ultrasound testing facilities.

On the other hand, in this journey of development, several unwanted vibration and sound called noise have been created. This noise is detrimental to human and animal health when exposed for a prolonged time, especially low-frequency noise [1]. Hearing impairment, ischemic heart disease, hypertension, annoyance, and sleep disturbance are very common and severe problems one can experience [2]–[5] when exposed to this unwanted noise for a long duration. Not only human health but the structures also get affected when exposed to excessive noise and vibration levels. Stress and fatigue life reduction [6], [7] are the most common problems for the structures.

Therefore, it is necessary to understand the generation and transmission mechanism of the noise and vibration problem in the day-to-day mechanical systems, especially in the transportation industries such as aerospace, automobile, marine or high-speed railways where the health of the commuters and crews, environmental pollution and structural safety are of paramount importance. This is particularly important in the modern era with exponential population growth and high demand for transport vehicles.

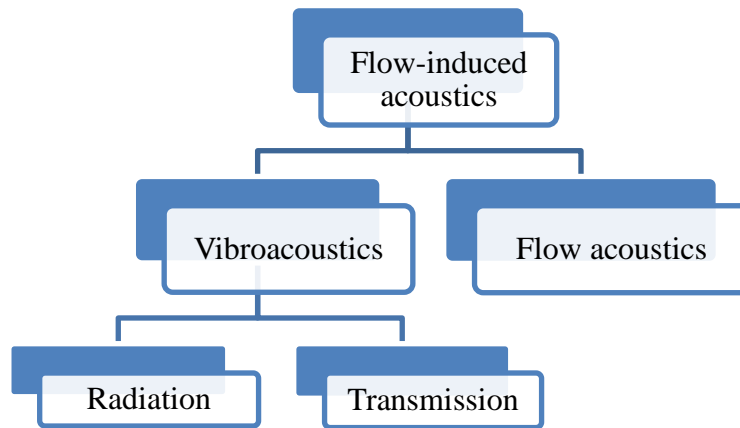
Although the initiation of vibroacoustic studies can be dated back to 3000 BC, the modern study on waves and acoustics can be attributed to Galileo Galilei (1564-1642) who established a correlation between pitch and frequency. Subsequently, a great number of studies have been performed involving sound generation, radiation, transmission, and even attenuation. In acoustics, the sound generation mechanism has broadly been classified into three categories, namely

- 1) Structure-induced: Sound caused by mechanical vibrations.
- 2) Flow-induced: Sound produced by a turbulent flow.
- 3) Thermal-induced: Sound caused by local variation in the temperature of the fluid.

There are many shaded areas in-between that require further studies. But, at this point, this classification is sufficient to proceed. If one keeps aside the structure-induced and thermal-induced sound generation, turbulent flow or to be precise turbulent boundary layer (TBL)-induced sound and vibration problems can be again classified into two categories, a) flow acoustics, which deals with sound generation within the flow itself, and b) structural acoustics or vibroacoustics, which deals with the sound and vibration produced due to flow-induced structural excitation. This genre of study is particularly important for an aircraft or an automobile where outer panels of the vehicles

are subjected to turbulent boundary layer (TBL) excitation and the resulting vibration produces noise that either radiates into the free field or gets transmitted into the enclosed vehicular cabin.

The flow-induced vibroacoustic problems involve two interaction phenomena, fluid-structure interaction, and structure-acoustic domain interaction. Depending upon the accuracy required, the interactions or energy transfer is formulated as one-way or two-way problem. Although there are problems where scattering sounds are significant contributors, radiation problems are predominant in the case of the vibroacoustic problems associated with the transportation industries. Sound radiation problems can be subdivided into two types of problems, a) radiated sound power into the free field, and b) transmission problem into the enclosed cavity.



The very first and one of the key steps of TBL-induced vibroacoustic modelling is to estimate the TBL pressure fluctuations. Real-time TBL pressure fluctuations can be measured, with a large experimental setup, either by using a wind tunnel [8]–[15] or an in-flight test [16]–[18]. They are really big facilities, and can not always be a feasible option. The TBL excitation is random and produces a broadband signal. To capture this signal, even if one attempts to use the established semi-empirical pressure spectrum models, the TBL parameters are to be measured through experimentation. Therefore, one of the rational options that remain available is to model turbulence, “the most important unsolved problem of classical physics.” (Richard Feynman).

“When I meet God, I am going to ask him two questions: why relativity? And why turbulence? I really believe he will have an answer for the first.” Werner Heisenberg.

However, despite the challenges involved, turbulence modelling is attempted for the last two centuries, starting with French engineer and physicist Claude-Louis Navier (1822) and Anglo-Irish mathematician and physicist George Gabriel Stokes (1842-1850). They incorporated the non-linear fluctuating velocity components in the Reynolds stress term in the famous Navier-Stokes (NS) equations. To estimate the mean velocity and pressure values one has to close the NS equations by estimating the Reynolds stress term. Joseph Valentin Boussinesq first attempted to close the NS equations with an eddy viscosity term (1877). In order to capture the varying eddy viscosity with the varying distance from the wall, Ludwig Prandtl introduced an additional term ‘mixing length’, for the wall-bounded flows. Subsequently, several Reynolds-averaged Navier

Stokes (RANS) steady-state turbulence models were developed based on these hypotheses [19]–[25]. They are Spalart–Allmaras (SA), $k - \omega$, $k - \epsilon$, $k - \omega$ Shear Stress Transport ($k - \omega$ SST), realizable $k - \epsilon$, etc., and are discussed later in this thesis. Joseph Smagorinsky first proposed a subgrid-scale eddy viscosity model for a large eddy simulation (LES) modelling technique [26], that was later supplemented with an important system coefficient [27] and implemented in a 3D turbulent channel flow [28]. LES is an important simulation technique that optimizes the accuracy and computation cost between RANS and direct numerical simulation (DNS). Detailed mathematical development of this technique is discussed later on.

The present work uses computational fluid dynamics (CFD) flow modelling to estimate the pressure fluctuations over a flat plate. RANS simulation provides global mean flow parameters that are used as inputs to the various semi-empirical wall-pressure spectrum models [16], [17], [29]–[42]. Empirical or semi-empirical TBL wall-pressure spectrum models are a popular and efficient choice to estimate the TBL loading over a structural panel, for simple flow and geometry cases. However, the inputs to these models are traditionally obtained from experiments. Therefore, the application of RANS simulations makes the process more efficient and cost-effective. The spectrum models with RANS inputs eventually estimate the wall-pressure power spectral density (PSD) values. In a different approach, the LES technique is used to directly estimate the local wall-pressure fluctuations and transformed into pressure PSD using Welch’s technique [43]. In order to obtain a continuous perturbation, artificial inflow turbulence is generated numerically and used at the inlet of the domain. This is an improvement to the available commercial LES solvers, such as, ANSYS Fluent. It is worth noting that for all the CFD simulations the wall under the turbulent boundary layer (TBL) is considered to be rigid. Once, the pressure fluctuations are estimated they are used as the loading to the same wall and the dynamic response is estimated considering the structural wall as flexible. In this process, multiple single-point wall-pressure PSD are correlated using the spatial coherence function [44], [45], and the cross-PSD is obtained, which is distributed over the plate. This wall-pressure cross-PSD plays a very important role as input forcing in the TBL-structure interaction modelling as discussed next.

TBL-induced panel vibration can be efficiently studied experimentally. However, this involves time and requires expensive set ups. Analytical and numerical techniques are most common to overcome this problem. It is already reported [46]–[51] that the FE approach of structural modelling provides the flexibility to model different structures having complex geometries and boundary conditions, thus making the work more versatile. Following the FE model of the structural panel, free vibration analysis is performed and these modal responses serve as the basis to develop the frequency response function (FRF). Subsequently, this FRF is coupled with previously obtained TBL wall-pressure cross-PSD, and the structural response is estimated in terms of displacement or velocity PSD.

It is quite obvious that this TBL-excited panel will either radiate sound in the free field or will transmit into an enclosed space depending on the situation. The sound radiation and/or transmission phenomenon due to TBL-induced vibration can be modelled either analytically or

numerically. An integral function based elemental radiator approach is often used to model the sound radiation behaviour from a flat panel. Following this approach RRM can be developed and can be coupled with panel velocity PSD to obtain the radiated sound power [18], [52]–[55]. Alternatively, wall pressure spectrum could be decomposed using Cholesky’s technique and this decomposed pressure fluctuations may be employed and radiated sound power is computed.

The transmission of sound into an enclosed space can be modelled numerically following a FE-based technique, a better alternative to the previously reported analytical modal expansion technique [56], [57], in terms of geometry and boundary conditions. In this modelling, first, the FRF for the panel and the cavity are calculated in the coupled condition. Subsequently, the TBL force is coupled with the panel FRF and cavity FRF leading to the estimation of panel vibration and sound pressure level into the enclosure. This model is extended further for a double wall panel system separated by a smaller cavity and backed by a larger enclosure, which is a more practical replication of a modern-day aircraft or automobile cabin, subjected to external turbulent disturbance.

1.2 MOTIVATION FOR THE PRESENT RESEARCH

Through various research, it is observed that the transport vehicles during its operation is subjected to various noise sources among which low-frequency noise is mostly responsible for human annoyance. However, with the rapid improvement in the engine technology and several isolation techniques the mechanical sources of noise have been mostly taken care of while TBL still remains one of the key noise sources. TBL-excited flexible panels produce broadband noise levels where the low-frequency regime becomes predominant due to the first few fundamental modes of the structure and their coupling with the initial acoustic modes. This low-frequency noise is particularly detrimental when commuters experience this for a very long time. Therefore, it is essential to address and understand this flow-induced vibroacoustic problem, especially in the low-frequency regime, in order to produce a more user-friendly transport vehicle attracting a larger customer base.

It is in this context; the present thesis work focuses on the TBL-excited vibroacoustic modelling for a flexible panel in a numerical framework. As the prediction of the TBL pressure fluctuations is essential for the subsequent modelling, various techniques to estimate the TBL pressure fluctuation are explored. Special emphasis is given to computational turbulence modelling. The sensitivity of the estimated mean square pressure (MSP) to the different turbulence models and model parameters is studied extensively in cohort with different wall pressure spectrum models, and the best predicting combined configuration is proposed. Separate attempts are made to decompose the wall pressure spectrum to obtain frequency-dependent wall pressure spectra, and to directly compute real-time wall pressure fluctuations.

As the physical model suggests, the flexible structural panel, if excited by any external disturbance, perturbs the adjacent acoustic medium and generates sound. Now, if there is no or negligible reverberation experienced, the free-field sound radiation model can be developed for

the half-space. If the panel is backed by a relatively smaller enclosure with a significant effect of the acoustic medium on the panel, the two-way coupled (fully or strongly coupled) model becomes imperative. In the present thesis work, both one-way and two-way coupling formulation is employed. The TBL-excited panel vibration and subsequent sound radiation or transmission models are developed in a FE environment, which provides essential flexibility in terms of geometry and boundary condition of the structural panel. The present work can therefore be broadly classified into the following subsections:

1. Estimation of TBL-pressure fluctuations
2. TBL-excited vibration of the flexible panel using the estimated pressure fluctuations
3. Estimation of acoustic radiation and transmission due to a TBL-excited vibrating panel

Based on the physical understanding, the basic components of the present work thus can be listed as follows:

- TBL wall-pressure estimation
 - Semi-empirical model with experimental feed
 - Semi-empirical model with CFD-RANS feed
 - LES with artificial inflow turbulence
- TBL-induced vibration model
 - Structural model
 - Fluid-structure interaction model
- Vibroacoustic model for the transmission problem
 - Structural model
 - Acoustic model
 - Coupling of structural and acoustic domains

A brief introduction of the chapters presented in this dissertation is discussed next.

1.3 ORGANIZATION OF THE DISSERTATION

The present dissertation contains six chapters. The current chapter, i.e., Chapter 1, provides a brief introduction to the TBL-induced vibroacoustic problem, and its adverse aspects related to human and structural health. A discussion on the approach toward the numerical modelling is also provided here.

A detailed review of the past research works on turbulence modelling, TBL wall-pressure estimation, and TBL-excited vibroacoustic modelling techniques is presented in Chapter 2. Both the sound radiation and transmission modelling are reviewed. The review is broadly classified into four sections:

1. Past works on TBL wall-pressure estimation (analytical, semi-analytical, computational)
2. Past works on TBL-excited structural vibration
3. Past works involving the TBL-induced free-field vibroacoustic problem

4. Past works involving the TBL-induced coupled structural-acoustic problems in an enclosed field

Through a critical appraisal of the past works, the scope of the present research work is comprehended, and the objectives of the present dissertation are determined. The required steps to attain the objectives are also described.

One major part of the thesis work is TBL wall pressure estimation, which is covered in detail and presented in Chapter 3. At first, semi-analytical models are explored in light of their prediction capability with respect to the wind tunnel experiment or in-flight tests. Next, a detailed work is performed to identify the sensitivity of mean square pressure (MSP) to the CFD-RANS turbulence model parameters. This CFD study can particularly be important in the early design stages where there is no reference experimental TBL parameters available. The LES technique powered by artificial inflow turbulence is performed to obtain real-time wall-pressure fluctuations and the findings are presented in the present chapter.

Once the TBL wall pressure is obtained, the pressure is used as the forcing function that excites the flexible panel beneath the TBL. Chapter 4 contains the numerical TBL-structure coupled modelling in the FE environment. The baffled structural panel is modelled using a four-node linear quadrilateral isoparametric finite element. The dynamic analysis of the panel eventually estimates the FRF of the structural panel, which in turn gets coupled with the TBL cross-PSD to finally provide the panel vibration. The numerical results are validated with the reported experimental results, for both point and surface averaged velocity PSD. The structural panels are modelled with different boundary conditions, stiffener orientations, and orthotropic lamina sequences. The panel vibration results are presented and discussed with reference to the unstiffened and isotropic panel case. In a separate study, Cholesky's technique is used to decompose the already obtained wall pressure spectrum, and the resulting frequency-dependent pressure fluctuation is employed to estimate complex panel response and presented in the later part of this chapter.

Chapter 5 addresses in detail both radiation and transmission problems due to the TBL-excited vibrating structural panel. In the first part of this chapter, a weak one-way coupling is assumed for the free-field radiation problem and is detailed with governing equations, numerical modelling, and implementation of the radiation resistance matrix (RRM). This RRM is then coupled with the panel velocity PSD to compute the radiated sound power. The numerically estimated radiated sound power is validated with established analytical results and is presented. In the validation work, structural panel is modelled both as a tensioned and a non-tensioned panel. Subsequently, TBL-induced free-field sound radiation estimation is carried out for different orthotropic lamina sequences. This work is then extended for double wall panels also, where the fully coupled structure-acoustic modelling is performed, as discussed in the following part.

In the second part of the Chapter 5, a FE model is developed to capture the mechanism of sound transmission into an enclosed cavity due to TBL-excited flexible panel vibration. The structural panel is modelled as described in Chapter 4. The acoustic domain is modelled as an 8-

node brick element with pressure as another degree of freedom. The detailed mathematical formulation to couple the structural and the acoustic domains is presented. The TBL cross PSD is used as the force to finally estimate the panel vibration and the pressure within the enclosure in a fully coupled condition. This work is further extended for a panel-gap-panel-cavity system. The required formulation is developed and numerically implemented. The results are validated with previously reported analytical results. This work is then performed with different panel and gap thicknesses, the results are presented and discussed.

Finally, Chapter 6 concludes the dissertation on the basis of the works presented in the previous chapters. It also summarizes the efforts and contributions of the present research work. The scope of further research is also discussed.

CHAPTER 2: LITERATURE REVIEW

2.1 INTRODUCTION

The study of TBL-excited structural vibration and the resulting sound radiation and transmission mechanism is a complex and multidisciplinary subject. The study deals with fields like fluid dynamics, structural mechanics, vibration, acoustics, and their coupling and use them as components of the overall study. Therefore, it is crucial to understand each one of these components separately to comprehend their mutual coupling in the later part. The estimation of TBL pressure fluctuations, modelling of TBL-structure interactions for calculating panel vibration responses, and coupled structural-acoustic modelling to simulate sound transmission and radiation phenomena make up the primary focus of the present study. These various areas have been the focus of work of several researchers, which ultimately improved the overall TBL-induced vibroacoustic study.

It is important to note at this point that because the current research focuses on TBL-induced vibroacoustics for flexible panels, the review of literature is kept limited to the scope of the flow-induced vibration and sound radiation/transmission study, along with various supporting techniques. In order to keep a focus on the main theme of the present study the study on panel vibration due to mechanical loading or acoustic energy transmission through single or double rigid walls is kept out of the purview of the literature review. A succinct classification of the earlier literature is given in the following subsection.

2.2 OVERVIEW AND CLASSIFICATION OF PREVIOUS LITERATURE

The focus of the current work is on the elements of flow-induced vibroacoustic study, as the introduction suggests. As a result, the literature review of the earlier works is also divided into a variety of pertinent sections and discussed in the following few subsections. Estimating the TBL wall-pressure fluctuations is one of the key elements. Several researchers and research groups have carried out studies to estimate pressure using various methods, which are described in subsection 2.3. These methods include a) analytical and semi-analytical pressure spectrum models; b) computational fluid dynamics (CFD) simulations; RANS simulation to feed semi-analytical pressure spectrum models; and c) LES to measure direct real-time wall pressure fluctuations. The results of the wind tunnel experiments or the data from in-flight tests serve as the foundation for all of the empirical or semi-analytical pressure prediction models. There are a very few works that recognize the use Cholesky's method to decompose the wall pressure spectrum in the frequency domain so that it can be used in the ensuing vibroacoustics studies. However, no explicit study using the Cholesky's technique is reported so far. Subsection 2.4 discusses the TBL-structure coupling models that have previously been developed and reported. The earlier research on coupled structure-acoustic modelling methods for the free-field sound radiation from TBL-induced vibrating flexible panels is covered in this section. This section reviews the structural modelling

of stiffened and tensioned panels with a focus on the modelling research for orthotropic laminated composite panels. The discussion includes both analytical and numerical developments.

It is necessary to understand the behaviour of the fully coupled structure-acoustic domain in order to model sound transmission into an enclosure. Therefore, with a focus to estimate sound transmission into an enclosed cavity, previous works on structure-acoustic coupling techniques are reviewed in subsection 2.5.

2.3 REVIEW OF PREVIOUS WORKS ON TBL WALL PRESSURE ESTIMATION STUDY

The initial step in the flow-induced vibroacoustic study, TBL wall pressure estimation determines how accurately the subsequent vibration and sound radiation/transmission calculations will be made. On the other hand, cost is also a major factor in real-world projects. As a result, the accuracy and expense of earlier TBL wall pressure estimation attempts are kept into the account.

2.3.1 Analytical and semi-analytical techniques

Analytical formulae were the only practical choice for wall pressure estimation prior to the rapid expansion of computational or large experimental facilities. Kraichnan [58] developed an analytical model in one of the earliest attempts to forecast wall-pressure fluctuations brought on by turbulence. A similarity argument is used to describe how his work expresses the wave number spectrum of the pressure fluctuation distribution over the surface of the plate in terms of transforms of two-point velocity correlations. The spectrum and correlation function of the surface pressure distribution is compared to the corresponding functions for a homogeneous turbulent flow using an idealized model of TBL flow. It is concluded that the mean velocity profile and the two-point quadratic correlation of the fluctuating velocity component perpendicular to the boundary surface should be the only variables that significantly influence the pressure fluctuations. There aren't many presumptions, such as adiabatic conditions, low compressibility, and a slow rate of boundary layer growth.

In his analytical work, Lawson [39] derived the governing equations for the pressure fluctuations in TBL from the known empirical formulations of RMS pressure fluctuations, obtained from experimental results and referring to incompressible Navier-Stokes equations. The attached boundary layer is discussed with the advancement of a new hypothesis, creating the physical framework for understanding pressure fluctuations. Thereafter this approach is applied to separated boundary layers also. Failure of some assumptions made in the previous case indicated a new source of pressure fluctuation in the separated boundary layer case. Lawson pointed out that Kraichnan found the ratio of the turbulence-turbulence contribution to that of the turbulence-mean shear as 1:32, which is estimated by Lilley-Hodgson [59] as 1:20. This suggests turbulence-mean shear interaction to be the predominating factor for the wall-pressure fluctuations. But, as per Corcos [44], the ratio is 1:1.6 which keeps the issue alive.

With the rapid advancement in experimental fluid mechanics empirical and semi-empirical models were developed to estimate TBL wall pressure. Turbulent Boundary Layer (TBL) wall pressure spectrum models aim to predict the statistical properties of wall pressure fluctuations in turbulent boundary layer flows. These models have been developed based on empirical formulations and theoretical considerations. In this section, several commonly used TBL wall pressure spectrum models are discussed in detail.

Lighthill's Acoustic Analogy

Lighthill's acoustic analogy provides a theoretical framework for predicting the wall pressure spectrum in turbulent flows. According to this analogy, the wall pressure fluctuations are related to the fluctuating vorticity field near the wall. Lighthill's formulation expresses the wall pressure spectrum as a convolution of the wall-shear spectrum and the quadrupole source spectrum. The wall-shear spectrum is often approximated using empirical relations derived from experimental data, while the quadrupole source spectrum can be estimated based on the flow conditions and geometries.

Curle's Analogy

Curle's analogy, similar to Lighthill's acoustic analogy, relates the wall pressure fluctuations to the vortex sheet strength along the wall. It assumes that the vortex sheet acts as a distributed noise source. Curle's formulation provides an expression for the wall pressure spectrum in terms of the vortex sheet strength and its spatial distribution. The vortex sheet strength is typically determined using experimental data or by solving appropriate integral equations. Curle's analogy has been widely used in aeroacoustic studies to estimate the noise generated by turbulent boundary layer flows.

Kirchhoff's Analogy

Kirchhoff's analogy is based on the assumption that the wall pressure fluctuations can be represented as the diffraction of incident sound waves by an equivalent scattering surface. This analogy considers the reflection and transmission coefficients of the equivalent surface to calculate the wall pressure spectrum. The coefficients are derived from the knowledge of the mean flow and acoustic properties of the boundary layer. Kirchhoff's analogy is particularly suitable for high-frequency sound predictions in the near-field of turbulent boundary layers.

The Compressible Fluctuating Pressure Equation (CFPE) Model

The CFPE model was developed to predict the wall pressure spectrum in compressible turbulent boundary layers. It incorporates the effects of compressibility and temperature fluctuations on the wall pressure fluctuations. The CFPE model uses a linearized form of the compressible Navier-

Stokes equations to derive an equation for the wall pressure spectrum. The model requires the knowledge of the mean flow properties, turbulence statistics, and the sound speed of the fluid. The CFPE model has shown good agreement with experimental data for high-speed flows.

Spectral Element Method (SEM) Models

Spectral Element Method (SEM) models employ high-order spectral discretization techniques to solve the linearized compressible Navier-Stokes equations for the prediction of wall pressure spectra. These models capture the complex spatial and temporal characteristics of wall pressure fluctuations in turbulent boundary layers. SEM models have been successful in predicting the wall pressure spectra in a wide range of flow conditions, including low-speed and high-speed flows. They provide detailed information about the spatial distribution of the wall pressure fluctuations.

Data-driven Models

Data-driven approaches, such as machine learning techniques, have gained attention in recent years for modelling turbulent boundary layer wall pressure spectra. These models utilize large datasets of experimental or numerical simulations to learn the mapping between flow features and wall pressure fluctuations. Machine learning algorithms, such as artificial neural networks and support vector machines, can capture the nonlinear relationships and provide accurate predictions. Data-driven models offer potential advantages in capturing complex flow physics and reducing the reliance on empirical formulations.

It is important to note that the choice of TBL wall pressure spectrum model depends on the specific flow conditions, desired accuracy, available data, and computational resources. Each model has its strengths and limitations, and careful consideration should be given to the underlying assumptions and validation against experimental results. Common approaches include the one-dimensional PSD models, which provide frequency domain representations of wall pressure spectra. Other models incorporate more complex representations, such as the superposition of discrete frequencies or wavelet-based methods. These empirical models often involve adjustable parameters, which are calibrated using experimental data.

Fundamentally, three types of empirical and semi-empirical TBL models are reported in the literature namely a) Mean-square pressure models, b) single-point wall-pressure spectrum, and c) the normalized wavenumber-frequency spectrum. The mean-square pressure is a measure of the total energy due to TBL pressure fluctuation where the single-point wall pressure spectrum and normalized wavenumber-frequency spectrum essentially represent the same spectral information but in different forms.

Exploration of pressure fluctuations associated with turbulent boundary layers has been a subject of significant interest spanning several decades. The primary focus on turbulent boundary layers and pressure fluctuations revolves around concerns related to structural vibration and noise generation. Gaining insights into the behaviour of velocity and pressure fluctuations arising from

turbulent boundary layers is crucial for understanding the origins of noise generation. Consequently, numerous researchers have dedicated themselves to extensive experimental and computational investigations within this realm.

In the year 1962, Willmarth and Wooldridge [8] undertook an experimental study with the aim of quantifying wall-pressure fluctuations. Their findings revealed that the fully turbulent tube flow exhibited the highest convection speed for low-frequency pressure fluctuations. Additionally, they observed that both small- and large-scale wall-pressure fluctuations displayed similar transverse and longitudinal scales. Williams and Lyon [60] formulated an equation for the resonant vibration response of a flat plate in the presence of a low-speed turbulent boundary layer. Pioneering work in this field was also carried out by Corcos [44], [61], who explored various aspects of near-wall turbulent boundary layer flow. In 1963, Corcos [44] investigated the effect of transducer size on measurements, highlighting the presence of significant errors associated with certain sizes. Furthermore, Corcos proposed a model for the frequency cross spectrum, which later prompted refinements by subsequent researchers. In a separate study, Corcos [61] examined statistical properties of the pressure field at the wall of turbulent attached shear flows. Willmarth and Roos [62] examined the impact of finite-sized circular transducers on wall-pressure measurements beneath a turbulent boundary layer. In 1964, Williams [63] put forth a compressibility-based theory describing surface pressure fluctuations within the boundary layer on a rigid surface. Chase [64] conducted measurements of the area-averaged turbulent boundary layer pressure spectrum using transducers of varying stream wise sizes, incorporating arbitrary spatial responses in the high-frequency domain. Additionally, Chase proposed an approximate form of the wave number frequency spectrum of pressure on the wall for the turbulent boundary layer, introducing the elliptic model [65], [66]. In 1982, Efimtsov [29] carried out an experimental investigation to measure pressure fluctuations on the surface of aircraft. The tests were conducted at large Reynolds numbers and a Mach number range of 0.41 to 2.1. Another experimental study conducted in a wind tunnel by Schewe [67] investigated the statistical properties of the characteristic wall pressure structures by signal averaging, its connection with the phenomena occurring in the buffer layer and visual analysis in the time domain. This work involved the measurement of wall-pressure fluctuations using pressure transducers of different sizes. Schewe emphasized the significance of maintaining a small ratio between the pressure transducer size and the smallest relevant length-scale of the flow. Experiments conducted by McGrath, [68] led to obtaining rational and consistent surface pressure fluctuation results for zero and favourable pressure gradient flows. Chandiramani [69], [70] modified the theory of sound transmission across an isotropic flat plate to be applied for high convective wavenumbers.

The investigation of turbulence modelling in aeroacoustics and underwater sound has garnered significant attention. Mellen [71] conducted a study on convective turbulence modelling and noted that the predictions of the Corcos [44] model were excessively high below the convective peak. To address this, Mellen proposed the elliptic model as a modification to the frequency cross spectrum of the Corcos model. Choi and Moin [72] performed a numerical

investigation utilizing direct numerical simulation (DNS) to compute the three-dimensional frequency wavenumber spectrum of wall-pressure fluctuations. Chase [73] examined the properties of the wave-vector-frequency spectrum of fluctuating pressure in a turbulent boundary layer flow over a smooth plane at low Mach numbers. Farabee and Casarella [35] carried out an experimental investigation on the spectral features of wall-pressure fluctuations beneath the turbulent boundary layers. Their results demonstrated the sensitivity of the wall-pressure field to energized structures in the outer flow. They recognized the turbulent source regions within the boundary layer as an important contributor to the frequency spectra of low-, mid-, and high-frequency ranges of the wall pressure field and frequency cross-spectra of the wall pressure fluctuations beneath a fully developed turbulent boundary layer. Keith *et al.* [74] compared turbulent boundary layer wall-pressure spectra from multiple studies. Mellen [66] further studied the analytical model proposed by Corcos and extended the comparison between the Corcos model and the elliptic model, including implications for wave vector filter experiments. Lueptow [75] investigated the impact of pressure transducer size on the accuracy of wall-pressure measurements beneath a turbulent boundary layer. Manoha [76] conducted an experimental investigation in a hydrodynamic tunnel to validate available semi-empirical models. The comparison between simulated and measured estimators indicated that Chase's model outperformed other models in the low wavenumber and convective domains. Additional investigations in the field of wall-pressure fluctuations in turbulent boundary layers were conducted by Bull [77], Sawada *et al.* [78], and Abraham and Keith [79]. Experiments of Gravante *et al.* [80], indicated that the wall region of the boundary layer is the governing source of the high-frequency pressure fluctuations. Efimtsov *et al.* [33] performed extensive investigations on forward and backward steps and proposed pressure fluctuation spectra for each case. Smol'yakov [81] developed a method for calculating wall-pressure spectra in turbulent boundary layers based on modelling the wavenumber spectrum of the sources resulting from the interaction of turbulence with mean shear. The calculated spectra and root mean square (RMS) values of pressure fluctuations were compared with experimental data, showing good agreement. Experiments to measure surface pressure fluctuations beneath low Reynolds number, two-dimensional turbulent boundary layers and high Reynolds-number three-dimensional boundary layers were performed by Goody and Simpson [14]. Tkachenko [82] examined the conditions for the existence of similarity in the non-dimensional cross spectra for frequency and spacing. Wang [83] developed a numerical procedure using a combination of large eddy simulation (LES) with wall modelling to simulate wall-bounded flows. This cost-effective method provided accurate predictions of low-order velocity statistics. Smol'yakov [84] continued investigations on the noise generated by turbulent boundary layers over plates and demonstrated that the logarithmic region of the velocity profile contributed to a zone of quadrupole noise spectrum with a hyperbolic frequency dependence. The study also showed that the surface roughness increased the radiation levels of a boundary layer flow in a certain frequency range. Efimtsov *et al.* [85] analyzed flight test data of pressure fluctuations (on Tu-144LL) in front of forward-facing and behind backward-facing steps across a Mach number range of 0.57 to 1.97.

Efimtsov *et al.* [86], [87], and Smol'yakov and Tkachenko [84] conducted studies on measuring wall-pressure fluctuations under different conditions. In 2004, Goody [41] presented an empirical model for the surface pressure spectrum, which demonstrated good agreement with experimental data. Rackl and Weston [16] adjusted the Efimtsov model based on in-flight test data [17] and was eventually established as the best predictor of the wall pressure spectrum in the low to medium frequency. Rocha and Palumbo [88] investigated the sensitivity of fuselage sidewall sound radiation corresponding to changes in TBL parameters. Wall pressure fluctuations measurement and direct measurements of wavevector-frequency spectra have been performed by Salze *et al.* [13]. A statistical post-processing technique was developed by Blitterswyk and Corey [89] for extracting coherent motions using intermittency of energy in the wavelet coefficients. Shahmohamadi and Rashidi [90] conducted experiments on a flat plate in a wind tunnel and suggested two new correlations for the friction coefficient and boundary layer thickness as functions of Reynolds number. In a very recent work Thomson and Rocha [12] adjusted Goody model based on flight test experiments conducted near the range of $M = 0.7$ and found the adjusted model to predict the magnitude and the shape of the pressure spectrum really well. They extended their work on semi-empirical pressure spectrum modelling to favourable pressure gradient [91].

Data from the wind tunnel experiments or CFD are fetched into semi-empirical model to estimate zero pressure gradient (ZPG) turbulent boundary layer (TBL) wall-pressure spectrum models with different TBL parameters. There are several semi-empirical single-point wall-pressure spectrum models available and widely used for practical purposes. However, these models are essentially dependent on the feeding of the experimental data. Here, a very interesting attempt was made by Leneveu *et al.* [92] to combine CFD simulation data and semi-empirical pressure spectrum models. They carried out CFD simulation using OpenFOAM solver, replicated the experimental data of Salze *et al.* [13], [93], and used these mean flow parameters as inputs to the semi-empirical pressure spectrum model. This work prepared the base of a reliable and efficient technique for wall pressure estimation, which is explored in detail and reported in Chapter 3.

Computational Fluid Dynamics (CFD)

Computational Fluid Dynamics (CFD) enables the estimation of turbulent boundary layer wall pressure by simulating the complex behaviour of turbulent flows near solid surfaces. By selecting appropriate turbulence models, defining accurate boundary conditions, optimizing mesh resolution, and configuring the solver settings, engineers can obtain valuable insights into the pressure distribution along the wall. CFD plays a crucial role in the design and analysis of various engineering systems, contributing to improved performance, safety, and efficiency. Generally, the CFD models can be classified in three broad categories.

Reynolds-averaged Navier Stokes (RANS) can accurately predict the time-averaged global flow quantities. However, it is unable to capture the varying quantities at their local scales. Models for Large Eddy Simulation (LES): These models model the eddies of smaller length scales and resolve

the large eddies up to a scale that is almost equal to the grid size. These models are able to predict the varying values up to a length scale, which is thought to hold the majority of the total energy. The turbulence phenomenon in actual flow problems can therefore be well approximated by these models. The most reliable and computationally intensive method is supposed to be the direct numerical simulation (DNS), where unsteady Navier-Stokes equations are solved at every node. This method is the most trustworthy, but it comes at a high computational cost.

Reynolds-averaged Navier Stokes (RANS) Modelling

The Reynolds stresses are the ones that are to be computed, to find a solution to the RANS Equation. To solve this, Boussinesq made an assumption in 1877 known as the Boussinesq hypothesis or Eddy-viscosity model (EVM). In this hypothesis, turbulence, here fluctuations which are in the form of eddies, are considered as particles in Brownian motion, although turbulence is not random in nature. But turbulence is caused by the shear of faster-moving fluid particles over slower-moving fluid particles and there is a momentum transfer from the faster to the slower-moving fluid particles. This can be further justified by saying that momentum is transferred in the direction of the velocity gradient. This is further explained in the mathematical formulation in Chapter 3.

In complicated flows, a model for the large-scale motion of inhomogeneous turbulence which enables the stresses in the turbulence to be estimated was given by Kolomogorov [94]. The standard $k - \epsilon$ model was presented in [95], in which the local turbulent viscosity was calculated from the solution of transport equations for the turbulence kinetic energy and the rate of energy dissipation. A form of the model was provided that is appropriate for regions with low turbulence. The model was employed to predict wall boundary-layer flows where stream wise accelerations are so significant that the boundary layer partially turns back to laminar, and the turbulence structure is directly affected by viscosity. The application of this model in some practical cases like isothermal low Reynolds number pipe flows, wall boundary layers with stream wise pressure gradient and wall injection are detailed in [96]. It has been observed that the structure of the viscous sublayer exhibits a notable influence on the flow of a variety of turbulent shear flows. The turbulence model used here, calculates the turbulence energy and turbulence dissipation rate using transport equations that are solved in parallel with the conservation equations for the mean flow. As a place of improvement, the authors suggested adjustment in the model coefficient, C_μ and similar refinements on the other viscosity dependent terms. The provision of a transport equation for the turbulent shear stress in the mean momentum equation was also suggested, hence the variables k and ϵ would remain the unknowns, necessitating the retention of the transport equations for these variables as well. Such a model was proposed by [97], but applicable specifically to regions where the viscosity has no direct impact on turbulence. The discrepancy and the evolution of the standard $k - \epsilon$ model is further addressed in [98] and [99]. Numerical predictions of turbulent flow are reviewed in [98] and it was shown that the turbulence models that

calculate the magnitudes of two turbulence quantities, the turbulence kinetic energy k and its dissipation rate, ϵ , from transport equations in tandem solved with those governing the mean flow behaviour are best suited for computational economy, range of applicability, and physical realism. The numerical applicability of the model was exemplified by using numerical calculations of nine significantly different types of turbulent flow. This type of model allowed for the prediction of both near-wall and free-shear flow phenomena without requiring modifications to constants or functions and successfully accounts for many low Reynolds number features of turbulence whose application resulted in reliable estimates of flows with recirculation in addition to those of the boundary-layer type. The wall functions used were based on the assumption that the length scale is a universal function of distance from the wall, and the low Re formulation was given. In the work of Launder *et al.* [99], the flow generated by a rotating disc in a quiescent atmosphere was considered that produces very high gradients of swirl velocity in the proximity of the disc which in turn highlights previously unnoticed terms in the kinetic energy and dissipation equations. This application thus provided a test of the model's universality for a significant class of fluid flows. It has been discovered to forecast accurately the flow, heat, and mass transfer in the vicinity of a revolving disc to predict certain low-Reynolds-number phenomena in boundary layers and duct flows, the outcome of which is important for estimating convective heat transfer rates in turbine discs. The model coefficients of the standard $k - \epsilon$ model estimated by [95], [98], [99] are shown in Table 2.1

Table 2.1 Evolution of the model coefficients of the standard $k - \epsilon$ model

Model	σ_k	σ_ϵ	C_1	C_2	C_3
Jones & Launder [95]	1.0	1.3	1.55	2.0	0.09
Launder & Spalding [98]	1.0	1.3	1.44	1.92	0.09
Launder & Sharma [99]	1.0	1.3	1.44	1.92	0.09

The CFD software like OpenFOAM, ANSYS Fluent, CFX, StarCCM uses the model coefficients given by Launder *et al.* [99].

The $k - \omega$ model originated as a development of the $k - \epsilon$ model as the latter cannot accurately predict boundary layers with adverse pressure gradients like that required in aerodynamics and turbomachinery, for instance separation in the trailing edge of an aerofoil for high angle of attack and in diffusing sections where the area increases. If $k - \epsilon$ model is used, then the point of separation of flow is predicted incorrectly and thus there are huge differences in the predicted flow parameters like coefficient of lift and drag than the actual ones. To overcome the above-mentioned problem, various other turbulence models were developed with time, the first one by Wilcox [100]. Many literatures have shown that small changes in freestream turbulent kinetic energy led to large changes in the turbulent viscosity and skin friction coefficient and the absence of cross diffusion term is the reason for which various values of the coefficients has been suggested by [101]. This affects the forces on the body and the inception of flow separation. Now, for an adverse pressure

gradient, the point of flow separation occurs where the coefficient of skin friction is zero and this depends on the freestream turbulence conditions. The remedy for this limitation of both the models was proposed in [102]. A blend of both the models is used by using the $k - \epsilon$ model far away from the wall in the free stream when it is not susceptible to small changes in k and ω ; and then near the wall the $k - \omega$ model is used. In between these, a blend of both the models is used which forms the basis of the $k - \omega$ SST model [21]. Wilcox [20] incorporated some changes in the model proposed in [21] in the form of turbulent eddy viscosity, constants and auxiliary functions that was present in the $k - \omega$ model. The one-equation Spalart-Allmaras model was proposed at this time by [23] as an improvement over the $k - \epsilon$ model, to build a model that can predict boundary layer for adverse pressure gradients, which is even complicated when shocks are present, like that in the case of supersonic flow. The $k - \omega$ model is further revisited in [103] in order to address and improve its sensitivity to free-stream boundary conditions on ω . The addition of only one new closure coefficient and a modification to the influence of eddy viscosity on turbulence parameters has been done, due to which, a substantially enhanced model that applies to both boundary layers and free shear flows and has very minimal sensitivity to finite freestream boundary constraints on turbulence parameters has been developed. The model outperforms previous versions in terms of accuracy for even more intricate separated flows.

A new model dissipation rate equation based on the dynamic equation for fluctuating vorticity and a new realizable eddy viscosity formulation, and a new eddy viscosity formulation had been proposed in [104]. These equations ascertain realizability and hold the effect of mean rotation on turbulence stresses. Applications are in rotating homogeneous shear flows, channel and flat boundary layer flows with and without pressure gradients, boundary-free shear flows and backward facing step flows. This model is studied to be numerically more stable in turbulent flow calculations as the spreading rate anomaly of planar and round jets was removed completely. Some of the eddy-viscosity models used in this work are: $k - \epsilon$, $k - \omega$, $k - \omega$ SST, realizable $k - \epsilon$, Spalart Allmaras models (RANS) and Smagorinsky, Dynamic Smagorinsky models (LES). A detailed explanation of statistical turbulence modelling is given in [105]. The journey from general Navier-Stokes equation to the closure of Reynolds stresses and solving of unknown scalar fluxes through various turbulence modelling is given in this book. Another detailed explanation regarding turbulent flows, RANS, LES and Probability Density Function (PDF) are given in [106]. The mathematical concepts and model equations are developed for various approaches. In this book, it is concluded that the suitability of a particular model depends on a weighted combination of various criteria specific to a particular turbulent flow problem.

There are certain limitations to the Eddy Viscosity models mentioned in [107]. A cubic relation between the strain, vorticity, and stress tensor was proposed in this study which captures the effects of streamline curvature across a variety of flows better than the traditional eddy-viscosity scheme. The variety of flows taken into account range from pipe flow and simple shear at high strain rates to flows with severe streamline curvature and stagnation. The processing time needed for this kind of cubic closure was found to be just 10% longer than for a linear EVM. Other

turbulence closure models along with cubic $k - \epsilon$ model is Reynolds stress, Full Sub-grid scale models.

Large Eddy Simulation (LES) Modelling

Large Eddy Simulation (LES) is a computational fluid dynamics (CFD) technique that has gained significant attention in recent years for simulating turbulent flow phenomena. It provides a balance between the computational cost of Direct Numerical Simulation (DNS) and the limitations of Reynolds-Averaged Navier-Stokes (RANS) models.

The development of Large Eddy Simulation (LES) can be traced back to the mid-1960s, although its foundations were laid much earlier with the advent of turbulence research. LES emerged as the computational fluid dynamics (CFD) technique aimed at resolving the large-scale turbulent structures while modelling the small-scale structures. The historical development of LES can be understood through key milestones and advancements in subgrid-scale modelling.

The study of turbulence began in the early 20th century, with pioneers like Osborne Reynolds and Albert Einstein. In the 1940s and 1950s, researchers such as Theodore von Kármán and Ludwig Prandtl made significant contributions to the turbulence theory. In the 1960s, the concept of Direct Numerical Simulation (DNS) was introduced, which involved solving the Navier-Stokes equations without any turbulence model. However, DNS was computationally expensive due to the need to resolve all scales of turbulence, limiting its practical application.

In the late 1960s, the concept of subgrid-scale (SGS) modelling emerged as a way to represent the unresolved small-scale turbulent motions in numerical simulations. Deardorff [108] introduced the first eddy viscosity model for SGS modelling, which later became known as the Deardorff model. The Deardorff model treated the unresolved turbulent motions as a diffusive process with an eddy viscosity coefficient. Despite its simplicity, the Deardorff model proved to be a significant step towards LES by providing a means to account for the unresolved scales.

In the early 1970s, Joseph Smagorinsky [26] developed a groundbreaking subgrid-scale model that became widely known as the Smagorinsky model. The Smagorinsky model extended the concept of eddy viscosity by introducing a dynamic approach based on local flow properties. The model estimated the eddy viscosity coefficient using a subgrid-scale length scale and the local strain rate of the resolved scales. The Smagorinsky model was simple yet effective, and it remains one of the most widely used subgrid-scale models in LES to this day. Later, Lilly contributed significantly to the development of important coefficient value [27].

Following the introduction of the Smagorinsky model, researchers focused on developing more accurate and advanced subgrid-scale models. Germano *et al.* [109] proposed the dynamic procedure, which improved the Smagorinsky model by dynamically estimating the eddy viscosity coefficient based on resolved-scale quantities. Other popular subgrid-scale models include the scale similarity model, the mixed model, and the dynamic Lagrangian model, among others.

These models aimed to capture the complex interactions between the resolved and the unresolved scales more accurately.

In the early years, DNS was the primary method for simulating turbulence, providing highly accurate results but limited to low Reynolds number flows. As computational resources became more powerful, researchers sought to develop techniques that bridged the gap between DNS and traditional turbulence models. LES emerged as a promising approach that could simulate high Reynolds number flows by resolving the larger scales and modelling the smaller scales. The LES methodology enabled the study of turbulent flows in practical engineering applications with a reasonable computational cost. In the late 20th century and early 21st century, LES saw significant advancements and applications in various fields. LES has been extensively used in aerospace engineering for studying aircraft aerodynamics, jet engines, etc.

The three-dimensional, time-dependent primitive equations of motion were numerically integrated by Moin *et al.* [110] for a turbulent channel flow using a partially implicit numerical method and an eddy viscosity model to simulate residual field motions and large-scale fields. A method for performing nested grid calculations with a large-eddy simulation code was described by Sullivan *et al.* [111]. They observed that inter-grid communication matches the velocity, pressure, and potential temperature fields in the overlapping region. Simulations of a convective, strong shear planetary boundary layer were carried out with varying surface-layer resolutions in their work. With surface-layer grid nesting, significant increases in resolved eddy fluxes and variances were found. The energy-scale content of the vertical velocity was mostly influenced by increased grid resolution. Outside of the nested region, average heat and momentum fluxes and spectra were slightly influenced by the fine resolution in the surface layer. Koren and Beets [112] modelled subgrid-scale effects implicitly through a monotone discretization method, resulting in satisfactory results for large-eddy simulation. Okong'o and Knight [113] developed an unstructured grid algorithm for tetrahedral cells for large eddy simulation. Inviscid flux computations were performed by applying a Riemann solver, viscous fluxes and heat transfer were obtained by Gauss' theorem. The numerical scheme is explicit with second-order spatial and temporal accuracy. They compared the results with DNS and experiments. Mahesh *et al.* [114], [115] developed a numerical algorithm and solver that can perform large eddy simulation in geometries as complex as a gas-turbine engine's combustor. The algorithm created for unstructured grids is robust at high Reynolds numbers on highly skewed grids and non-dissipative at low Reynolds numbers. They simulated results for the incredibly complex geometry of a Pratt & Whitney gas-turbine combustor along with results from validation in simple geometries. Balaras [116] introduced an interpolation scheme to simulate large-eddy simulations around complex boundaries on Cartesian grids. It is second-order accurate and mimics solid boundaries accurately, with results in good agreement with analytical and numerical data. Templeton *et al.* [117] proposed a near-wall treatment based on eddy viscosity, to allow large eddy simulation to be run on coarse grids. In their formulation they combined eddy viscosity in the vicinity of the wall with boundary conditions that impose wall stress. They used an averaged velocity profile of a resolved large eddy

simulation of a channel flow at $Re = 395$ to calculate the wall stress and eddy viscosity, both of which have a Reynolds-averaged Navier Stokes (RANS) like character and were used to tabulate instantaneous quantities. Using the resolved turbulent stress, the tabulated eddy viscosity is further corrected. They presented numerical results for a Reynolds number ranging from 395 to 100000. Frohlich *et al.* [118] presented block-structured Finite Volume Large Eddy Simulations of plane channel flow at friction Reynolds numbers of 180 and 395, reducing computational cost by using local grid refinement and subgrid-scale models. They found that the computed fluctuations are significantly impacted by numerical discretization. In their investigation Sengupta *et al.* [119] observed that the discontinuous Galerkin (DG) spectral element method secures geometrical flexibility, allows for arbitrary order of accuracy, and has excellent stability properties. Bose *et al.* [120] used explicit filtering in large-eddy simulation in order to obtain a numerical solution that is grid-independent. The convergence of simulations for a turbulent channel flow at $Re = 180, 395,$ and 640 that use a fixed filter width and a variety of mesh resolutions to a real large-eddy simulation solution is examined. It is demonstrated through the use of explicit filtering that the mesh resolution has no effect on turbulent statistics or energy spectra. Drikakis *et al.* [121] concluded that the high-resolution LES methods are needed to accurately simulate complex flows, with results from implicit LES for a range of flows and schemes.

In an extremely important investigation on grid resolution, Choi and Moin [122] modified the resolution requirements for large eddy simulation, as estimated by Chapman [123] using precise formulae for high Reynolds number boundary layer flow. That updated estimates show that while a wall-resolving LES requires grid points as $N \sim Re_{L_x}^{13/7}$, where L_x is the flat plate length in streamwise direction, a wall-modelled LES requires $N \sim Re_{L_x}$. On the other hand, $N \sim Re_{L_x}^{37/14}$ is needed for direct numerical simulation (DNS) to resolve Kolomogorov length scale.

2.4 REVIEW OF EARLIER WORKS ON TBL-STRUCTURE INTERACTION MODELLING AND FREE FIELD SOUND RADIATION

One of the most comprehensive works on the problem of flow-induced panel vibration and noise radiation inside a typical aircraft cabin can be attributed to Maury *et al.* [53]. They estimated the TBL-induced vibroacoustic response by using harmonic deterministic forcing function to prepare the structural response function, and the stochastic description of the TBL wall-pressure fluctuations as the external forcing [124]. At cruising conditions, a typical aircraft skin panel experiences longitudinal and transverse tension due to pressurization. In order to replicate the real condition, they took into account the in-plane tension, alongside non-tensioned panels. Through their modal-expansion technique-based analytical model, they found that each structural mode independently radiates sound power, necessitating the vibration of each mode to be controlled in an independent manner. On increasing the structural damping from 1% to 5% the resonant peaks are found to be damped and an overall reduction of 10dB in inwardly radiating sound power is observed. Besides the structural damping, they identified two other significant parameters

affecting the flow-induced sound radiation; a) the hydrodynamic coincidence, and b) the radiation efficiency of the structural modes. In a set of complementary works, they first discussed the generalized vibroacoustic theory combining system response to the deterministic harmonic excitation, and the stochastic forcing such as TBL excitation [54] and then compared the developed analytical model with experimental results for high subsonic turbulent flow [55]. They performed the convergence study with different structural mode numbers in order to determine the number of highly excited non-resonant modes and neglected the radiation damping which was found to be less significant in comparison to the structural damping. They observed that the influence of cross-modal coupling terms on the overall response of the plate is negligible and thus can be neglected. This in turn drastically reduces the computational cost.

One of the earliest attempts to develop a quasi-numerical model describing TBL-induced sound radiation from a single, flat, elastic, isotropic vibrating panel can be attributed to W. R. Graham [125], [126]. He used the analytical modal expansion technique for plate modelling and a combined computational-asymptotic technique [127] to evaluate the modal integral and eventually estimated the dimensionless radiated power spectrum. He considered the wall pressure as the combination of the boundary layer pressure on a rigid wall and plate vibration-induced acoustic pressure [128]. He concluded that increasing structural damping, decreasing plate stiffness, and the number of stiffeners reduce the radiated sound power. The effect of resonance between TBL and plate elastic wave velocity is found to be insignificant for smaller variations in cruising speed and structural parameters.

Hwang *et al.* [48] formulated the coupling of structural mode and flow in all three regions including the intermediate region between low and high wavenumber and observed that this particular region is of significance in cases. They used various boundary conditions for plate response prediction and found that in the case of simply supported and clamped boundary conditions the low to intermediate wavenumber region of the TBL pressure spectrum plays the most important role. In the case of high wavenumber forcing the number of finite elements drastically becomes huge and unfeasible. In order to overcome this problem, Hwang [49] proposed a model that ignores the high-wavenumber convective ridge region in very low-wavenumber dominant cases. The finite element (FE) approach was introduced to solve the multiple input-output problems of flow-induced panel vibration in physical space by Hambric *et al.* [50] following the works of Bendat and Piersol [129] and Lin [46]. They modified the Corcos model in order to reduce low wavenumber content. This work was carried out in the low-frequency region (0-600Hz) with low Mach number flow and low-wavenumber forcing, representing the surface interaction for an all-side-clamped steel plate. The low-wavenumber truncation reduces the requirement of mesh density. They further modelled the plate with a free edge to account for the edge interaction [51]. They validated their numerical model with the experiments conducted at Purdue University by Han *et al.* [130], wherein an extensive study captured the different aspects of the TBL-induced vibroacoustic problem, both experimentally and numerically. Their study [130] included separated-reattached flow and its effect on the underneath plate vibration and

resulting sound radiation. They used a fence upstream of the test plate to create flow separation and performed the CFD analysis to properly simulate the setup. Low-speed wind tunnel experiments were conducted to evaluate the statistical energy flow analysis (SEA) method which is a better alternative to the finite element analysis (FEA) in the high-frequency regime in terms of mesh requirements. They found that the FEA method provides an accurate prediction of the transverse plate velocity in the high-frequency region. They extended their work [131] to structural vibration and radiated sound pressure due to complex vortical flows, involving CFD with similarity arguments, FEA, and experimentation. They idealized the input non-uniform distributed fluid loading as a summation of discrete forces acting on the structure, each discrete force acting on the incremental plate area. Though the FEA model was developed for the high-frequency analysis, they noted that the mobility of a finite plate significantly varies from the mobility of an infinite plate at the lower frequencies. This problem can however be addressed by performing space or frequency averaging. They used the radiation efficiency method to estimate the free-field sound radiation from a flow-excited vibrating plate. Birgersson *et al.* [132] used the spectral finite element method (SFEM) to solve the turbulence-induced vibration problem of pipes. They noted the advantages of the finite element method (FEM) in handling frequency-dependent material properties and boundary conditions. In their work Fritze *et al.* [133] compared *three* popular approximation methods to evaluate radiated sound power of a diesel engine under realistic load case; a) boundary element method (BEM), b) equivalent radiated power (ERP), and c) lumped parameter model (LPM). They used structural surface velocity as input to determine the radiated sound power. It was observed that the LPM provides reasonable predictions only if there is phase information present.

Rocha developed an analytical framework to predict structural vibration and sound radiation for turbulent flow-excited composite panels [134]. She used empirical wall-pressure spectrum models for TBL flow excitation and considered each fuselage panels to be vibrating independently and are simply supported. Considering stationary and homogeneous turbulence, the structural vibration was estimated in the form of plate velocity power spectral density (PSD) as the product of TBL cross-PSD and the conjugate and transpose of the system transfer function. Eventually, the velocity PSD was coupled with the radiation resistance matrix (RRM) and the radiated sound power (RSP) was estimated. She identified the difference of the flow-induced vibroacoustic response of composite sandwich panels with that of the isotropic panels. She used different face sheet and core properties in her study. The composite panels were generally found to exhibit a lower level of vibroacoustic response, with exceptions at certain frequencies. She carried out parametric studies with different panel size, thickness of core and surface layers. The vibroacoustic behaviour of both isotropic and composite panels was observed for correlated TBL excitation and uncorrelated random noise excitation. A higher number of modes were found to be excited by TBL excitation than the random excitation. This observation was more prominent in the case of composite panels. Therefore, it was suggested not to use uncorrelated random noise excitation to replicate a TBL flow.

Maxit and Denis [135] studied radiated sound and vibration of an infinite periodically stiffened panel excited by TBL. Their analytical model involved the wavenumber-point reciprocity technique. They applied the developed model to a naval test case and identified the effects of Bloch-Floquet waves on the fluid-loaded panel vibration and sound radiation. Berton *et al.* [136] discussed different deterministic vibroacoustic models that are coupled with the stochastic TBL force acting on a heavy fluid-loaded panel. They studied different coupling techniques involving a) physical space, b) an uncorrelated wall plane wave field, c) realizations of the stochastic uncorrelated plane wave model, and d) reciprocity technique that was previously introduced by the authors. They used Patch Transfer Function (PTF) in order to evaluate different transfer functions of the fluid-loaded panel and identified that all the approaches provide similar results for some optimized parameters. Moreover, they observed that the estimation in the physical space is the most time-consuming if the output excitation is not restricted to a small area, and the Cholesky decomposition of the wall-pressure cross-spectrum could be an efficient technique in terms of computing time.

In an experimental approach conducted in the Acoustic Wind-Tunnel Braunschweig (AWB) facility at the German Aerospace Center (DLR) Hu and Misol [137] measured the boundary layer pressure fluctuations over a flat flexible plate and the resulting response in terms of plate acceleration PSD. They used miniature piezo-resistive pressure sensors to measure surface pressure fluctuations, and a matrix of miniature accelerometers to measure the averaged plate vibration characteristics. In another experimental work conducted in the transonic wind tunnel at the CIRA (Italian Aerospace Research Center) Ciappi *et al.* [138] measured TBL-excited plate vibration of composite panels for high Mach number flow (0.4 to 0.8). They used a tripping system to achieve full-scale size pressure spectra representing the real flight condition and used a viscoelastic layer embedded into the CFRP (Carbon Fiber-Reinforced Polymer) layers. They performed experimental modal analysis for model updating and obtained the frequency-dependent structural modal damping values. The computational framework was developed in the wavenumber-frequency domain using the analytical spectral element method. Purohit *et al.* [139] conducted experiments in an open-ended wind tunnel to estimate the flow-induced vibration of a flexible plate. The plate was harmonically actuated, and the vibration was mainly due to the downstream wake formed due to an obstacle. They studied the individual influence of external harmonic excitation and flow excitation. They found that at the lower excitation amplitude influence of both excitations is significant, though at the higher excitation amplitude the effect of the flow excitation fades away.

Jeyaraj *et al.* [140], [141] used commercial finite element software for vibroacoustic study of isotropic and orthotropic rectangular plate in a thermal environment. Zhao *et al.* [142], [143] used an analytical model to predict the vibroacoustic response of composite plates in a hygroscopic environment and validated the model with finite element (FE) results.

Sound Transmission Efficiency and Sound Transmission Loss

In one of the earliest works to measure sound transmission efficiency and transmission loss (TL), lower limits of validity are established for the transmission room method of measuring transmission loss. This article describes a different way to measure low loss panels [144]. In their study Efimtsov and Larazev [145] found that the resonant elements can increase the transmission loss of panels in narrow frequency bands, and three main principles of increasing transmission loss are discussed: soft reflection, hard reflection, and compensation. They presented a universal expression to compare the efficiency of different types of resonators and determine their optimum parameters [146]. In the investigation of Xie *et al.* [147] two boundary element analyses were used to investigate the sound transmission characteristics of an aluminum panel and two composite sandwich panels. Air loading, modal energy loss factor, and wave impedance analysis were used to make sound transmission loss predictions. Comparisons between predictions and experimental measurements were presented. Zhou *et al.* [148] investigated the sound transmission loss property of a single sinusoidal corrugated panel using a modal expansion method. The results show that the predicted sound transmission loss has a good agreement with the measured one, yielding smaller prediction errors than the classic wave approach. Arunkumar *et al.* [149] presented a bi-objective optimization of double-walled panels to minimize weight while maximizing acoustic transmission loss. Biot's theory was used to model the poroelastic material, and Pareto fronts were obtained to trade off the two objectives. Santoni *et al.* [150] developed a prediction model to evaluate the sound transmission loss provided by ETICS, including mechanical bridges. The model was developed within the transfer matrix method framework and was based on a decoupled approach. Validity of the model was verified with experimental data and reliability was investigated. Ehsan Moosavimehr *et al.* [151] observed that FRP sandwich panels have better vibroacoustic and sound transmission loss characteristics due to their high stiffness and material damping. Resonant amplitudes are controlled by modal damping factors and can be used to replace aluminium without losing acoustic comfort.

Zhang *et al.* [152] combined the Bloch-wave analysis and the finite element method to understand wave propagation and sound transmission in sandwich panels with a truss lattice core. Results show that even without optimization, significant enhancements in sound transmission loss performance can be achieved in truss lattice core sandwich panels compared to traditional sandwich panels. A theoretical investigation on the sound transmission loss characteristics of four-side simply supported sandwich panels was presented by Li *et al.* [153] considering the flexural rigidity of the face sheet. The theoretical prediction model proposed has high accuracy on predicting the natural frequencies and sound transmission loss. Droz *et al.* [154] found that the small-scale resonators can improve sound transmission loss of curved panels by varying the spatial distribution and using multi-frequency resonators with fixed spatial distribution. The numerical approach proposed by Errico *et al.* [155] is efficient for predicting the sound transmission loss of complex curved aircraft panels under diffuse acoustic field excitation. Wen *et al.* [156] proposed

an ultra-lightweight sandwich panel with closed octahedral core, which demonstrates excellent acoustic and mechanical performance.

2.5 REVIEW OF COUPLED TBL-INDUCED VIBROACOUSTIC PROBLEMS IN ENCLOSED FIELD

Bremner and Zhu [157] used unsteady CFD to generate the input wind pressure acting as a forcing function on the outer surface of an automobile body. They used statistical energy analysis (SEA) to model the structure and the acoustic enclosure and estimated the flow induced sound transmission into the vehicle interior cabin. They separated the contribution of two types of modes contributing to the radiated sound power, namely a) stiffness-controlled resonant mode, and b) mass-controlled non-resonant modes, and found that for diffuse acoustic field excitation the non-resonant modes are predominant below 2000Hz, and resonant modes dominate above 2000Hz. de Lima *et al.* [158] used energy finite element analysis (EFEA) to compute the TBL-induced structural vibration and interior noise of a full-scale business jet.

In their analytical work, Rocha *et al.* [159] developed a structure-acoustic coupled model and validated the model. Modal expansion technique was used to develop the structural transfer function for simply supported boundary conditions. Efimtsov single point wall-pressure spectrum model and Corcos coherence function were used to estimate the pressure cross-spectral density (CSD) depicting the TBL forcing. In an extension of their earlier work, they predicted TBL-induced sound transmission into a Blended Wing Body (BWB) aircraft cabin using a system of single-panel coupled with the enclosed cabin [52]. They analyzed multiple isotropic or orthotropic laminated flow-excited aircraft panel systems to estimate sound pressure level (SPL) inside the cabin for a frequency range of 1-1000Hz. They used experimental data of aircraft noise levels and fuselage skin vibration spectra provided by NASA for validation purposes. Contribution of the individual panel to the cabin interior SPL was also investigated and it was reported that the SPL at different locations was due to contributions of different panels.

Caiazza *et al.* [56], [57] developed an analytical model to predict the structural vibration and transmitted sound power through a double-panel system backed by an acoustic enclosure. They used Goody's semi-empirical spectrum model to describe the TBL wall pressure and modal expansion technique to model the structural panels. The panel-gap-panel-cavity coupling is performed in the analytical framework. They found the first fundamental mode and panel-air-panel coupled mode to be the most efficient sound radiator into the acoustic cavity.

A three-dimensional vibroacoustic coupling model is established by Du *et al.* [160] to analyze sound attenuation of elastically restrained plate silencer backed by irregular acoustical cavity. Numerical results are presented to illustrate the correctness and effectiveness of the proposed model. Experimental study is also conducted to verify the theoretical prediction.

2.6 CRITICAL APPRAISAL OF THE PREVIOUS WORKS

It is clear from a thorough review of the previously published works that there are various established methods for estimating turbulent boundary layer wall pressure and several different methods for modelling structural vibroacoustic problems caused by TBL in both the free field and enclosed cavity in the low to mid frequency range. The common modelling approaches that have been discussed in the literature in the past can be summed up as follows:

1. Various wall-pressure spectrum models are developed over the years and used with experimental data inputs. Later, Reynolds-averaged Navier Stokes (RANS) equations are employed to estimate the mean flow quantities which replaced the experimental data feeding process. Large Eddy Simulation (LES) techniques are extensively developed for precise computation of flow quantities.
2. Turbulence-structure interaction modelling involved analytical approach, where an analytical modal expansion technique is used to model the structural panel, and analytical or semi-analytical TBL loading is used to estimate the forced behaviour of the panel. Though common in many applications, the analytical technique is more suitable for structures with regular shapes and simple geometry that adhere to a specific axis system. Analytical computation frequently entails complex mathematical calculations, which limits its applicability.
3. FE modelling of TBL-structure interaction using traditional semi-empirical pressure spectrum models are reported. Involvement of CFD in the interaction process is rarely found, which prevails the dependency and requirement of the experimental investigations.
4. Analytical models are presented, which measure free field sound radiation from a TBL-excited vibrating panel. The panel is modelled as tensioned or non-tensioned panel, and orthotropic laminated composites are used for material modelling. Analytical radiation resistance matrix (RRM) is developed for sound radiation estimation. But again, restrictions are the geometry and support conditions.
5. Fully coupled analytical model for TBL-induced sound transmission into an enclosure backed by single as well as double wall is developed. The excited structural panel perturbs either directly the inside acoustic medium (single wall) or through the small cavity between the panels (double wall). The analytical method is fast but difficult to compute for a complex system.
6. For the interior vibroacoustic problem, a modal coupling method based on Green's function is used, in which the FE governing equations for the structural and acoustic domains are transformed to the modal domain. The structural (in-vacuo) and acoustic cavity (rigid-walled) mode shapes based on Green's function are then used to couple the two domains. In this method, in order to capture the complex shape of the cavity three-dimensional discretization becomes challenging.

Although several modelling techniques of TBL-induced vibroacoustic study is developed in the past few decades and efficiently used in practical-purposes, few critical aspects can be identified for further investigation.

- All the TBL wall pressure spectrum models are used with experimental inputs of flow parameters. Only a few works are observed where RANS simulation is combined with those spectrum models like [13], [93] but in their work they did not study various turbulence models or model parameters which dictates the final pressure spectrum or mean square pressure (MSP) values. An extensive sensitivity study on MSP to different turbulence model parameters is missing.
- There are only a handful of literature available like that by Hambric *et al.* [51] where FE framework is used for TBL-induced structural vibration modelling. However, they used traditional semi-empirical pressure spectrum models. Later, they used CFD, but with no sensitivity study. Also, they did not extend their work to acoustic study in any form. Han *et al.* [130], [131] used CFD to estimate wall pressure, studied the acoustic response but, they did not use FE modelling technique, thus limiting their model to study simple geometric forms.
- The majority of the literature on the subject of sound transmission into enclosures considers only one panel to be flexible, which limits the application to simple geometries and a small number of special cases. There are a few rare cases in the literature where the estimation of sound transmission is made through an enclosed acoustic domain between two flexible panels into another enclosed field. As a result, the estimated free-field transmission is used to measure the transmitted sound. One such work is from Caiazzo *et al.* [56], [57]. But they worked in the analytical framework, restricting the future realistic development with complex shape of the structural panels and enclosure.

It is also seen that the TBL-induced vibroacoustic study on stiffened double wall system, or enclosure backed by double wall with stiffened or orthotropic panel is almost non-existent.

2.7 THE OBJECTIVE AND THE APPROACH

In the present research work, it is therefore attempted to,

- identify the **best predicting** RANS turbulence model parameters corresponding to wall-pressure fluctuation estimation vis-a-vis wind-tunnel experiment and in-flight test
- develop a **numerical model** to estimate and understand one-way fluid-structure interaction and resulting TBL-induced flexible panel vibration
- develop a **numerical model** to estimate and understand the free field sound radiation by a TBL-excited flexible panel
- develop a **numerical model** to estimate and understand transmission behaviour into any acoustic cavity enclosed by a TBL-excited flexible panel
- estimate the **vibroacoustic behaviour** of **stiffened, tensioned, orthotropic** and double-wall panels subjected to TBL excitation

To accomplish the research objectives as listed, the following steps are taken:

- A two-folded sensitivity study is performed to properly estimate the near-wall TBL pressure fluctuation. First, the best predicting semi-analytical pressure spectrum models are identified corresponding to the wind tunnel experiments, and in-flight tests. In-house MATLAB (ver. 2013b) scripts are used for the computations. Next, the change in the mean square pressure (MSP) is studied with RANS turbulent model parameter variations, and the most suitable CFD configuration is identified. OpenFOAM (v-2012 in Ubuntu 20.04 LTS) and ANSYS Fluent (V14.5) is used for CFD simulations.
- Numerical modelling of the structure and the acoustic domain is done using the FE technique. The structural panel and acoustic domain are modelled in ANSYS APDL (V14.5) to extract the modal parameters and their geometry data which are used as inputs to the FE model developed in the MATLAB (ver. R2013b) environment.
- The developed one-way coupled TBL-induced structural vibration model is validated with an existing experimental result.
- The free field vibroacoustic model for a TBL-excited panel is validated with published analytical result. Both tensioned and non-tensioned panels are used.
- The sound transmission model for an acoustic enclosure backed by a double wall panel subjected to TBL excitation is validated with another analytical framework.
- A two-way coupling is included for a coupled vibroacoustic problem for an acoustic cavity enclosed by flexible structural panels, using a mobility relationship that relates the structural surface normal velocity and the acoustic back pressure. The developed model is further extended to understand TBL-excited sound transmission mechanism through a double wall panel system encompassing a secondary acoustic domain.

The semi-analytical pressure spectrum models supported by CFD RANS simulations are used to generate the TBL wall-pressure, using finite volume (FV)-based flow solvers and MATLAB. The flow-excited structural panel vibration is estimated using the one-way coupled fluid-structure interaction (FSI) model. In-house FE-based vibroacoustic models are developed to capture the free field sound radiation or sound transmission mechanism into an enclosed cavity, for a flow-induced flexible panel in MATLAB environment. Different types of panels, such as stiffened, tensioned, laminated composite panels are studied and their flow-excited vibroacoustic behaviour are reported.

In the next Chapter a detailed account of TBL wall pressure estimation is presented. Several semi-analytical pressure spectrum models and CFD (RANS, LES) turbulence models are explored extensively.

CHAPTER 3: TBL WALL PRESSURE ESTIMATION

3.1 INTRODUCTION

Flow-induced vibroacoustic studies require an accurate estimation of turbulent boundary layer pressure variations. As has been seen from the review of literatures there are several different methods available that can be used to estimate this pressure fluctuations beneath a fully developed turbulent boundary layer. Semi-analytical models are amongst the most popular choices. They are quick, efficient, and cost-effective resulting in being primarily preferred in industrial applications. However, these models require inputs in the form of TBL parameters which are typically estimated through expensive experimentations. Due to the recent explosive expansion in the area of computational fluid dynamics, newer techniques are now being widely used. In the present Chapter a detailed description of several CFD models used in TBL pressure estimation is presented with a focus on Reynolds-Averaged Navier Stokes (RANS) and Large Eddy Simulation (LES).

3.2 MATHEMATICAL DESCRIPTION

3.2.1 Semi-analytical models

Semi-analytical models are typically developed based on the blending of the analytical formulations and extensive experimental findings. Thus, these models have got more realistic prediction capabilities, and widely used in real life problems. Semi-analytical models are constructed with the help of various input parameters with different target outputs, like mean square pressure, wall pressure spectra, etc.

3.2.1.1 Empirical Mean Square Pressure Models

In 1956, Kraichnan [58] proposed mean-square pressure fluctuation estimation as a function of wall shear stress, τ_w for low to moderate Mach numbers. The RMS pressure fluctuation is tentatively estimated from incomplete data available.

$$\overline{p'^2} = (6\tau_w)^2 \quad (3.2.1)$$

Subsequently Lilley and Hodgson [59] conducted wind tunnel test and estimated the mean square wall pressure fluctuation as a function of dynamic pressure q . They obtained a relationship as

$$\overline{p'^2} = (0.008 q)^2 \quad (3.2.2)$$

Willmarth and Wooldridge [8] measured the mean-square wall pressure at 150 and 200 ft/s wind velocity. The mean-square wall pressure given by Willmarth and Wooldridge was

$$\overline{p'^2} = (2.15\tau_w)^2 \quad \text{for 150 ft/s} \quad (3.2.3a)$$

$$\overline{p'^2} = (2.19\tau_w)^2 \quad \text{for 200 ft/s} \quad (3.2.3b)$$

Corcos [44] provided the formulation for the mean-square wall pressure measured with help of piezo-electric transducer and considering the pressure field stationary and homogenous.

He suggested a relationship for mean-square wall pressure as a function of wall shear stress, τ_w , for Reynolds number of $\delta U_0/\nu \cong 300,000$ and is given by

$$\overline{p'^2} = [(3.0 \pm 0.5)\tau_w]^2 \quad (3.2.4)$$

In a later work Corcos [45] concluded that the dependence on the Reynolds number is small.

Bull [10], [77] in his experimental work found that the mean-square wall pressure value increased with the Reynolds number and the mean-square pressure value is a function of wall shear stress

$$\overline{p'^2} = (2.11\tau_w)^2 \quad \text{for } Re_\theta = 6400 \text{ (M = 0.3)} \quad (3.2.5a)$$

$$\overline{p'^2} = (2.80\tau_w)^2 \quad \text{for } Re_\theta = 33800 \text{ (M = 0.5)} \quad (3.2.5b)$$

Lowson [39] estimated the mean-square wall pressure as a function of Mach number that can be obtained using the dynamic pressure. The empirical relationship he proposed is given by

$$\overline{p'^2} = \left(\frac{0.008 q}{1+0.14M^2} \right)^2 \quad (3.2.6)$$

Blake [161] noted that the experimental studies, stated earlier, were limited to the finite size of microphones and by extraneous tunnel disturbances. So, an experiment was conducted in a low-noise wind tunnel facility and with microphones capable of better resolution. Due to the improvement in the resolution of microphones, the constants of these relationships were found higher than the previously published works. He developed two relationships-one of them was based on the dynamic pressure and the one on the wall shear stress.

$$\overline{p'^2} = (0.00879q)^2 \quad (3.2.7a)$$

$$\overline{p'^2} = (3.59\tau_w)^2 \quad (3.2.7b)$$

Schewe [162] used various sizes of transducers and conducted a modern wind-tunnel measurement with a flow speed of 6.3 m/s. He found the mean-square wall-pressure value as function of dynamic pressure.

$$\overline{p'^2} = (0.0102q)^2 \quad (3.2.8)$$

Lauchle and Daniels [163] conducted a test and studied wall pressure fluctuation due to TBL for a flow of glycerin in a long pipe and found the mean-square wall pressure value as

$$\overline{p'^2} = (0.0106q)^2 \quad (3.2.9)$$

Farabee and Casarella [164] also noted that the deviation of wall-pressure for various investigators depended on the size of transducers and the Reynolds number. They obtained a relationship dependent on the Reynolds number ($Re_\theta = U_r \delta / \nu$)

$$\overline{p'^2} = 6.5\tau_w^2 \quad \text{for } Re_\theta \leq 333 \quad (3.2.10a)$$

$$\overline{p'^2} = [6.5 + 1.86 \ln \left(\frac{Re_\theta}{333} \right)]\tau_w^2 \quad \text{for } Re_\theta > 333 \quad (3.2.10b)$$

Lueptow [75] investigated measurement effects and the turbulent wall-pressure spectrum to develop the mean-square pressure fluctuation value as a function of the dynamic pressure.

$$\overline{p'^2} \cong (0.012q)^2 \quad (3.2.11)$$

While comparing the empirical models with experimental data for a range of Mach numbers it is seen that the predictions from the Kraichnan and Lueptow model overestimates whereas the models by Bull and Willmarth and Wooldridge underestimate the predicted results. Farabee and Casarella model falls in between the above two predictions. The results of Lowson and Corcos model are approximately the same and similarly, the prediction of Farabee & Casarella and Blake 1 are in the same range.

3.2.1.2 Wall Pressure Spectrum Models

Some of the single-point wall-pressure spectrum models are presented here.

A. Robertson Model

Robertson [38] investigated an early single-point wall-pressure spectrum model based on the work of Lowson [39]. He compared Lowson's formula with measurements at the NASA Ames Research Center, at supersonic velocity, and found the formula as underestimating the spectral levels at low Strouhal numbers and giving too large a roll off at higher Strouhal numbers. So, he suggested a new formula representing the measured data for a wide Mach number range. He used δ^* and U_∞ as normalization parameters.

$$\Phi(\omega) = \frac{\overline{p'^2}}{\omega_0[1+(\omega/\omega_0)^{0.9}]^2}, \text{ where } \omega_0 = 0.5 \frac{U_\infty}{\delta^*} \quad (3.2.12a)$$

Integrating Robertson single-point wall spectrum model numerically at $M = 0.1$ with integration limits from 50 Hz to 20000 Hz (arbitrary), as chosen by Farabee and Casarella [35], gives 20.44 Pa²

$$\int_{50}^{20,000} W(f)df = \int_{50}^{20,000} \Phi(\omega)d\omega = \overline{p'^2} = 20.44 \text{ Pa}^2 \quad (3.2.12b)$$

B. Chase-Howe Model

Howe [34] proposed the following model and attributed it to Chase [30]

$$\frac{\phi(\omega)U_\infty}{\tau_\omega^2 \delta^*} = \frac{2(\omega\delta^*/U_\infty)^2}{(\omega\delta^*/U_\infty)^2 + 0.0144}^{3/2} \quad (3.2.13)$$

This model is a simplification of the previous model developed by Chase [30], which was more comprehensive for the wave vector-frequency spectrum. Based on the above equation, the model spectrum is proportional to ω^2 at low frequencies and varies as ω^{-1} at higher frequencies.

C. Efimtsov Model

Efimtsov [31], [32] proposed two single-point wall-pressure spectrum models where the first model is referred to as the first model of Efimtsov or Efimtsov 1 and the second one is referred to as the second model of Efimtsov or Efimtsov 2. Efimtsov stated that a single-point wall-pressure

spectrum model should be dependent on Mach number (M), Reynolds number (Re), and Strouhal number (Sh). The Strouhal number is $Sh = \omega\delta / U\tau$. Efimtsov collected a series of flight test data in the range of Mach numbers of $M = 0.41$ to 2.1 with Reynolds number of $Re_x = 0.5 \times 10^8$ to 4.85×10^8 . The pressure fluctuations were measured at various zones along the fuselage. Efimtsov' proposed the following equation

$$\Phi(\omega) = \frac{0.01\tau_\omega^2\delta}{U_\tau[1.0+0.02(\omega\delta/U_\tau)^{2/3}]^2} \quad (3.2.14a)$$

Efimtsov 2 was an updated model in which the principal independent variables are the Strouhal number and the Reynolds number

$$\Phi(\omega) = \frac{2\pi\alpha U_\tau^3 \rho^2 \delta \beta}{[1+8\alpha^3(\frac{\omega\delta}{U_\tau})^{1/3} + \alpha\beta Re_\tau [(\frac{\omega\delta}{U_\tau})/Re_\tau]^{10/3}]^2} \quad (3.2.14b)$$

where $Re_\tau = \frac{\delta U_\tau}{\nu_w}$; $Re_{\tau 0} = 3000$; $\beta = [1 + (\frac{Re_{\tau 0}}{Re_\tau})]^{1/3}$; $\alpha = 0.01$; $\nu_w = \nu \frac{\rho}{\rho_w} (\frac{T_w}{T_\infty})^\Upsilon$; $\Upsilon = 0.905$;
 $T_w = T_\infty(1 + r \frac{k-1}{2} M^2)$; $r = 0.89$; $k = 1.4$; $\rho_w = \rho \frac{T_\infty}{T_w}$.

D. Goody Model

Goody [14], [41] proposed an empirical model of the single-point wall-pressure spectrum beneath a two-dimensional, zero-pressure-gradient boundary layer which was based on the experimental surface pressure spectra measured by seven different research groups. The final form of his proposed empirical model was

$$\frac{\phi(\omega)U_\infty}{\tau_\omega^2\delta^*} = \frac{3.0(\omega\delta^*/U_\infty)^2}{[(\omega\delta^*/U_\infty)^{0.75} + 0.5]^{3.7} + [(1.1R_T^{-0.57})(\omega\delta/U_\infty)]^7} \quad (3.2.15)$$

where the ratio of the outer-layer to inner-layer timescale (R_T) is defined as

$$R_T = \frac{\delta}{U_\infty} \frac{U_\tau^2}{\nu} = \left(\frac{U_\tau\delta}{\nu}\right) \sqrt{\frac{c_f}{2}}$$

It can be seen that by increasing the Reynolds number, the timescale ratio is increased. This measurement covered a large range of Reynolds numbers, 1.4×10^3 to 2.34×10^4 .

E. Smol'yakov Model

In the year 2000, Smol'yakov [81] found that the single-point wall-pressure spectrum scales on different variables, depending on the frequency. He described the three regions as low frequency, universal and high frequency and proposed three separate equations as presented in Eqs. (3.2.16a) to (3.2.16c) for low frequency, universal frequency, and high frequency, respectively. The first part of the equations describes the main laws governing the behaviour of the spectra and the second part which is given in brackets provides a smooth matching between the three regions.

$$\Phi(\omega) = \frac{1.49 \times 10^{-5} \tau_\omega^2 \nu Re_\theta^{2.74} \omega^{-2}}{U_\tau^2} \{1 - 0.117 Re_\theta^{0.44} \omega^{-1/2}\} \text{ at } \bar{\omega} < \bar{\omega}_0 \quad (3.2.16a)$$

$$\Phi(\omega) = \frac{2.75\tau_{\omega}^2\nu}{U_{\tau}^2\omega^{-1.11}} \{1 - 0.82\exp[-0.51(\bar{\omega}/\bar{\omega}_o - 1)]\} \text{ at } \bar{\omega}_o < \bar{\omega} < 0.2 \quad (3.2.16b)$$

$$\Phi(\omega) = \frac{(38.9 e^{-8.35\bar{\omega}} + 18.6 e^{-3.58\bar{\omega}} + 0.31 e^{-2.14\bar{\omega}})\tau_{\omega}^2\nu}{U_{\tau}^2} \{1 - 0.82e^{-0.51(\frac{\omega}{\bar{\omega}_o}-1)}\} \text{ at } \bar{\omega} > 0.2 \quad (3.2.16c)$$

Rozenberg *et al.* [165] proposed an empirical model to predict wall-pressure fluctuations spectra. Though it is based on Goody's model, it is somewhat unconventional as the model presented is for an adverse pressure gradient. The model is tested in both internal (channel) and external (airfoil) flows and validated with 6 test cases from 5 experimental or numerical studies covering a large range of Reynolds number $5.6 \times 10^2 < Re_{\theta} < 1.72 \times 10^4$.

3.3 COMPUTATIONAL FLUID DYNAMICS

The utilization of Computational Fluid Dynamics (CFD) is a potent numerical methodology employed for the examination and evaluation of various fluid flow phenomena. This approach offers a mechanism for emulating and forecasting fluid dynamics by resolving the governing equations of fluid mechanics through numerical techniques. Reynolds-Averaged Navier-Stokes (RANS) and Large Eddy Simulation (LES) are computational fluid dynamics (CFD) techniques that are typically used to simulate turbulent flows.

Turbulent flow is characterized by its chaotic nature, velocity fluctuations, and the presence of vortices and eddies. Eddies are essential components of turbulent flow, influencing mixing, transport, and the dissipation of energy. Understanding the length and time scales of turbulence is crucial for modelling and predicting turbulent flows in various engineering and environmental applications. A detailed account of RANS and LES methodologies and various closure models is presented next.

3.3.1 Reynolds-Averaged Navier Stokes (RANS)

RANS is a time-averaged approach that models turbulent flows using statistical averaging. The RANS equations are derived by applying Reynolds averaging to the Navier-Stokes equations. The governing equations for RANS can be written as

Continuity Equation:

$$\nabla \cdot (\rho \bar{U}) = 0 \quad (3.3.1)$$

Momentum Equations:

$$\frac{\partial}{\partial t}(\rho U) + \nabla \cdot (\rho \bar{U}U) = -\nabla P + \nabla \cdot (\mu(\nabla \bar{U} + (\nabla \bar{U})^T) - \rho \overline{u'u'}) \quad (3.3.2)$$

where ρ is the fluid density, \bar{U} represents the time-averaged velocity, P is the pressure, μ is the dynamic viscosity, and $\overline{u'u'}$ denotes the Reynolds stress tensor. The Reynolds stress tensor is usually modelled for the closure of the Navier-Stokes equation using turbulence models, such as the eddy viscosity models (e.g., $k - \varepsilon$, $k - \omega$). RANS simulations are computationally efficient but provide time-averaged information and do not resolve the complete range of turbulent scales.

In RANS, the N-S Equations are written in terms of mean quantities by using time averages, where a time average is taken over a long time ($t \rightarrow \infty$) to give a stationary mean. This is because RANS is a type of solving the N-S Equations to some extent and turbulence is considered through a set of statistical data. This method cannot take interactions of every scale of turbulence, qualitatively or quantitatively, into consideration, and thus, assuming the time-dependency of turbulence to be a very complex phenomenon, it is not incorporated in a physical model or as a turbulence model. Now, to get a solution to the N-S Equations, the flow velocity is discretized into a mean flow velocity component (\bar{U}) and fluctuating velocity component (u'). This is known as Reynolds decomposition. The mean velocity is obtained by time averaging the velocity over a long period of time:

$$\bar{U}(x) = \frac{1}{T} \int_{t_0}^{t_0+T} U(x, t) dt \quad (3.3.3)$$

The Reynold decomposition is

$$u(x, t) = \bar{U}(x) + u'(x, t) \quad (3.3.4)$$

A few identities for linearity that are to be followed are:

- $\overline{u'} = 0$
- $\overline{u + v} = \bar{u} + \bar{v}$
- $\overline{\bar{u}} = \bar{u}$
- a) $\overline{\bar{a} \cdot \bar{b}} = \bar{a} \cdot \bar{b}$; b) $\overline{a \cdot b} \neq \bar{a} \cdot \bar{b}$
- $\left(\frac{\partial \bar{a}}{\partial s}\right) = \frac{\partial \bar{a}}{\partial s}$
- $\overline{u'^2} \neq 0$

This decomposition is next plugged into the continuity equation, Eq. 3.3.1,

$$\frac{\partial \bar{U}}{\partial x} + \frac{\partial \bar{V}}{\partial y} + \frac{\partial \bar{W}}{\partial z} + \frac{\partial u'}{\partial x} + \frac{\partial v'}{\partial y} + \frac{\partial w'}{\partial z} = 0 \quad (3.3.5)$$

And on plugging into the momentum equation, the x-component becomes,

$$\bar{U} \cdot \bar{U}_x + \bar{V} \cdot \bar{U}_y + \bar{W} \cdot \bar{U}_z + \frac{\partial \overline{u'u'}}{\partial x} + \frac{\partial \overline{u'v'}}{\partial y} + \frac{\partial \overline{u'w'}}{\partial z} = -\bar{p}_x + \frac{1}{Re} \nabla^2 \bar{U} \quad (3.3.6)$$

Thus, the RANS Equation in tensor notation can be finally written as

$$\frac{\partial(\rho U_i)}{\partial t} + \frac{\partial(\rho U_i U_j)}{\partial x_j} = -\frac{\partial P}{\partial x_i} + \frac{\partial}{\partial x_j} \left[\mu \left(\frac{\partial U_i}{\partial x_j} + \frac{\partial U_j}{\partial x_i} \right) - \rho \overline{u'_i u'_j} \right] \quad (3.3.7)$$

where U is the mean flow velocity (m/s) in i th or j th directions (2D), P is the pressure, t is time, ρ is the fluid density (kg/m^3), μ is the absolute viscosity of the fluid (Pa-s). $\rho \overline{u'_i u'_j}$ in Eq. (3.3.7) is known as the Reynolds stress term. The Reynolds stresses are solved using the Boussinesq constitutive relation [166] or the Eddy-viscosity model. From the Boussinesq hypothesis, it can be said that Reynolds stress is proportional to the velocity gradient and, the limit of proportionality of this relation is turbulent viscosity (μ_t). This relation can be shown by: (in x-profile)

$$-\rho \overline{u'v'} = \mu_t \frac{\partial U}{\partial y} \quad (3.3.8)$$

μ_t is a fictitious quantity for which the modelling is shifted from Reynolds stress tensor to eddy viscosity (μ_t), thus the naming. Further, it controls the strength of diffusion, that is, more the μ_t , more is the transfer of momentum from faster to slower-moving fluid particles.

As the order of multiplication does not matter, so the shear stress components can be written as,

$$-\rho \overline{u'v'} = -\rho \overline{v'u'} = \mu_t \left(\frac{\partial U}{\partial y} + \frac{\partial V}{\partial x} \right) \quad (3.3.9)$$

This is why the Reynolds stress tensor is symmetric and there are six independent components.

Eq. 3.3.8 and Eq. 3.3.9 are the diagonal terms of the Reynolds stress tensor, but for the normal components, Eq. 3.3.9 becomes,

$$-\rho \overline{u'u'} = 2\mu_t \frac{\partial U}{\partial y} \quad (3.3.10)$$

Now, by the definition of turbulent kinetic energy (k), it is the sum of the Reynolds stress terms. But, by adding the Reynolds stress terms, an inconsistent solution of turbulent kinetic energy is obtained, as shown below:

$$-\rho (\overline{u'u'} + \overline{v'v'} + \overline{w'w'}) = 2\mu_t \left(\frac{\partial U}{\partial y} + \frac{\partial V}{\partial x} + \frac{\partial W}{\partial z} \right) \quad (3.3.11)$$

As,

$$k = \frac{1}{2} (\overline{u'u'} + \overline{v'v'} + \overline{w'w'}) \quad (3.3.12)$$

So, sum of the normal components of Reynolds stress terms should be

$$-\rho (\overline{u'u'} + \overline{v'v'} + \overline{w'w'}) = 2\rho k \quad (3.3.13)$$

which is not equal to Eq. 3.3.11.

Again, for an incompressible flow, Eq. 3.3.11 becomes a problem, because

$$\frac{\partial U}{\partial y} + \frac{\partial V}{\partial x} + \frac{\partial W}{\partial z} = 0 \quad (3.3.14)$$

Therefore 1/3rd of the sum of the normal components is subtracted from the over predicting error Reynolds stress term giving

$$-\rho \overline{u'u'} = 2\mu_t \left\{ \frac{\partial U}{\partial x} - \frac{1}{3} \left(\frac{\partial U}{\partial x} + \frac{\partial V}{\partial y} + \frac{\partial W}{\partial z} \right) \right\} - \frac{1}{3} (2\rho k) \quad (3.3.15)$$

$$-\rho \overline{v'v'} = 2\mu_t \left\{ \frac{\partial V}{\partial x} - \frac{1}{3} \left(\frac{\partial U}{\partial x} + \frac{\partial V}{\partial y} + \frac{\partial W}{\partial z} \right) \right\} - \frac{1}{3} (2\rho k) \quad (3.3.16)$$

$$-\rho \overline{w'w'} = 2\mu_t \left\{ \frac{\partial W}{\partial x} - \frac{1}{3} \left(\frac{\partial U}{\partial x} + \frac{\partial V}{\partial y} + \frac{\partial W}{\partial z} \right) \right\} - \frac{1}{3} (2\rho k) \quad (3.3.17)$$

This is done, so that the summation of these equations, that is, the normal components justify the turbulent kinetic energy.

Combining Eq. 3.3.9, Eq. 3.3.15, Eq. 3.3.16, and Eq. 3.3.17 in tensor notation, in terms of mean rate of strain tensor (S_{ij}) and its deviatoric part (S_{ij}^*) one obtains

$$-\rho \overline{u'_i u'_j} = 2\mu_t \left(S_{ij} - \frac{1}{3} \frac{\partial U_k}{\partial x_k} \delta_{ij} \right) - \frac{2}{3} \rho k \delta_{ij} \quad (3.3.18)$$

and,

$$-\rho \overline{u'_i u'_j} = 2\mu_t S_{ij}^* - \frac{2}{3}\rho k \delta_{ij} \quad (3.3.19)$$

Shear stresses can be written as mean rate of strain tensor

$$S_{ij} = \mu_t \left(\frac{\partial U_i}{\partial x_j} + \frac{\partial U_j}{\partial x_i} \right) \quad (3.3.20)$$

$$S_{ij}^* = \frac{1}{2} \left(\frac{\partial U_i}{\partial x_j} + \frac{\partial U_j}{\partial x_i} - \frac{1}{3} \frac{\partial U_k}{\partial x_k} \delta_{ij} \right) \quad (3.3.21)$$

where the repeated indices (k, k) represent summation and δ_{ij} is the Kronecker delta,

$$\delta_{ij} = \begin{cases} 1 & i = j \\ 0 & i \neq j \end{cases}$$

Eq. 3.3.18 can be written in vector notation as well, known as Boussinesq hypothesis approach, commonly used in OpenFOAM or ANSYS Fluent solver as

$$-\rho \overline{u'_i u'_j} = \mu_t [\nabla U + (\nabla U)^T] - \frac{1}{3} (\nabla U) I - \frac{2}{3} \rho k I \quad (3.3.22)$$

Depending on the turbulence model, the eddy-viscosity is calculated. The different turbulence models developed over the time in order to best predict the flow parameters are dependent on y^+ , Reynolds number and used for external aerodynamics, turbomachinery etc. The development of the turbulence models is explained next.

Before the $k - \epsilon$ model, there were models that used the concept of mixing length, which represents the range of size of the eddies or the turbulence structure that exist in the flow. The more energetic the flow, more is the mixing length, and it can be formulated as: $\mu_t = \rho k^{1/2} l_m$ or $\mu_t = \rho l_m^2 \left| \frac{\partial U}{\partial y} \right|$

This is further specified in Prandtl mixing length hypothesis, which says that the mixing length of the eddies are affected at a distance of 'y' due to the presence of the wall, $l_m = \kappa y$; $\kappa = 0.41$.

The presence of a wall along with the viscosity in the viscous sub-layer impacts the mixing length by damping the eddies and reducing their size. An account of this damping can be given by the Van Driest model, which says, $l_m = \kappa y \left[1 - \exp \left(-\frac{y^+}{A^+} \right) \right]$; $A^+ = 26.0$

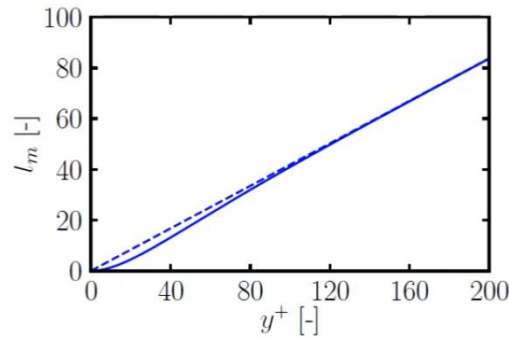


Figure 3.3.1: Prandtl mixing length vs van Driest model mixing length

The dashed line represents the linear Prandtl model, and the solid line represents the Van Driest model which shows that the mixing length reduces as the wall is approached.

The mixing length is actually specified algebraically, which indicates that the distance of the wall is specified throughout the entire domain. But turbulent fluid encounters convection and diffusion so instead of the mixing length, a transport equation is solved. This is when the transport equation for turbulent kinetic energy and the turbulence dissipation rate comes into action.

Some of the popular turbulence closure models are detailed in the following subsections.

3.3.1.1 $k - \epsilon$ Model: [167]

$k - \epsilon$ model was developed as an improvement over the previous mixing length model. In this model the eddy viscosity (μ_t) is calculated as

$$\mu_t = \rho C_\mu \frac{k^2}{\epsilon}; \quad C_\mu = 0.09 \quad (3.3.23)$$

The Reynolds stress in the RANS equation need to be modelled to close the equations. This can be written in vector notation as

$$\frac{\partial(\rho U)}{\partial t} + \nabla \cdot (\rho U U) = -\nabla p + \nabla \cdot \mu [(\nabla U + (\nabla U)^T)] + \rho g - \nabla \left(\frac{2}{3} \mu (\nabla \cdot U) \right) - \nabla \cdot (\rho \overline{U'U'}) \quad (3.3.24)$$

or,

$$\frac{\partial(\rho U)}{\partial t} + \nabla \cdot (\rho U U) = -\nabla p + \nabla \cdot (\mu + \mu_t) [(\nabla U + (\nabla U)^T)] - \frac{2}{3} \mu (\nabla \cdot U) I + \rho g \quad (3.3.25)$$

The mixing length can be calculated from the turbulence dissipation rate by

$$l_m = \frac{C_\mu k^{3/2}}{\epsilon} \quad (3.3.26)$$

The transport equation for turbulence kinetic energy is same for standard, RNG and realizable $k - \epsilon$ model.

$$\frac{\partial(\rho k)}{\partial t} + \nabla \cdot (\rho U k) = \nabla \cdot \left[\left(\mu + \frac{\mu_t}{\sigma_k} \right) \nabla k \right] + P_k + P_b - \rho \epsilon + S_k \quad (3.3.27)$$

$\frac{\partial(\rho k)}{\partial t}$: Time

$\nabla \cdot (\rho U k)$: Convection

$\nabla \cdot \left[\left(\mu + \frac{\mu_t}{\sigma_k} \right) \nabla k \right]$: Diffusion

$P_k + P_b - \rho \epsilon + S_k$: Sources and sink, where P_k = Production due to mean velocity shear; P_b = Production due to buoyancy; S_k = User-defined source

The transport equation for turbulence dissipation rate is

$$\frac{\partial(\rho \epsilon)}{\partial t} + \nabla \cdot (\rho U \epsilon) = \nabla \cdot \left[\left(\mu + \frac{\mu_t}{\sigma_\epsilon} \right) \nabla \epsilon \right] + C_1 \frac{\epsilon}{k} (P_k + C_3 P_b) - C_2 \rho \frac{\epsilon^2}{k} + S_\epsilon \quad (3.3.28)$$

$\frac{\partial(\rho \epsilon)}{\partial t}$: Time

$\nabla \cdot (\rho U \epsilon)$: Convection

$\nabla \cdot \left[\left(\mu + \frac{\mu_t}{\sigma_\epsilon} \right) \nabla \epsilon \right]$: Diffusion

$C_1 \frac{\epsilon}{k} (P_k + C_3 P_b) - C_2 \rho \frac{\epsilon^2}{k} + S_\epsilon$: Sources and sink

C_1, C_2 and C_3 depend on the selection of the $k - \epsilon$ model. Comparing the two transport equations, eddy viscosity can be obtained from Eq. 3.3.23.

The model coefficients are present in many journal papers which has evolved consequently and are used in various CFD software.

In mixing length model, the Van Driest approach depicts the damping of the turbulence dissipation rate unlike the $k - \epsilon$ model, where the damping functions (f_1, f_2, f_μ) damps the model coefficients (C_1, C_2, C_μ) to reduce the dissipation rate close to the wall. This means that the equations of $k - \epsilon$ model can be applied up to the wall, that is, even when the first cell from the wall is present in the viscous sub-layer ($y^+ < 5$). This is known as low-Re formulation.

The damping functions are

$$f_1 = 1; \quad f_2 = 1 - 0.3 \exp(-Re_T^2); \quad f_\mu = \exp\left(\frac{-3.4}{(1 + (Re_T/50))^2}\right) \quad (3.3.29)$$

and $Re_T =$ Turbulent Reynolds number $= \frac{\rho k^2}{\mu \epsilon}$

$$Re_T = \frac{\rho k^{1/2} l_m}{\mu} \sim \left(\frac{\rho U L}{\mu}\right) \quad (3.3.30)$$

Replacing the mixing length, one obtains

$$Re_T = \frac{\rho k^2}{\mu \epsilon} \quad (3.3.31)$$

In low Re formulation, the eddy/turbulent viscosity is computed from k and epsilon as,

$$\mu_t = f_\mu C_\mu \frac{\rho k^2}{\epsilon} \quad (3.3.32)$$

Large Re_T means turbulent forces are dominating and thus it means the point of consideration is far away from the wall. On the other hand, very small Re_T means molecular viscosity is dominating the turbulent viscosity close to the wall. So, the laminar viscosity will dominate the diffusion term in the momentum equations.

$$\dots + \nabla \cdot [(\mu + \mu_t)(\nabla U + (\nabla U)^T]$$

The damping functions are not point specific values rather applied to every cell in the mesh and it is less than 1 near the wall and increases on moving further away from the wall.

The damping function f_1 was found to be not making any considerable improvement and thus is considered to be 1.

$$\frac{\partial(\rho \epsilon)}{\partial t} + \nabla \cdot (\rho U \epsilon) = \nabla \cdot \left[\left(\mu + \frac{\mu_t}{\sigma_\epsilon} \right) \nabla \epsilon \right] + C_1 \frac{\epsilon}{k} (f_1 P_k + C_3 P_b) - C_2 \rho \frac{\epsilon^2}{k} + S_\epsilon \quad (3.3.33)$$

The damping function f_2 however applies more to the dissipation of turbulent dissipation rate:

$$\frac{\partial(\rho \epsilon)}{\partial t} + \nabla \cdot (\rho U \epsilon) = \nabla \cdot \left[\left(\mu + \frac{\mu_t}{\sigma_\epsilon} \right) \nabla \epsilon \right] + C_1 \frac{\epsilon}{k} (f_2 P_k + C_3 P_b) - C_2 \rho \frac{\epsilon^2}{k} + S_\epsilon \quad (3.3.34)$$

The $k - \epsilon$ model is useful to resolve the mesh at the viscous sub-layer, that is, near the wall, at low Reynolds number, like that in case of knowing wall shear stress and heat transfer applications, where y^+ values are less than 5 or 1. This is done in external aerodynamic simulation or turbomachinery simulations. But over the years it has been found that the $k - \omega$ SST model is better at resolving the mesh at y^+ less than 5, than the $k - \epsilon$ model. So, the $k - \epsilon$ model is presently used in high Re applications with $y^+ > 30$, for which the high Re formulations are solved and there are no requirements of damping functions.

3.3.1.2 $k - \omega$ Model [168]

The Eq. 3.3.23 and Eq. 3.3.25 have been solved by this new closure model. Generic meaning of the terms ϵ and ω are described below.

ϵ is the turbulent dissipation rate, the rate at which turbulent kinetic energy is converted into thermal energy by viscosity. The plot of turbulent energy cascade describes the amount of energy contained in different size of the eddies. This plot explains that all of the turbulent kinetic energy is contained when there are large eddies, and it is dissipated when there are small eddies.

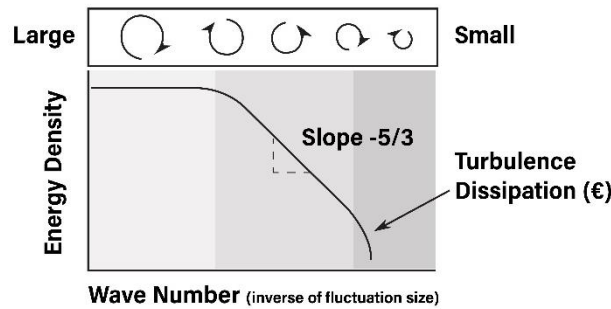


Figure 3.3.2: Energy cascading; turbulence dissipation with wave number

$$\epsilon = \nu \frac{\partial U'_1}{\partial x_j} \frac{\partial U'_1}{\partial x_j} \quad (3.3.35)$$

The fluctuations (U'_i) are unknown, so ϵ cannot be directly evaluated from Eqn. 3.3.35. So, transport equations, Eqn. 3.3.36 is solved to calculate ϵ .

$$\frac{\partial(\rho k)}{\partial t} + \nabla \cdot (\rho k U) = \nabla \cdot \left(\left(\mu + \frac{\mu_t}{\sigma_k} \right) \nabla k \right) + P_\epsilon - \rho \epsilon \quad (3.3.36)$$

In Eq.3.3.36, ϵ has a negative sign before it indicates that it acts as a sink where the turbulent kinetic energy is dissipated. In practical case, there is high dissipation near wall, shear layer and where turbulence is going to be high. ω is another representation of dissipation of turbulence, so often known as a specific turbulence dissipation rate, given by:

$$\omega = \frac{\epsilon}{c_\mu k}; \quad C_\mu = 0.09 \quad (3.3.37)$$

This model is detailed in the work by [100]. The transport Equation for calculating ω ,

$$\frac{\partial(\rho \omega)}{\partial t} + \nabla \cdot (\rho \omega U) = \nabla \cdot \left(\left(\mu + \frac{\mu_t}{\sigma_\omega} \right) \nabla \omega \right) + \frac{\gamma}{\nu_t} P_k - \beta \rho \omega^2 \quad (3.3.38)$$

The main difference between the above mentioned two turbulence models is that in $k - \omega$ model there are various empirical coefficients depending on the form of model being used. Choice of these coefficients in different solvers may alter the end results.

Although both the models are similar, $k - \omega$ model is better for aerodynamics and turbomachinery which the $k - \epsilon$ model is not, as explained earlier. This is because in $k - \epsilon$ model the damping functions (f_1, f_2, f_μ) used are not that accurate in the presence of adverse pressure gradients. But $k - \omega$ model does not need these damping functions when adverse pressure gradient is present. The limitations of this model are explained in Chapter 2 (Literature Review), as mentioned in [101], that this model is dependent on free-stream turbulence conditions.

The remedy for this limitation of both the models was proposed by [169]. A blend of both the models is used by using the $k - \epsilon$ model far away from the wall in the free stream when it is not susceptible to small changes in k and ω ; and then near the wall the $k - \omega$ model is used. In between these, a blend of both the models is used which forms the basis of the $k - \omega$ SST (1992) model.

3.3.1.3 $k - \omega$ BST and SST model: [170]

These models are explained in detail in [168]. ϵ in the transport Equations of $k - \epsilon$ model, Eqn. 3.3.27 and Eqn. 3.3.28 is substituted with ω from the relation, Eqn. 3.3.39 and Eqn. 3.3.40 is obtained which is same as the transport Equations of $k - \omega$ model Eqn. 3.3.38, but with an additional term.

$$\epsilon = C_\mu k \omega \quad (3.3.39)$$

$$\frac{\partial(\rho\omega)}{\partial t} + \nabla \cdot (\rho\omega U) = \nabla \cdot \left(\left(\mu + \frac{\mu_t}{\sigma_k} \right) \nabla \omega \right) + \frac{\gamma}{\nu_t} P_k - \beta \rho \omega^2 + 2 \frac{\rho \sigma_\omega^2}{\omega} \nabla k : \nabla \omega \quad (3.3.40)$$

A blending function, $(1 - F_1)$ is chosen which builds a relation between the two models,

$$2(1 - F_1) \frac{\rho \sigma_\omega^2}{\omega} \nabla k : \nabla \omega \quad (3.3.41)$$

$$\nabla k : \nabla \omega = \frac{\partial k}{\partial x_j} \frac{\partial \omega}{\partial x_j} = \frac{\partial k}{\partial x} \frac{\partial \omega}{\partial x} + \frac{\partial k}{\partial y} \frac{\partial \omega}{\partial y} + \frac{\partial k}{\partial z} \frac{\partial \omega}{\partial z} \quad (3.3.42)$$

The model is $k - \epsilon$, if $F_1 = 0$ and the model is $k - \omega$, if $F_1 = 1$. Thus, the Eqn. 3.3.27 and Eq. 3.3.40 form the transport Equations for this model. This is known as the $k - \omega$ Baseline Stress Transport (BST) model. The blending function F_1 is considered at the cells nearest to the wall and its value decreases to 0 through the farther cells. F_1 is given by:

$$F_1 = \tanh(\text{arg}_1^4) \quad (3.3.43)$$

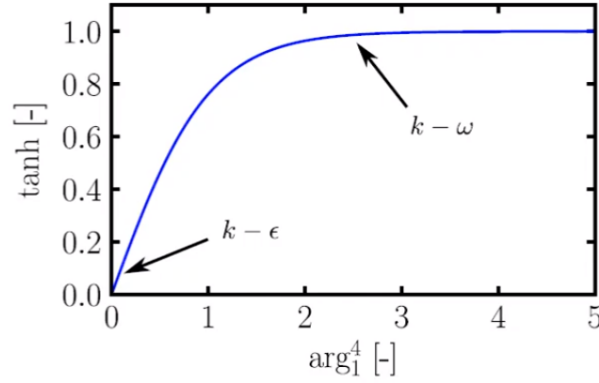


Figure 3.3.3: Blending function between $k - \omega$ and $k - \epsilon$ models

The hyperbolic tan is used so that there is a smooth transition between the two models. The argument arg_1^4 depends on the distance, 'd' closest to the wall, which is sometimes same as the wall normal distance 'y'.

$$arg_1 = \min \left[\max \left(\frac{\sqrt{k}}{\beta^* \omega d}, \frac{500\nu}{d^2 \omega} \right), \frac{4\rho\sigma_{\omega_2} k}{CD_{k\omega} d^2} \right] \quad (3.3.44)$$

From the relation, it is clear that when 'd' is small arg_1 will be large and thus F_1 will tend to be 1, that is, near to the wall. [This 'd' is specified at the beginning for a stationary mesh, but for a moving mesh 'd' is to be specified for each computation or change in position.]

F_1 not only blends the Equations together but also blends the empirical constants of the two models and that is done by,

$$\phi = F_1 \phi_{\omega} + (1 - F_1) \phi_{\epsilon} \quad (3.3.45)$$

ϕ_{ω} is the model constant (β^*) in $k - \omega$ model and ϕ_{ϵ} (C_{μ}) in $k - \epsilon$ model.

3.3.1.4 $k - \omega$ Shear Stress Transport (SST) model: [169]

The $k - \omega$ BST model was found to be overpredicting the wall shear stress, so the BST model was extended into the SST model with a viscosity limiter [171].

$$\text{Original: } \mu_t = \frac{\rho k}{\omega}; \quad \text{SST Model: } \mu_t = \frac{a_1 \rho k}{\max(a_1 \omega, SF_2)} \quad (3.3.46)$$

The purpose is to limit the viscosity thus reduce the wall shear stress to a more accurate level, closer to the experimental measurements of separated flow. 'S' is the magnitude of shear strain. F_2 is another blending function, which if large then eddy viscosity is reduced.

$$F_2 = \tanh(arg_2^2) \quad (3.3.47)$$

$$arg_2 = \max \left(\frac{2\sqrt{k}}{\beta^* \omega d}, \frac{500\nu}{\omega d^2} \right) \quad (3.3.48)$$

'd' is same as that for F_1 but can never be the wall normal distance 'y'. The main difference between the original model, BST model and SST model is expressed in Eqn. 3.3.46 and lies in the formulation of production term (P_{ω}) of ω in the SST model.

The production term, P_ω :

$$P_\omega = \gamma \frac{\omega}{k} \tau_{ij} \cdot \frac{\partial u_i}{\partial x_j} \quad (3.3.49)$$

The dimensionless group, $\nu_t \left(= \frac{\omega}{k} \right)$ is introduced in front of the strain rate tensor which is equal to one in the original and BST models.

It had been concluded that k - ω SST model is in better agreement to experiments for mildly separated flows, that is, external aerodynamics or simulations where separation is required. This model has undergone improvements and changes since its development, and it is updated in [170].

3.3.1.5 Spalart Allmaras Model [172]

This model was proposed by Spalart and Allmaras [172] as an improvement over the k - ϵ model, to build a model that can simulate boundary layer for adverse pressure gradients. It is stated in [173] that the profile of ν_t near the wall of a flat plate, in the log-law region ($y^+ > 30$) is linear and in the viscous sub-layer ($y^+ < 5$), the profile is quartic, i.e., varies with $(y^+)^4$.

To resolve the quartic variation, the mesh needs to be quite fine close to the wall, as flow quantities vary linearly through cells in CFD. So, to solve this incongruity, instead of ν_t , a similar variable, the Spalart-Allmaras variable called $\tilde{\nu}$ is solved in order to make the solution more stable and easier with a smaller number of cells closer to the wall. $\tilde{\nu}$ varies linearly between ν_t and y^+ . This linear profile is most suitable for flow over flat plates.

For boundary layer over a flat plate with zero pressure gradient,

$$\tilde{\nu} = \kappa y^+ \quad (3.3.50)$$

Other than the case of a flat plate, the likely-to-be-linear profile would not be sufficient for any solution by the CFD code. This is when the transport equation for $\tilde{\nu}$ is solved and from that ν_t is obtained (Eqn. 3.3.50) and fetched into the momentum equations.

$$\nu_t = \tilde{\nu} f_{v1} \quad \text{where } f_{v1} = \frac{\chi^3}{\chi^3 + c_{v1}^3} \quad \text{and } \chi = \frac{\tilde{\nu}}{\nu} \quad (3.3.51)$$

The linear profile near to a wall for finite Re is explained in [172]. The transport Equation for the Spalart-Allmaras variable, $\tilde{\nu}$, is given by,

$$\frac{\partial \tilde{\nu}}{\partial t} + \nabla \cdot (U \tilde{\nu}) = c_{b1} \bar{S} \tilde{\nu} + \frac{1}{\sigma} [\nabla \cdot (\nu + \tilde{\nu}) \nabla \tilde{\nu} + c_{b2} (\nabla \tilde{\nu})^2] - c_{w1} f_w \left(\frac{\tilde{\nu}}{d} \right)^2 \quad (3.3.52)$$

which makes numerical solutions easier and tends to be linear on solving. $\tilde{\nu}$ is identical to ν_t , far away from the wall.

$c_{b1} \bar{S} \tilde{\nu}$: This term is for turbulence generation in the model, even in the regions of high shear to replicate turbulence generation in real flows. This is done by assuming shear rate to be proportional to the mean velocity profile. ‘S’ is the shear rate tensor.

$$S' = \frac{1}{2} (\nabla U + (\nabla U)^T), \quad \text{and, } S = \sqrt{S' : S'} \quad (3.3.53)$$

$\frac{1}{\sigma} [\nabla \cdot (\nu + \tilde{\nu}) \nabla \tilde{\nu} + c_{b2} (\nabla \tilde{\nu})^2]$: The diffusion term here has an additional non-linear term. This term is often split into a linear diffusion term, for the finite volume discretization and a non-linear explicit source term.

The term that shows the damping of turbulence near to any wall is, $c_{w1}f_w(\frac{\tilde{\nu}}{d})^2$. This is done by a combination of inviscid damping of pressure fluctuations and the viscous damping very close to the wall. The negative sign indicates destruction of turbulence. 'd' is the distance to the nearest wall and lesser 'd' indicates more turbulence destruction. The viscous damping is done by f_{v1} [Eq. (3.3.51)] that imposes the quartic behaviour close to the wall on nut which implicitly contains a lot of the viscous destruction terms and inviscid damping of pressure fluctuations is done by this term.

$f_w \rightarrow 0$ as $d \rightarrow 0$ to prevent division by zero error.

The boundary conditions for $\tilde{\nu}$ is taken as $\tilde{\nu} = 0$ at the wall for its linear behaviour in the viscous sub-layer. In the freestream, that is, far away from the wall, $\tilde{\nu}$ is taken to be the same as ν_t . So, at the inlet to the domain,

$$\tilde{\nu} = \nu_t = \frac{C_\mu k^2}{\epsilon} \quad \text{or} \quad \tilde{\nu} = \nu_t = \frac{k}{\omega} \quad (3.3.54)$$

k and ω can be calculated from turbulent length scale, typically 10% of the aerofoil chord length and turbulence intensity, I, typically of 5%,

$$k = \frac{3}{2} U_\infty^2 I^2 \quad \epsilon = C_\mu \frac{k^{3/2}}{l} \quad (3.3.55)$$

This term is important at the wake edge of the turbulent region, where diffusion dominates. Away from the boundary, if there is a wake region, there will be more spreading and more diffusion. Thus, to control this spreading and bring the numerical simulations close to that of the experiments, c_{b2} was calibrated to be 0.622 that gives a more accurate spreading of the wake profile. This is useful in the downstream of an aerofoil or a diffusion section in a duct.

3.3.1.6 Realizable $k - \epsilon$ Model [104]

In this model, a new model dissipation rate Equation and a new realizable eddy viscosity formulation, was proposed. The new model dissipation rate Equation was based on the dynamic equation of the mean-square vorticity fluctuation at Reynolds number of large turbulent scale. The new eddy viscosity formulation is based on the realizability constraints: normal Reynolds stress positivity and Schwarz' inequality for turbulent shear stresses. The flows examined included:

- (1) rotating homogeneous shear flows
- (2) boundary-free shear flows including a mixing layer, planar and round jets
- (3) a channel flow, and flat plate boundary layers with and without a pressure gradient, and
- (4) backward facing step separated flows

This model was proved to be significantly better than the standard k-epsilon eddy viscosity model.

3.3.2 Large Eddy Simulation (LES)

LES is a time-resolved approach that aims to capture large-scale turbulent structures while modelling the effect of smaller scales, unlike in RANS where the effect of smaller scale eddies are

not prominently captured. In LES, the flow field is decomposed into resolved large-scale eddies and unresolved small-scale eddies. The governing equations for LES can be written as:

Continuity Equation:

$$\nabla \cdot U = 0 \quad (3.3.56)$$

Momentum Equations:

$$\rho \left(\frac{\partial U}{\partial t} + \nabla \cdot (UU) \right) = -\nabla P + \nabla \cdot (\mu(\nabla U + (\nabla U)^T)) - \nabla \cdot \tau \quad (3.3.57)$$

where U represents the velocity, P is the pressure, μ is the dynamic viscosity, and τ denotes the subgrid-scale (SGS) stress tensor. The SGS stress tensor τ is typically modeled using SGS models, such as the Smagorinsky model or dynamic models. LES captures a wide range of turbulent scales but requires resolving the smallest scales, making it computationally more expensive than RANS. LES is suitable for simulating flows with significant turbulent structures and unsteady phenomena.

Closure Models

Both RANS and LES require closure models to represent the unresolved turbulent quantities (Reynolds stress in RANS and SGS stress in LES).

In LES closure models the nonlinearity in the flow effectively couples with the spatial scales, i.e., large structures depend through the nonlinearity of the smaller scales and vice versa, through the convection term in the N-S equation. Closure models introduce additional equations or assumptions to close the system of equations. Therefore, one has to model the underlying phenomena that happens inside the coarse grids. That essentially leads to sub-grid scale (SGS) models, which can be thought of similar to the eddy viscosity model in RANS. The idea is to model the vortices with higher wavenumber. Various closure models exist which have different levels of accuracy and complexity.

A thorough stepwise calculation of turbulence parameters is described next.

3.3.2.1 Part 1: Calculation of Mean Velocity

The CFD code computes the instantaneous velocity, U in the following described manner. The mean velocity \bar{U} is calculated by time-averaging. The averaging should be done after initial transient. Once the mean velocity field is computed by the RANS model, the fluctuating velocity component u' can conceptually be estimated by subtracting time-averaged mean velocity, \bar{U} from instantaneous velocity, U .

To isolate the fluctuations, u'

$$u' = U - \bar{U} \quad (3.3.58)$$

There are 3 fluctuating velocity components, the other two being,

$$v' = V - \bar{V} \quad (3.3.59)$$

$$w' = W - \bar{W} \quad (3.3.60)$$

3.3.2.2 Part 2: Calculation of Fluctuating Velocity

The kinetic energy is calculated in the fluctuations, which is resolved by the mesh by calculating the fluctuating velocity component in each of the cells. But in RANS, the fluctuating velocity component, u' is modelled and not calculated. Thus, 'k' would not be resolved in RANS calculation. Kinetic energy per unit mass is $\frac{1}{2}u * u$, so the fluctuating velocity components are to be multiplied together.

The instantaneous Reynolds stresses that are resolved by the mesh are:

$$u'u', u'v', u'w', v'u', v'v', v'w', w'u', w'v', w'w' \quad (3.3.61)$$

The normal components are only used to calculate the resolved turbulent kinetic energy. Time average is calculated for each of the product of fluctuating velocity components.

$$\overline{u'u'}, \overline{u'v'}, \overline{u'w'}, \overline{v'u'}, \overline{v'v'}, \overline{v'w'}, \overline{w'u'}, \overline{w'v'}, \overline{w'w'} \quad (3.3.62)$$

The average of the fluctuating velocity is zero.

$$\overline{u'} = 0 \quad (3.3.63)$$

This is the reason the time averaging is done after multiplication.

Taking the time average first will lead to the value of zero as the area under the curve above x-axis and below it will be same. So, the fluctuating components are to be multiplied first and then time averaged.

3.3.2.3 Part 3: Resolving Turbulent Kinetic Energy

There are 9 components of the resolved Reynolds Stress tensor per unit density:

$$\frac{R_{ij}}{\rho} = \begin{bmatrix} \overline{u'u'} & \overline{u'v'} & \overline{u'w'} \\ \overline{v'u'} & \overline{v'v'} & \overline{v'w'} \\ \overline{w'u'} & \overline{w'v'} & \overline{w'w'} \end{bmatrix} \quad (3.3.64)$$

The order of multiplication does not matter, by the commutative law, thus

$$\overline{u'v'} = \overline{v'u'}, \quad \overline{u'w'} = \overline{w'u'}, \quad \overline{v'w'} = \overline{w'v'} \quad (3.3.65)$$

Therefore, there are only 6 independent quantities (symmetric tensor)

$$\frac{R_{ij}}{\rho} = \begin{bmatrix} \overline{u'u'} & \overline{u'v'} & \overline{u'w'} \\ \boxed{} & \overline{v'v'} & \overline{v'w'} \\ \boxed{} & \boxed{} & \overline{w'w'} \end{bmatrix} \quad (3.3.66)$$

The diagonal components are used to calculate the resolved turbulent kinetic energy.

$$k_{res} = \frac{1}{2}(\overline{u'u'} + \overline{v'v'} + \overline{w'w'}) \quad (3.3.67)$$

It is also written as

$$k_{res} = \frac{1}{2}(\overline{u'^2} + \overline{v'^2} + \overline{w'^2}) \quad (3.3.68)$$

The reason of adding the diagonal components is that within the flow field, there are some turbulences in the x, y and z-axis, but the turbulent kinetic energy at a point is of concern, which is a scalar value.

In OpenFOAM, the matrix calculation (units: m^2/s^2) of Eq. 3.3.66 is done with the command uPrime2Mean. ANSYS Fluent calculates the root mean square velocity (units: m/s)

$$U_{RMSE} = \sqrt{(u')^2} \quad (3.3.69)$$

$$k_{res} = \frac{1}{2}(U_{RMSE}^2 + V_{RMSE}^2 + W_{RMSE}^2) \quad (3.3.70)$$

To calculate k_{res} a new field is to be calculated in the post-processor.

$$k_{res} = 0.5 * (UPrime2MeanXX + UPrime2MeanYY + UPrime2MeanZZ) \quad (3.3.71)$$

$$k_{res} = 0.5 * (URMSE * URMSE + VRMSE * VRMSE + WRMSE * WRMSE) \quad (3.3.72)$$

3.3.2.4 Part 4: Calculating Total Turbulent Kinetic Energy

k_{res} is the turbulent kinetic energy resolved by the mesh, not the total kinetic energy (k).

$$k = k_{res} + k_{sgs} \quad (3.3.73)$$

k_{sgs} is the turbulent kinetic energy of the eddies smaller than mesh size. In RANS, 'k' is modelled and in LES 'k' is calculated via k_{res} and k_{sgs} .

3.3.2.5 Part 5: Calculating Sub-Grid Scale Turbulent Kinetic Energy

OpenFOAM calculates k_{sgs} for the users and writes it as a field (k). But ANSYS Fluent users need to calculate k_{sgs} in the post-processor.

The method used to determine k_{sgs} depends on the sub-grid scale (SGS) model. The CFD codes solve a transport equation for k_{sgs} if a kinetic energy transport model is used,

$$\frac{\partial(\rho k_{sgs})}{\partial t} + \nabla \cdot (\rho U k_{sgs}) = \nabla \cdot (\rho D_k \nabla k_{sgs}) - C_\epsilon \frac{\rho k_{sgs}^{3/2}}{\Delta} + \rho G_{sgs} - \frac{2}{3} \rho k_{sgs} \nabla \cdot U \quad (3.3.74)$$

The post-processor then directly reads k_{sgs} . But for other models, k_{sgs} is to be calculated. It can be calculated from the sub-grid length scale, l_{sgs} .

$$k_{sgs} = \left(\frac{\mu_{sgs}}{\rho l_{sgs}} \right)^2 \quad (3.3.75)$$

3.3.2.6 Part 6: Calculating Sub-Grid Length Scale

l_{sgs} can be described as the size of an eddy that has same turbulent kinetic energy as the average of all the eddies smaller than the mesh size, similar to the integral length scale (l_0).

l_{sgs} should be smaller than the mesh size,

$$l_{sgs} = C_s * (Cell Volume)^{1/3} \quad (3.3.76)$$

C_s is the Smagorinsky coefficient which is equal to 0.1. C_s is less than 1 in order to have the length scale smaller than the cell size.

The eddies are damped near the walls. l_{sgs} is limited by the distance to the wall, y, for thin high aspect ratio cells. So, l_{sgs} can be expressed as

$$l_{sgs} = \min (\kappa y, C_s \Delta^{1/3}), \quad \kappa = 0.41 \quad (3.3.77)$$

3.3.2.7 Part 7: Calculating Tubulent Kinetic Energy Ratio

After obtaining both the residual turbulent kinetic energy, k_{res} and sub-grid scale turbulent kinetic energy, k_{sgs} , the ratio $\frac{k_{res}}{(k_{res}+k_{sgs})}$ is calculated in the post-processor to check whether the mesh is resolving more than 80% of the turbulent kinetic energy.

3.3.2.8 Part 8: Mesh Refinement

Mesh refinement increases k_{res} and decreases k_{sgs} . It leads to change in balance of the two types of turbulent kinetic energy.

Understanding the Sub-Grid Models:

Large turbulent eddies are unstable in nature and tend to break down into smaller and even smaller eddies, by a process known as eddy or energy cascade. This cascading action leads to smallest eddies that dissipates into heat through molecular viscosity. The smallest eddies just larger than the cell size, that on further breakdown creates eddies which cannot be resolved and are also not small enough to be dissipated to heat by molecular viscosity, are removed by increasing the turbulent kinetic energy.

Turbulence Dissipation Rate (ϵ) is the rate at which turbulent kinetic energy is converted into thermal energy, that is, turbulent kinetic energy per unit time (SI unit: m^2/s^2). An increase in Turbulence dissipation rate (ϵ) leads to an increase in the rate at which the turbulent eddies are dissipated. It is calculated by the product of molecular viscosity and two velocity gradients.

$$\epsilon = \nu \frac{\partial U_i}{\partial x_j} \frac{\partial U_i}{\partial x_j} \quad (3.3.78)$$

The velocity gradient considers the mean and fluctuating components of velocity. As the fluctuations are neglected in RANS, so a transport equation for Turbulence Dissipation Rate (ϵ) is solved. But in comparison to the energy of the flow, the molecular viscosity is very small. As the eddies get smaller in size, the velocity gradient increases till the molecular viscosity are large enough to dissipate them. To dissipate these eddies, the viscosity is increased from ν to $\nu + \nu_{sgs}$, where ν_{sgs} is the sub-grid scale viscosity. Due to this, the dissipation rate also increases as

$$\epsilon = (\nu + \nu_{sgs}) \frac{\partial U_i}{\partial x_j} \frac{\partial U_i}{\partial x_j} \quad (3.3.79)$$

But ν is increased specifically to remove the targeted eddies just larger than the cell size. Thus, this is not the true dissipation rate, rather this artificial dissipation mimics the breakdown process.

Increasing dissipation in LES

Starting with the Navier Stokes and continuity equation,

$$\frac{\partial \rho}{\partial t} + \frac{\partial(\rho U_j)}{\partial x_j} = 0 \quad (3.3.80)$$

$$\frac{\partial \rho U_j}{\partial t} + \frac{\partial(\rho U_i U_j)}{\partial x_j} = -\frac{\partial P}{\partial x_j} + \frac{\partial}{\partial x_j}(\tau_{ij}) \quad (3.3.81)$$

τ_{ij} is the viscous stress term, that dissipates energy through molecular viscosity. Its strength is only to dissipate the smallest (Kolmogorov) eddies and not the ones just larger than the grid size. So, to dissipate these eddies just larger than grid size, the dissipation is increased by adding an extra stress term, τ_{sgs} and Eq. 3.3.81 becomes,

$$\frac{\partial \rho U_j}{\partial t} + \frac{\partial(\rho U_i U_j)}{\partial x_j} = -\frac{\partial P}{\partial x_j} + \frac{\partial}{\partial x_j}(\tau_{ij} + \tau_{sgs}) \quad (3.3.82)$$

This term can be mathematically derived by filtering the Navier-Stokes equations. The eddies smaller than the mesh size are not directly resolved but act as a resistive force on the eddies that are resolved. So instead of trying to resolve those small eddies, the resistive force is modelled. This resistive force dissipates energy and breaks down the eddies just larger than the cell size.

The sub-grid stress can be calculated with an eddy-viscosity model. As the eddies get smaller, the velocity gradient increases, the sub-grid stress and force also increases. This sub-grid force is increased enough so that the eddies just larger than cell size is dissipated.

$$\tau_{sgs} = 2\rho\nu_{sgs}S_{ij}^* - \frac{2}{3}\rho k_{sgs}\delta_{ij} \quad (3.3.83)$$

$$\text{where } S_{ij}^* = \frac{1}{2} \left(\frac{\partial \bar{u}_i}{\partial x_j} + \frac{\partial \bar{u}_j}{\partial x_i} - \frac{1}{3} \frac{\partial \bar{u}_k}{\partial x_k} \delta_{ij} \right)$$

S_{ij}^* is the strain rate of the resolved eddies on the CFD mesh.

ν_{sgs} is the factor that controls the strength of the stress that is applied. If ν_{sgs} is too high, the eddies will break down and the kinetic energy will drop too low. But if there is no ν_{sgs} then the eddies just larger than cell size won't get dissipated as τ_{sgs} will not be large enough. So, ν_{sgs} is the controller of the strength of the stress τ_{sgs} . The calculation of ν_{sgs} is described next.

It is assumed that the eddies smaller than the cell size are isotropic, as shown in the Figure 3.3.4. Isotropic means the eddies have the same shape but not the same size. Thus, the eddy size is essential to be considered and not the eddy shape.

As the eddies are isotropic, the value of sub-grid scale viscosity, ν_{sgs} will be scalar, which depend on the size of the eddies. Larger cells will have larger eddies and will require higher ν_{sgs} . There are various sub-grid models to calculate ν_{sgs} , but all of those are based on the same principle of the eddies to be isotropic. The ν_{sgs} required on a coarse mesh will be larger than that for a fine mesh.

Thus, the sub-grid viscosity can be expressed as a function of the mesh size,

$$v_{sgs} = f(\Delta) \quad (3.3.84)$$

This means that different equations are solved on each mesh with different sub-grid viscosity. So, a mesh independence study cannot be done for LES, instead the criteria of resolving 80% of the total turbulent kinetic energy is considered to be as remarkable. On the other hand, in RANS calculation, the equations solved for eddy viscosity is same throughout even if the resolution of the field changes.

The Smagorinsky Turbulence Model

With the assumption of sub-grid scale eddies being isotropic, the determination of v_{sgs} is carried out. According to Smagorinsky, the kinematic viscosity is decomposed into a product of velocity and length from the perspective of units.

Kinematic viscosity (m^2/s) = Velocity (m/s) \times length (m)
 So, $v_{sgs} \sim U_0 \times l_0$ (3.3.85)

As the eddies are isotropic, so a length scale (l_0) is enough to categorize the shape of the eddies. The velocity profile of an eddy is similar to that shown in Figure 3.3.4(a). The average velocity in Cartesian coordinates is zero.

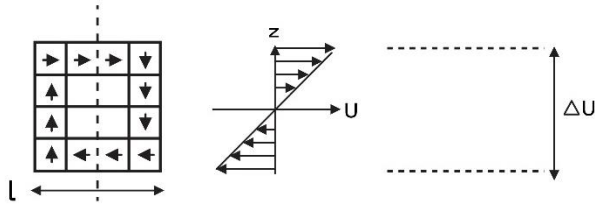


Figure 3.3.4(a): Calculating velocity scale using vertical line

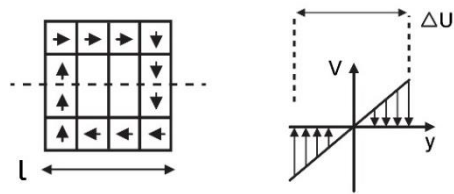


Figure 3.3.4(b): Calculating velocity scale using horizontal line

To find a velocity scale for the eddies, a velocity that characterizes the eddy is chosen. It is better if the velocity difference (ΔU) across the eddy is known. It can be calculated as:

$$\Delta U = l_0 * \frac{\partial U}{\partial z} \quad (3.3.86)$$

Thus, the velocity scale is

$$U_0 \sim l_0 * \frac{\partial U}{\partial z} \quad (3.3.87)$$

Now, if instead of a vertical line through an eddy, a horizontal line is drawn, as shown in Figure 3.3.4(b), the velocity scale (Eq. 3.3.87) shall be

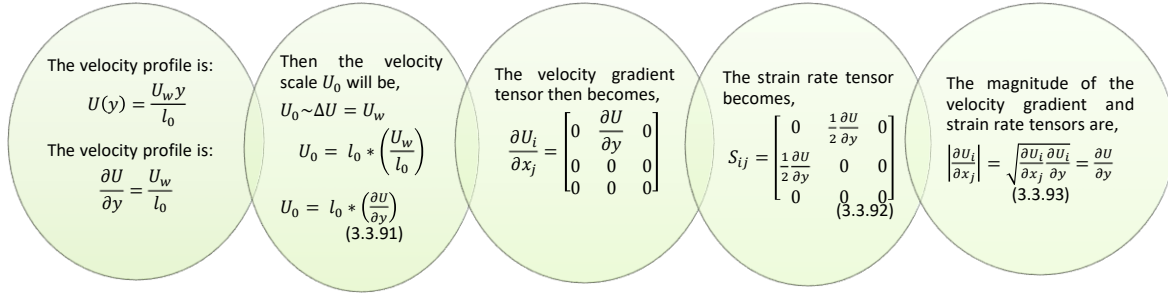
$$U_0 \sim l_0 * \frac{\partial U}{\partial z} \quad \text{or,} \quad U_0 \sim l_0 * \frac{\partial V}{\partial y} \quad (3.3.88)$$

To get a more generalized form of velocity scale for any coordinate system in any direction, the method used in Smagorinsky model is the method of strain rate tensor (S_{ij}).

$$S_{ij} = \frac{1}{2} \left(\frac{\partial U_i}{\partial x_j} + \frac{\partial U_j}{\partial x_i} \right) \quad (3.3.89)$$

$$S_{ij} = \begin{bmatrix} \frac{\partial U}{\partial x} & \frac{1}{2} \left(\frac{\partial U}{\partial y} + \frac{\partial V}{\partial x} \right) & \frac{1}{2} \left(\frac{\partial U}{\partial z} + \frac{\partial W}{\partial x} \right) \\ \frac{1}{2} \left(\frac{\partial V}{\partial x} + \frac{\partial U}{\partial y} \right) & \frac{\partial V}{\partial y} & \frac{1}{2} \left(\frac{\partial V}{\partial z} + \frac{\partial W}{\partial y} \right) \\ \frac{1}{2} \left(\frac{\partial W}{\partial x} + \frac{\partial U}{\partial z} \right) & \frac{1}{2} \left(\frac{\partial W}{\partial y} + \frac{\partial V}{\partial z} \right) & \frac{\partial W}{\partial z} \end{bmatrix} \quad (3.3.90)$$

But a scalar value is required for the velocity scale. The magnitude of S_{ij} would be an incorrect approach.



The magnitude of strain rate tensor (S_{ij}) comes as,

$$|S_{ij}| = \sqrt{S_{ij} S_{ij}} \sqrt{\left(\frac{1}{2} \frac{\partial U}{\partial y} \right)^2 + \left(\frac{1}{2} \frac{\partial U}{\partial y} \right)^2} = \frac{1}{\sqrt{2}} \frac{\partial U}{\partial y} \quad (3.3.94)$$

Hence, if the strain rate tensor is to be used for the velocity scale U_0 , $\sqrt{2}$ is to multiply,

$$U_0 \sim l_0 * \sqrt{2 S_{ij} S_{ij}} \quad (3.3.95)$$

So, the expression for the sub-grid scale kinematic viscosity (ν_{sgs}) becomes,

$$\nu_{sgs} = U_0 \times l_0 \quad (3.3.96)$$

The velocity scale is substituted as,

$$\nu_{sgs} = (l_0 \times \sqrt{2 S_{ij} S_{ij}}) \times l_0 \quad (3.3.97)$$

$$\nu_{sgs} = l_0^2 \sqrt{2 S_{ij} S_{ij}} \quad (3.3.98)$$

Therefore, the strain rate tensor can be calculated from the smallest resolved eddies. Next, the calculation of characteristic length scale, l_0 is required. The size of the eddies is calculated as they are assumed to be isotropic.

The sub-grid scale eddies are actually a range of different sized eddies. Hence, l_0 is chosen such that, the eddy contains the same turbulent kinetic energy as that of an average sized eddy, smaller than the cell size. This is conceptually similar to that of integral length scale. l_0 is expected to be smaller than the cell size and thus can be expressed as,

$$l_0 = C_s \Delta, \text{ where } 0 < C_s < 1 \quad (3.3.99)$$

C_s is the Smagorinsky coefficient and can be called as a fraction of the cell size that calculates the sub-grid length scale.

Substituting Eq. 3.3.99 in Eq. 3.3.98,

$$\nu_{sgs} = (C_s \Delta)^2 \sqrt{2S_{ij}S_{ij}} \quad (3.3.100)$$

The value of Smagorinsky coefficient, C_s for homogenous isotropic turbulence (HIT) was derived by Lilly [174]. HIT means the turbulence was assumed to be far away from walls, that is, with no shear. Lilly [174] referred the explanation by Pope [175] for the derivation of C_s ,

$$C_s = \frac{1}{\pi} \left(\frac{2}{3C_k} \right)^{3/4} \quad (3.3.101)$$

C_k is called Kolmogorov constant, derived from Kolmogorov energy spectrum and found out to be 1.5.

$$E(\kappa) = C_k \epsilon^{2/3} \kappa^{-5/3} \quad (3.3.102)$$

So, for homogenous isotropic turbulence, after solving analytically, $C_s = 0.173$

But at regions of high shear or near the walls, this value of C_s leads to high dissipation of the eddies. In modern CFD codes the value of C_s is chosen as follows:

ANSYS Fluent: $C_s = 0.1$

Phoenics: $C_s = 0.17$

The value of C_s should be checked and noted before running simulations. The limitation of the original model is that a variable sub-grid length, l_0 and C_s is required as the sub-grid eddies vary throughout the domain, particularly near the walls.

There is a region of laminar flow in the viscous sub-layer ($y^+ < 5$), close to the walls. Here, the sub-grid scale eddies are small enough to get dissipated by the viscosity. Hence, there shouldn't be any sub-grid eddies here. Some damping of eddies is expected at the buffer and log-law region.

In the original Smagorinsky model [176], the sub-grid eddies are represented as an additional stress term, τ_{sgs} . This mimics the energy cascade and breaks down the eddies just larger than grid size. Absence of sub-grid eddies mean $\tau_{sgs} = 0$.

In Eq. 3.3.83, the second term ($\frac{2}{3}\rho k_{sgs}\delta_{ij}$) is often neglected by merging it with resolved pressure to obtain a modified pressure.

Now, it is to be checked whether the τ_{sgs} reaches zero towards the wall, in the original Smagorinsky model [176]. In the laminar flow region, the velocity profile is linear, and the strain rate tensor is as given in Eq. 3.3.92.

Thus, $S_{ij}^* \neq 0$ and from that,

$$\tau_{sgs} = 2\rho\nu_{sgs}S_{ij}^* \quad (3.3.103)$$

$\tau_{sgs} \neq 0$, unless $\nu_{sgs} = 0$, but in the original Smagorinsky model [176], $C_s \sim 0.17$ and the cell size $\Delta > 0$, so from Eq. 3.3.103 it is understood that $\nu_{sgs} \neq 0$ even in the viscous sub-layer. Thus, the

original Smagorinsky model [176] does not think that the sub-grid eddies near the wall are dissipated, as it happens practically. These sub-grid eddies are to be damped. The different options for correcting ν_{sgs} near the wall are,

- SGS Kinetic Energy: Model has to be changed
- Van Driest Damping Dynamic Smagorinsky: Length scale has to be changed
- WALE: Velocity scale has is to be changed

The Van Driest Damping

The eddies tend to get smaller as they approach the walls. This is because there are two wall conditions to be satisfied,

- No penetration condition: The fluid does not penetrate the wall
- No slip condition: The tangential velocity of the fluid close to the wall is zero or of the same velocity as that of the wall.

These conditions apply to both mean flow and fluctuations, that is, the eddies.

The rotational flow from the eddies is blocked by the wall, thus there should not be any eddy larger than the distance to the wall. But eddy of any size tends to move and when it reaches the wall, it gets blocked. This has a net effect of reducing the size of the eddies close to the wall. Hence, the eddies smaller than the distance to the wall are also damped by the wall.

The eddy size close to the wall is quantified using a RANS approach, by solving the RANS equations close to the wall, using an eddy-viscosity approach to calculate the Reynolds stresses,

$$-\rho \overline{u'v'} = \rho \nu_T \frac{\partial u}{\partial y} \quad (3.3.104)$$

This Eq. 3.3.100 is used by Pope [175] to derive a length scale for all the eddies close to the wall. In the logarithmic region, the mean velocity profile is modelled by,

$$U^+ = \frac{1}{\kappa} \log(y^+) + C \quad (3.3.105)$$

Therefore, the mean velocity gradient is,

$$\frac{\partial U^+}{\partial y^+} = \frac{1}{\kappa y^+} \quad \text{Or,} \quad \frac{\partial U}{\partial y} = \frac{u_\tau}{\kappa y} \quad (3.3.106)$$

$$\text{Since, } y^+ = \frac{\rho u_\tau y_p}{\mu}$$

In the logarithmic or log-law region the Reynolds shear stress is relatively constant and balances the wall shear stress as,

$$-\rho \overline{u'v'} = \tau_w = \rho u_\tau^2 \quad (3.3.107)$$

Substituting Eq. 3.3.107 and Eq. 3.3.106 in Eddy viscosity equation,

$$-\rho \overline{u'v'} = \rho \nu_T \frac{\partial U}{\partial y} \quad (3.3.108)$$

$$\rho u_\tau^2 = \rho \nu_T \left(\frac{u_\tau}{\kappa y} \right) \quad (3.3.109)$$

$$v_T = u_T \kappa y \quad (3.3.110)$$

Kinematic viscosity being a product of length scale (mixing length, l_m) and velocity scale (square root of Reynolds shear stress), and from Eq. 3.3.110,

$$u_T \kappa y = l_m * (\overline{u'v'})^{1/2} \quad (3.3.111)$$

Solving for mixing length from Eq. 3.3.111,

$$u_\tau \kappa y = l_m * (u_\tau^2)^{1/2} \quad (3.3.112)$$

$$l_m = \kappa y \quad (3.3.113)$$

The mixing length can be called a measure of how large the eddies are. This is a metric of the eddy size in the logarithmic region. From Eq. 3.3.113, which is a logarithmic solution, it is understood that as y reduces or tends to zero, the mixing length also tends to zero, that is, eddies get smaller on approaching the wall.

Concept of mixing length

Considering that a fluid volume being transported by large eddies which dissipate into smaller eddies, mixing length can be defined as the distance travelled by this fluid volume prior to its dissipation into smaller eddies. It is not similar to the integral length scale, rather smaller than that but it is larger than the sub-grid length, because it is being dissipated into smaller eddies. So, it can be written as,

$$l_0 = \min (l_m, C_s \Delta) \quad (3.3.114)$$

Substituting Eq. 3.3.113 in Eq. 3.3.114,

$$l_0 = \min (\kappa y, C_s \Delta) \quad (3.3.115)$$

Eq. 3.3.115 will reduce the sub-grid length scale in the logarithmic region.

For the viscous sub-layer and buffer region, it is intended to get a continuous solution to the logarithmic region. Van-Driest proposed a solution for this, mentioned in Pope [175] (1986). The coefficient $A^+ = 26$ makes the velocity profile have good agreement with experimental data.

$$U^+ = \int_0^{y^+} \frac{2 dy'}{1+(1+4(l_m^+)^2)^{1/2}} \quad (3.3.116)$$

$$\text{Where, } l_m = \kappa y \left(1 - \exp\left(-\frac{y^+}{A^+}\right)\right) \quad (3.3.117)$$

Eq. 3.3.117 is written as $l_m = \kappa y * D$, where $D = \left(1 - \exp\left(-\frac{y^+}{A^+}\right)\right)$ and is known as Van-Driest Damping Function. D tends to zero close to the wall and tends to 1 far away from the wall, in the logarithmic region where viscous effects are small. Thus, D can be expressed as a function which accounts for viscous effects.

Putting Eq. 3.3.117 in Eq. 3.3.114,

$$l_0 = \min \left[\kappa y * \left(1 - \exp\left(\frac{y^+}{A^+}\right) \right), C_s \Delta \right] \quad (3.3.118)$$

This is the Van-Driest Dynamic Smagorinsky model. This mathematical form is used differently by different CFD codes.

3.4 NUMERICAL METHODOLOGY

3.4.1 Combined Semi-Analytical Model and RANS approach

In this sub section the numerical methodology used in combined approach for the semi-analytical pressure spectrum models and the RANS turbulence models is discussed. Mesh sensitivity studies are performed and quantified in terms of various convergence indices, along with discussion on the different semi-empirical wall-pressure spectrum models and turbulence models. At first, wall-pressure spectra are calculated using several semi-empirical models with experimental TBL parameters. Out of them, Smol'yakov – Tkachenko model [42] is found to be the best predictor of the wind tunnel test results as shown in Figure 3.4.4 and for in-flight test results, the Rackl-Weston model [16] is found to be the best predictor as shown in Figure 3.4.3.

Subsequently, a flat plate TBL wind tunnel experiment conducted by Salze *et al.*, [13] is numerically replicated. The schematic of the test case is shown in Figure 3.4.1 and simulation is performed using the five RANS turbulence closure models, namely:

- i) Standard $k - \omega$
- ii) $k - \omega$ SST
- iii) $k - \varepsilon$
- iv) Realizable $k - \varepsilon$
- v) Spalart-Allmaras

In the field of Computational Fluid Dynamics (CFD), mesh sensitivity study plays a crucial role in ensuring accurate and reliable simulations. It involves varying the mesh parameters, such as the size, density, and distribution of grid cells or elements, to assess their effect on the simulation outcomes. The main objective of a mesh sensitivity study is to evaluate the convergence and stability of the CFD solution with respect to mesh refinement. It also aids in understanding the influence of mesh quality on specific flow features of interest, such as areas of high gradients, boundary layer behaviour, or flow separation regions. Additionally, mesh sensitivity studies contribute to the validation and verification of CFD models by systematically examining the mesh dependency of the results.

In the present work, mesh sensitivity study is performed for a flat plate boundary layer case experimented by Salze *et al.* [13]. Different flow solvers like OpenFOAM and ANSYS Fluent are used along with different turbulence models. These different configurations are employed to simulate the flow field and extract the TBL parameters in alignment with the experiment at two different locations (point 1: 1495mm and point 2: 1595 mm downstream of the domain inlet) and at two different wind speeds (30 m/s and 50 m/s). Then, different CFD models with different y^+ values are compared with experimental results both at the component level (U_τ , δ , δ^* , θ) and

overall pressure spectrum level (Φ_p). Finally, sensitivity mapping is performed between the pressure fluctuation, wall spectrum model and CFD-RANS turbulence model parameters.

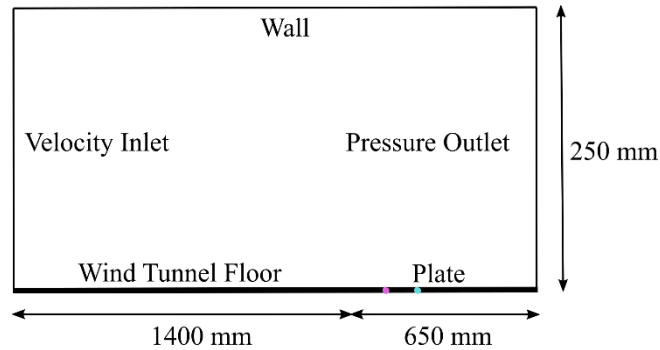


Figure 3.4.1: Schematic of the domain for flat plate TBL simulation; replication of the experimental set up by Salze *et al.*, 2014

Three types of meshing with uniform rectangular cells in 2D plane are studied for both OpenFOAM and Fluent solvers and are presented in Table 3.4.1. A section of the mesh for the mesh sensitivity study has been shown from Figure 3.4.2(a) to Figure 3.4.2(c). The representative cell length (h) is calculated as, $h = \frac{1}{N} \sum_{cell} A_p^{1/2}$, where N is the number of cells and A_p , is the area of each cell.

Table 3.4.1: Three different 2D meshes

Mesh	Number of cells	Representative Cell Length (h) [m]
Coarse	60000	0.0029
Medium	120000	0.0021
Fine	240000	0.0015

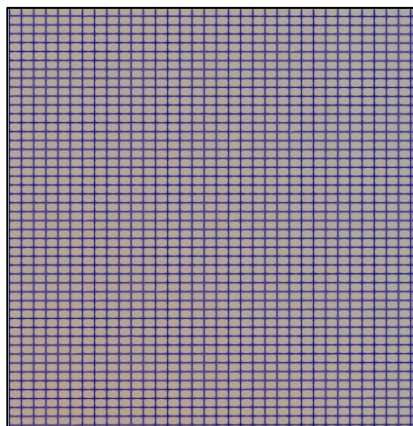


Figure 3.4.2(a): Coarse Mesh

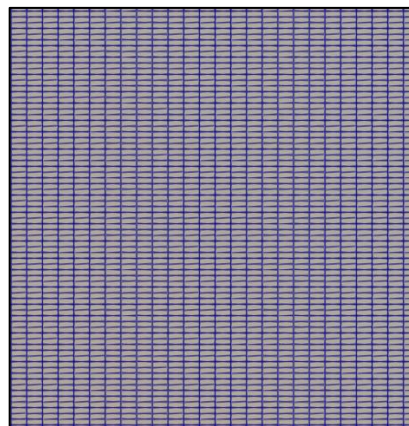


Figure 3.4.2(b): Medium Mesh

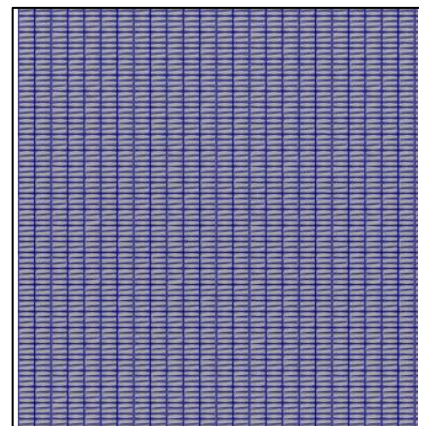


Figure 3.4.2(c): Fine Mesh

The present meshing satisfies the recommendations of Celik *et al.*, [177], that the representative cell lengths should be at least 30% different for each mesh. The most ideal mesh is having an infinite number of cells, corresponding to a representative cell length (RCL) (h) approaching zero, estimated using Richardson extrapolation technique. On designating fine, medium, and coarse mesh as 1, 2, and 3, respectively, friction velocity at $h = 0$ can be expressed as,

$$U_{\tau 0} = \frac{r_{21}^p U_{\tau 1} - U_{\tau 2}}{r_{21}^p - 1} \quad (3.4.1)$$

where refinement ratio, $r_{21} = \frac{h_2}{h_1}$, and p is the order of convergence. The order of convergence p is estimated using the method proposed by Celik *et al.* [177] as it is a more general approach suitable for both monotonic and oscillatory convergence. In the beginning, differences in calculated friction velocities are determined for the fine mesh-medium mesh (ϵ_{21}), and the medium mesh-coarse mesh (ϵ_{32}) as:

$$\epsilon_{21} = U_{\tau 2} - U_{\tau 1}; \epsilon_{32} = U_{\tau 3} - U_{\tau 2} \quad (3.4.2)$$

Next, their ratio is calculated to find $s = \text{sign}\left(\frac{\epsilon_{32}}{\epsilon_{21}}\right)$

The final form of the implicit non-linear equation is:

$$\frac{1}{\ln(r_{21})} \left| \ln \left| \frac{\epsilon_{32}}{\epsilon_{31}} \right| + \ln \left(\frac{r_{21}^p - s}{r_{32}^p - s} \right) \right| - p = 0 \quad (3.4.3)$$

This equation is solved using the Newton-Raphson iteration technique. In the present mesh sensitivity study, *three* types of errors are estimated for each case, namely relative error (e_{21}), extrapolated relative error (e_{21}^{ext}), and Grid Convergence Index (GCI_{21}).

$$e_{21} = \left| \frac{U_{\tau 2} - U_{\tau 1}}{U_{\tau 1}} \right|; e_{21}^{ext} = \left| \frac{U_{\tau 1} - U_{\tau 0}}{U_{\tau 0}} \right|; GCI_{21} = \left| \frac{e_{21}}{r_{21}^p - 1} \right| \quad (3.4.4)$$

The formulation for normalized wall distance, y^+ , describing various grid convergence is provided below, along with the estimation of δ^* and θ from the CFD-obtained velocity profiles. For all the studied cases these parameters are calculated using in-house MATLAB scripts.

$$y^+ = \frac{y_p U_{\tau}}{\nu} \quad (3.4.5)$$

where y_p is the distance of the centroid of the first cell adjacent to the wall.

Displacement thickness (δ^*) and momentum thickness is expressed as

$$\delta^* = \sum_{i=2}^{N-1} \left(1 - \frac{u_i}{U_0}\right) \left(\frac{y_{i+1} - y_{i-1}}{2}\right) \quad (3.4.6)$$

$$\theta = \sum_{i=2}^{N-1} \frac{u_i}{U_0} \left(1 - \frac{u_i}{U_0}\right) \left(\frac{y_{i+1} - y_{i-1}}{2}\right) \quad (3.4.7)$$

The numerical set up for the present work is done in a way to simulate the experimental set up given by Salze *et al.*, [13]. The mesh for clustering and convergence, for varying y^+ and for flow velocity 30 m/s has been presented in Figure 3.4.3(a) to Figure 3.4.3(c). The mesh for $y^+ = 1$ and $y^+ = 30$ has been given for an elevation of the entire fluid domain over the flat plate. The mesh

for $y^+ = 100$ is having a Biasing Factor (BF) of 1, so only a magnified section has been presented here. The entire BF results are shown later in Table 3.5.5 and Table 3.5.6.

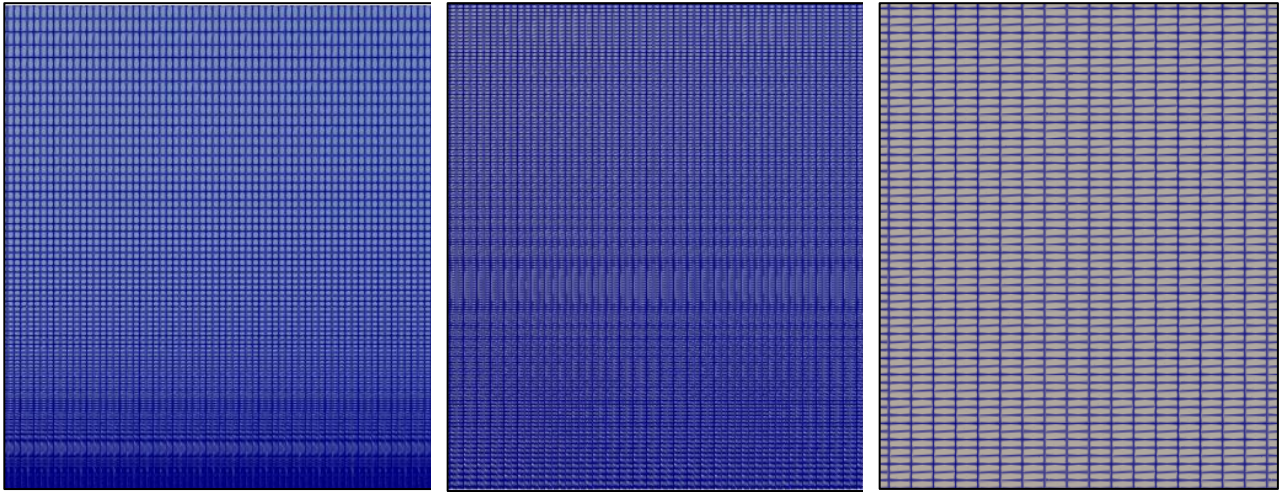


Figure 3.4.3(a): Mesh for $y^+ = 1$ for $U = 30$ m/s

Figure 3.4.3(b): Mesh for $y^+ = 30$ for $U = 30$ m/s

Figure 3.4.3(c): Mesh for $y^+ = 100$ for $U = 30$ m/s

3.4.2 Large Eddy Simulation (LES)

Mesh Sensitivity Study

To estimate turbulent pressure fluctuations over a flat plate, a 2D vertical domain is considered along the centreline (stream-wise) of the plate. This is for 2D simulation of the turbulent flow field. Once, the steady-state TBL parameters are estimated they can further be used in semi-analytical models to obtain the wall-pressure spectrum. Alternatively, transient simulation (LES) is performed using ANSYS Fluent solver to estimate the pressure fluctuations on a point over the plate, involving artificial inflow turbulence augmented in Fluent.

At first, the steady-state flow field is simulated using both an in-house Python solver, and ANSYS Fluent solver. In Python solver, flow is allowed to reach steady-state, and mean flow data are extracted. In Fluent, the realizable $k-\epsilon$ model is used with enhanced wall treatment to supply additional equations for kinetic energy (k) and energy dissipation rate (ϵ). A grid convergence study is carried out with different mesh qualities as detailed in Table 3.4.2. Once the mean velocity field is obtained, numerical integration is performed up to the boundary layer, and TBL parameters are obtained. They are a) used to estimate wall-pressure spectrum, and b) used in grid convergence study as presented in Table 3.4.3. The Python solver seems to provide rough estimates. This is due to the central difference scheme adopted for convection term, which demands diffusive transport to be dominant for better numerical stability.

Table 3.4.2: Geometry and meshing information; 2D LES study of TBL over flat plate

U_0 (m/s)	L_x (m)	L_z (m)	Mesh quality	N_x	N_z	Δy ($\times 10^{-6}$ m)
44.7	0.47	0.10	coarse	500	100	6.5
			medium	500	200	1.0
			fine	1000	200	1.0

L_x = stream wise length, L_z = vertical distance, N_x = number of elements in the stream-wise direction, N_z = number of elements in the vertical direction

Table 3.4.3: Mesh sensitivity study

U_0 (m/s)	L_x (m)	L_z (m)	Method	δ ($\times 10^{-3}$ m)	δ^* ($\times 10^{-4}$ m)	θ ($\times 10^{-4}$ m)	τ_w (MPa)
44.7	0.47	0.10	empirical	3.70	4.27	3.59	5.46
			coarse	3.64	4.17	3.39	5.44
			medium	3.64	4.18	3.42	5.44
			fine	3.64	4.18	3.43	5.45
			coarse	5.00	5.60	5.20	--
			(Python)				

L_x = stream wise length, L_z = vertical distance

As Table 3.4.3 suggests, the ‘medium’ grid is sufficiently precise and considered for subsequent transient simulations. Large eddy simulation is performed involving artificial inflow turbulence as described in Eq. (3.4.11) and Eq. (3.4.12). In order to resolve a lion’s share of the kinetic energy, the grid clustering near the wall is implemented (refer to Figure 3.4.4a), and the resulting non-dimensional velocity profile is found to be in a very good agreement with the universal law of the wall (refer to Figure 3.4.4b).

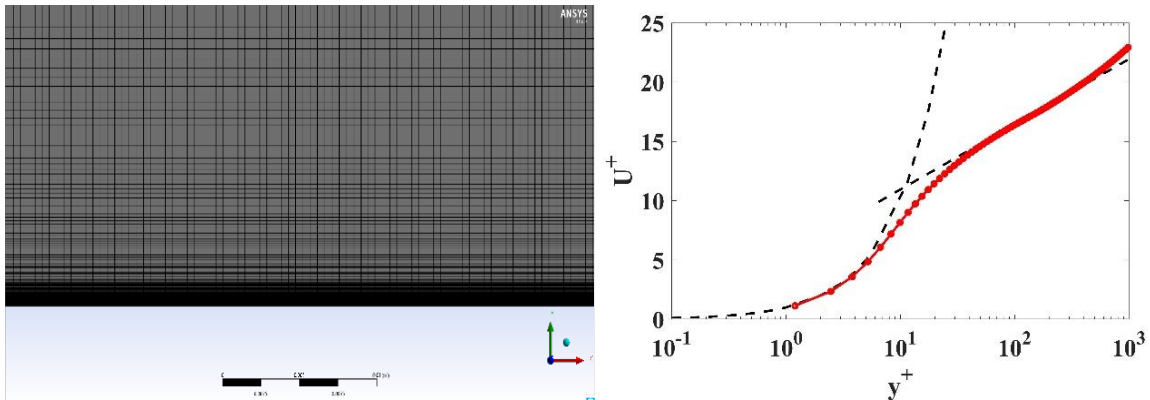


Figure 3.4.4: a) grid clustering near the wall, b) normalized velocity profile; black – universal velocity profile, red – present LES study

Artificial Inflow Turbulence

One common approach for generating artificial inflow turbulence in Computational Fluid Dynamics (CFD) simulations is by applying a synthetic turbulence method known as the Synthetic Eddy Method. The method involves generating random fluctuations in the velocity field to simulate the turbulent behaviour of the incoming flow. A mathematical formulation of the Synthetic Eddy Method is given below.

Let us define the mean velocity profile as:

$$\bar{U}(x, y, z) = U(x) + u'(y, z) \quad (3.4.8)$$

where $U(x)$ is the mean velocity component in the streamwise direction (x-axis). $u'(y, z)$ is the deviation of the velocity in the cross-sectional directions (y and z axes) from the mean.

Generating synthetic turbulence fluctuations:

The velocity fluctuations in the cross-sectional directions, $u'(y, z)$, can be modeled as a superposition of discrete eddies. Each eddy has a specified size, intensity, and location within the computational domain. The velocity fluctuations are typically represented using a random Gaussian distribution. The fluctuating velocity components are calculated as

$$u'(x, y, z) = u'(y, z)f(x, y, z) \quad (3.4.9)$$

$f(x, y, z)$ is a function that varies with the streamwise direction (x-axis) and can be used to model the spatial decay of the eddies.

The function $f(x, y, z)$ can be defined based on empirical or analytical considerations, such as an exponential decay or a power-law decay. Adding the mean and fluctuating velocity components yield

$$U(x, y, z) = \bar{U}(x, y, z) + u'(x, y, z) \quad (3.4.10)$$

The resulting velocity field $U(x, y, z)$ represents the artificial inflow turbulence, which can be used as an inlet boundary condition for the CFD simulation.

It has been noted that the majority of LES programs are unable to accurately anticipate instantaneous pressure variations unless they are given artificial turbulence as an inflow, which aids in continuous flow field perturbation. There are two approaches to create this artificial turbulence: (1) using the recycling and rescaling method, and (2) creating a random flow field in the inlet. In the current work, the second way is chosen since it was not practical to include the first method into a solution that has been built commercially, such as Fluent. According to Gloerfelt and Gerrec [178], the changing velocity components overlaid over the mean flow can be calculated using the current method.

$$u' = \varepsilon U_{\infty} \text{rand}(y) e^{-\left(\frac{y-\delta_{in}/2}{1.2\delta_{in}/3}\right)^2} \quad (3.4.11)$$

$$v' = \varepsilon U_{\infty} \text{Cos}(\omega t) e^{-\left(\frac{y-\delta_{in}/2}{1.2\delta_{in}/10}\right)^2} + \varepsilon U_{\infty} \text{rand}(y) e^{-\left(\frac{y-\delta_{in}/2}{1.2\delta_{in}/3}\right)^2} \quad (3.4.12)$$

where, $\omega = \frac{2\pi U_0}{8\delta_{in}}$, δ_{in} is taken as the boundary layer thickness at the 3/4th of the length, ε is considered as 5×10^{-3} to preserve small perturbation and ‘rand’ is a set of random numbers ranging from -1 and 1. User defined functions (UDFs) are developed in order to incorporate the artificial inflow turbulence in ANSYS Fluent code to enhance the pressure fluctuation estimation capability.

Extraction of the Boundary Layer Parameters

In the case of turbulent flow over a flat plate, analytical formulations for displacement thickness (δ^*) and momentum thickness (θ) can be written as,

$$\delta^* = \int_{y=0}^{\delta} \left(1 - \frac{U}{U_0}\right) dy \quad (3.4.13)$$

$$\theta = \int_{y=0}^{\delta} \frac{U}{U_0} \left(1 - \frac{U}{U_0}\right) dy \quad (3.4.14)$$

They are numerically estimated and compared with the established empirical estimation of boundary layer thickness (δ), displacement thickness (δ^*), and momentum thickness (θ) approximated by Hafeez *et al.* [179] and Mahmoudnejad *et al.* [180]

$$\delta \approx \frac{0.16x}{Re_x^{1/7}} \quad (3.4.15)$$

$$\delta^* \approx \frac{0.0174x}{Re_x^{0.139}} \quad (3.4.16)$$

$$\theta \approx \frac{7}{72} \delta \quad (3.4.17)$$

Here Eq. (3.4.17) is obtained from Eq. (3.4.14) with the approximation that the turbulent velocity profile follows one-seventh-power law, and $\delta = 0$ at the leading edge ($x = 0$) [179].

It is a better idea to represent any flow parameter in the frequency domain rather than in the time domain because due to the extremely small time-step size, the number of time steps increases unrealistically. Therefore, the wall-pressure fluctuations are presented (in the next section) in the frequency domain, using Welch’s technique.

3.5 RESULTS AND DISCUSSION

3.5.1 Combined Semi-Analytical Model and RANS approach

[results presented in this sub-section are from author’s original article published in CFD Letters [181]]

3.5.1.1 Comparison of Spectrum Models with Wind Tunnel PSD

Several semi-empirical spectrum models as previously described are compared with PSD values from wind tunnel experiment conducted by Goody and Simpson [14] and Rackl-Weston’s in-flight test [16], and presented in Figure 3.5.1(a) and Figure 3.5.1 (b). The experimental spectrum is single

sided, for a two-dimensional ZPG flow as described by Thomson and Rocha [12]. They used naturally developed turbulent boundary layers to study wall-pressure fluctuations.

The findings are in-line with Thomson and Rocha [12] as Goody [41] and Smol'yakov [81] spectrum models are found to be the best in terms of replicating the wind tunnel test. The study presented ascertains this finding, but in addition shows that Smol'yakov and Tkachenko model [42] is also a good predictor of the wind tunnel test results along with Goody [41], Smol'yakov [81] and Laganelli [37] models as can be seen in Figure 3.5.1 (a). The present study is performed on Smol'yakov and Tkachenko model [42] as the present study focuses on the low-frequency vibroacoustic problem (as is most disturbing for the commuters and thin-walled structures), and for practical purpose this model is found to be providing better estimation of TBL-induced plate vibration in the low-frequency regime [51].

Similar study has been done with various semi-empirical models by comparing them with the PSD values from in-flight test data conducted by Rackl and Weston [16], presented in Figure 3.5.1 (b) and Rackl and Weston spectrum model [16] certainly is found to be predicting the best.

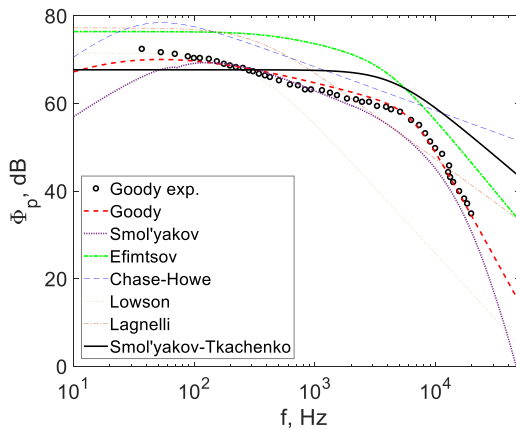


Figure 3.5.1(a): Comparison of wall-spectrum models with Goody-Simpson wind tunnel experiment. Ref. $4 \times 10^{-10} Pa^2$

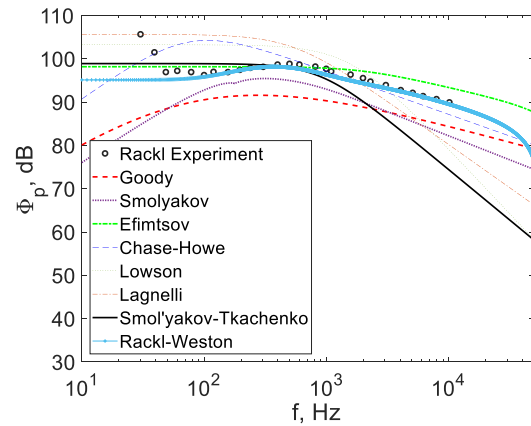


Figure 3.5.1(b): Comparison of wall-spectrum models with Rackl and Weston in-flight test data. Ref. $4 \times 10^{-10} Pa^2$

3.5.1.2 CFD: Mesh Sensitivity Study

The sensitivity of friction velocity to various mesh sizes is studied using Eqs. (3.4.1) to (3.4.7) at two different locations, for all the five turbulence models, with free stream velocity (U_∞) 30 m/s and 50 m/s using OpenFOAM and Fluent. Out of these 40 combinations, only *four* results are presented in Tables 3.5.1 to 3.5.4 as representative results. The mesh sensitivity study is performed by referencing the friction velocity value obtained from the experiment conducted by Salze *et al.*, [13] and presented in Figures 3.5.2 (a) to 3.5.2 (d). ‘h’ is the representative cell length (RCL).

Table 3.5.1: Point 1; $k - \omega$ SST; OpenFOAM; $U_\infty = 30m/s$

RCL (h) [m]	U_τ [m/s]	$U_\tau extr$ [m/s]	e_{21} [%]	e_{21}^{ext} [%]	GCI_{21}
0.0015	1.156				
0.0021	1.154	1.159	0.19	0.29	0.36
0.0029	1.159				

Table 3.5.2: Point 1; $k - \omega$ SST; Fluent; $U_\infty = 30m/s$

RCL (h) [m]	U_τ [m/s]	$U_\tau extr$ [m/s]	e_{21} [%]	e_{21}^{ext} [%]	GCI_{21}
0.0015	1.140				
0.0021	1.140	1.140	0.00	0.00	0.00
0.0029	1.150				

Table 3.5.3: Point 2; $k - \omega$ SST; OpenFOAM; $U_\infty = 30m/s$

RCL (h) [m]	U_τ [m/s]	$U_\tau extr$ [m/s]	e_{21} [%]	e_{21}^{ext} [%]	GCI_{21}
0.0015	1.151				
0.0021	1.148	1.156	0.22	0.48	0.60
0.0029	1.153				

Table 3.5.4: Point 2; $k - \omega$ SST; Fluent; $U_\infty = 30m/s$

RCL (h) [m]	U_τ [m/s]	$U_\tau extr$ [m/s]	e_{21} [%]	e_{21}^{ext} [%]	GCI_{21}
0.0015	1.130				
0.0021	1.140	1.120	0.88	0.93	1.15
0.0029	1.150				

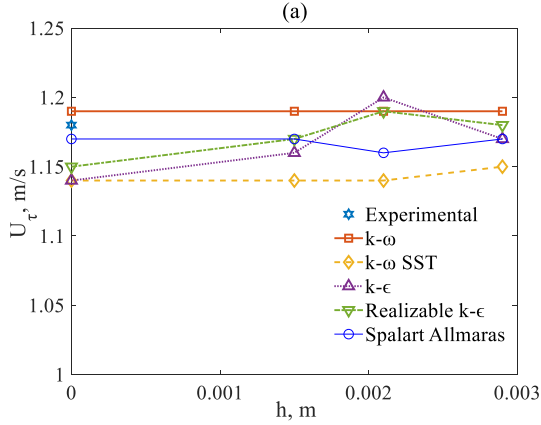


Figure 3.5.2(a): Point 1; $U_\infty = 30\text{m/s}$; OpenFOAM

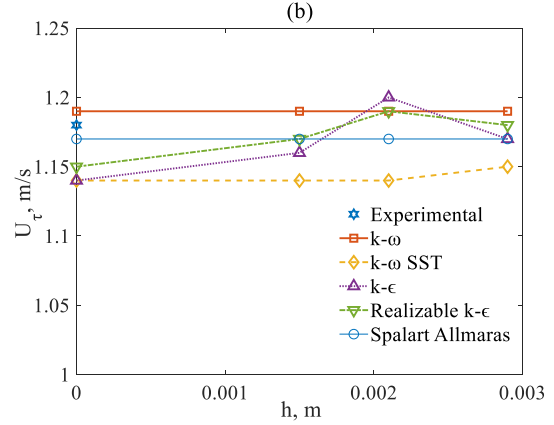


Figure 3.5.2(b): Point 1; $U_\infty = 30\text{m/s}$; ANSYS Fluent

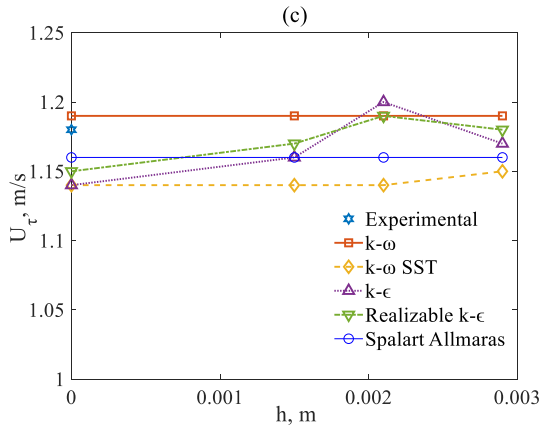


Figure 3.5.2(c): Point 2; $U_\infty = 30\text{m/s}$; OpenFOAM

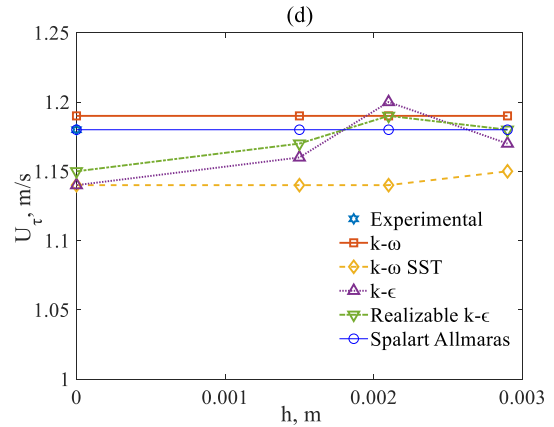


Figure 3.5.2(d): Point 2; $U_\infty = 30\text{m/s}$; ANSYS Fluent

As observed from the mesh sensitivity studies, it is found that the ‘medium’ mesh is sufficient for all subsequent studies, and thus the accuracy analysis of different CFD variants is conducted with this meshing. Different solvers (OpenFOAM, Fluent), turbulence models ($k - \omega$, $k - \omega$ SST, $k - \epsilon$ and Realizable $k - \epsilon$, Spalart Allmaras), and y^+ values (1, 30, and 100) are examined with the experimental values ($U_\tau, \delta, \delta^*, \theta$) as obtained by Salze *et al.*, [13].

3.5.1.3 CFD Simulation; Part 1: Clustering and convergence

To simulate TBL parameters properly, near-wall grid clustering is essential and the turbulent parameters like δ, δ^*, θ are calculated using the Eq. 3.4.15 to Eq. 3.4.17. For different y^+ values, the first cell height ($2y_p$) is initially calculated as per Eq. 3.4.5 and is presented in Table 3.5.5 and Table 3.5.6 for flow velocity of 30 m/s and 50 m/s respectively. Bias Factor (BF) is the ratio of last cell height to the first cell height. Figure 3.5.3 and Figure 3.5.4 depict typical universal velocity plots for the realizable $k - \epsilon$ model at two different locations with $U_\infty = 30\text{ m/s}$, where $U^+ = \frac{U}{U_\tau}$, U is the local velocity and U_τ is the friction velocity.

Table 3.5.5: y^+ calculation for $U = 30\text{m/s}$

y^+	U [m/s]	ν [$10^{-5} \text{ m}^2/\text{s}$]	$2y_p$ [10^{-5} m]	Biasing Factor
1			2.47	284.3
30	1.18	1.46	74.5	2.6
100			247	1

Table 3.5.6: y^+ calculation for $U = 50\text{m/s}$

y^+	U [m/s]	ν [$10^{-5} \text{ m}^2/\text{s}$]	$2y_p$ [10^{-5} m]	Biasing Factor
1			1.55	496.29
30	1.18	1.46	46.5	5.64
100			155	1

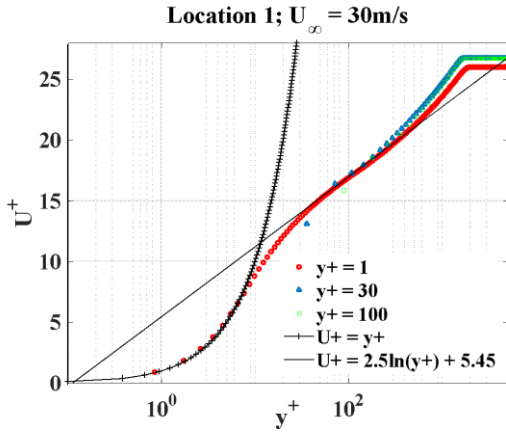


Figure 3.5.3: Universal velocity plot for $U_\infty = 30 \text{ m/s}$ at location 1; OpenFOAM

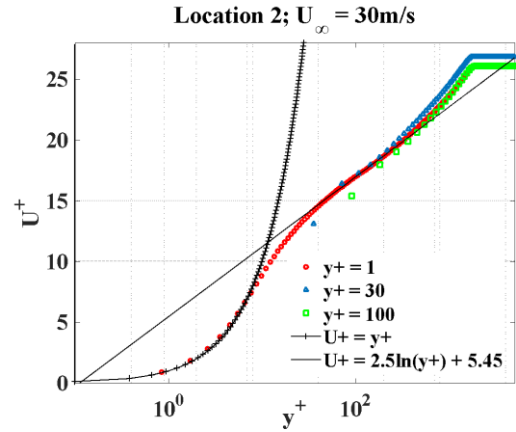


Figure 3.5.4: Universal velocity plot for $U_\infty = 30 \text{ m/s}$ at location 2; OpenFOAM

3.5.1.4 CFD Simulation; Part 2: Component Error Analysis

The accuracy of the turbulence models with various y^+ is analyzed in terms of estimating TBL components, and the error % are presented in the form of stacked bar graphs in Figure 3.5.5(a) to Figure 3.5.5(d). The stacks on each bar represent the amount of error with respect to the wind tunnel experiment results as obtained by Salze *et al.*, [13]. The mean square pressure (MSP) is obtained by fetching the flow variables in the Smol'yakov-Tkachenko Model [42]. The accuracy of the best predicting model, $k - \omega$ model, is presented here. It can be observed that in spite of the considerable error amounts of the flow parameters obtained between experiment and CFD, the final error amount in mean square pressure is quite less.

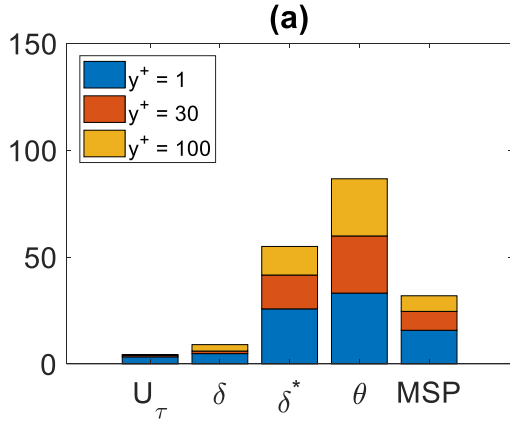


Figure 3.5.5(a): Estimation of error in MSP and turbulent wall parameters at point 1; $U_\infty = 30$ m/s; OpenFOAM, $k - \omega$ turbulence model, Smol'yakov-Tkachenko spectrum model

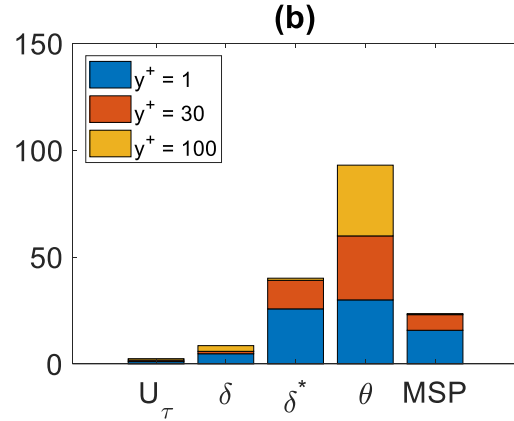


Figure 3.5.5(b): Estimation of error in MSP and turbulent wall parameters at point 1; $U_\infty = 30$ m/s; ANSYS Fluent, $k - \omega$ turbulence model, Smol'yakov-Tkachenko spectrum model

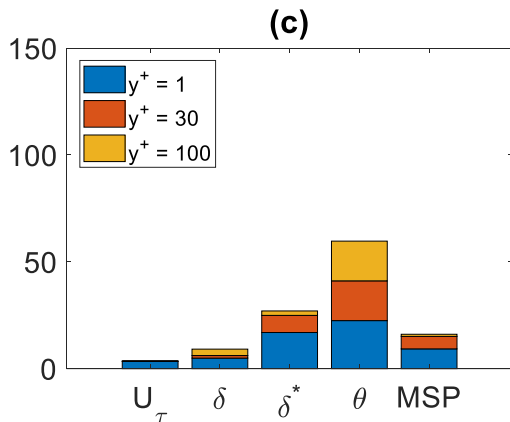


Figure 3.5.5(c): Estimation of error in MSP and turbulent wall parameters at point 1; $U_\infty = 50$ m/s; OpenFOAM, $k - \omega$ turbulence model, Smol'yakov-Tkachenko spectrum model

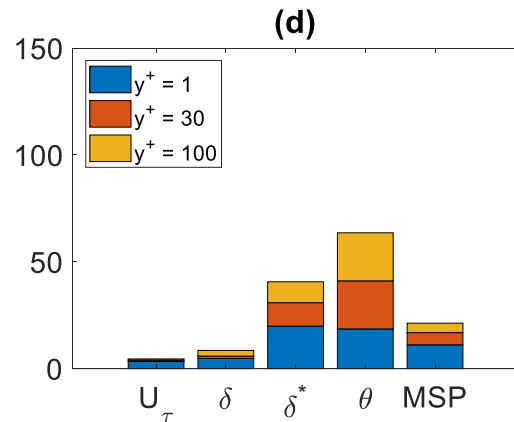


Figure 3.5.5(d): Estimation of error in MSP and turbulent wall parameters at point 1; $U_\infty = 50$ m/s; ANSYS Fluent, $k - \omega$ turbulence model, Smol'yakov-Tkachenko spectrum model

Similarly, the accuracy of the turbulence models with various y^+ is analysed by comparing with Rackl-Weston Model [16], in terms of estimating TBL components, and presented in the stacked bar graphs in Figure 3.5.6 (a) to Figure 3.5.6 (d). The accuracy of the best predicting model, $k - \omega$ model, is presented here. Similar observations have been obtained here as well.

The detailed results on the experimental values and the numerical estimation of shear velocity (U_τ), boundary layer thickness (δ), boundary layer displacement thickness (δ^*), momentum thickness (θ), mean square pressure fluctuations ($\overline{p^2}$) for Point-1, $U_\infty = 30$ m/s, are presented in Table 3.A.1 (Refer to [APPENDIX A](#)) and that of for Point-1, $U_\infty = 50$ m/s, are detailed in Table 3.A.2 (Refer to [APPENDIX A](#)).

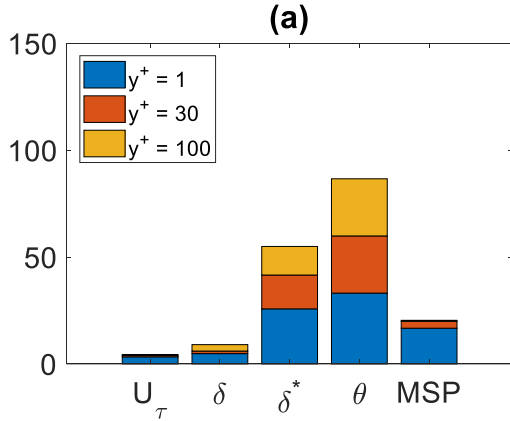


Figure 3.5.6(a): Estimation of error in MSP and turbulent wall parameters at point 1; $U_\infty = 30$ m/s; OpenFOAM, $k - \omega$ turbulence model, Rackl-Weston spectrum model

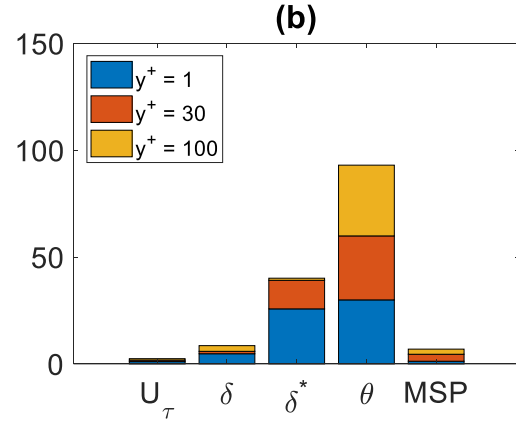


Figure 3.5.6(b): Estimation of error in MSP and turbulent wall parameters at point 1; $U_\infty = 30$ m/s; ANSYS Fluent, $k - \omega$ turbulence model, Rackl-Weston spectrum model

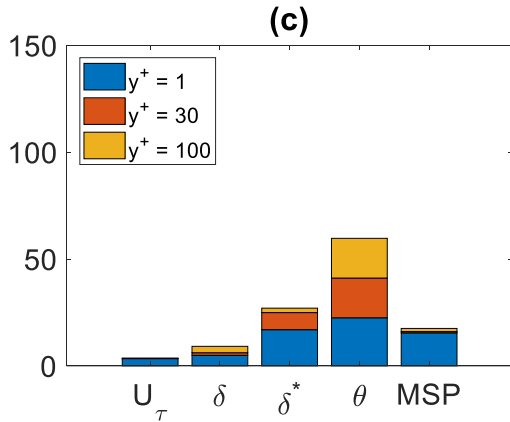


Figure 3.5.6(c): Estimation of error in MSP and turbulent wall parameters at point 1; $U_\infty = 50$ m/s; OpenFOAM, $k - \omega$ turbulence model, Rackl-Weston spectrum model

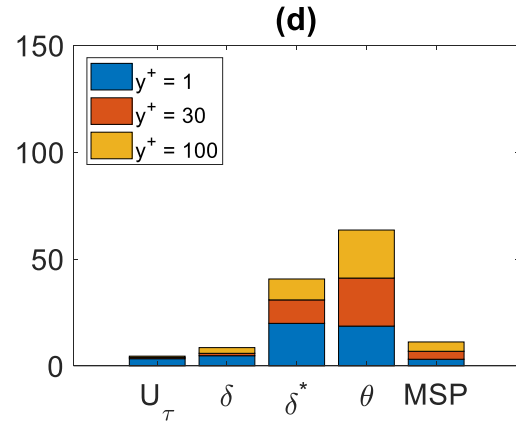


Figure 3.5.6(d): Estimation of error in MSP and turbulent wall parameters at point 1; $U_\infty = 50$ m/s; ANSYS Fluent, $k - \omega$ turbulence model, Rackl-Weston spectrum model

3.5.1.5 CFD Simulation; Part 3: \bar{p}^2 Error Analysis

Initially, the single-sided wall pressure spectra (Φ_p) are calculated using Goody [41], Smol'yakov [81] and Smol'yakov-Tkachenko [42] models for the CFD-obtained TBL parameters. As the best prediction is done by putting the TBL parameters obtained from CFD in the Smol'yakov Tkachenko Model, so the results corresponding to that model are presented here. Subsequently, the summation of the spectrum over its collapsing frequency (50 kHz for the present case) is done as per Eqn. (3.5.1) and the mean square of pressure fluctuations (\bar{p}^2) are estimated.

$$\bar{p}^2 = \int_0^\infty \Phi_p(f) df \quad (3.5.1)$$

Finally, a comparison is done with the experimental (\bar{p}^2) values. This is a rather practical approach

as it accounts for the global energy over the entire frequency range and not the local pressure PSD values.

A grid independence study is performed, and results are presented in Figure (3.5.7) to Figure (3.5.10) in the form of \bar{p}^2 vs. y^+ . The Richardson extrapolation technique as discussed in Eqn. (3.4.1) through Eqn. (3.4.5) for friction velocity is used same as it is for \bar{p}^2 to obtain the MSP value for the finest possible grid clustering ($y^+ = 0$), \bar{p}^2_0 . This extensive study

- i) Shows the convergence of different turbulence models as the y^+ tends to ZERO.
- ii) Error in MSP calculation for different CFD configurations, w.r.t. the experimental values.
- iii) Clearly distinguish the contribution of turbulence models, spectrum models, y^+ , location and flow velocity towards the final error.

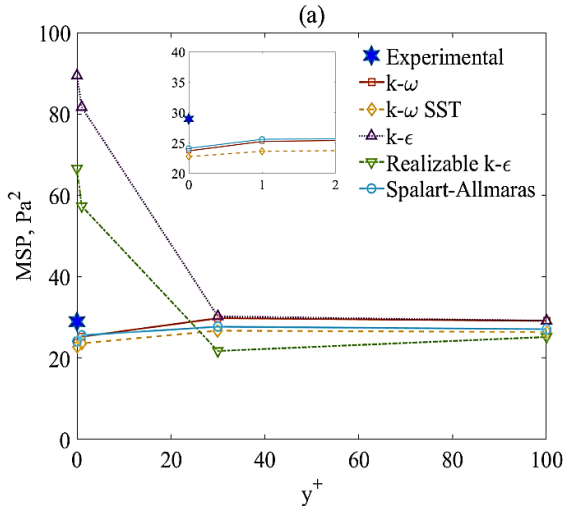


Figure 3.5.7(a): Convergence of \bar{p}^2 (MSP) with y^+ . Point 1; $U_\infty = 30$ m/s; OpenFOAM, Smol'yakov-Tkachenko spectrum model

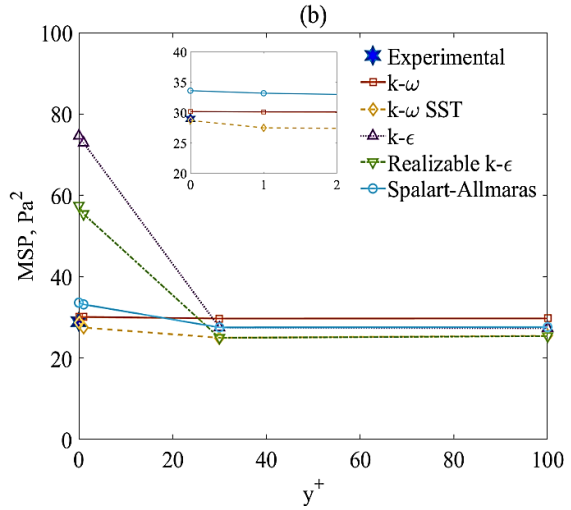


Figure 3.5.7(b): Convergence of \bar{p}^2 (MSP) with y^+ . Point 1; $U_\infty = 30$ m/s; ANSYS Fluent, Smol'yakov-Tkachenko spectrum model

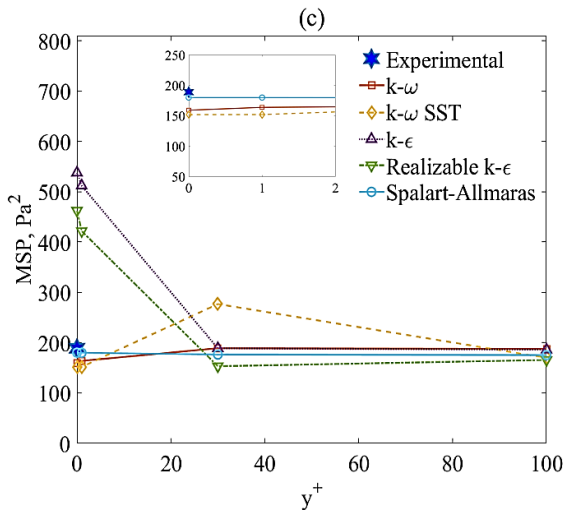


Figure 3.5.7(c): Convergence of \bar{p}^2 (MSP) with y^+ . Point 1; $U_\infty = 50$ m/s; OpenFOAM, Smol'yakov-Tkachenko spectrum model

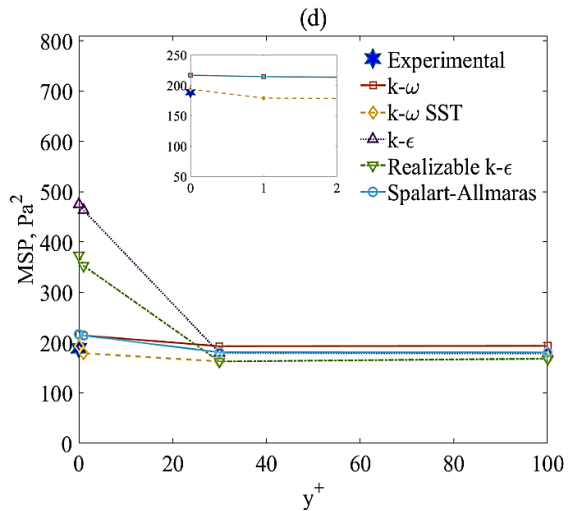


Figure 3.5.7(d): Convergence of \bar{p}^2 (MSP) with y^+ . Point 1; $U_\infty = 50$ m/s; ANSYS Fluent, Smol'yakov-Tkachenko spectrum model

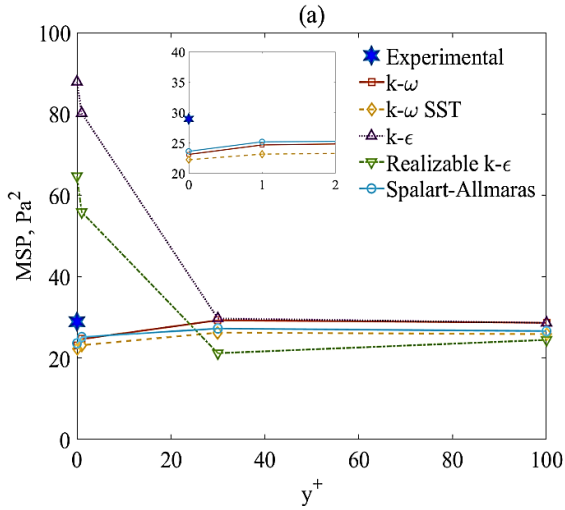


Figure 3.5.8(a): Convergence of \bar{p}^2 (MSP) with y^+ . Point 2; $U_\infty = 30$ m/s; OpenFOAM, Smol'yakov-Tkachenko spectrum model

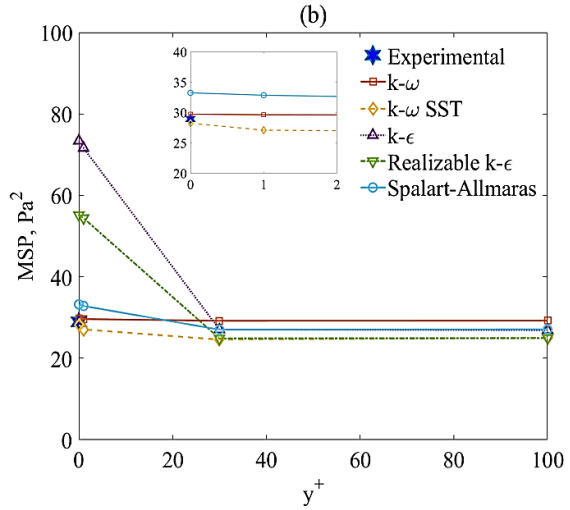


Figure 3.5.8(b): Convergence of \bar{p}^2 (MSP) with y^+ . Point 2; $U_\infty = 30$ m/s; ANSYS Fluent, $k - \omega$ model, Smol'yakov-Tkachenko spectrum model

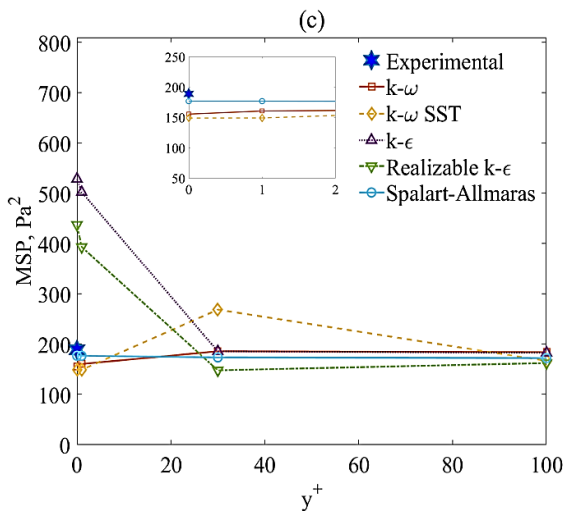


Figure 3.5.8(c): Convergence of \bar{p}^2 (MSP) with y^+ . Point 2; $U_\infty = 50$ m/s; OpenFOAM, Smol'yakov-Tkachenko spectrum model

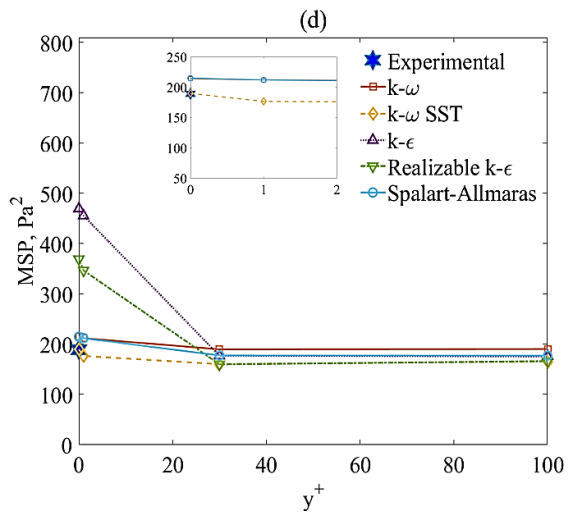


Figure 3.5.8(d): Convergence of \bar{p}^2 (MSP) with y^+ . Point 2; $U_\infty = 50$ m/s; ANSYS Fluent, Smol'yakov-Tkachenko spectrum model

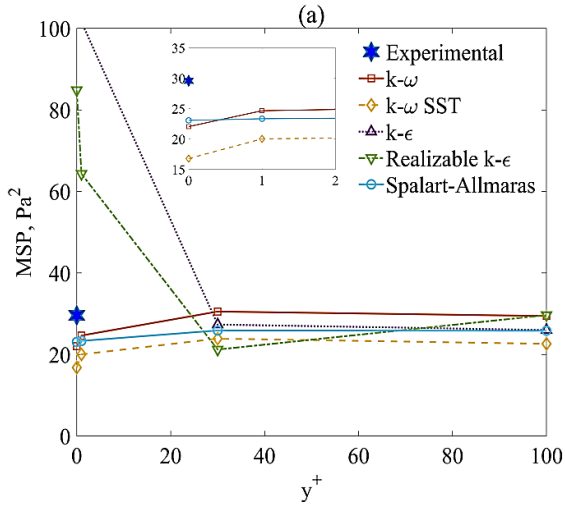


Figure 3.5.9(a): Convergence of \bar{p}^2 (MSP) with y^+ . Point 1; $U_\infty = 30$ m/s; OpenFOAM, Rackl-Weston spectrum model

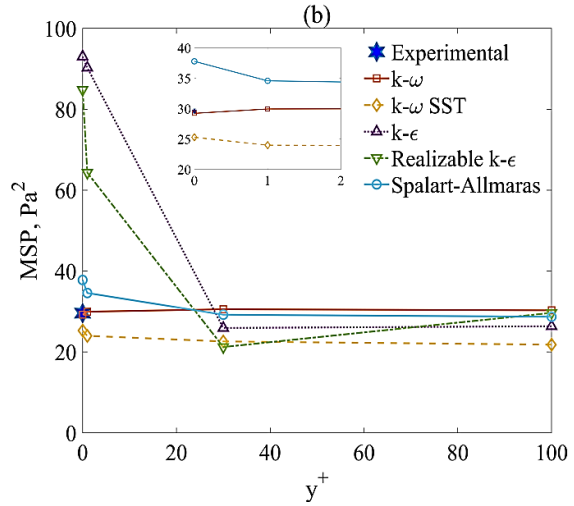


Figure 3.5.9(b): Convergence of \bar{p}^2 (MSP) with y^+ . Point 1; $U_\infty = 30$ m/s; ANSYS Fluent, $k - \omega$ model [20], Rackl-Weston spectrum model

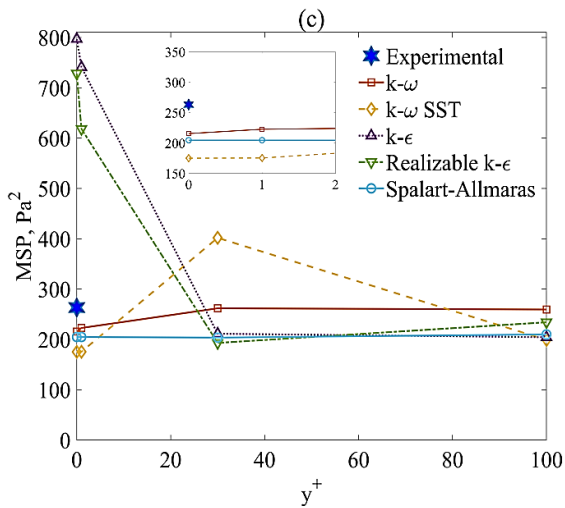


Figure 3.5.9(c): Convergence of \bar{p}^2 (MSP) with y^+ . Point 1; $U_\infty = 50$ m/s; OpenFOAM, Rackl-Weston spectrum model

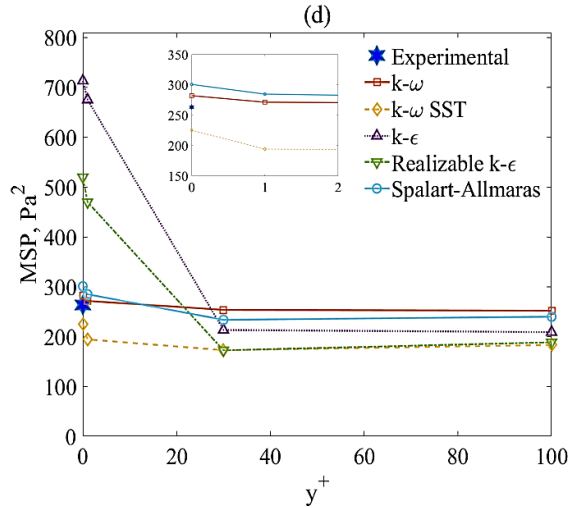


Figure 3.5.9(d): Convergence of \bar{p}^2 (MSP) with y^+ . Point 1; $U_\infty = 50$ m/s; ANSYS Fluent, Rackl-Weston spectrum model

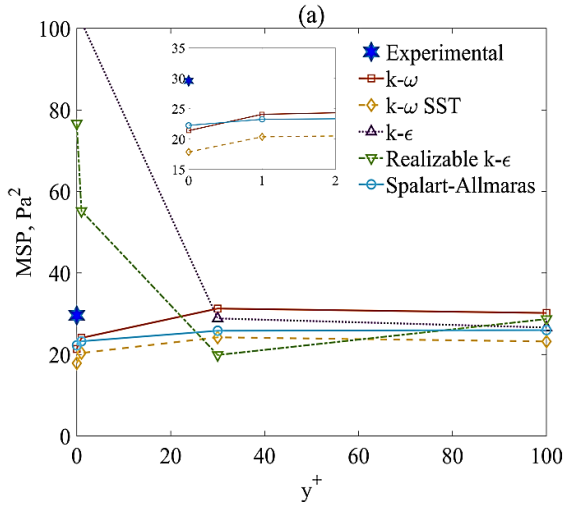


Figure 3.5.10(a): Convergence of \bar{p}^2 (MSP) with y^+ . Point 2; $U_\infty = 30\text{m/s}$; OpenFOAM, Rackl-Weston spectrum model

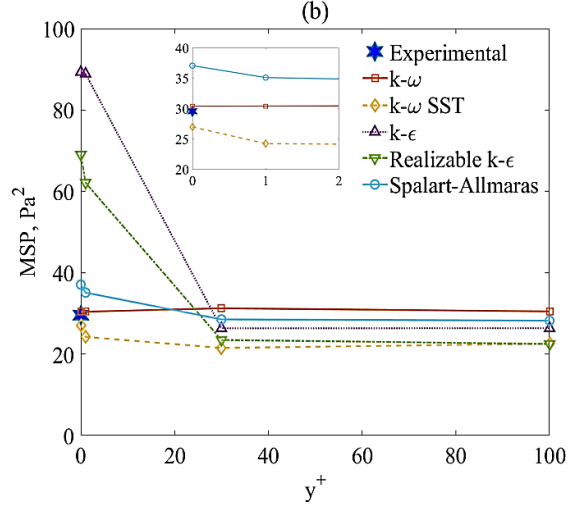


Figure 3.5.10(b): Convergence of \bar{p}^2 (MSP) with y^+ . Point 2; $U_\infty = 30\text{m/s}$; ANSYS Fluent, $k - \omega$ model [20], Rackl-Weston spectrum model

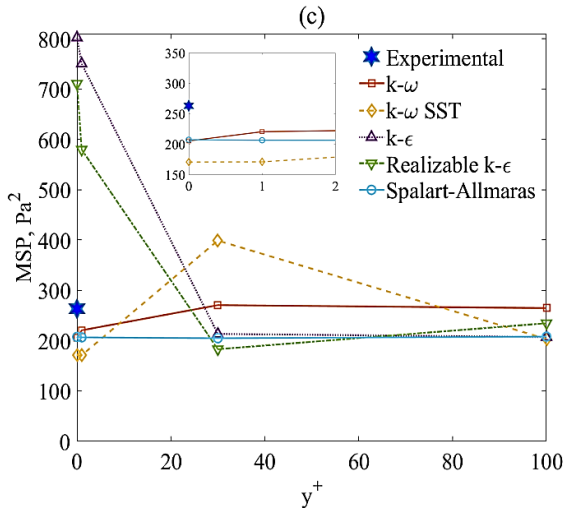


Figure 3.5.10(c): Convergence of \bar{p}^2 (MSP) with y^+ . Point 2; $U_\infty = 50\text{m/s}$; OpenFOAM, Rackl-Weston spectrum model

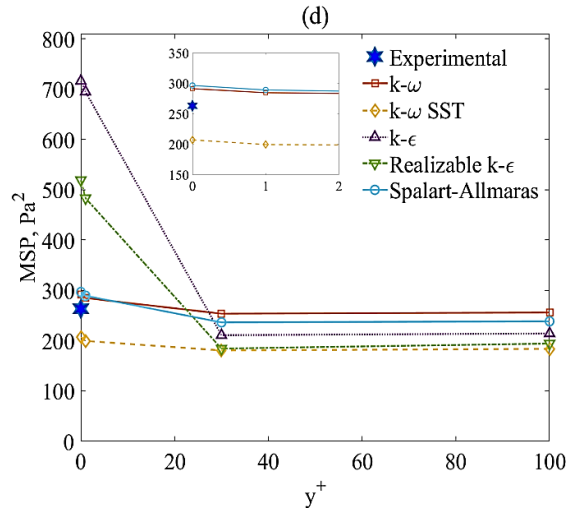


Figure 3.5.10(d): Convergence of \bar{p}^2 (MSP) with y^+ . Point 2; $U_\infty = 50\text{m/s}$; ANSYS Fluent, Rackl-Weston spectrum model

The grid convergence results of MSP show a clear pattern that the Spalart-Allmaras, $k - \omega$ and $k - \omega$ SST turbulence models are quite reliable in terms of convergence of the numerical schemes. Moreover, they calculate MSP values with a very good accuracy w.r.t the MSP values estimated with the experimental TBL wall parameters. This observation remains valid irrespective of the solver, location, or the flow velocities within the study range. $k - \epsilon$ family of models ($k - \epsilon$ and realizable $k - \epsilon$) are found to be diverging whenever the y^+ value comes close to zero. It is expected as these models does not capture the near-wall flow well. Although, these models can

suitably be used for $y^+ > 30$, if required. This marginal value can change if further study is carried out in the zone of $1 < y^+ < 30$.

Among the turbulence models $k - \omega$ in general is found to be the best predictor for Smol'yakov and Tkachenko model, and Rackl and Weston model. Overall, $k - \omega$ family of models along with Spalart-Allmaras one equation model in some cases are recommended for flat plate TBL pressure fluctuation estimation. $k - \epsilon$ family of models are not suggested for these type of near wall investigations due to its numerical divergence and magnified error in the near wall region. This happens because the $k - \omega$ model is generally found to be better at resolving the eddies at y^+ less than 5, than the $k - \epsilon$ or realizable $k - \epsilon$ model. In practice, there is high dissipation [37] of turbulent kinetic energy near walls, shear layer and where turbulence is going to be high. Moreover, $k - \omega$ model is better performer for aerodynamics and turbomachinery which the $k - \epsilon$ model is not, as explained earlier. This is because in the $k - \epsilon$ model the damping functions (f_1, f_2, f_μ) used are not that accurate in the presence of adverse pressure gradients. But $k - \omega$ family of models does not need these damping functions when adverse pressure gradient is present.

As, $k - \omega$ family of models is found to be the best predicting RANS turbulence models, so error analysis for $k - \omega$ model is presented in Table 3.A.3 for Point 1, Smol'yakov-Tkachenko model; Table 3.A.4 for Point 2, Smol'yakov-Tkachenko (ST) model; Table 3.A.5 for Point 1, Rackl-Weston (RW) model and Table 3.A.6 for point 2, Rackl-Weston (RW) model (Refer APPENDIX A).

3.5.1.6 Effect of Turbulence Intensity on Velocity Profile and MSP

Another sensitivity study is performed to understand the effect of turbulence intensity (TI) on the velocity profile within the TBL and the final mean square pressure (MSP). For this purpose, parameters as referred in Table 3.5.7 along with Smol'yakov and Tkachenko model are considered. TI is varied as 0.05%, 0.1%, 0.5% and 1%. It is varied up to 1%, as for external aerodynamics typical TI is considered to be $\cong 1\%$ The effect of change in TI on velocity profile is presented in Figure 3.5.11, and the effect on MSP is presented in Table 3.5.8. As seen, there isn't much sensitivity obtained for TI variation.

Table 3.5.7: Model parameters for estimation of velocity and MSP sensitivity to turbulence intensity

Turbulence model properties	
Turbulence model	$k - \omega$
y^+	1
Free stream velocity [m/s]	30
Kinematic viscosity [m ² /s]	1.46×10^{-5}
Air density [kg/m ³]	1.225

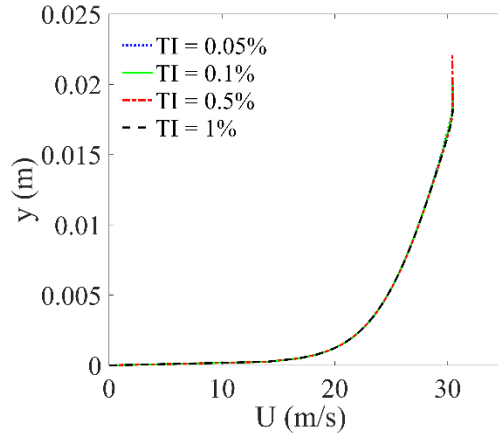


Figure 3.5.11: Effect of change in turbulence intensity on velocity profile

Table 3.5.8: Change in MSP due to varying turbulence intensity

TI (%)	0.05	0.1	0.5	1	Exp. [13], [93]
MSP (Pa ²)	27.74	27.68	27.68	27.62	28.96

3.5.2 Large Eddy Simulation (LES)

3.5.2.1 2-Dimensional Simulation

Wall-bounded Flow: Validation

A well-known validation case of flow passed circular cylinder is independently performed in the present work, with two-fold objective, 1) validation of the present CFD work, 2) estimating the effectivity of the two eddy viscosity models SLWF and DSL, detailed later.

Problem Statement

A flow domain of 21.0D height is considered for the problem, where D is the diameter of the cylinder. Upstream and downstream boundaries of the domain are kept at 8.5D and 20.5D distances from the center of the cylinder respectively. D is taken as 19 mm or 0.019 m. Inlet flow velocity is kept uniform with a magnitude of 69.2 m/s, which leads to a flow Reynolds number of 90,000. An attempt has been made to numerically replicate the experiment performed by Revell *et al.*, 1977. The schematic of the problem is presented in Figure 3.5.12.

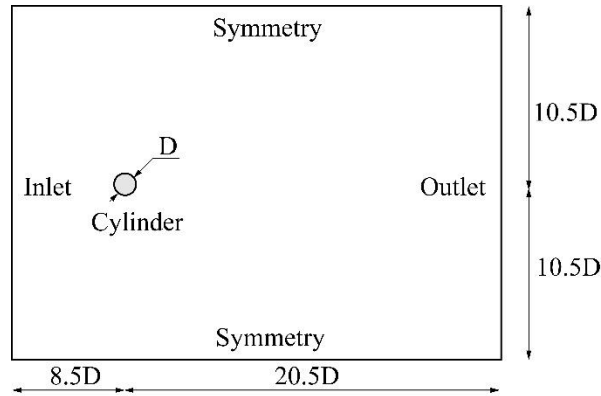


Figure 3.5.12: Schematic of flow passed 2-D circular cylinder case

Solution Methods

Firstly, a steady-state (RANS) simulation is performed to extract globally averaged flow parameters, like wall shear stress, τ_w coefficient of skin friction C_f , etc. at different points on the cylinder wall. Subsequently, Large Eddy Simulation (LES) technique is used for transient simulation. The commercial software package ANSYS Fluent is used for this purpose. The mesh refinement is optimized as suggested by Wang *et al.* [83]. A total of 94,651 quadrilateral cells are used. An unstructured grid with necessary refinement close to the cylinder wall is used in the form of 360 and 80 mesh nodes in the circumferential and radial directions, respectively. Incompressible Navier-Stokes equations are solved at each grid in a pressure-based transient solver. To reduce the computation cost, the Non-Iterative Time-Advancement scheme is opted along with the Fractional Step method (FSM). This allows for reducing the splitting error in the order of the truncation error. Spatial discretization is performed using the Bounded Central Difference scheme, commonly used for typical transient simulations. To interpolate the unsteady pressure over the entire domain PRESTRO algorithm is used. In order to keep Courant-Friedrichs-Lewy (CFL) number below 1.5, which essentially describes how far fluid moves within the cell in a particular time step, for the present case time step size is considered as 10^{-6} s. Two different sub-grid eddy viscosity models are used for computation, a) the Smagorinsky-Lilly model with Wall Function (SLWF) and b) the Dynamic Smagorinsky-Lilly model (DSL). Results are compared with the published experimental findings and presented in Figure 3.5.13(a) and Figure 3.5.13(b). It is observed that SLWF model is more accurate in the case of wall-bounded flows. Therefore, streamlines and static pressure contours are obtained using SLWF model, presented in Figure 3.5.14 and Figure 3.5.15, respectively. A periodicity close to 0.0016 s is observed which is also reported by Wang *et al.* [83]. Moreover, in the subsequent section for TBL over flat plate cases, SLWF is considered as the eddy-viscosity model.

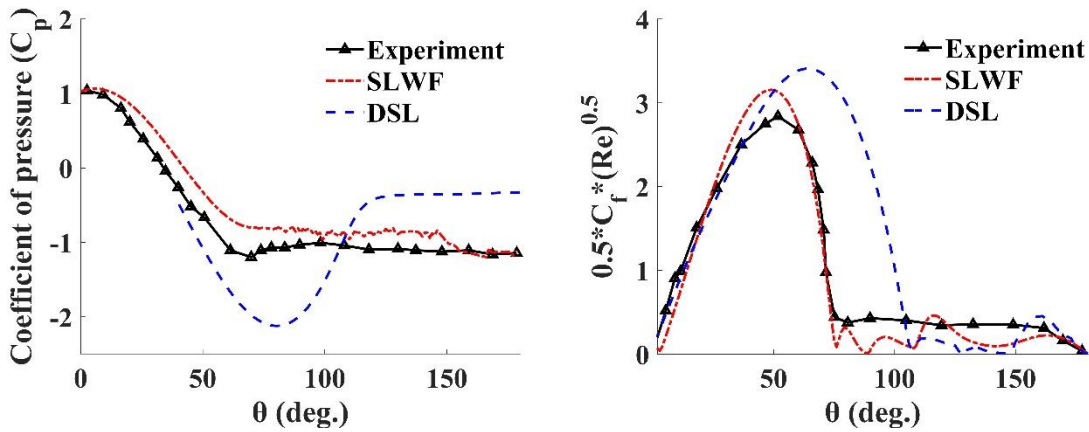


Figure 3.5.13: a) Coefficient of pressure and b) Scaled skin friction coefficient at different θ , θ being the angle of the points over the body, measured from the trailing edge. (Experimental results are as reported by Revell *et al.*, 1977)

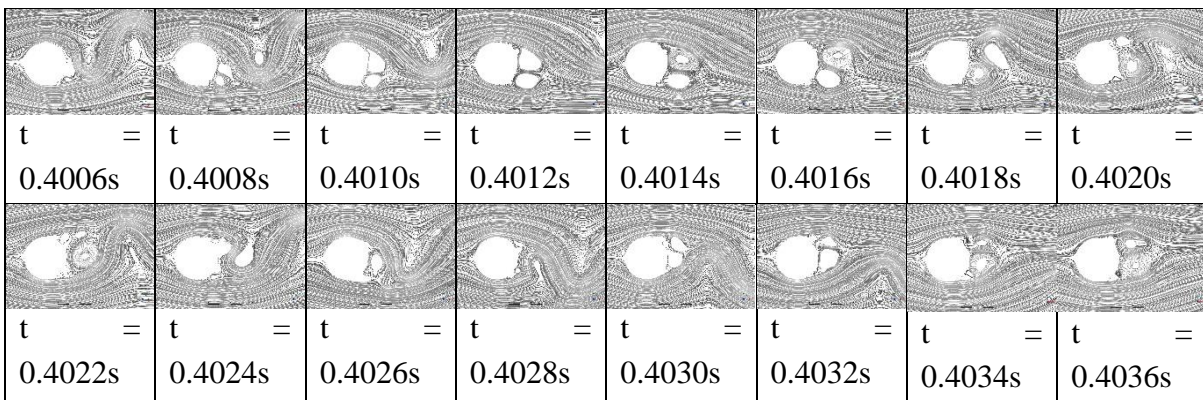


Figure 3.5.14: Streamlines at different time steps

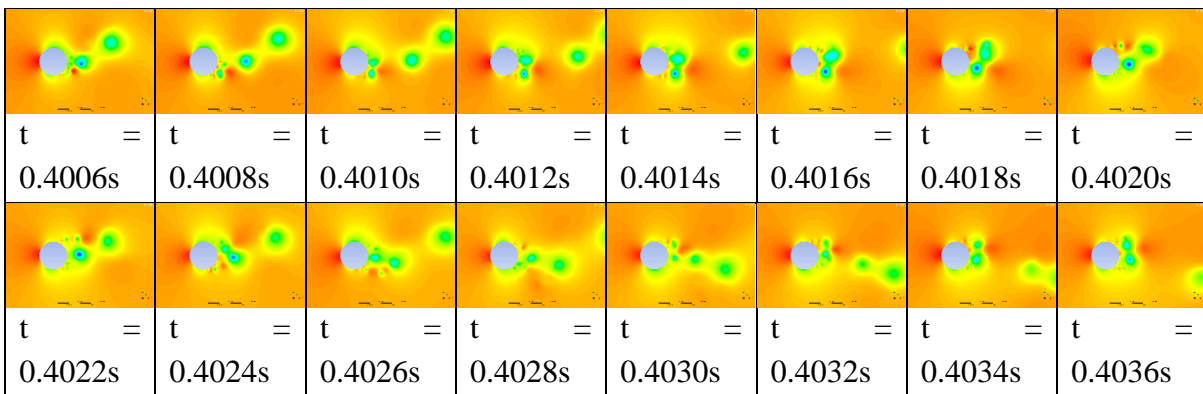


Figure 3.5.15: Pressure contours at different time steps

Turbulent Flow over Flat Plate: Validation

Problem Statement

Two different cases of flows over flat plate are simulated in this stage. The schematic is presented in Figure 3.5.16. Physical dimensions along with different meshing information required for grid sensitivity study are presented in Table 3.5.9. It is ensured that the number of elements in each refined mesh is greater than 30% of the previous one.

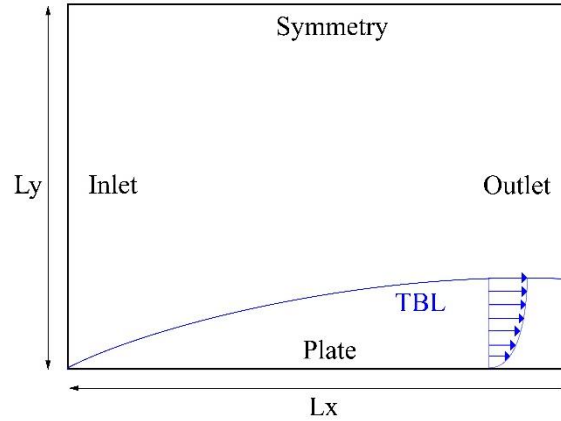


Figure 3.5.16: Schematic of turbulent flow over flat plate cases

Table 3.5.9: Geometry and meshing information for flow over flat plate cases

Case	U_0 (m/s)	L_x (m)	L_y (m)	Mesh quality	N_x	N_y	Δy (10^{-6} m)
I	44.7	0.47	0.10	Coarse	500	100	6.5
				Medium	500	200	1.0
				Fine	1000	200	1.0
II	170	0.30	0.03	Coarse	500	100	7.5
				Medium	500	200	1.54
				Fine	1000	200	1.54

Solution Methods

One of the most important aspects of the numerical modelling of a ‘flow over flat-plate problem’ is the near-wall meshing to resolve smaller eddies. To capture the circular motion of a 2-D eddy, there must be at least four cells around it. Therefore, near-wall grid clustering is implemented to achieve a distance of the centroid of the first cell in the wall-normal direction (Δy) in such a way that the normalized wall distance, $y^+ (= \frac{\Delta y u_\tau}{\nu})$ for the entire plate remains below unity.

In order to generate the artificial inflow turbulence, an in-house user-defined function (UDF) is developed following Eq. (3.4.11) and Eq. (3.4.12) and is used at the inlet of the domain. Pressure

outlet boundary condition with zero pressure gradient for the outlet, no-slip boundary condition, i.e., zero velocity for the plate, and symmetry condition for the top boundary of the domain is employed. The realizable k-epsilon (RANS) model with enhanced wall treatment is used for steady-state simulations. Scaled residual is set strictly as 10^{-6} . Velocity profile, wall shear stress (τ_w), etc. are estimated at specified locations over the plate. Subsequently, based on Eq. (3.4.13) and Eq. (3.4.14), in-house numerical exercises are performed in a MATLAB environment to compute different boundary layer parameters using the RANS simulation data.

$$\delta^* = \sum_{i=2}^{n-1} \left(1 - \frac{u_i}{U_0}\right) \left(\frac{y_{i+1} - y_{i-1}}{2}\right) \quad (3.5.2)$$

$$\theta = \sum_{i=2}^{n-1} \frac{u_i}{U_0} \left(1 - \frac{u_i}{U_0}\right) \left(\frac{y_{i+1} - y_{i-1}}{2}\right) \quad (3.5.3)$$

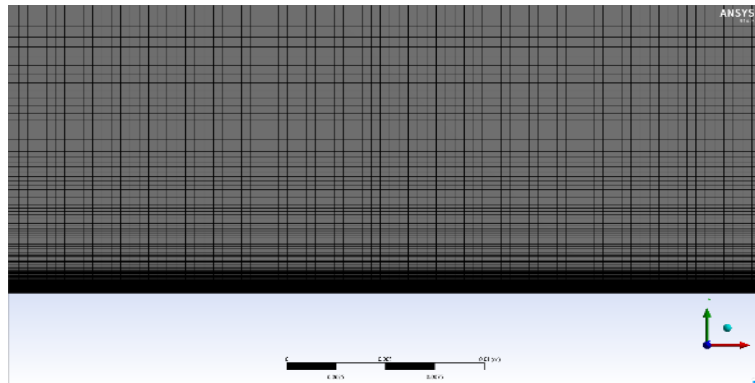
where u_i and y_i are the local velocity and wall-normal distance of i th node, and n is the number of nodes up to boundary layer thickness (δ). The wall-normal distance (Δy) corresponding to $0.99U_0$ is noted as δ for all the cases. The computed results are then presented in Table. 3.5.10 and compared with the values obtained using the empirical formula as given in Eq. (3.4.15) to Eq. (3.4.17). A grid sensitivity study is performed by repeating the entire process with different grid resolutions (coarse, medium, and fine) and presented in Table 3.5.10.

Table 3.5.10: Grid sensitivity study based on turbulent boundary layer parameters

Case	U_0 (m/s)	Location of monitor point (m)	Method*	δ (10^{-3} m)	δ^* (10^{-4} m)	Θ (10^{-4} m)	τ_w (MPa)
I	44.7	0.15	Empirical	3.70	4.27	3.59	5.46
			Coarse	3.64	4.17	3.39	5.44
			Medium	3.64	4.18	3.42	5.44
			Fine	3.64	4.18	3.43	5.45
II	170	0.25	Empirical	4.80	5.50	4.67	53.11
			Coarse	4.41	4.90	4.25	53.66
			Medium	4.41	4.90	4.26	53.75
			Fine	4.41	4.89	4.26	53.71
		0.29	Empirical	5.40	6.25	5.25	51.44
			Coarse	4.91	5.69	4.54	52.63
			Medium	4.91	5.71	4.55	52.66
			Fine	4.91	5.71	4.55	52.75

*Empirical estimations are done as described by Hafeez *et al.* [179] and Mahmoudnejad [180]. Numerical (coarse, medium, fine) values are obtained from the present study.

As the grid sensitivity study suggests, ‘Medium’ meshing is found to be sufficient and used for subsequent transient simulations for all the cases. Near-wall grid clustering is performed for both the flat plate TBL cases (case I and Case II) and shown for Case II in Figure 3.5.17(a). Normalized wall distance throughout the span is well below 1 (refer to Figure 3.5.17(b). The normalized velocity vs normalized wall distance plot (refer to Figure 3.5.17(c)) follows the universal law of the wall. Transient simulations are performed using the LES SLWF model for both Case I and Case II with $C_s = 0.1$. To keep Courant-Friedrichs-Lewy (CFL) number below 1.5, for the present case time step size is considered as 10^{-7} s. Pressure data at every 100 steps are stored, transformed into zero-mean data set, and presented in Figure 3.5.18(a) (Case I) and Figure 3.5.19(a) (Case II). In the low ($M = 0.13$) and high ($M = 0.5$) Mach flows, the zero mean pressure fluctuations are observed in the range +50Pa to -50Pa and +200Pa to -200Pa, respectively. The spectral synthesizer method is found to produce damped pressure fluctuations whereas using the present approach the pressure fluctuations are observed in the order of the results as reported in the open literature (refer to Figure 3.5.18(c)). CFL number is checked and found to be below 1.5 in most of the cells. Next, applying Welch’s method, the power spectral density (PSD) of the wall-pressure fluctuations is obtained and shown in Figure 3.5.18(b) (Case I) and Figure 3.5.19(b) (Case II). Normal Power-spectral density (PSD) of wall-pressure fluctuations for Case I (Mach=0.13) is compared with that of the Smol’yakov and Tkachenko model [42], and PSD of Case II (Mach = 0.5) is compared with Goody [41] and Efimtsov 1 model [29]. They are providing a fairly good agreement except at a higher frequency regime (>3000 Hz) for low Mach number flow. The reason may be the limitations in resolving energy-containing eddies with higher frequencies in three-dimensional space.



(a)

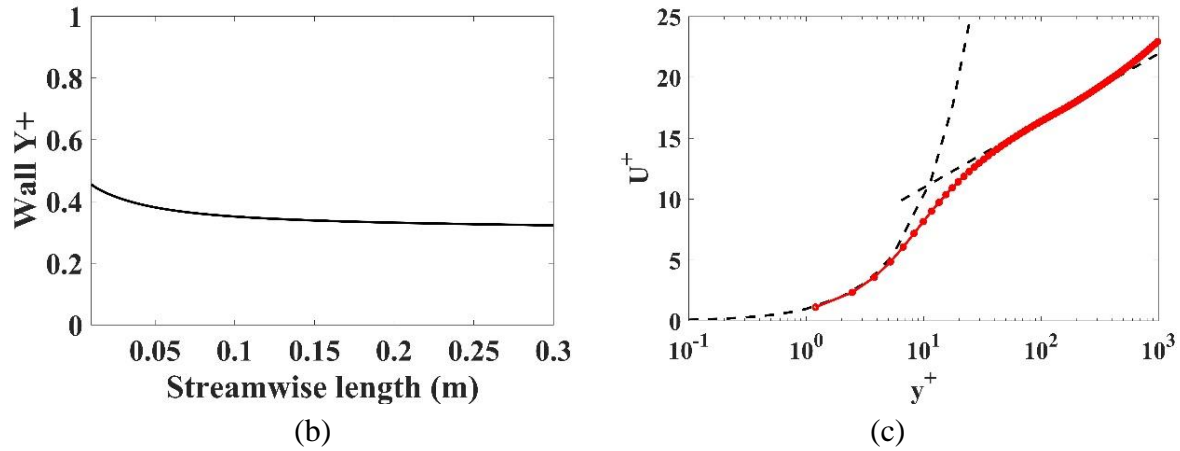


Figure 3.5.17: (a) Grid clustering near the wall, (b) Wall y^+ values along the stream-wise length, (c) Normalized velocity vs normalized wall distance, the red line represents the present study [Case II]

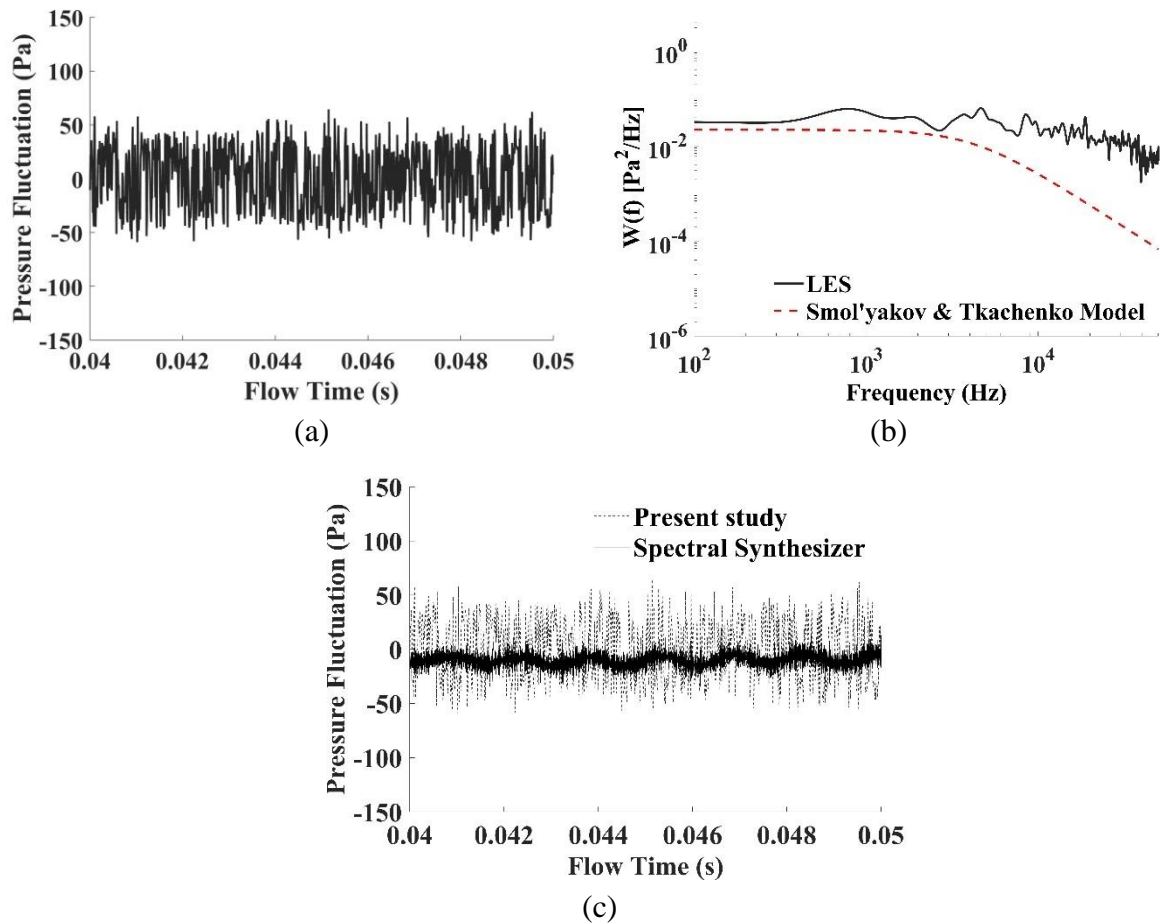


Figure 3.5.18: (a) Pressure fluctuations over time, (b) Power spectral density (PSD) of wall pressure fluctuations (c) comparison between results obtained through the present study powered by artificial inflow turbulence UDF and spectral synthesizer method (Fluent V14.5) [Case I: Free stream velocity 44.7 m/s]

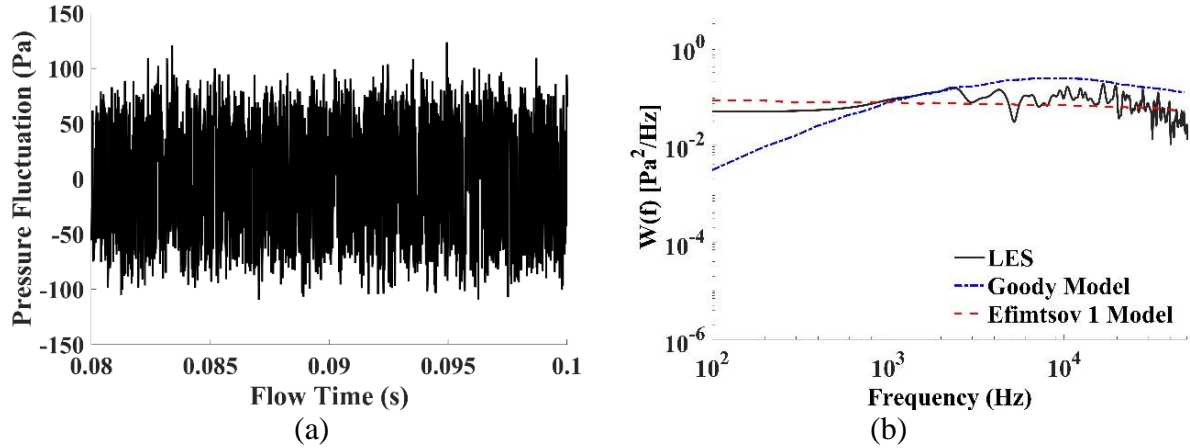


Figure 3.5.19: (a) Pressure fluctuations over time, (b) Power spectral density (PSD) of wall pressure fluctuations [Case II: Free stream velocity 170 m/s]

3.5.2.2 3-Dimensional Simulation

A 3-dimensional Large Eddy Simulation (LES) is also attempted in the present research work. Fluctuating velocity components in all 3-dimensions are superimposed on the mean velocity in order to develop the artificial inflow turbulence. The required user defined function (UDF) is created and augmented in ANSYS Fluent. After initial simulation for some time the inlet velocity profiles are obtained as presented in Figure 3.5.20. The simulation domain and other flow parameters are considered same as reported by Majmoudnejad [180] in the DNS study.

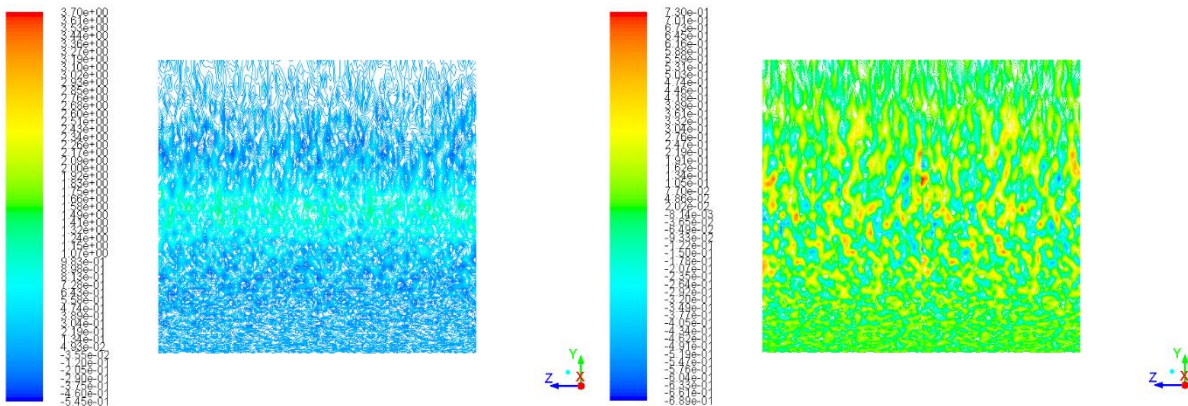


Figure 3.5.20: Velocity contour of artificial inflow turbulence generated using UDF in ANSYS Fluent; a) y-velocity contour, b) z-velocity contour

Unfortunately, the computational resource available within the University is insufficient to simulate for a time significant enough, to generate a stationary turbulence and the wall pressure fluctuation data that could be extracted. The 2-D simulation with 0.2 million nodes in DELL Workstation with 8 cores and 32 GB RAM itself took days of CPU time to simulate the turbulent flow for 0.1 s, with time step size of 10^{-7} s, i.e., 10^6 number of time steps. The 3-D simulation

was projected for an unrealistic CPU time. Therefore, this 3-D LES is abandoned for the time being, and it is scheduled for the future.

3.6 SPATIAL CORRELATION FUNCTION AND PRESSURE CROSS POWER SPECTRAL DENSITY (CPSD)

Once the single point power spectrum is obtained, cross-spectra of the pressure fluctuations are obtained similar in lines to that presented by Hambric *et al.* [51]. A modified Corcos model is adopted to obtain the correlation function $\Gamma(\xi_1, \xi_3, \omega)$ which is multiplied with the single point power spectrum of pressure fluctuations to obtain cross power spectrum at different points, as a function of frequency and separation vectors along both the stream wise and crossflow direction. Cross-spectrum is calculated as,

$$\Phi_{pp}(x_\mu, x_\nu, \omega) = \sqrt{\Phi_p(x_\mu, \omega)\Phi_p(x_\nu, \omega)}\Gamma(\xi_1, \xi_3, \omega) \quad (3.6.1)$$

The spatial correlation function originally proposed by Corcos [44], [45] is

$$\Gamma(\xi_1, \xi_3, \omega) = A_1\left(\frac{\omega\xi_1}{U_c}\right)B_1\left(\frac{\omega\xi_3}{U_c}\right) \quad (3.6.2)$$

with ξ_1 and ξ_3 being the separation vectors between two points, along x (stream-wise) and z (crossflow) direction, respectively. U_c describes the average convective velocity approximated by Bull [77] as

$$U_c \cong U_0\left(0.59 + 0.30e^{-\frac{0.89\omega\delta^*}{U_0}}\right) \quad (3.6.3)$$

$$A_1\left(\frac{\omega\xi_1}{U_c}\right) = \left(1 + \alpha_1\left|\frac{\omega\xi_1}{U_c}\right|\right)e^{-\alpha_1\left|\frac{\omega\xi_1}{U_c}\right|}e^{i\frac{\omega\xi_1}{U_c}} \quad (3.6.4)$$

$$B_1\left(\frac{\omega\xi_3}{U_c}\right) = e^{-\alpha_3\left|\frac{\omega\xi_3}{U_c}\right|} \quad (3.6.5)$$

where α_1 and α_3 are decay constants. For spatially homogenous pressure fields α_1 and α_3 are considered as 0.11 and 0.70 [51].

3.7 CONCLUSION

3.7.1 Combined RANS-Semi-Analytical Model Approach

A two-fold sensitivity of the zero-pressure gradient flat plate turbulent boundary layer wall-pressure spectrum is investigated for flow over flat plate. One aspect of this sensitivity lies in the approximations of the pressure spectrum models. Another important part deals with the variation in mean square pressure fluctuations caused by the choice of model parameters like (i) solver, (ii) near wall grid clustering, (iii) measuring location and the flow velocity, etc. The study is performed by numerically replicating the wind tunnel experiments and in-flight tests considering different RANS configurations. The important take-away from this study are

(a) Smol'yakov-Tkachenko model for wind tunnel experiments, and Rackl-Weston model for in-flight tests are observed to be a fair point to start with.

(b) The $k - \omega$ family of models are found to be the best predictor of MSP with very good convergence, when experimental wall parameters are fed into the spectrum models and compared. $k - \epsilon$ family of models are recommended to be avoided for this type of near wall studies.

Thus, the present study has been able to bridge the gap in selection of a suitable RANS turbulence closure model for predicting the wall pressure parameters with compatible grid clustering and suitable wall-pressure spectrum models. Also, it addresses the split in the error contribution; one part is the suitability of the pressure spectrum models, and another one is the choice of CFD model parameters.

3.7.2 Large Eddy Simulation (LES) and Artificial Inflow Turbulence

TBL wall pressure fluctuation is estimated using large eddy simulation (LES) technique. Artificial inflow turbulence is generated and used at the inlet to continuously perturb the flow and to obtain significant pressure fluctuation near the wall. It has been observed that introduction of the artificial inflow turbulence works better than the 'spectral synthesiser method' presently existing in ANSYS Fluent. Moreover, the estimated pressure fluctuations are Fourier transformed and the power spectra are obtained. This LES-predicted wall pressure spectra found to be matching very well with the established semi-analytical spectra. For low-Re flow the spectrum is observed to be very close to that of formulated using Smol'yakov-Tkachenko model, whereas, for high-Re flow the spectrum matches quite well with the spectra developed by Efimtsov and Goody models.

The wall pressure fluctuation estimated in this Chapter is used in the subsequent chapters to compute vibroacoustic response of flexible panels and detailed in Chapter 4 (vibration response) and Chapter 5 (acoustic response).

CHAPTER 4: TBL-EXCITED STRUCTURAL VIBRATION

4.1 INTRODUCTION

In an attempt towards understanding the response of structural system representing an automobile or an aircraft subjected to TBL excitation (modelling of which is presented in the earlier chapter) one has to have a proper understanding of the interaction between the fluid flow and the structure over which the flow is taking place. This fascinating field of turbulent boundary layer-induced vibration of flexible panels is dealt within this chapter with a primary focus on understanding the physics and thereafter developing suitable numerical techniques for the analysis.

In real life automobile or aircraft, the panels which are subjected to TBL excited flow are generally curved but for all practical purposes for small sized panel it can be considered as flat flexible panel. Such flexible panels can either be stiffened or unstiffened. Stiffened panels are flat plates that incorporate stiffeners in a grid pattern to enhance their bending and torsional stiffness. In the present research work the focus is on understanding the behaviour of flat panels both stiffened and unstiffened, subjected to TBL excitation. Furthermore, due to certain engineering advantages manifested by laminated orthotropic materials due to their enhanced material properties they are now being widely used in automobile and aerospace industries. Hence the study is extended for structures made up of orthotropic laminated composites as well.

To study the complex vibration behaviour of structural panels induced by turbulent boundary layer, this chapter emphasizes on the application of numerical methods. In particular, special purpose MATLAB codes developed in-house are employed to conduct simulations and analyze the dynamic response of flexible panels. MATLAB provides a versatile and convenient platform for implementing and solving mathematical models, enabling efficient simulations and detailed analysis of the panel's vibration behaviour.

A comprehensive introduction to the subject matter is presented in this chapter, highlighting the importance of understanding turbulent boundary layer-induced vibrations and the role of numerical techniques in their analysis. The present study might be helpful for future researchers to gain insights into the intricate turbulence-structure interaction behaviour and predict the dynamic behaviour of these panels under turbulent flow conditions.

4.2 MATHEMATICAL DESCRIPTION

A schematic of the TBL-excited structural vibration problem is presented in Figure 4.2.1.

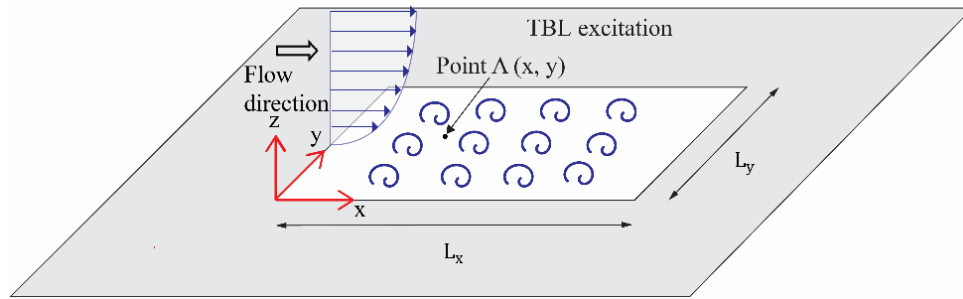


Figure 4.2.1: Schematic of TBL excited plate placed on an infinite baffle

A comprehensive mathematical description is essential for capturing the complex fluid-structure interaction and accurately predicting the response of panels subjected to TBL excitation. The mathematical models enable one to understand the underlying physics, identify critical parameters, and develop effective strategies for structural design and optimization. By formulating the governing equations and appropriate boundary conditions, mathematical descriptions provide a basis for numerical simulations and facilitate the development of computational techniques to analyze TBL-induced panel vibration. It involves the formulation of governing equations that govern the fluid and structural dynamics. The flow physics describing the TBL flow and the detailed numerical formulation of the same is discussed in detail earlier in Chapter 3. The necessary formulation to evaluate structural response due to one-way coupled fluid-structure interaction is presented in this chapter.

Two different techniques to obtain structural response due to TBL excitation are presented in this chapter – (i) Considering TBL excitation as stationary random process and thereafter obtaining the response in the spectral domain and (ii) Decomposing the TBL excitation using Cholesky decomposition technique and obtaining structural response in frequency domain.

4.2.1 Vibration of Panels; Random Excitation

As is evident from the earlier chapter the TBL pressure generated due to fluid flow is random both in space and time. The pressure obtained from any CFD simulation is in the form of power spectral density (PSD). This pressure when impinges on plate like structures is supposed to generate a response which is also random in nature. For all practical consideration the TBL pressure spectrum can be considered as a stationary random process with Gaussian probability distribution. As a standard procedure to obtain the response one can follow the general mathematical steps as described in the following equations.

Let the external excitation is considered as a stationary random process, denoted by $x(t)$, having statistical properties such as mean and autocorrelation constant over time. For simplicity, one can assume $x(t)$ as a zero-mean process, i.e., $E[x(t)] = 0$, where $E[\cdot]$ is the expected value.

Using convolution theorem one can obtain the response of a linear system subjected to any arbitrary excitation $x(t)$ as,

$$y(t) = \int_{-\infty}^{\infty} x(\tau) h(t - \tau) d\tau \quad (4.2.1)$$

or alternately as,

$$y(t) = \int_{-\infty}^{\infty} x(t - \tau) h(\tau) d\tau \quad (4.2.2)$$

where $h(t)$ is the impulse response and τ is a dummy variable.

Expressing the response in the Fourier domain one obtains,

$$Y(\omega) = \int_{-\infty}^{\infty} y(t) e^{-i\omega t} dt = \int_{-\infty}^{\infty} x(t) \left[\int_{-\infty}^{\infty} h(t - \tau) e^{-i\omega t} dt \right] d\tau \quad (4.2.3)$$

and on substituting, $t - \tau = \sigma$

$$Y(\omega) = \int_{-\infty}^{\infty} x(\tau) e^{-i\omega\tau} d\tau \left[\int_{-\infty}^{\infty} h(\sigma) e^{-i\omega\sigma} d\sigma \right] \quad (4.2.4)$$

$$Y(\omega) = X(\omega)H(\omega) \quad (4.2.5)$$

The Fourier transformed expression $H(\omega)$ for the impulse response $h(t)$ is the Frequency Response Function of the system analyzed.

If the arbitrary excitation happens to be a stationary random process the response of the random process is also stationary. If the first and second order statistics of the excitation process is known the statistical parameter for the response random process can be calculated. Averaging the expression in Eq. (4.2.2) over the ensemble one can write the mean value of the response random process as,

$$E[y(t)] = E\left[\int_{-\infty}^{+\infty} x(t - \tau)h(\tau) d\tau\right] \quad (4.2.6)$$

Now, for a stationary random process $E[x(t-\tau)] = E[x(t)] = \text{constant}$ and it can be shown that

$$E[y(t)] = H(0)E[x(t)] = \text{constant} \quad (4.2.7)$$

The above relation implies that if the excitation is a stationary random process, the mean value of the response of a system subjected to that excitation is also constant and proportional to the mean value of the excitation.

Similarly, the autocorrelation function of the response random process can be expressed as,

$$R_y(\tau) = E[y(t)y(t + \tau)] = E\left[\int_{-\infty}^{+\infty} h(\lambda_1)x(t - \lambda_1)d\lambda_1 \int_{-\infty}^{+\infty} h(\lambda_2)x(t + \tau - \lambda_2)d\lambda_2\right] \quad (4.2.8)$$

which can finally be expressed as,

$$R_y(\tau) = \int_{-\infty}^{+\infty} \int_{-\infty}^{+\infty} h(\lambda_1)h(\lambda_2) R_x(\tau + \lambda_1 - \lambda_2)d\lambda_1 d\lambda_2 \quad (4.2.9)$$

After performing the Fourier Transform of the LHS and the RHS one can obtain the mean auto power spectral density of the response as,

$$S_y(\omega) = |H(\omega)|^2 S_x(\omega) \quad (4.2.10)$$

For systems whose geometry is spatially varied in two-dimension and the disturbance also being spatially varied the Auto-PSD and the Cross-PSD can be expressed as,

$$S_{xx}(\omega) = |H_{xx}(\omega)|^2 \phi_p(\omega)$$

$$S_{xy}(\omega) = H_{xy}(\omega)\phi_{pp}(\omega)H_{xy}^*(\omega) \quad (4.2.11)$$

where $H_{xx}(\omega)$ is the frequency response function (FRF) of the response at a single DOF, representing the transfer function between the input excitation and the response at that DOF, $H_{xy}(\omega)$ is the FRF between two responses at different DOFs, $\phi_p(\omega)$ is the auto PSD and $\phi_{pp}(\omega)$ is the cross PSD of the excitation force (input).

The FRFs, $H_{xx}(\omega)$ and $H_{xy}(\omega)$, are frequency-dependent and can be calculated using the modal analysis of the flexible plate structure. The auto PSD of the excitation force, $\phi_p(\omega)$, can be obtained based on the characteristics of the random excitation (e.g., white noise) and its PSD.

Frequency Response Function, H Calculation for MDOF System

The equation of motion of a MDOF system subjected to external excitation can be written as

$$M\ddot{q}(t) + C\dot{q}(t) + Kq(t) = Q(t) \quad (4.2.12)$$

With M, C, and K being the n x n symmetric inertia, damping and stiffness matrices and then-dimensional displacement vector q(t) contains the generalized coordinates $q_i(t)$, whereas the n-dimensional vector Q(t) contains the associated generalized forces $Q_i(t)$ ($i = 1, 2, \dots, n$). In the present dissertation $Q_i(t)$ represent ergodic random processes, from which it follows that the responses $q_i(t)$ are also ergodic random process.

Considering the system having proportional damping the mode shape matrix associated with the undamped linear system can be used as a linear transformation vector to uncouple the system of equations. If one considers the classical modal matrix $U = [u_1 \ u_2 \ u_3 \ \dots \ u_n]$ associated with the undamped system one can write the displacement coordinates as,

$$q(t) = U\eta(t) \quad (4.2.13)$$

Where the components $\eta_r(t)$ ($r = 1, 2, \dots, n$) of the vector $\eta(t)$ are generalized coordinates consisting of linear combinations of the random variables $q_i(t)$ ($i = 1, 2, \dots, n$).

Using the orthonormality relations,

$$U^T M U = I, \quad U^T K U = \Omega \quad (4.2.14)$$

where I is the identity matrix and $\Omega = \text{diag}[\omega_1^2 \ \omega_2^2 \ \dots \ \omega_n^2]$ is the diagonal matrix of the eigenvalues. Hence one can obtain a set of independent equations for the natural coordinates as,

$$\ddot{\eta}_r(t) + 2\zeta_r\omega_r\dot{\eta}_r(t) + \omega_r^2\eta_r(t) = u_r^T Q(t), \quad r = 1, 2, \dots, n \quad (4.2.15)$$

or,

$$\ddot{\eta}_r(t) + 2\zeta_r\omega_r\dot{\eta}_r(t) + \omega_r^2\eta_r(t) = \omega_r^2 N_r(t), \quad r = 1, 2, \dots, n \quad (4.2.16)$$

where,

$$N_r(t) = \frac{1}{\omega_r^2} u_r^T Q(t), \quad r = 1, 2, \dots, n \quad (4.2.17)$$

The next objective is to obtain the cross-correlation between two response processes. One can express the Fourier transform of $\eta_r(t)$ and $N_r(t)$ as,

$$\eta_r(\omega) = \int_{-\infty}^{\infty} \eta_r(t) e^{-i\omega t} dt \quad (4.2.18)$$

and

$$N_r(\omega) = \int_{-\infty}^{\infty} N_r(t) e^{-i\omega t} dt = \frac{1}{\omega_r^2} \mathbf{u}_r^T \int_{-\infty}^{\infty} \mathbf{Q}(t) e^{-i\omega t} dt \quad (4.2.19)$$

respectively.

Thereafter transforming Eq. (4.2.15) in the Fourier domain one obtains

$$(-\omega^2 + i2\zeta_r\omega\omega_r + \omega_r^2)\eta_r(\omega) = \omega_r^2 N_r(\omega), \quad r = 1, 2, \dots, n \quad (4.2.20)$$

Equation (4.2.20) can be solved for η_r as,

$$\eta_r(\omega) = H_r(\omega) N_r(\omega), \quad r = 1, 2, \dots, n \quad (4.2.21)$$

where

$$H_r(\omega) = \frac{1}{1 - (\omega/\omega_r)^2 + i2\zeta_r\omega/\omega_r}, \quad r = 1, 2, \dots, n$$

the frequency response associated with the r th natural mode.

In the next step one has to obtain the cross correlation between two random responses q_i and q_j ($i, j = 1, 2, \dots, n$). The cross correlation function $R_{q_i q_j}(\tau)$ relating the two random responses q_i and q_j ($i, j = 1, 2, \dots, n$) can be arranged as a $n \times n$ matrix which is termed as Response Correlation Matrix and is expressed as,

$$\begin{aligned} R_q(\tau) &= \left[R_{q_i q_j}(\tau) \right] \\ &= \lim_{T \rightarrow \infty} \frac{1}{T} \int_{-T/2}^{T/2} \begin{bmatrix} q_1(t)q_1(t+\tau) & q_1(t)q_2(t+\tau) & \dots & q_1(t)q_n(t+\tau) \\ q_2(t)q_1(t+\tau) & q_2(t)q_2(t+\tau) & \dots & q_2(t)q_n(t+\tau) \\ \dots & \dots & \dots & \dots \\ q_n(t)q_1(t+\tau) & q_n(t)q_2(t+\tau) & \dots & q_n(t)q_n(t+\tau) \end{bmatrix} dt \\ &= \lim_{T \rightarrow \infty} \frac{1}{T} \int_{-T/2}^{T/2} \mathbf{q}(t) \mathbf{q}^T(t+\tau) dt \\ &= \lim_{T \rightarrow \infty} \frac{1}{T} \int_{-T/2}^{T/2} \mathbf{U} \boldsymbol{\eta}(t) \boldsymbol{\eta}^T(t+\tau) \mathbf{U}^T dt = \mathbf{U} R_{\boldsymbol{\eta}}(\tau) \mathbf{U}^T \end{aligned} \quad (4.2.22)$$

where $R_{\boldsymbol{\eta}}(\tau) = \lim_{T \rightarrow \infty} \frac{1}{T} \int_{-T/2}^{T/2} \boldsymbol{\eta}(t) \boldsymbol{\eta}^T(t+\tau) \mathbf{U}^T dt$ is the modal response correlation matrix. The response correlation matrix has to be expressed in terms of quantities defining the excitation random process.

Recognizing that the cross-correlation function $R_{\eta_s \eta_r}(t)$ is equal to the Fourier transform of the cross spectral density function $S_{\eta_s \eta_r}(\omega)$ one can write the modal response correlation matrix as,

$$R_{\boldsymbol{\eta}}(\tau) = \frac{1}{2\pi} \int_{-\infty}^{\infty} \bar{H}(\omega) S_N(\omega) H(\omega) e^{i\omega\tau} d\omega \quad (4.2.23)$$

In which, $H(\omega) = \text{diag}[H_1(\omega) \quad H_1(\omega) \quad \dots \quad H_n(\omega)]$ is the diagonal matrix of the modal frequency responses, $\bar{H}(\omega)$ is the complex conjugate of $H(\omega)$ and $S_N(\omega)$ is the $n \times n$ modal excitation spectral density matrix.

Hence from Equation (4.2.22) the response correlation matrix is,

$$R_q(\tau) = \frac{1}{2\pi} U \left[\int_{-\infty}^{\infty} \bar{H}(\omega) S_N(\omega) H(\omega) e^{i\omega\tau} d\omega \right] U^T \quad (4.2.24)$$

The modal excitation spectral density matrix can be related to the modal excitation correlation matrix by the following equation,

$$S_N(\omega) = \int_{-\infty}^{\infty} R_N(\omega) e^{-i\omega\tau} d\tau \quad (4.2.25)$$

The modal excitation correlation matrix can be expressed in terms of modal force vector

$$N(t) = \Omega^{-1} U^T \mathbf{Q}(t) \text{ as}$$

$$R_N(\tau) = \lim_{T \rightarrow \infty} \frac{1}{T} \int_{-T/2}^{T/2} \mathbf{N}(t) \mathbf{N}^T(t + \tau) U^T dt \quad (4.2.26)$$

which can be further written as,

$$\begin{aligned} R_N(\tau) &= \lim_{T \rightarrow \infty} \frac{1}{T} \int_{-T/2}^{T/2} \Omega^{-1} U^T \mathbf{Q}(t) \mathbf{Q}^T(t + \tau) U \Omega^{-1} dt \\ &= \Omega^{-1} U^T R_Q(\tau) U \Omega^{-1} \end{aligned} \quad (4.2.27)$$

where $R_Q(\tau) = \lim_{T \rightarrow \infty} \frac{1}{T} \int_{-T/2}^{T/2} \mathbf{Q}(t) \mathbf{Q}^T(t + \tau) dt$ is the actual force correlation matrix.

Hence the modal excitation spectral density matrix can be written as,

$$S_N(\omega) = \Omega^{-1} U^T \left[\int_{-\infty}^{\infty} R_Q(\tau) e^{-i\omega\tau} d\tau \right] U \Omega^{-1} = \Omega^{-1} U^T S_Q(\omega) U \Omega^{-1} \quad (4.2.28)$$

where

$$S_Q(\omega) = \int_{-\infty}^{\infty} R_Q(\tau) e^{-i\omega\tau} d\tau$$

is the excitation spectral density matrix expressed in terms of actual forces.

Inserting Equation (4.2.28) in Equation (4.2.24) one can obtain the response correlation matrix

$$R_q(\tau) = \frac{1}{2\pi} U \left[\int_{-\infty}^{\infty} \bar{H}(\omega) \Omega^{-1} U^T S_Q(\omega) U \Omega^{-1} H(\omega) e^{i\omega\tau} d\omega \right] U^T \quad (4.2.29)$$

Thereafter using the standard methodology one can write the response PSD as,

$$S_q(\omega) = U \bar{H}(\omega) \Omega^{-1} U^T S_Q(\omega) U \Omega^{-1} H(\omega) U^T \quad (4.2.30)$$

4.2.2 Finite Element Modelling; Structural Panel

The process of development of the excitation spectral density matrix $S_Q(\omega)$ is already described in Chapter 3 in details. In this section the necessary modelling aspect for numerically obtaining the frequencies, mode shape vectors and the modal frequency response function of the structures in question is presented. To this end it is important to point out that the entire structural modelling is carried out using a finite element framework in ANSYS (V14.5) APDL platform.

In the present dissertation a few different forms of flat structural panels are considered namely (i) isotropic (ii) orthotropic (iii) stiffened isotropic/orthotropic and (iv) tensioned panels. APDL based ANSYS codes are developed for each one of the structural forms. The structural

panels are discretized using SHELL181 element from the ANSYS element library. For the sake of completeness, the necessary features of SHELL181 element is presented here.

SHELL181 is suitable for analyzing thin to moderately thick shell structures. It is a four-node element with six degrees of freedom at each node: translations in the x, y, and z directions, and rotations about the x, y, and z-axes. SHELL181 uses a penalty method to relate the independent rotational degrees of freedom about the normal (to the shell surface) with the in-plane components of displacements. SHELL181 can be used for layered applications for modelling composite shells or sandwich construction. The accuracy in modelling composite shells is governed by the first-order shear-deformation theory (usually referred to as Mindlin-Reissner shell theory).

The shell section commands allow for layered shell definition. Options are available for specifying the thickness, material and orientation.

The displacement field within the element is represented using the concept of isoparametric formulation, where the shape functions for the element are also used to interpolate the displacement field. For the Shell181 element, as indicated in Figure 4.2.2, the element is characterized by its nodal coordinates (x, y) and corresponding nodal displacements (u, v).

The geometry of the element is expressed as,

$$x_j = \sum_{i=1}^4 N_i(\eta_1, \eta_2)(x_j)_i ; j = 1,2,3 \quad (4.2.31)$$

where N_i 's are the bilinear shape functions given by [182],

$$\begin{aligned} N_1 &= \frac{1}{4}(1 - \eta_1)(1 - \eta_2); N_2 = \frac{1}{4}(1 + \eta_1)(1 - \eta_2) \\ N_3 &= \frac{1}{4}(1 + \eta_1)(1 + \eta_2); N_4 = \frac{1}{4}(1 - \eta_1)(1 + \eta_2) \end{aligned} \quad (4.2.32)$$

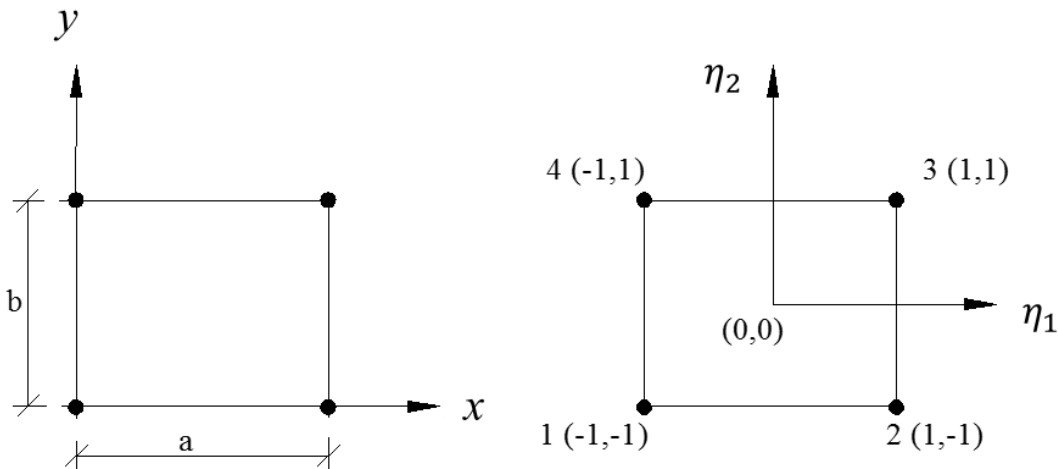


Figure 4.2.2: Four-node quadrilateral element in Cartesian co-ordinate and isoparametric element in natural co-ordinate

The derivatives of the shape functions with respect to the local coordinates are given by:

$$\frac{\partial N_1}{\partial \eta_1} = -\frac{1}{4} (1 - \eta_2)$$

$$\frac{\partial N_1}{\partial \eta_2} = -\frac{1}{4} (1 - \eta_1)$$

$$\frac{\partial N_2}{\partial \eta_1} = \frac{1}{4} (1 - \eta_2)$$

$$\frac{\partial N_2}{\partial \eta_2} = -\frac{1}{4} (1 + \eta_1)$$

$$\frac{\partial N_3}{\partial \eta_1} = \frac{1}{4} (1 + \eta_2)$$

$$\frac{\partial N_3}{\partial \eta_2} = \frac{1}{4} (1 + \eta_1)$$

$$\frac{\partial N_4}{\partial \eta_1} = -\frac{1}{4} (1 + \eta_2)$$

$$\frac{\partial N_4}{\partial \eta_2} = \frac{1}{4} (1 - \eta_1)$$

The Jacobian matrix J relates the derivatives of the shape functions to the derivatives with respect to the global coordinates (x, y) . It is defined as:

$$J = \begin{bmatrix} \frac{\partial x}{\partial \eta_1} & \frac{\partial y}{\partial \eta_1} \\ \frac{\partial x}{\partial \eta_2} & \frac{\partial y}{\partial \eta_2} \end{bmatrix} \quad (4.2.33)$$

The determinant of the Jacobian matrix is given by:

$$\det(J) = \frac{\partial x}{\partial \eta_1} \frac{\partial y}{\partial \eta_2} - \frac{\partial y}{\partial \eta_1} \frac{\partial x}{\partial \eta_2} \quad (4.2.34)$$

The element stiffness matrix K is computed using the following formula:

$$[K_e] = \int ([B]^T [D] [B] \det(J)) d\eta_1 d\eta_2 \quad (4.2.35)$$

where B is the strain-displacement matrix, D is the elasticity matrix, and \int represents the integration over the element domain.

For a 4-node isoparametric element, with 2 degrees of freedom per node, the strain-displacement matrix B takes the form:

$$B = \begin{bmatrix} \frac{\partial N_1}{\partial x} & 0 & \frac{\partial N_2}{\partial x} & 0 & \frac{\partial N_3}{\partial x} & 0 & \frac{\partial N_4}{\partial x} & 0 \\ 0 & \frac{\partial N_1}{\partial y} & 0 & \frac{\partial N_2}{\partial y} & 0 & \frac{\partial N_3}{\partial y} & 0 & \frac{\partial N_4}{\partial y} \\ \frac{\partial N_1}{\partial y} & \frac{\partial N_1}{\partial x} & \frac{\partial N_2}{\partial y} & \frac{\partial N_2}{\partial x} & \frac{\partial N_3}{\partial y} & \frac{\partial N_3}{\partial x} & \frac{\partial N_4}{\partial y} & \frac{\partial N_4}{\partial x} \end{bmatrix} \quad (4.2.36)$$

And the elasticity matrix D is a 3×3 matrix representing the material properties.

The element mass matrix M is computed using the following formula:

$$[M_e] = \int ([N]^T [\rho] [N] \det(J)) d\eta_1 d\eta_2 \quad (4.2.37)$$

where N is the shape function matrix and ρ is the density of the material.

Shear Deformation: Reissner-Mindlin's Plate Theory

Mindlin's plate theory introduces the concept of transverse shear strains in addition to the conventional plate bending strains. The strain-displacement relations can be expressed as:

$$\varepsilon_x = \frac{\partial u}{\partial x} - z \frac{\partial w}{\partial x}$$

$$\varepsilon_y = \frac{\partial v}{\partial y} - z \frac{\partial w}{\partial y}$$

$$\gamma_{xy} = \frac{\partial u}{\partial y} + \frac{\partial v}{\partial x}$$

$$\gamma_{xz} = \frac{\partial w}{\partial x}$$

$$\gamma_{yz} = \frac{\partial w}{\partial y}$$

where ε_x , ε_y , γ_{xy} , γ_{xz} , γ_{yz} are the in-plane and shear strains, and z is the thickness coordinate.

Based on Mindlin's plate theory, the equilibrium equations can be written as:

$$D \cdot \{\varepsilon\} + D_s \cdot \{\gamma\} = \{q\} \quad (4.2.38)$$

where $\{\varepsilon\}$ and $\{\gamma\}$ are the vectors of strains, D is the in-plane stiffness matrix, D_s is the transverse shear stiffness matrix, and $\{q\}$ is the vector of applied transverse shear forces.

The element stiffness matrix K is computed using the following formula:

$$[K_e] = \int ([B]^T [D] [B] + [B_s]^T [D_s] [B_s]) \det(J) d\eta_1 d\eta_2 \quad (4.2.39)$$

where B is the strain-displacement matrix for bending strains, B_s is the strain-displacement matrix for shear strains, D is the bending stiffness matrix, D_s is the shear stiffness matrix, J is the Jacobian matrix, and \int represents the integration over the element domain.

For thin to moderately thick plate structures where transverse shear effects are significant, Shell181 element uses a shear-correction factor $k = 5/6$.

Stiffened Isotropic Panel

The FE modelling of a stiffened panel the panel and stiffeners are considered as separate elements within the mesh. The constitutive equations relate the stress and strain in the stiffened panel. In the case of linear elastic material behaviour, the constitutive equations are as follows:

$$\sigma = [D]\varepsilon \quad (4.2.40)$$

where σ is the stress vector (normal and shear stresses)

[D] is the elasticity matrix

ε is the strain vector (normal and shear strains)

For an isotropic material, the elasticity matrix $[D]$ can be defined as:

$$[D] = \frac{[E]}{(1+\nu)} [I] - \frac{[E]}{(1+\nu)} [\nu][\nu]^T \quad (4.2.41)$$

where,

$[E]$ is the Young's modulus

ν is the Poisson's ratio

$[I]$ is the identity matrix

$[\nu]$ is a matrix with elements $-\nu$ except for the diagonal elements, which are 1.

Coordinate Transformation

To model the stiffeners as plate elements, a coordinate transformation is required. Typically, a plate element formulation uses a local coordinate system that aligns with the stiffener's orientation. The transformation matrix $[T]$ is used to convert the local stiffness matrix to the global coordinate system.

$$[T] = [R]^T [T]' \quad (4.2.42)$$

where $[R]$ is the rotation matrix that aligns the local coordinate system with the global coordinate system.

$[T]'$ is the local stiffness matrix.

The rotation matrix $[R]$ is defined based on the orientation of the stiffener. For example, if the stiffener is aligned with the global x-axis, then $[R]$ would be an identity matrix. It is to be noted that the stiffener modelling is also carried out using SHELL181 elements with the option KEYOPT(3) = 2.

Orthotropic Panel

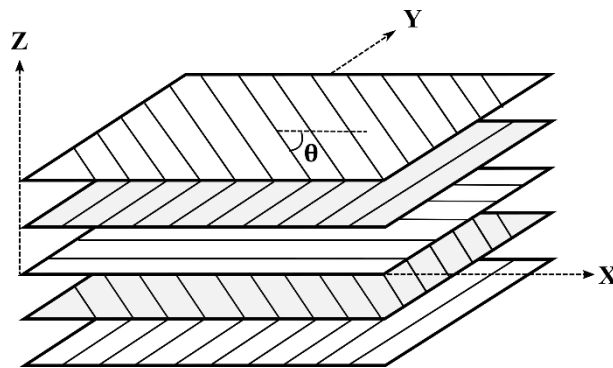


Figure 4.2.3: Orthotropic laminated composite ply sequence

As per the standard procedure, the element stiffness matrix $[K_e]$ and the element mass matrix $[M]$ for a 2-D shell element can be written as,

$$[\mathbf{K}_e] = \int_0^a \int_0^b [\mathbf{B}]^T [\mathbf{D}] [\mathbf{B}] dx dy \quad (4.2.43)$$

and,

$$[\mathbf{M}_e] = \int_0^a \int_0^b [\mathbf{N}]^T [\boldsymbol{\rho}] [\mathbf{N}] dx dy \quad (4.2.44)$$

The layered fiber reinforced plastic lamina introduces coupling between in-plane, out of the plane, and shear behaviour in the laminated panel which is modelled through the [D] matrix. The [D] matrix is given by,

$$[\mathbf{D}] = \begin{bmatrix} A_{11} & A_{12} & A_{16} & B_{11} & B_{12} & B_{16} & 0 & 0 \\ A_{12} & A_{22} & A_{26} & B_{12} & B_{22} & B_{26} & 0 & 0 \\ A_{16} & A_{26} & A_{66} & B_{16} & B_{26} & B_{66} & 0 & 0 \\ B_{11} & B_{12} & B_{16} & D_{11} & D_{12} & D_{16} & 0 & 0 \\ B_{12} & B_{22} & B_{26} & D_{12} & D_{22} & D_{26} & 0 & 0 \\ B_{16} & B_{26} & B_{66} & D_{16} & D_{26} & D_{66} & 0 & 0 \\ 0 & 0 & 0 & 0 & 0 & 0 & A_{44} & A_{45} \\ 0 & 0 & 0 & 0 & 0 & 0 & A_{45} & A_{55} \end{bmatrix} \quad (4.2.45)$$

The coefficients are given by

$$A_{ij} = \sum_{k=1}^n (Q'_{ij})_k (z_k - z_{k-1}); B_{ij} = \frac{1}{2} \sum_{k=1}^n (Q'_{ij})_k (z_k^2 - z_{k-1}^2); D_{ij} = \frac{1}{3} \sum_{k=1}^n (Q'_{ij})_k (z_k^3 - z_{k-1}^3); i, j = 1, 2, 6$$

As referred earlier a shear correction factor is multiplied with the shear coefficients which are expressed as, $A_{ij} = k_s \sum_{k=1}^n (Q'_{ij})_k (z_k - z_{k-1}); i, j = 4, 5$ and $k_s = \frac{5}{6}$

The on-axis constitutive matrix coefficients are given as follows –

$$Q_{11} = \frac{E_1}{1 - \nu_{12}\nu_{21}}; Q_{12} = \frac{\nu_{12}E_2}{1 - \nu_{12}\nu_{21}}; Q_{22} = \frac{E_2}{1 - \nu_{12}\nu_{21}}; Q_{66} = G_{12}; Q_{44} = G_{23}; Q_{55} = G_{13}$$

The inertia matrix [ρ] is expressed as,

$$[\boldsymbol{\rho}] = \begin{bmatrix} I_1 & 0 & 0 & I_3 & 0 \\ 0 & I_1 & 0 & 0 & I_3 \\ 0 & 0 & I_1 & 0 & 0 \\ I_3 & 0 & 0 & I_2 & 0 \\ 0 & I_3 & 0 & 0 & I_2 \end{bmatrix} \quad (4.2.46)$$

$$\text{with } \{I_1, I_2, I_3\} = \int_{-h/2}^{h/2} \rho(z) \{1, z, z^2\} dz$$

Once the structural panels in question are modelled using FEA technique in ANSYS and upon applying proper boundary conditions modal analyses are carried out and the frequencies along with the mode shape vectors are extracted to be used subsequently for further processing in the MATLAB code developed for the response analysis. It is important to note at this present point that the vector $Q(t)$ defined in Equation (4.2.12) can be identified as the force generated due to the TBL flow.

The cross-power spectral density matrix Φ_{pp} obtained in Chapter 3 gives the pressure spectrum distribution at the grid points on the panel. In order to obtain the force spectrum, the influence elemental area dA for individual grid point have to be multiplied with the grid point pressure. Hence the power spectral densities (PSD) of the TBL induced structural response between any two DOF on the plate surface can be written from the Eq. (4.2.30) derived earlier.

$$\mathbf{S}_{ww}(y_i, y_j, \omega) = \iint \mathbf{H}_{u,F}^*(y_i/x_\mu, \omega) \Phi_{pp}(x_\mu, x_\nu, \omega) \mathbf{H}_{u,F}(y_j/x_\nu, \omega) dA_\mu dA_\nu \quad (4.2.47)$$

Here, \mathbf{S}_{ww} is the plate displacement PSD, and can be transformed to plate velocity PSD as,

$$\mathbf{S}_{vv} = \omega^2 \mathbf{S}_{ww} \quad (4.2.48)$$

4.3 NUMERICAL METHODOLOGY

To solve the governing equations detailed in the previous section and predict the TBL-induced panel vibration, various computational methods can be employed. Numerical techniques, such as the finite element method (FEM), finite difference method (FDM), or finite volume method (FVM) are some of the popular methods that can be adopted. These methods allow for the simulation of complex fluid-structure interaction, considering the coupled effects of the TBL and panel dynamics. The advancements in computational power and software capabilities have significantly enhanced the accuracy and efficiency of these numerical simulations.

The present vibration study focuses on the use of FE method which offers a powerful approach to simulate the complex fluid-structure interaction in TBL-induced panel vibration. The method discretizes the panel and surrounding fluid domain into finite elements, where the behaviour of each element is represented by mathematical equations. By assembling these elements, a system of equations is formed, capturing the overall response of the panel. FEM facilitates the incorporation of various boundary conditions, material properties, and loading conditions, allowing for accurate prediction of panel vibrations.

To apply FEM with semi-analytical TBL wall pressure spectrum models, the structural response equations, such as the equations of motion, are coupled with the TBL flow equations and the wall pressure spectrum model.

Once the finite element model is formulated and the mesh is generated, the system of equations representing the coupled fluid-structure problem, including the TBL wall pressure spectrum model, is solved using appropriate solution techniques. These techniques include direct solvers or iterative methods to obtain the panel's dynamic response.

4.3.1 Turbulence-Structure Coupling: PSD Domain

In the solution process of the TBL induced structural excitation and resulting sound radiation, the external TBL pressure fluctuation is assumed to be statistically homogeneous, stationary, and Gaussian. The panel vibration due to any stochastic excitation like TBL pressure fluctuation is obtained by Hambric *et al.* [51], Rocha *et al.* [18], following the convention of Bendat and Piersol [129] and Lin [46], where the panel response is measured in terms of cross power spectral density

matrix at each frequency step. Rocha [134], in her analytical framework, performed subsequent calculation to predict the radiated sound power from the panel into the free field. She followed the work of Wallace [183] and used TBL-excited panel velocity spectrum and radiation resistance of simply supported panel.

The panel displacement and subsequent velocity cross-spectrum is calculated by solving Eq. (4.2.19) in discretized form as expressed in Eq. (4.2.20). For a particular frequency, the plate displacement PSD between i th and j th DOF, $S_{ww,ij}$, is calculated as

$$\begin{bmatrix} S_{ww,11} & \cdots & S_{ww,1n} \\ \vdots & \ddots & \vdots \\ S_{ww,n1} & \cdots & S_{ww,nn} \end{bmatrix} = \begin{bmatrix} H_{11} & \cdots & H_{1n} \\ \vdots & \ddots & \vdots \\ H_{n1} & \cdots & H_{nn} \end{bmatrix} A_i \begin{bmatrix} \Phi_{pp,11} & \cdots & \Phi_{pp,1n} \\ \vdots & \ddots & \vdots \\ \Phi_{pp,n1} & \cdots & \Phi_{pp,nn} \end{bmatrix} A_j \begin{bmatrix} H_{11}^* & \cdots & H_{1n}^* \\ \vdots & \ddots & \vdots \\ H_{n1}^* & \cdots & H_{nn}^* \end{bmatrix}^T \quad (4.3.1)$$

where H_{ij} and $\Phi_{pp,ij}$ are the structural transfer function and TBL pressure cross-power spectrum between i th and j th DOFs. The structural transfer function is estimated using free vibration analysis data obtained from FE analysis performed in ANSYS. As in the present study, only transverse displacements of the plate are considered, the number of DOFs is reduced to the number of finite element (FE) nodes. A_i is the elemental area around the i th node. The displacement PSD matrix, S_{ww} is then transformed into a velocity PSD matrix as

$$[S_{vv}] = \begin{bmatrix} S_{vv,11} & \cdots & S_{vv,1n} \\ \vdots & \ddots & \vdots \\ S_{vv,n1} & \cdots & S_{vv,nn} \end{bmatrix} = \omega^2 \begin{bmatrix} S_{ww,11} & \cdots & S_{uu,1n} \\ \vdots & \ddots & \vdots \\ S_{ww,n1} & \cdots & S_{ww,nn} \end{bmatrix} \quad (4.3.2)$$

4.3.2 Turbulence-Structure Coupling: Frequency Domain; Cholesky's Decomposition

In the present section, a new technique to obtain vibration response is proposed based on the work by Wittig and Sinha [184]. In a seminal work, Wittig and Sinha [184] showed that for any Gaussian random process for which Cross Spectral Density function $G_{\nu\mu}(\omega)$ between two random time processes x_ν and x_μ is available it can be factored into a lower triangular matrix $[L_{\nu\mu}(\omega)]$ and its complex transpose such that

$$[G_{\nu\mu}(\omega)] = [L_{\nu\mu}(\omega)][L_{\nu\mu}^*(\omega)]^T \quad (4.3.3)$$

where $*$ denotes the complex conjugate and $\nu, \mu = 1, 2, \dots, M$ are discrete points.

If one considers a random time series with time interval h having a total number of N points the Fourier transform pair will have a frequency interval of $\frac{1}{Nh}$. Now if a Fourier transform pair exist such that x_ν and X_ν are Fourier transform pair, they can be related by

$$x_p(nh) = \frac{1}{N} \sum_{k=0}^{N-1} X_p(k/Nh) \exp\left(j \frac{2\pi kn}{N}\right) \quad (4.3.4)$$

and

$$X_p\left(k/Nh\right) = \sum_{n=0}^{N-1} x_p(nh) \exp\left(-j \frac{2\pi kn}{N}\right) \quad (4.3.5)$$

The term X_p can then be expressed in the matrix form.

$$\begin{Bmatrix} X_1 \\ X_2 \\ \vdots \\ X_M \end{Bmatrix} = \left(\frac{N}{2h}\right)^{1/2} \begin{pmatrix} L_{11} & 0 & \cdots & 0 \\ L_{21} & L_{22} & \cdots & 0 \\ \vdots & \vdots & \ddots & \vdots \\ L_{M1} & L_{M2} & \cdots & L_{MM} \end{pmatrix} \begin{Bmatrix} \zeta_{1k} \\ \zeta_{2k} \\ \vdots \\ \zeta_{Mk} \end{Bmatrix} \quad (4.3.6)$$

In the present formulation the lower triangular matrix $[L_{ij}]$ is obtained through Cholesky decomposition of the wall-pressure cross-spectrum Φ_{pp} , with ζ_{ik} as independent Gaussian random number set having mean = 0 and variance = 0.5. The vector $\{X_v\}$ can thus be regarded as the random TBL induced pressure fluctuation which can be related to forcing function in the frequency domain $\{F(\omega)\}$ by a suitable mapping matrix $[R]$

$$\{F(\omega)\} = [R]\{X_v\} \quad (4.3.7)$$

Using suitable modal transformation and converting the same into frequency domain, the structural response equation given in Eq. (4.3.7) in the modal domain can be written as

$$\{q(\omega)\} = [H(\omega)]\{F(\omega)\} \quad (4.3.8)$$

where $[H(\omega)]$ is the frequency response function defined by

$$H(\omega) = \frac{\varphi \varphi^T}{\bar{m}(-\omega^2 + 2\xi\omega_n\omega + \omega_n^2)} \quad (4.3.9)$$

with φ being the eigen vector (mode shape) and \bar{m} the modal mass.

The finite element modelling of the structural panel is carried out in ANSYS (V14.5) simulation package to obtain the structural modal parameters. The structural frequency response function (FRF) is prepared with these modal parameters and the FRF is multiplied with the decomposed pressure fluctuations, and the complex panel displacement is estimated as in Eq. (4.3.8), which further yields complex panel velocity.

Subsequently, the modal displacement $q(\omega)$ is transformed into the nodal domain using mode summation procedure and expressed as $d_s(\omega)$.

Once the vibration responses are obtained for all the points on the panel the average quadratic velocities in the frequency domain are calculated as

$$\text{Average Quadratic Velocity } \langle \mathbf{V}^2 \rangle = \frac{\omega^2}{2A} \int_A d_s(\omega) d_s^*(\omega) dA \quad (4.3.10)$$

The average quadratic velocity thus obtained is finally expressed in dB scale referenced to $2.5 \times 10^{-15} \text{ (m/s)}^2$.

A boundary element modelling is used for subsequently calculating radiated sound power, which is discussed in the next Chapter. FRF preparation and coupled modelling are performed using in-house MATLAB simulation. The entire workflow is presented in Figure 4.3.1.

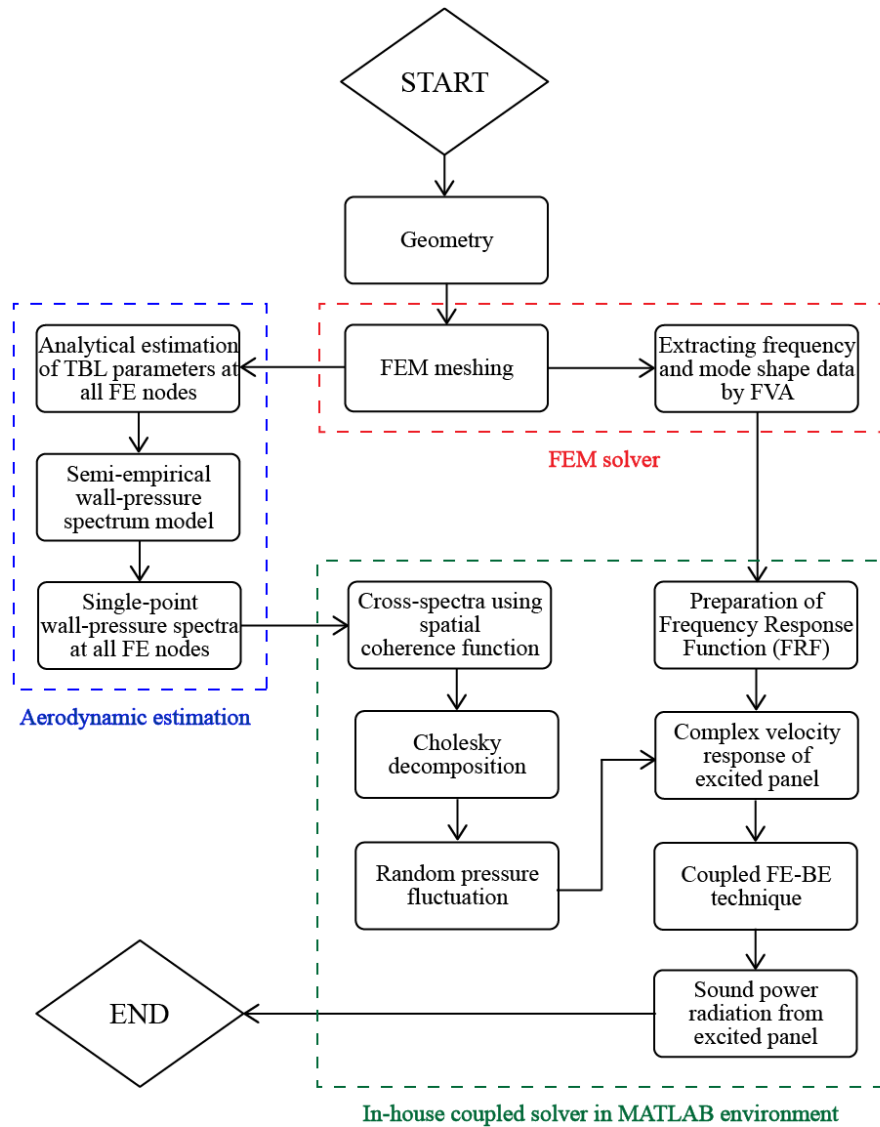


Figure 4.3.1: Flow chart representing TBL induced structural vibration and radiated sound power estimation using Cholesky decomposition and FE-BE coupled solver

4.4 RESULTS AND DISCUSSION

This section presents the results and discussion of the study on TBL-induced flexible panel vibration using numerical finite element (FE) technique and in-house MATLAB coding. The analysis considers three types of flexible panels: stiffened panels, tensioned panels, and orthotropic panels. The study aims to provide a comprehensive understanding of the dynamic response of these panels under the influence of turbulent boundary layers (TBL). The FE technique and MATLAB coding offer a robust platform for simulating TBL-induced vibrations. The study investigates the effects of parameters such as TBL intensity, panel geometry, and material properties on the panel's vibration behaviour.

This study also explores the relationship between TBL characteristics and panel response, providing insights into the underlying mechanisms governing TBL-induced vibrations. The comparison of results among different panel types reveals the influence of structural configurations and material properties on the panel's susceptibility to TBL-induced vibrations. The findings contribute to understanding TBL-induced vibrations and provide a basis for engineering design and optimization strategies in various applications.

4.4.1 Validation Study

A wind tunnel experiment conducted at Purdue University [130] is simulated for validation purpose using suitable RANS configurations, as suggested by the sensitivity study performed in the previous chapter. Unlike Salze *et al.* [13], [93] they considered homogeneous turbulence [130]. Therefore, instead of having multiple points, CFD simulation at a single point located at the edge of the plate at a distance of 0.525 m from the wind tunnel inlet duct is considered to be sufficient for the present validation study.

4.4.1.1 TBL-Pressure Fluctuations: Validation

At first the TBL wall parameters are estimated using CFD simulations, and those parameters are used as inputs to the Smol'yakov and Tkachenko spectrum model [10]. $k - \omega$ turbulence model is used in OpenFOAM solver for both 35.8 m/s and 44.7 m/s flow velocity. The accuracy of the CFD-based \bar{p}^2 values is then compared with the experimental results [130] and presented in Table 7. The RANS-simulated parameters ($U_\tau, \delta, \delta^*, \theta$) are found to be with a desired degree of accuracy and are then used to generate the wall-pressure spectra and used in all subsequent TBL-induced vibration studies.

Table 4.4.1: Accuracy of $k - \omega$ model

U_∞ (m/s)	y^+	\bar{p}^2 (CFD) (Pa ²)	\bar{p}^2 (Exp.) [40](Pa ²)	Error (%)
35.8	100	51.23	51.77	-1.03
44.7	30	120.56	122.73	-1.77

4.4.1.2 TBL-Induced Panel Vibration using Constant Damping and RANS-Spectrum Model: Validation

In this subsection the present developed TBL-induced plate vibration model is validated. For this purpose, the experimental set up used by Han *et al.* [130] is considered. The 0.47 m x 0.37 m steel test plate is clamped at all four edges. Two different flow speeds, 35.8 m/s and 44.7 m/s are considered to estimate TBL-excited plate vibration. Mechanical and physical properties are

presented in Table 4.4.2. RANS-Wall pressure spectrum model is used to estimate the pressure fluctuation.

Table 4.4.2: Model properties

Properties of the flow	
Free stream velocity [m/s]	35.8, 44.7
Convective flow speed [m/s]	23.7,
Displacement thickness [m]	0.0018, 0.0015
Kinematic viscosity [m ² /s]	1.46×10^{-5}
Friction velocity [m/s]	2.29, 3.54
Air density [kg/m ³]	1.225
Properties of the structural panel	
Length [m]	0.47
Width [m]	0.37
Thickness [m]	0.0016
Elastic modulus [GPa]	205
Poisson ratio	0.3
Damping ratio	0.001, 0.0025

Prior to the main validation works, two studies are performed to estimate the plate response due to a) homogeneous and non-homogeneous TBL, b) different finite element meshing, and the results are presented in Figure 4.4.1 and Figure 4.4.2. It is clearly observed that the effect of non-homogeneity is not significant in the present case, and 50 x 35 element meshing is sufficient for accurate plate response prediction. Next, the TBL-excited plate responses are predicted with help of the present FE model and compared with the experimental results [130]. It is worth noting that for 44.7 m/s flow case point velocity PSD is estimated and presented in absolute form (Figure 4.4.3), and for 35.8 m/s flow case the plate velocity PSD averaged over the panel surface is estimated and presented in dB form (Figure 4.4.4). In both the cases the present numerical predictions are found to be in very good agreement with the experimental results, especially the vibrating frequency peaks which are exceedingly important in decision making at the early design stage.

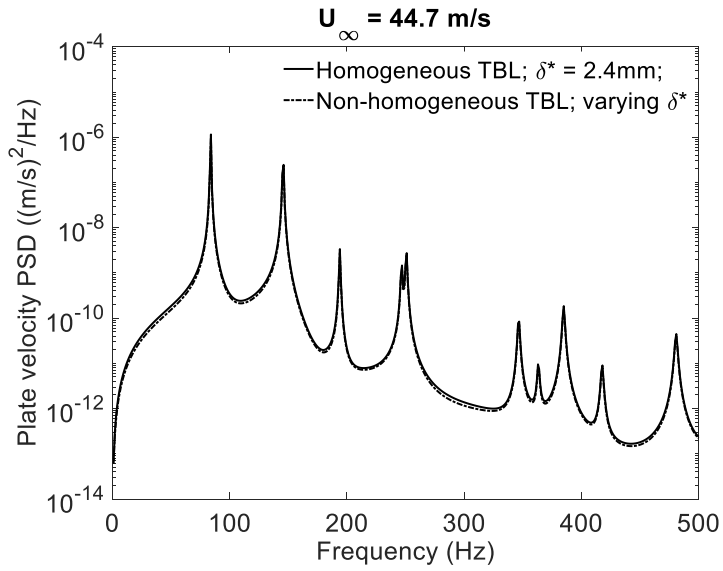


Figure 4.4.1: Effect of homogeneity in turbulence on plate velocity PSD of all side clamped steel plate at $(x, y) \equiv (0.15 \text{ m}, 0.12 \text{ m})$; flow velocity 44.7 m/s

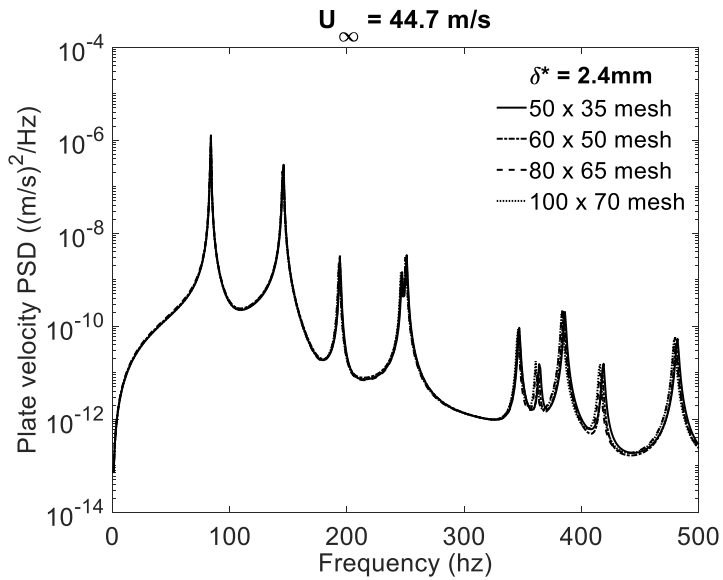


Figure 4.4.2: Grid convergence study for all side clamped steel plate at $(x, y) \equiv (0.15 \text{ m}, 0.12 \text{ m})$; flow velocity 44.7 m/s

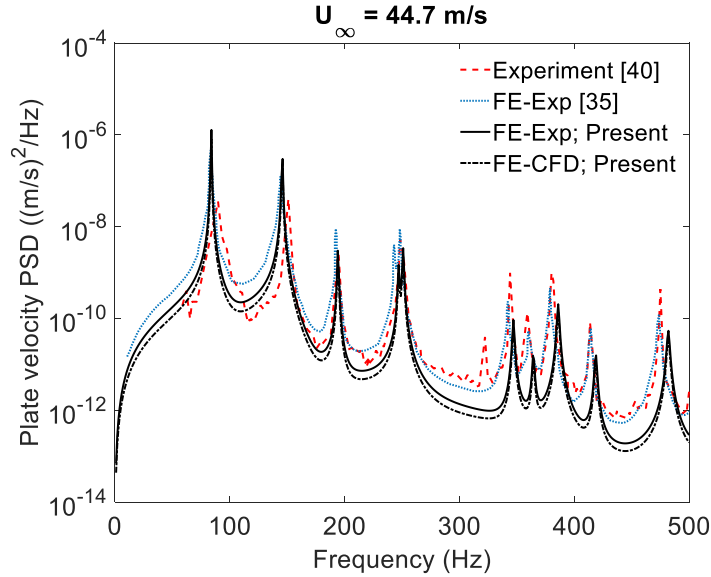


Figure 4.4.3: Numerical and experimental point plate velocity PSD of all side clamped steel plate at $(x, y) \equiv (0.15 \text{ m}, 0.12 \text{ m})$; flow velocity 44.7 m/s

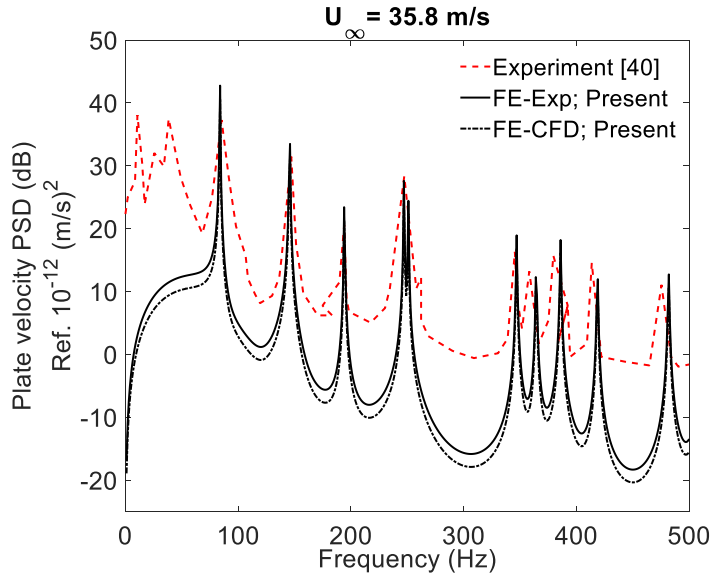


Figure 4.4.4: Numerical and experimental averaged plate velocity PSD of all side clamped steel plate; flow velocity 44.7 m/s

4.4.1.3 TBL-Induced Panel Vibration using Frequency Dependent Damping and Large Eddy Simulation: Validation

A rectangular steel plate with all four sides clamped and placed in an infinite baffle is considered for the validation case of TBL-induced structural vibration. An attempt is made to numerically replicate the experiment conducted at Purdue University by Han *et al.* [130] Dimensions of the steel plates are $L_x = 0.47 \text{ m}$, $L_y = 0.37 \text{ m}$, and thickness = 1.59 mm. The modulus of elasticity is considered 210 GPa. Large Eddy Simulation (LES) technique with artificial inflow turbulence is

used to estimate the pressure fluctuation (refer Figure 3.5.18(a), Chapter 3). Free stream velocity is taken as 44.7 m/s. Next, wall pressure spectrum is calculated by Fourier transform of the LES-obtained pressure fluctuation using Welch’s technique. The spectrum is validated with established spectrum model (refer Figure 3.5.18(b), Chapter 3) and used for subsequent vibration study. 60×40 finite 4-noded iso-parametric SHELL 181 element meshing is adopted to discretize the plate in the ANSYS platform (V14.5). Frequency-dependent structural loss factor is used for the plate. The frequency versus damping ratio (Table 4.4.3) as reported by Han *et al.* [130] is used and is fitted with a 5th degree polynomial, shown in Figure 4.4.5(a). From the fitted polynomial, structural loss factor values are extracted at 1 Hz frequency step, up to 500 Hz. These loss factor values, along with free vibration analysis data, are further used to prepare the structural frequency response function (FRF) or transfer function. TBL cross-power spectra of wall-pressure fluctuations are pre and post multiplied with the transfer function and its complex conjugate, following Eq. (4.3.19). The resulting plate velocity spectrum is calculated at point A (0.15m, 0.12m, refer to Figure 4.3.1) and presented in Figure 4.4.5(b). The predicted plate velocity spectrum agrees quite well with the measured spectrum. Hence the developed model is used for all subsequent estimations of plate velocity response and presented next.

Table 4.4.3: measured structural loss factor (Han *et al.*, 1999)

Frequency (Hz)	81.3	141.9	188.8	240.0	246.2	372.5
Structural loss factor	0.0158	0.0085	0.0075	0.0063	0.0061	0.0030

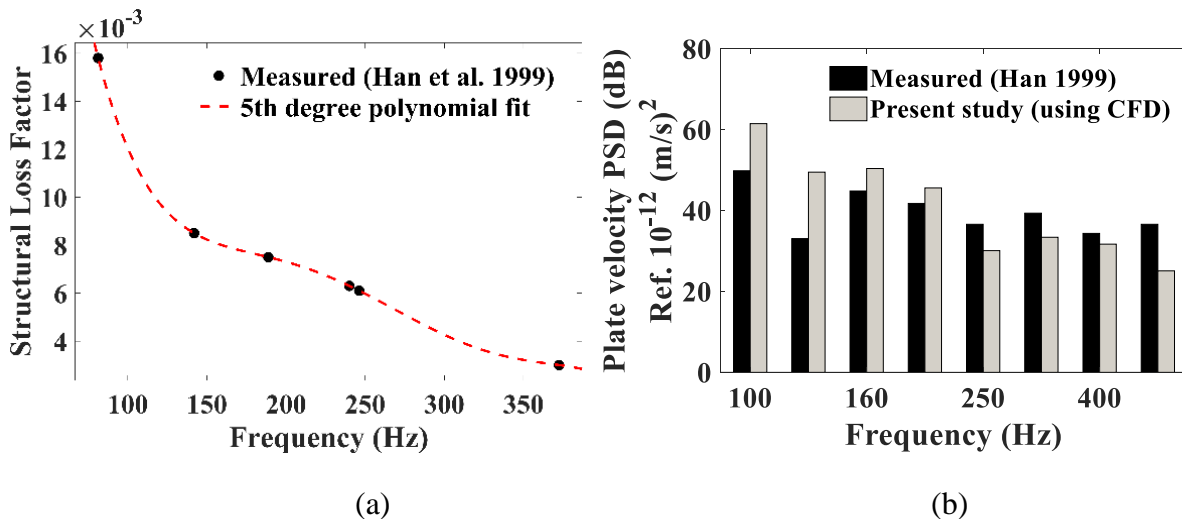


Figure 4.4.5: a) Measured and curve fitted structural loss factor, b) Measured and numerically predicted plate velocity spectrum. Free stream velocity 44.7 m/s; LES.

4.4.2 TBL-Induced Vibration of Single Stiffened Panels

In this subsection stiffeners made of Aluminium are attached to the Aluminium panel. Panel dimensions for all the cases are $0.5 \text{ m} \times 0.35 \text{ m} \times 2 \text{ mm}$. The flow speed considered is 35.8 m/s (other flow parameters are as per Table 4.4.1), and averaged plate velocity PSDs (expressed in dB) are presented for all the cases.

Two different stiffener orientations are studied here. Longitudinal stiffeners (2 in nos.) are placed along stream wise direction. Transverse stiffeners (2 in nos.) are placed along the crossflow direction. All the stiffener positions are at equidistance from the edges (refer. Figure 4.4.6 and Figure 4.4.7). Depth and thickness of the stiffeners are 20 mm and 2 mm , respectively.

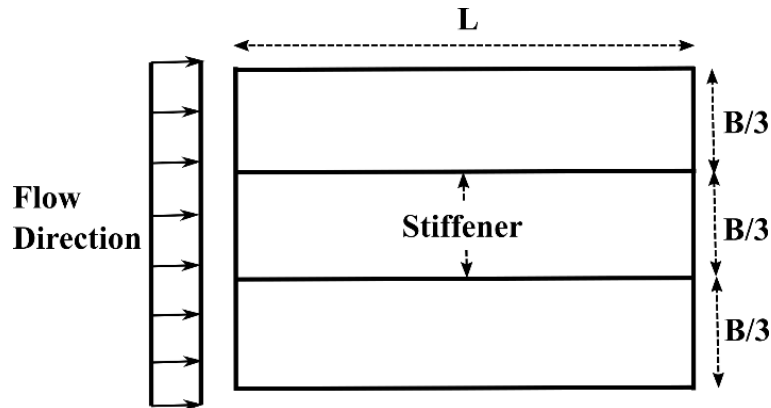


Figure 4.4.6: Schematic of the longitudinally stiffened panel; simply supported $0.5 \text{ m} \times 0.35 \text{ m} \times 2 \text{ mm}$ aluminium plate; $20 \text{ mm} \times 2 \text{ mm}$ stiffeners throughout

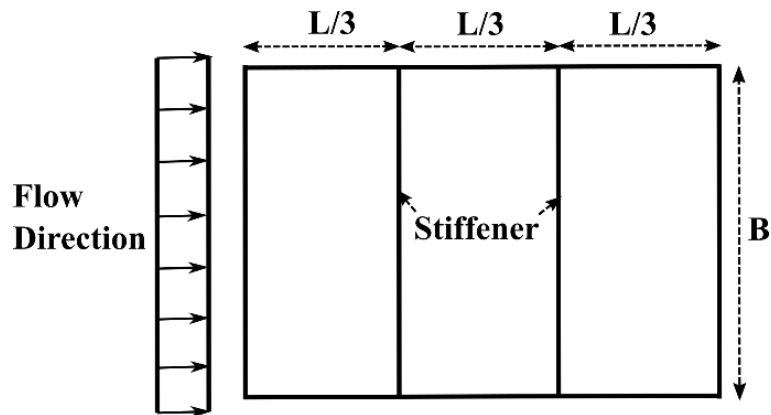


Figure 4.4.7: Schematic of the transversely stiffened panel; simply supported $0.5 \text{ m} \times 0.35 \text{ m} \times 2 \text{ mm}$ aluminium plate; $20 \text{ mm} \times 2 \text{ mm}$ stiffeners throughout

The effects of the stiffener orientation on the energy transmission behaviour are shown in the Figure 4.4.8. It is observed that the transversely stiffened panels exhibit greater energy transmission than the longitudinally stiffened panels for the present TBL-excited panel vibration problem. This can be explained with the frequency and mode shapes of the plate in longitudinally and transversely stiffened condition. The transverse stiffening provides lower stiffness to the

system, thus exhibits higher response. In case of longitudinal stiffened plate, the behaviour is just opposite. The longitudinal stiffeners cause frequencies to shift to the higher side, which confirms the comments on the stiffness previously made.

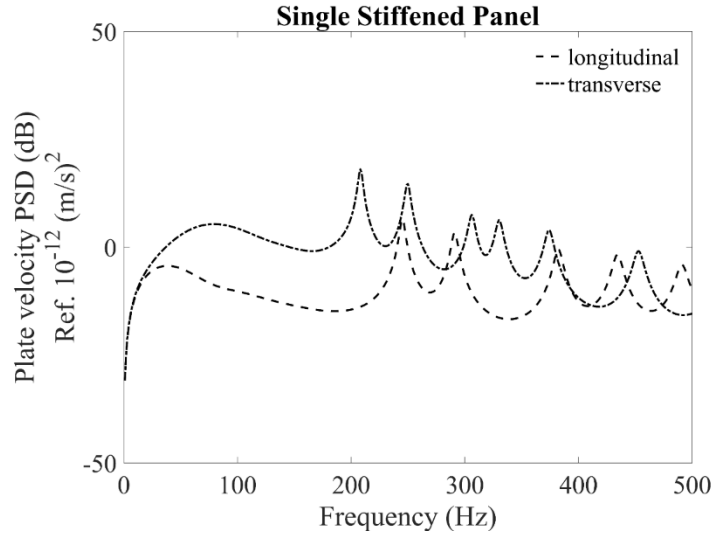


Figure 4.4.8: Averaged plate velocity PSD (in dB) for two stiffener orientations, i) longitudinal and ii) transverse. Simply supported aluminium panel of dimension 0.5m x 0.35 m x 2 mm with aluminium stiffeners of 20 mm x 2 mm throughout. Flow speed 35.8 m/s

4.4.3 TBL-Induced Vibration of Orthotropic Panels

In this segment, simply supported Aluminium and Carbon Fibre Reinforced Polymer (CFRP) panels are considered for different case studies, and TBL-induced vibroacoustic responses are estimated in terms of averaged plate velocity spectra and averaged radiated sound power. The dimensions and CFRP lamina sequences considered are presented in Table 4.4.3. Finite element discretization is performed using a 60×40 mesh, and the damping ratio is considered as 0.0025 for all the cases. Free stream velocity is taken to be 44.7 m/s and used in Smol'yakov and Tkachenko's single-point wall-pressure spectrum model [42]. Different cases considered as:

- Case 1 Aluminium
- Case 2a CFRP Laminated composite with (0/90) lamination sequence
- Case 2b CFRP laminated composite with (0/90/0/90) lamination
- Case 3a CFRP laminated composite with (30/-30) lamination
- Case 3b CFRP laminated composite with (30/-30/30/-30) lamination
- Case 4a CFRP laminated composite with (45/-45) lamination
- Case 4b CFRP laminated composite with (45/-45/45/-45) lamination.

Material properties used to model the plates are as follows:

Aluminium:

Young's modulus (E) = 70 GPa, Poisson's ratio = 0.3, Density (ρ) = 2700 kg/m³

CFRP laminates:

Young's modulus	$E_{11} = 138 \text{ GPa}, E_{22} = E_{33} = 6.9 \text{ GPa}$
Shear modulus	$G_{12} = G_{13} = 4.5 \text{ GPa}, G_{23} = 4.05 \text{ GPa}$
Poisson's ratio	$\nu_{12} = 0.31, \nu_{23} = \nu_{13} = 0.3$
Density	$\rho = 1570 \text{ kg/m}^3$

The frequency and mode shape data for all these cases are presented in Table 4.4.3. TBL induced averaged plate velocity PSD for all these cases are presented in Figure 4.4.9.

Table 4.4.4: Frequency (Hz) and mode numbers for aluminium and different orthotropic laminated composite plates

Case 1	Case 2a	Case 2b	Case 3a	Case 3b	Case 4a	Case 4b
58.43 (1,1)	52.96 (1,1)	58.55 (1,1)	50.11 (1,1)	60.78 (1,1)	55.57 (1,1)	69.75 (1,1)
116.11 (2,1)	87.08 (2,1)	111.13 (2,1)	106.63 (2,1)	137.36 (1,3)	101.46 (2,1)	136.34 (2,1)
176.45 (1,2)	134.63 (1,2)	191.72 (1,2)	109.97 (1,2)	141.10 (2,1)	134.73 (1,2)	181.90 (1,2)
212.52 (3,1)	164.67 (3,1)	220.45 (3,1)	178.80 (2,2)	237.47 (2,2)	167.14 (3,1)	231.14 (3,1)
234.00 (2,2)	165.09 (2,2)	222.08 (2,2)	192.36 (3,1)	256.11 (1,3)	196.64 (2,2)	271.98 (2,2)
330.21 (3,2)	230.01 (3,2)	302.20 (3,2)	207.93 (1,3)	266.01 (3,1)	257.12 (4,1)	357.75 (4,1)
348.00 (4,1)	264.86 (4,1)	376.70 (4,1)	274.61 (3,2)	371.40 (2,3)	265.54 (1,3)	362.99 (1,3)
374.29 (1,3)	307.19 (1,3)	427.30 (1,3)	280.50 (2,3)	376.93 (3,2)	277.02 (3,2)	391.56 (3,2)
431.68 (2,3)	325.76 (4,2)	439.38 (4,2)	314.54 (4,1)	421.43 (1,4)	330.44 (2,3)	464.97 (2,3)
465.45 (4,2)	329.82 (2,3)	447.99 (2,3)	342.81 (1,4)	437.99 (4,1)	372.03 (5,1)	---

The frequency-mode shape table (Table 4.4.4) suggests that the aluminium plate has a higher fundamental frequency than the two-layered laminates. Moreover, as the number of layers increases from two to four for a particular ply case (say, cross-ply Case 2a and Case 2b) the fundamental frequency increases (Case 2a: 52.96 Hz, Case 2b: 58.55 Hz) due to increase in stiffness. This leads to decreased averaged plate velocity PSD at the fundamental mode, making the results presented in Figure 4.4.9 consistent for Case 2 and Case 3. But for Case 4 as the number of layers increase, the averaged plate velocity PSD increases. Antisymmetric laminate sequence-driven extension-twisting and shear-bending coupling (B_{16} and B_{26}), along with distributed TBL cross-spectrum may have played an important role here. In general, 4-layer laminates exhibit greater velocity than that of the isotropic (aluminium) panel, though fundamental frequencies of the 4-layer laminates are higher. In general, antisymmetric laminated panels exhibit greater response than the isotropic aluminium panel. To verify this a separate case with same length, width, and overall thickness as other cases (Case 1 to Case 4b) is considered as symmetric quasi-isotropic

lamina sequence $0/-45^\circ/45^\circ/90^\circ/90^\circ/45^\circ/-45^\circ/0$, which turns out to respond in similar way with the aluminium panel (refer Table 4.4.5).

Table 4.4.5: TBL-induced plate velocity PSD (dB, ref. $10^{-12} \text{ m}^2/\text{s}^2$) at the *first* mode; flow velocity 44.7 m/s

Case 1	Case 2a	Case 2b	Case 3a	Case 3b	Case 4a	Case 4b	Quasi-isotropic
62.61	77.51	67.00	75.79	71.78	67.09	70.55	65.81

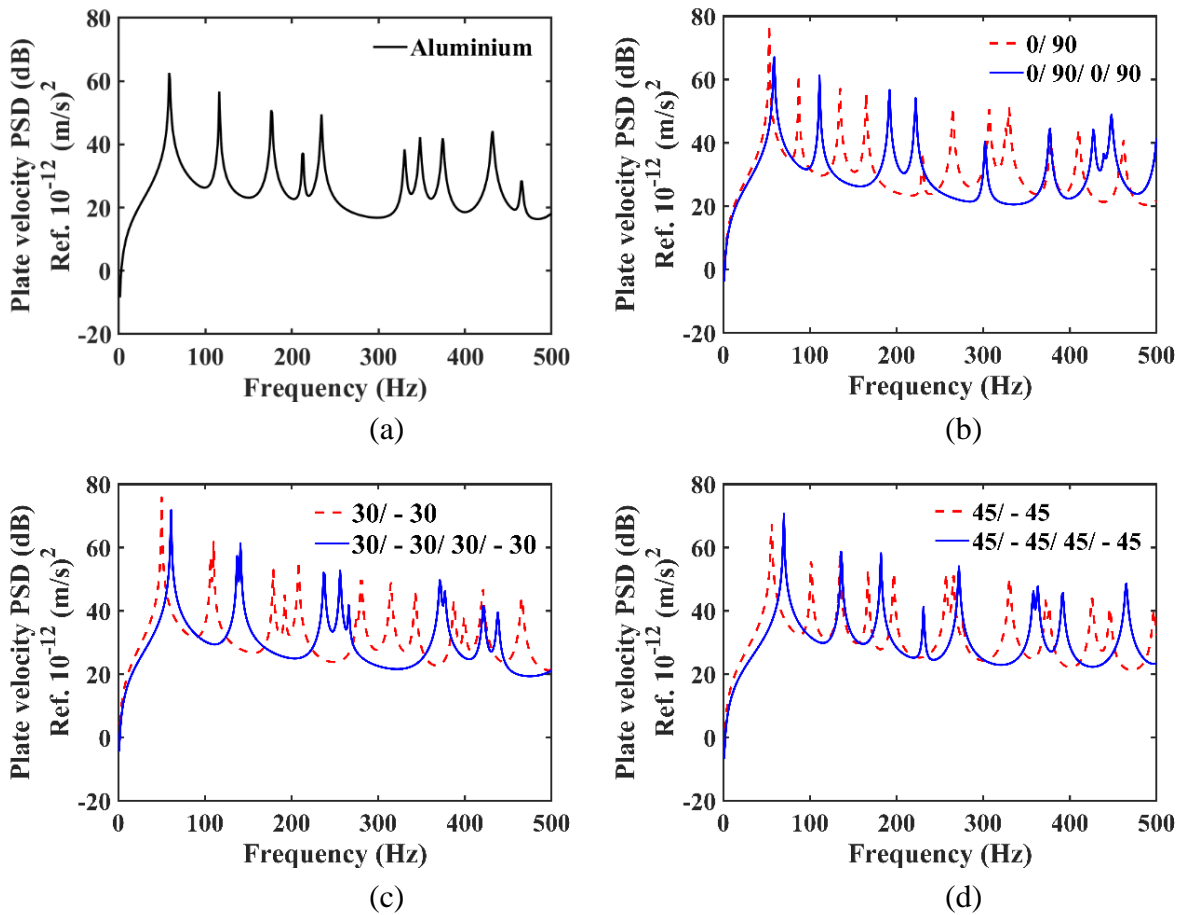


Figure 4.4.9: Averaged plate velocity PSD, all sides simply supported; flow speed 44.7 m/s; a) Case 1, b) Case 2a & 2b, c) Case 3a & 3b, d) Case 4a & 4b

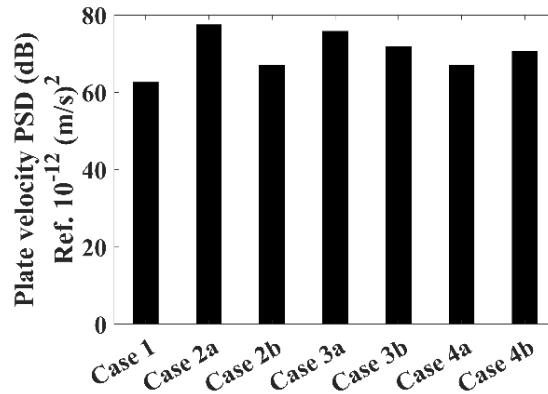


Figure 4.4.10: Comparison of the averaged plate velocity PSD for different lamina sequences; all sides simply supported; flow speed 44.7 m/s

4.4.4 Vibration Response of Isotropic and Orthotropic Panels in Frequency Domain: New Approach

[Results presented in this sub-section are the part of the author's 'In Press' article accepted in the Journal of Applied Mechanics and Technical Physics]

Until now, all the structural panel response calculations have been done in the energy domain and expressed as power spectral densities (PSDs). This approach is particularly useful when the input force is in form of PSD (TBL wall pressure cross-PSD in the present case). However, using Cholesky's technique, it is possible to decompose the wall pressure PSD into frequency dependent pressure fluctuations. This results in response computation in the normal frequency domain and provides complex panel velocity as the response. In this sub-section an attempt is made to use the decomposed pressure fluctuations and estimate panel response in the normal frequency domain under TBL excitation. This velocity response is finally used as input to the finite element-boundary element (FE-BE) approach for calculating radiated sound power, which is detailed in the succeeding chapter.

This sub-section contains results for case studies which are simulated to estimate vibration behaviour of isotropic and orthotropic laminated plates subjected to TBL excitation.

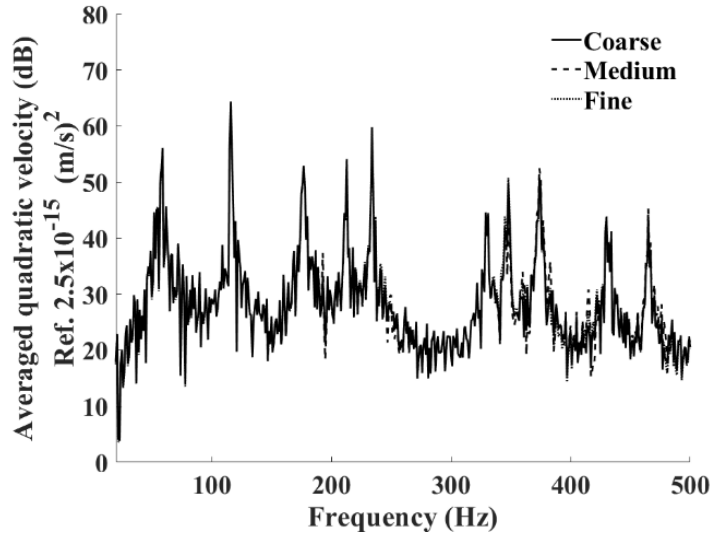


Figure 4.4.11: Sensitivity of averaged quadratic velocity $\langle V^2 \rangle$ (in dB) to grid resolution; simply supported Aluminium plate with $L_x = 0.5\text{m}$, $L_y = 0.35\text{m}$, thickness = 2mm; flow velocity of 44.7 m/s

The developed model is used to obtain the average quadratic velocities for isotropic and antisymmetric orthotropic panels subjected to TBL excitation due to a flow velocity of 44.7 m/s. The panels considered for the analysis are having dimensions L_x as 0.5 m, and L_y as 0.35 m (refer Figure 4.2.1) with 2 mm thickness having simply supported boundary conditions on all along the four edges. The left edge with 0.35 m width is considered as the inlet for the flow (refer Figure 4.2.1). Prior to any further analysis, the sensitivity study is performed to examine the sensitivity of the TBL-induced averaged quadratic velocity to the grid resolution of FE computation domain. This additional sensitivity study is essential as the plate dimension, materials, support conditions are different from the previous study. Aluminium plate is used for this study, and the results are presented in Figure 4.4.11. The results demonstrate negligible sensitivity to the grid resolution of the computation domain (FE), and the resulting error in the pressure fluctuations. Thus, the coarse mesh (60 x 40) is selected for the subsequent studies. Next, seven (7) different cases are considered for the analysis and the geometry and material properties are same as described in the sub section 4.4.3.

Primarily the structural frequencies and the mode shapes for the panels are obtained and they are listed in Table 4.4.4. Thereafter, using suitable modal transformation and converting the same into frequency domain, the structural response equation in the modal domain can be written as

$$\{q(\omega)\} = [H(\omega)]\{F(\omega)\} \quad (4.4.1)$$

where $[H(\omega)]$ is the frequency response function defined by

$$H(\omega) = \frac{\varphi \varphi^T}{\bar{m}(-\omega^2 + 2\xi\omega_n\omega + \omega_n^2)} \quad (4.4.2)$$

with φ being the eigen vector (mode shape) and \bar{m} the modal mass.

Subsequently, the modal displacement $q(\omega)$ is transformed into the nodal domain using mode summation procedure and expressed as $d_s(\omega)$. Once the vibration responses are obtained for all the points on the panel and the average quadratic velocities in the frequency domain are calculated as

$$\text{Average Quadratic Velocity } \langle \mathbf{V}^2 \rangle = \frac{\omega^2}{2A} \int_A \dot{d}_s(\omega) \dot{d}_s^*(\omega) dA \quad (4.4.3)$$

The average quadratic velocity thus obtained is finally expressed in dB scale referenced to $2.5 \times 10^{-15} \text{ (m/s)}^2$.

The average quadratic velocity for the aluminium panel is shown in Figure 4.4.12(a). The average quadratic velocities for the orthotropic panels are presented in Figures 4.4.12(b), 4.4.12(c) and 4.4.12(d).

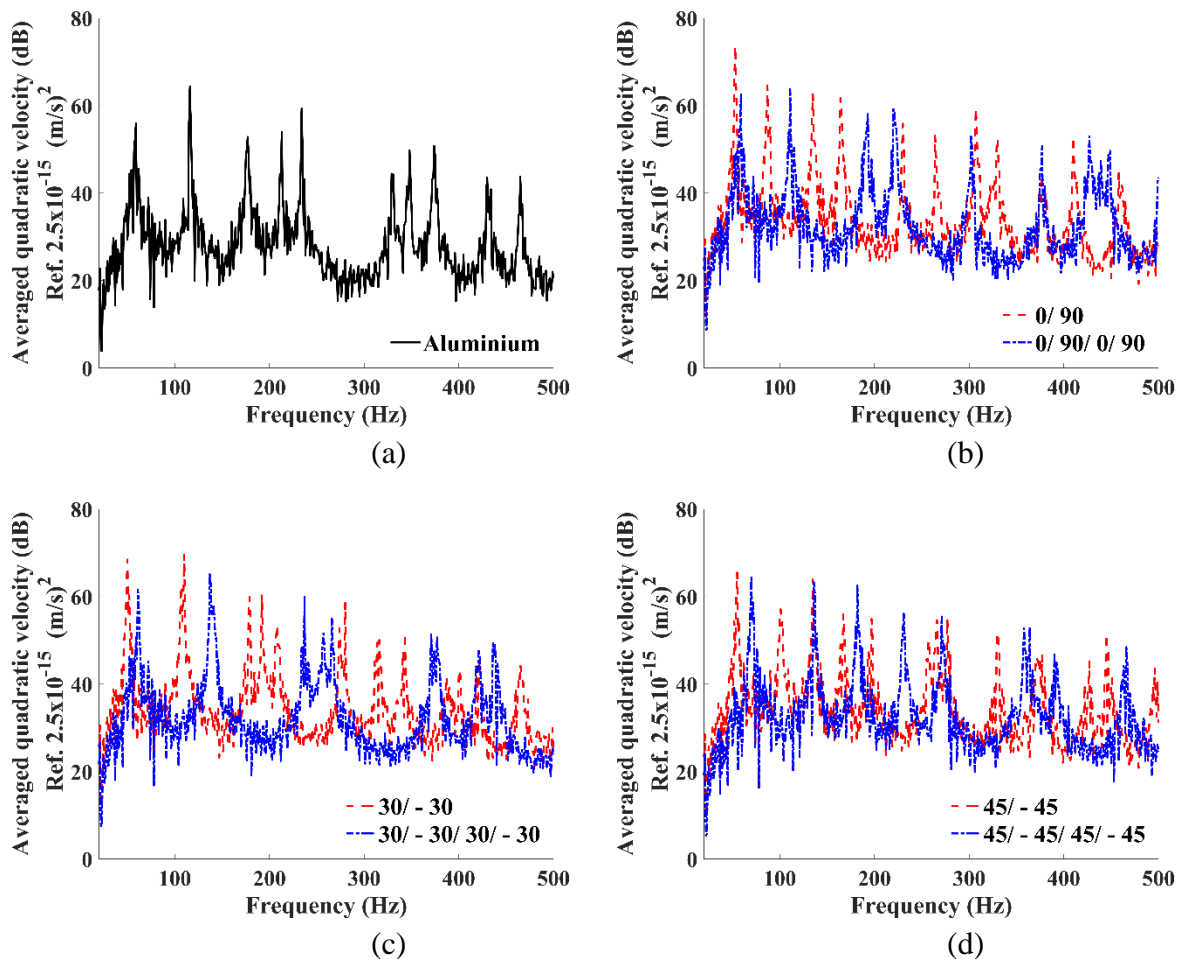


Figure 4.4.12: Averaged quadratic velocity $\langle \mathbf{V}^2 \rangle$ (in dB) of simply supported plate with $L_x = 0.5\text{m}$, $L_y = 0.35\text{ m}$, thickness = 2 mm subjected to a TBL flow with flow velocity of 44.7 m/s (a) Case I; aluminium (b) Case II & III; orthotropic $(0/90)_n$ (c) Case IV & V; orthotropic $(30/-30)_n$ (d) Case VI & VII; orthotropic $(45/-45)_n$

On comparing the results presented in Table 4.4.4 it is seen that the fundamental frequency of the aluminium panel is higher compared to those for 2-layer orthotropic lamina and as a consequence the average quadratic velocity for the aluminium panel is lower than the 2-layer laminates. This behaviour fully complies with the general understanding of mechanics where the response for a stiffer panel is lower. Whereas, for the 4-layer laminated panels the fundamental frequencies even though are higher compared to that of the aluminium panel, the average quadratic velocities for the orthotropic panels are also higher. It is to note that in all the case studies the damping ratio is considered 0.0025. This phenomenon suggests that the response for carbon fiber reinforced laminates is higher when compared with isotropic panels of the same size subjected to TBL loading.

Also, it is very interesting to note here that among the three configurations of 4-layer laminates considered for the present study, (45/-45/45/-45) laminate shows the maximum velocity response when subjected to TBL excitation. A static deflection study is carried out for the (θ /- θ / θ /- θ) angle ply laminates and (0/90/0/90) lamina by applying a distributed 1 N transverse load over the panels and the central deflection of the panel is presented in Table 4.4.6.

Table 4.4.6: Central deflection ($\times 10^{-4}$ m) of 0.5m x 0.35 m simply supported orthotropic plates subjected to a uniformly distributed load of 5.714 N/m²

Case	Case 1	Case 2a	Case 2b	Case 3a	Case3b	Case 4a	Case 4b
Deflection	---	---	0.213	---	0.197	---	0.149

The central deflection for the lamination sequence with $\theta = 45^\circ$ is the least suggesting it to be the stiffest laminate; whereas the TBL-induced dynamic response for the same is the maximum. The extension–bending coupling provided by the antisymmetric laminate sequence along with the cross-spectrum phenomenon of the TBL model plays an important role in this not-so-normal behaviour of response for antisymmetric laminates subjected to TBL excitation.

4.5 CONCLUSION

This study investigates TBL-induced flexible panel vibration using a numerical finite element (FE) technique, in-house MATLAB coding, and a semi-analytical pressure spectrum model. It examines three types of flexible panels: stiffened and orthotropic panels. The results provide insights into the dynamic response of these panels under turbulent boundary layers (TBL). The study reveals the influence of TBL characteristics, panel geometry, and material properties on vibration behaviour. The findings have significant implications for engineering applications, offering guidance for design considerations, mitigation strategies, and performance optimization. However, the limitations and assumptions of the numerical FE technique and semi-analytical pressure

spectrum model require further refinement to account for more complex flow phenomena and structural dynamics. Here are some conclusive remarks for the present study cases:

4.5.1 PSD analysis: Stiffened panel

The study investigates TBL-induced vibrations on flexible panels with longitudinal and transverse stiffeners, providing valuable insights into their dynamic behaviour. It highlights the complex interactions between turbulence, boundary layer effects, and stiffener presence, which significantly affect structural integrity and performance. Stiffeners play a crucial role in altering vibrational response, influencing design and performance.

- Panels with transverse stiffeners transmit more vibrational energy than the panels with longitudinal stiffeners due to the change in overall stiffness, without significantly affecting the mass.
- Transverse stiffeners provide lesser stiff system, resulting in more panel response when subjected to TBL-excitation.
- In case of panels with transverse stiffeners a greater number of modes get excited due to turbulent excitation in the low frequency regime (0 – 500 Hz).

4.5.2 PSD analysis: Orthotropic panel

- It is observed that the orthotropic laminated composite panels have significantly higher panel velocity response in comparison to that of the isotropic panels.
- Although the stiffness of $(45/-45)_n$ increases with the increase in the number of layers as evident from the natural frequencies, the velocity response and the radiated sound power are higher for a higher number of layers. This is in complete contradiction to the other fiber orientation studied in this work.

4.5.3 Frequency analysis (Cholesky decomposition): Orthotropic panel

Some of the salient features as observed from the results can be listed as follows:

- Averaged plate velocity PSD of the aluminium plate is the least among all the cases studied in the present work.
- In general, the 4-ply laminates having a higher stiffness show lower averaged plate velocity PSD as compared to 2-ply laminates with the exception of $(45/-45)_n$ lamina.
- These features as is observed in the present study may help in the choice of the lamination sequence to be used for fuselage skin in vehicular structure at an early design stage, as far as the TBL induced panel response and resulting sound radiation in the free field is concerned.

CHAPTER 5: TBL-EXCITED STRUCTURAL VIBROACOUSTICS

5.1 INTRODUCTION

A detailed mathematical description on TBL induced excitation of flat panels and the resulting structural response behaviour is presented in the earlier chapter. This chapter focuses on the resulting sound radiation into the free field and sound transmission into enclosed cavities from the TBL excited panels. This field encompasses various aspects of structural dynamics, fluid mechanics, and acoustics, and plays a crucial role in the design and optimization of engineering systems where noise control is of utmost importance.

In the study of TBL excited structural vibroacoustics, one key area of interest is the understanding of sound radiation into the free field. When a flexible panel or structure is subjected to turbulent boundary layer excitation, it can act as a source of noise, generating acoustic waves that propagate into the surrounding environment. The prediction and control of sound radiation from these structures are essential in numerous applications, ranging from aerospace and automotive industries to building acoustics.

Another significant aspect of TBL excited structural vibroacoustics is the investigation of sound transmission into enclosed cavities. Enclosed cavities can act as resonators, amplifying and transmitting sound waves. When a flexible panel separates the cavity from the external environment, the interaction between the panel vibrations and the acoustic field inside the cavity becomes crucial. This interaction affects the sound transmission characteristics of the system and has implications for noise reduction and control strategies.

In order to model and analyze TBL excited structural vibroacoustics, various approaches are employed. One commonly used technique is the semi-empirical model, which combines experimental data with theoretical formulations to predict the acoustic behaviour of structures subjected to turbulent boundary layer excitation. This approach allows for a balance between accuracy and computational efficiency.

In numerical simulations and analytical studies, the Cholesky decomposition method can be employed to solve large systems of equations arising from the modelling of TBL excited structural vibroacoustics. This technique enables efficient matrix operations and facilitates the prediction of structural vibrations and acoustic responses.

In the context of sound radiation into free field the radiation resistance matrix approach is frequently used. This method characterizes the interaction between the vibrating structure and the surrounding fluid by representing the structural and acoustic properties in terms of a radiation resistance matrix. This matrix relates the structural vibrations with the acoustic pressures and allows for the estimation of sound radiation and transmission characteristics.

In the present dissertation sound emitted from vibrating panels is studied. Flexible panels come in different forms, and this study specifically considers two types of panels a) stiffened

panels and b) pre-tensioned panels. Stiffened panels are flat plates that incorporate stiffeners in a grid pattern to enhance their bending and torsional stiffness. On the other hand, tensioned panels are pre-tensioned membranes held in place by a frame or support structure. Additionally, the analysis extends to include orthotropic laminated composites, which are widely used in engineering applications due to their enhanced mechanical properties.

In this chapter two different types of vibroacoustic responses from TBL excited panels are studied namely,

1. Sound radiation into the free field
2. Sound transmission into an enclosed cavity

5.2 MATHEMATICAL DESCRIPTION

5.2.1 Free Field Sound Radiation

Key mathematical concepts and numerical approaches to address TBL excited structural vibroacoustics include the finite element method and modal analysis technique, which capture the structural response in terms of displacements, velocities, and accelerations. In order to estimate acoustic wave propagation and radiation of the sound into free field modelling of wave equations is necessary which can be achieved using numerical methods like the radiation resistance matrix (RRM) or boundary element (BE) method. Coupling techniques, such as the radiation impedance method, are employed to incorporate the interaction between the structure and surrounding fluid.

In sound transmission into enclosed cavities, Helmholtz equation along with modal expansion method is employed to capture the coupling between the vibrating structure and the acoustic field. A detailed description of the mathematical processes employed in the present work to estimate acoustic response is presented in the next few sections.

In this sub-section two different approaches are discussed in order to model the free field sound radiation from any TBL-excited vibrating panel.

- 1) Finite Element-Boundary Element (FE-BE) approach
- 2) Finite Element-Radiation Resistance Matrix (FE-RRM) approach

In the FE-BE method, the input TBL pressure PSD spectrum is first decomposed and expressed in the frequency domain, and the structural response in the form of complex panel velocity is obtained in the frequency domain. In contrast, the input for the FE-RRM technique is the wall pressure spectrum, and the output is typically the power spectral density (PSD) of the panel response.

5.2.1.1 Frequency Domain Analysis: Finite Element-Boundary Element (FE-BE) Approach

In the event of free field radiation as the panel vibrates due to the TBL-induced excitation, the structure perturbs the acoustic medium adjacent to it and as a result, the energy is dissipated in the form of sound into the other half-space. The governing equation that mathematically describes the acoustic domain is the three-dimensional Helmholtz equation as shown below,

$$(\nabla^2 + k^2)p = 0 \tag{5.2.1}$$

The solution of this homogenous wave equation $p = (A/r)e^{j(\omega t - kr)}$ (where r is the location vector and A is a real constant) demonstrates that the solution is present everywhere except at $r = 0$. This implies that the wave must originate from a source at $r = 0$. Thus, an acoustic point source is introduced along with the corresponding Green's function transforming the Eq. (5.2.1) to the form of

$$(\nabla^2 + k^2)p^* = -\bar{q}\delta(X - Y) \quad (5.2.2)$$

with \bar{q} being the source strength and $\delta(X - Y)$ being the three-dimensional dirac delta function. The Green's function can be expressed as,

$$g(X, Y) = \frac{e^{-jkr(X, Y)}}{4\pi r(X, Y)} \quad (5.2.3)$$

Using the advantage of the boundary element formulation, the three-dimensional acoustic domain is then reduced to the surface problem over the panel only, by applying Gauss' second identity,

$$\int_v (p\nabla^2 g - g\nabla^2 p)dV = \int_s \left(p \frac{\partial g}{\partial n} - g \frac{\partial p}{\partial n} \right) dS \quad (5.2.4)$$

Since, the panel radiates the sound into an infinite half-space, there is no reflection of the acoustic energy from the infinite boundary. This is ensured by applying the Sommerfeld radiation conditions for the external acoustic problem [185]. Considering the momentum balance between the structure and the adjacent fluid particles, the final boundary integral equation is written as follows;

$$C(X)p(X) - \int_s p(Y) \frac{\partial g(X, Y)}{\partial n} dS(Y) = \int_s j\rho\omega \dot{d}_s(Y)g(X, Y)dS(Y) \quad (5.2.5)$$

where, $p(X)$ is the sound pressure radiated by the panel at a point due to the structural panel vibrating with a velocity $\dot{d}_s(Y)$ and $g(X, Y)$ is the free space Green's function. $C(X)$ is a geometrical constant, which makes it possible to apply the equation for any structure having complex geometry and/or boundary conditions.

The input velocity of the vibrating panel is taken from the study described in the previous Chapter, where the wall pressure spectrum is decomposed using Cholesky's technique and used to solve the fluid-structure interaction (FSI) problem in the frequency domain.

5.2.1.2 Energy Domain Analysis: Radiation Resistance Matrix Approach

The acoustic radiation filter concept can be understood by considering basic structural acoustic concepts. Acoustic wave propagation through a homogeneous elastic fluid such as air is described by the well-known wave equation. In the case of harmonic time dependence, this equation reduces to Helmholtz differential equation, which is as follows,

$$\nabla^2 p(r) + k^2 p(r) = -i\omega\rho_0 q(r) \quad (5.2.6)$$

where $p(r)$ is the complex acoustic pressure amplitude at location r , $k = \omega/c_0$ is the acoustic wave number with c_0 the speed of sound in the medium, ρ_0 is the density of the medium and $q(r)$ is the external sound source. The Helmholtz differential equation can be rewritten in an integral form

which is called the Helmholtz integral equation. In this equation the surface normal velocity $v_n(r_s)$ on a vibrating source with a closed boundary S and the radiated pressure field $p(r)$ are related by

$$\alpha(r)p(r) = \oint_S \left(p(r_s) \frac{\partial G(r, r_s)}{\partial n} + i\omega\rho_0 v_n(r_s) G(r, r_s) \right) dS \quad (5.2.7)$$

where $G(r, r_s)$ is a Green's function. Here r_s defines a boundary point whereas r denotes a field point. The value of $\alpha(r)$ is the free space angle and depends upon where the pressure is evaluated. When the vibrating surface is subjected to a free field condition (Sommerfield radiation condition, or non-reflecting boundary), the Green's function is the solution of the Helmholtz differential equation excited by a Dirac pulse:

$$G(r, r_s) = \frac{e^{-ik|r-r_s|}}{4\pi|r-r_s|} \quad (5.2.8)$$

where $|r-r_s|$ is the distance between a surface point and a field point.

Sound pressure is a quantity which depends on the location of a receiver with respect to the sound source. A more convenient measure for the strength of a sound source is the time averaged sound power. The sound power is directly related to the time averaged sound intensity. In the case of harmonic time dependence, the sound intensity is given by:

$$I(r) = \frac{1}{2} \text{Re}(p(r)v^*(r)) \quad (5.2.9)$$

where $v^*(r)$ denotes the complex conjugate of the acoustic particle velocity.

The sound power generated within a given volume is equal to the surface integral of the normal component of the sound intensity:

$$W = \frac{1}{2} \text{Re} \left(\oint_S p(r_s) v_n^*(r_s) dS \right) \quad (5.2.10)$$

In the present work the analysis is restricted to flat plate like structure. The detail of the structure is given in the subsequent sections. When it is assumed that the structure is placed in a baffle, the Helmholtz integral equation reduces to Rayleigh integral given by,

$$p(r) = \frac{i\omega\rho_0}{2\pi} \int_S v_n(r_s) \frac{e^{-ik|r-r_s|}}{|r-r_s|} dS \quad (5.2.11)$$

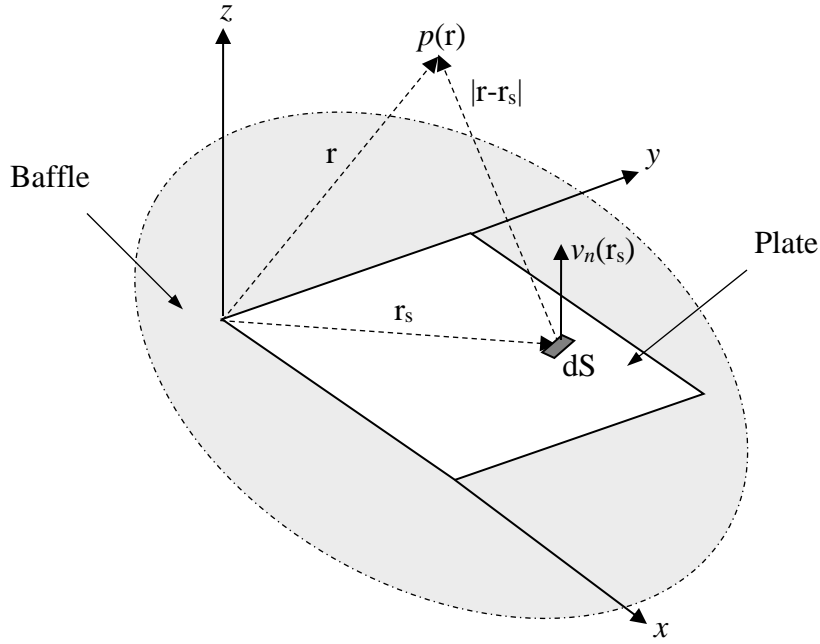


Figure 5.2.1: Geometric Interpretation of Rayleigh Integral

The Rayleigh integral is solved with a primitive numerical scheme. The plate is divided into N rectangular elements of equal size, which are small compared to the acoustic wavelength. It is assumed that the normal velocity is constant across each element. That makes each element behave like an elemental radiator or piston that moves with constant harmonic velocity. For this discretization, the Rayleigh integral can also be written as

$$p_f = Z_f v_n \quad (5.2.12)$$

where p_f is the vector with pressures in a set of field points, v_n is the vector with normal surface velocities of the elemental radiators, and Z_f is a frequency dependent transfer matrix, whose elements are given by,

$$(Z_f)_{ij} = \frac{i\omega\rho_0 S_e}{2\pi} \frac{e^{-ikr_{ij}}}{r_{ij}} \quad (5.2.13)$$

S_e defines the area of the elemental radiator and r_{ij} is the distance between the field point 'i' and a surface point 'j' ($r_{ij} = |\mathbf{r}_i - \mathbf{r}_j|$)

For the same discretization, the expression for the sound power reduces to the summation:

$$W = \frac{S_e}{2} \text{Re}(v_n^H p) \quad (5.2.14)$$

where p is the vector with surface pressures, evaluated at the same points on the surface as v_n .

With the substitution of $p = Zv_n$, the sound power ' W ' can be obtained in terms of discrete number of velocity measurements as

$$W = v_n^H R v_n \quad (5.2.15)$$

In this equation $R = (S_e/2)\text{Re}(Z)$ is the so called radiation resistance matrix, and N is the number of elements. Now, as $v_n^H v_n$ is nothing but the plate velocity spectrum, S_{vv} , which is already obtained and discussed in the previous Chapter, the radiated sound power can be calculated by multiplying the S_{vv} and R matrices at each frequency step. The only care that should be taken is to interpolate the nodal velocity PSD values and assign the averaged values to each element that are subsequently used for radiated sound power (RSP) calculation. Once the RSP matrices are obtained, the diagonal values are used to calculate the overall plate radiated sound power for each frequency.

This matrix R can be written as

$$\mathbf{R} = \frac{\omega^2 \rho_0 S_e^2}{4\pi c_0} \begin{bmatrix} 1 & \frac{\sin(kr_{21})}{kr_{21}} & \dots & \frac{\sin(kr_{1N})}{kr_{1N}} \\ \frac{\sin(kr_{12})}{kr_{12}} & 1 & & \vdots \\ \vdots & & \ddots & \vdots \\ \frac{\sin(kr_{N1})}{kr_{N1}} & \dots & \dots & 1 \end{bmatrix} \quad (5.2.16)$$

If both ‘i’ and ‘j’ are considered to be on the plate surface, the sound power is evaluated on the plate surface, but it may be developed on any surface enclosing the plate. Since, $r_{ij} = r_{ji}$, the radiation resistance matrix R is symmetric and positive definite. The elements of the matrix depend on the properties of the acoustic medium, the frequency, and the geometry of the plate.

5.2.2 Sound Transmission Mechanism into an Enclosed Cavity

In this subsection the underlying mathematics for sound transmission mechanism from a vibrating flexible panel into an enclosed cavity is discussed. Here the discussion is focused to various structural and acoustic configurations that can transfer sound through vibrating modes, altering the acoustic performance and sound quality in enclosed spaces. The double wall configuration is given a special attention as in engineering applications, double panels—two parallel panels divided by an air gap—are frequently utilized to improve sound insulation and lessen noise transmission.

As has been described in the previous Chapter, TBL excitation is modelled as a random input expressed in terms of Power Spectral Density (PSD) function distributed over a spatial domain. Hence, the FSI system that needs to be addressed also should be modelled in the spectral domain. It is in this context, the Frequency Response Function (FRF) of the structure-cavity coupled system has to be developed.

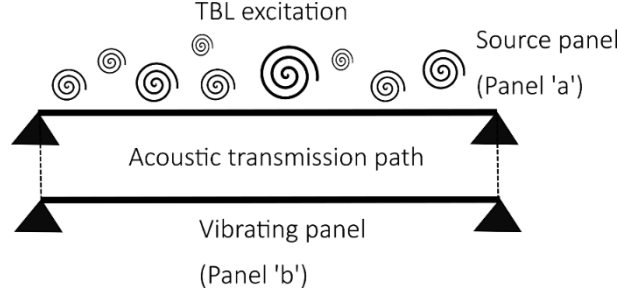


Figure 5.2.2: Schematic of TBL-induced vibroacoustic problem through double wall panel

Considering the schematic presented in Figure 5.2.2 for a system consisting of multiple panel and cavity excited by external TBL excitation the general governing finite element equations for the respective panels take the form

$$M\ddot{x}_a + Kx_a = F_{tbl} - P_g \quad (5.2.17)$$

$$M\ddot{x}_b + Kx_b = P_g \quad (5.2.18)$$

$M_a, K_a, x_a, \ddot{x}_a$: mass matrix, stiffness matrix, displacement and acceleration of the panel 'a'

$M_b, K_b, x_b, \ddot{x}_b$: mass matrix, stiffness matrix, displacement and acceleration of the panel 'b'

F_{tbl} is the TBL excitation on the outer panel (panel 'a') and the P_g is the cavity pressure.

The acoustic gap pressure is estimated by solving the following Helmholtz's equation

$$\nabla^2 P_g - \frac{1}{c_0^2} \frac{\partial^2 P_g}{\partial t^2} = 0 \quad (5.2.19)$$

$$\text{with constraints: } \frac{\partial P_g}{\partial \mathbf{n}} = \begin{cases} \rho \ddot{w}_a & \text{on panel 'a'} \\ -\rho \ddot{w}_b & \text{on panel 'b'} \\ 0 & \text{on the rigid wall} \end{cases}$$

where ρ is the cavity fluid density and \mathbf{n} is the normal direction directed outwards. w_a and w_b are the *normal* structural displacements.

Primarily an undamped free vibration analysis for each plate is carried out separately and the Eigen vectors are obtained. Next, by introducing constant modal loss factor $\zeta_{a,i}$ and $\zeta_{b,i}$ for panel 'a' and panel 'b', and considering $q_{a,i}$ and $q_{b,i}$ to be the modal coordinates of the panels 'a' and 'b', respectively, the dynamic equilibrium equations for panel 'a' and panel 'b' are obtained as follows [186]

$$\ddot{q}_{a,i} + 2\zeta_{a,i}\omega_{a,i}\dot{q}_{a,i} + \omega_{a,i}^2 q_{a,i} = \frac{1}{m_{a,i}} \{ \tilde{F} \varphi_{a,i}(x_e, y_e) - \iint P_g \varphi_{a,i} dx dy \} \quad (5.2.20)$$

and

$$\ddot{q}_{b,j} + 2\zeta_{b,j}\omega_{b,j}\dot{q}_{b,j} + \omega_{b,j}^2 q_{b,j} = \frac{1}{m_{b,j}} \{ \iint P_g \varphi_{b,j} dx dy \} \quad (5.2.21)$$

where $\omega_a, \omega_b, m_a, m_b, \varphi_a$ and φ_b are modal frequency, modal mass and mode shape for panel 'a' and panel 'b', respectively.

Subsequently on decomposition of P_g described with the help of acoustic mode shapes $\varphi_{g,k}$ as $P_g = \sum_k \varphi_{g,k} p_{g,k}(t)$ and putting in Eq. (5.2.17) one obtains

$$\nabla^2 \varphi_{g,k} - \left(\frac{\omega_{g,k}}{c_0}\right)^2 \varphi_{g,k} = 0 \quad (5.2.22)$$

with

$$\frac{1}{V_g} \int_{V_g} \varphi_{g,k} \varphi_{g,l} dv = \begin{cases} 0 & k \neq l \\ m_{g,kk} & k = l \end{cases} \quad (5.2.23)$$

where $p_{g,k}$, $\psi_{g,k}$ and $m_{g,kk}$ are the pressure, frequency and mass in the modal domain.

Green's theorem is used for two scalar functions P_g and φ_g smooth and non-singular in domain V_g enclosed by surface S_a and S_b and expressed as Eq. (5.2.24)

$$\int_{V_g} (P_g \nabla^2 \varphi_g - \varphi_g \nabla^2 P_g) dV = \int_{S_a+S_b} \left(P_g \frac{\partial \varphi_g}{\partial \mathbf{n}} - \varphi_g \frac{\partial P_g}{\partial \mathbf{n}} \right) ds \quad (5.2.24)$$

Using Eq. (5.2.19) and Eq. (5.2.22), for k th mode of the air gap, Eq. (5.2.24) is written as,

$$\int_{V_g} \left[-\varphi_{g,k} p_{g,k}(t) \left(\frac{\omega_{g,k}}{c_0}\right)^2 \varphi_{g,k} - \varphi_{g,k} \frac{1}{c_0^2} \varphi_{g,k} \ddot{p}_{g,k}(t) \right] dV = \int_{S_a} \varphi_{g,k} \rho \dot{w}_a ds + \int_{S_b} \varphi_{g,k} \rho \dot{w}_b ds \quad (5.2.25)$$

Using Eq. (5.2.3)

$$\frac{m_{g,kk} V_g}{c_0^2} [\ddot{p}_{g,k} + \omega_{g,k}^2 p_{g,k}] = \rho \left[S_a \sum_i \int_{S_a} \varphi_{g,k} \varphi_{a,i} ds \ddot{q}_{a,i}(t) - S_b \sum_j \int_{S_b} \varphi_{g,k} \varphi_{b,j} ds \ddot{q}_{b,j}(t) \right] \quad (5.2.26)$$

Modal coupling coefficients may be expressed as follows

$$L_{k,i}^{ag} = \frac{1}{S_b} \int_{S_a} \varphi_{g,k} \varphi_{a,i} ds \quad \text{and} \quad L_{k,j}^{bg} = \frac{1}{S_b} \int_{S_b} \varphi_{g,k} \varphi_{b,j} ds$$

Introducing modal loss factor term, Eq. (5.2.26) is expressed as Eq. (5.2.27)

$$\ddot{p}_{g,k} + 2\zeta_{g,k} \omega_{g,k} \dot{p}_{g,k} + \omega_{g,k}^2 p_{g,k} = \frac{\rho c_0^2}{m_{g,kk} V_g} \left[S_a \sum_i L_{k,i}^{ag} \ddot{q}_{b,j} - S_b \sum_j L_{k,j}^{bg} \ddot{q}_{b,j} \right] \quad (5.2.27)$$

where ζ_g is modal loss factor of the gap cavity, ρ is the density of the fluid (air in the present case), c_0 is the sound speed in the air, $L_{k,i}^{ag}$ and $L_{k,j}^{bg}$ are the modal coefficients which couples the k th acoustic mode with the i th panel 'a' mode and j th panel 'b' mode, respectively.

It is to be noted that all the subsequent coupled systems (subsections 5.2.2.1, 5.2.2.2, and 5.2.2.3) are modelled and solved with the help of FEA technique using in-house MATLAB codes.

In the next few subsections, a detailed numerical discussion on several different panel-enclosure configurations is presented.

5.2.2.1 Panel-Enclosure System; Two Equation Problem

The enclosed cavity considered in the present system consists of a single-leaf panel as one of the cavity walls whereas, all the other walls are considered rigid. The flexible structural panels are modelled using 4-node isoparametric plate elements with *five* degrees of freedom per node. The acoustic cavity is modelled using 8-node octahedral brick element with pressure DOF. As is

obvious, for the present system one would be interested to obtain responses from the vibrating panel in the form of structural displacement or its derivatives and from the enclosed cavity in the form of acoustic pressure. Hence, the induced response of the panel-cavity system due to the external force can be expressed following the Eq. (4.2.30) of Chapter 4 as,

$$\mathbf{Y}(\omega) = \mathbf{H}(\omega)\mathbf{X}(\omega) \quad (5.2.28)$$

Here, $\mathbf{H}(\omega)$ and $\mathbf{X}(\omega)$ are the frequency-dependent transfer function and forcing function, respectively.

$$\mathbf{H}(\omega) = \begin{bmatrix} \mathbf{H}_{11} & \mathbf{H}_{12} \\ \mathbf{H}_{21} & \mathbf{H}_{22} \end{bmatrix}^{-1} \quad (5.2.29)$$

Designation: 1-panel; 2-enclosure

The uncoupled and coupled transfer functions (\mathbf{H}_{ij}) are derived from the dynamic equations of the panel and cavity in modal domain, as detailed in Eq. (5.2.20) and Eq. (5.2.27) [186].

Subscripts, $i = j$ represent auto coupling, and $i \neq j$ represent cross-coupling. The TBL forces act on the panel only, and hence the force vector can be written as,

$$\mathbf{X}(\omega) = \begin{Bmatrix} \mathbf{F}_{tbl} \\ 0 \end{Bmatrix} \quad (5.2.30)$$

On assembling Eq. (5.2.24) and Eq. (5.2.25) as described in Eq. (5.2.23) and rearranging, one obtains the response function of the panel (\mathbf{H}_w) and the enclosed cavity (\mathbf{H}_e) for the coupled system as,

$$\mathbf{H}_w = (\mathbf{H}_{11} - \mathbf{H}_{12}\mathbf{H}_{22}^{-1}\mathbf{H}_{21})^{-1} \quad (5.2.31)$$

and

$$\mathbf{H}_e = -\mathbf{H}_{22}^{-1}\mathbf{H}_{21}\mathbf{H}_w \quad (5.2.32)$$

The modal response functions are so arranged that they can be solved for any number of modes for panel 'a' and cavity. Once, the response functions are obtained for the coupled system, the panel displacement PSD (S_{ww}) and the enclosure pressure PSD (S_{ee}) can be calculated as,

$$\mathbf{S}_{ww}(\omega) = \mathbf{H}_w^*(\omega)\mathbf{S}_{tbl}(\omega)\mathbf{H}_w^T(\omega) \quad (5.2.33)$$

$$\mathbf{S}_{ee}(\omega) = \mathbf{H}_e^*(\omega)\mathbf{S}_{tbl}(\omega)\mathbf{H}_e^T(\omega) \quad (5.2.34)$$

Here, $\mathbf{S}_{tbl}(\omega)$ is the TBL cross PSD of the force, calculated as,

$$\mathbf{S}_{tbl}(\omega) = A_\mu\Phi_{pp}A_\nu \quad (5.2.35)$$

A_μ and A_ν are the elemental areas around the nodes μ and ν , respectively, and Φ_{pp} is the cross PSD between these two points. Φ_{pp} is calculated as described in Section 3.6, Chapter 3.

5.2.2.2 Panel-Cavity-Panel System; Three Equation Problem

In order to replicate a realistic outer skin-cavity-trim panel configuration typical for an aircraft or high-end automobile skin panel a system is developed in the present section. The outer panel, i.e., Panel 'a' is considered either as an unstiffened or stiffened panel whereas, the Panel 'b' is modelled as an unstiffened one. The other side panels of the configuration are considered rigid. Unlike the

1-D beam like elements used by Zhou *et al.* [187] to model the stiffeners, in the present work *four*-node plate elements are used to model the stiffeners which are placed orthogonal to the plane of the plate and necessary transformation is used to form the global stiffness and mass matrix for the outer panel, as described in the previous Chapter.

Combining Eqs. (5.2.20), (5.2.21) and (5.2.27) with harmonic forcing assumption, yields the equation governing the coupled system in the modal domain

$$\begin{bmatrix} \mathbf{H}_{11} & 0 & \mathbf{H}_{13} \\ 0 & \mathbf{H}_{22} & \mathbf{H}_{23} \\ \mathbf{H}_{31} & \mathbf{H}_{32} & \mathbf{H}_{33} \end{bmatrix} \begin{Bmatrix} \mathbf{r}_a \\ \mathbf{r}_b \\ \mathbf{r}_c \end{Bmatrix} = \begin{Bmatrix} \mathbf{F}_{tbl} \\ 0 \\ 0 \end{Bmatrix} \quad (5.2.36)$$

\mathbf{F}_{tbl} is the TBL excitation applied on the primary panel ‘a’. \mathbf{r}_a , \mathbf{r}_b and \mathbf{r}_c are the modal response of panel ‘a’, panel ‘b’ and the cavity, respectively.

\mathbf{H}_{11} – modal dynamic stiffness of panel ‘a’.

\mathbf{H}_{22} – modal dynamic stiffness of panel ‘b’.

\mathbf{H}_{13} and \mathbf{H}_{23} – coupling coefficients taking account of acoustic pressure of the gap cavity on the structural response on panel ‘a’ and panel ‘b’, respectively.

\mathbf{H}_{31} and \mathbf{H}_{32} – coupling coefficients taking account of structural response on panel ‘a’ and panel ‘b’ on the acoustic pressure of the gap cavity, respectively.

\mathbf{H}_{33} – modal dynamic stiffness of the gap cavity.

On rearranging Eq. (5.2.36) one obtains,

$$\begin{Bmatrix} \mathbf{r}_a \\ \mathbf{r}_b \\ \mathbf{r}_c \end{Bmatrix} = \begin{bmatrix} \mathbf{H}_{11} & 0 & \mathbf{H}_{13} \\ 0 & \mathbf{H}_{22} & \mathbf{H}_{23} \\ \mathbf{H}_{31} & \mathbf{H}_{32} & \mathbf{H}_{33} \end{bmatrix}^{-1} \begin{Bmatrix} \mathbf{F}_{tbl} \\ 0 \\ 0 \end{Bmatrix} \quad (5.2.37)$$

and rearranging, one obtains

$$\mathbf{H}_{11}\mathbf{H}_{w,a} + \mathbf{H}_{13}\mathbf{H}_p = \mathbf{I} \quad (5.2.38)$$

$$\mathbf{H}_{22}\mathbf{H}_{w,b} + \mathbf{H}_{23}\mathbf{H}_p = 0 \quad (5.2.39)$$

$$\mathbf{H}_{31}\mathbf{H}_{w,a} + \mathbf{H}_{32}\mathbf{H}_{w,b} + \mathbf{H}_{33}\mathbf{H}_p = 0 \quad (5.2.40)$$

where the response function of the panels ($\mathbf{H}_{w,a}$ and $\mathbf{H}_{w,b}$) and the cavity (\mathbf{H}_p) for the coupled system can be estimated in the following way:

$$\mathbf{H}_{w,a} = \mathbf{H}_{11}^{-1}(\mathbf{I} - \mathbf{H}_{13}\mathbf{H}_p) \quad (5.2.41)$$

$$\mathbf{H}_{w,b} = -\mathbf{H}_{22}^{-1}\mathbf{H}_{23}\mathbf{H}_p \quad (5.2.42)$$

On putting the values of $\mathbf{H}_{w,a}$ and $\mathbf{H}_{w,b}$ in the Eq. (5.2.40) it takes the form,

$$\mathbf{H}_{31}\mathbf{H}_{11}^{-1}(\mathbf{I} - \mathbf{H}_{13}\mathbf{H}_p) - \mathbf{H}_{32}\mathbf{H}_{22}^{-1}\mathbf{H}_{23}\mathbf{H}_p + \mathbf{H}_{33}\mathbf{H}_p = 0 \quad (5.2.43)$$

At this stage \mathbf{H}_p is taken out from the Eq. (5.2.43) and the final form of \mathbf{H}_p is written as

$$\mathbf{H}_p = (\mathbf{H}_{31}\mathbf{H}_{11}^{-1}\mathbf{H}_{13} + \mathbf{H}_{32}\mathbf{H}_{22}^{-1}\mathbf{H}_{23} - \mathbf{H}_{33})^{-1}\mathbf{H}_{31}\mathbf{H}_{11}^{-1} \quad (5.2.44)$$

The modal response functions are so arranged that they can be solved for any number of modes for panel ‘a’, panel ‘b’ and the cavity. Once, the response functions are obtained in a coupled

system, the panel displacement PSD ($\mathbf{S}_{ww,a}$ & $\mathbf{S}_{ww,b}$) and cavity pressure PSD (\mathbf{S}_{pp}) can be calculated as,

$$\mathbf{S}_{ww,a}(\omega) = \mathbf{H}_{w,a}^*(\omega)\mathbf{S}_{tbl}(\omega)\mathbf{H}_{w,a}^T(\omega) \quad (5.2.45)$$

$$\mathbf{S}_{ww,b}(\omega) = \mathbf{H}_{w,b}^*(\omega)\mathbf{S}_{tbl}(\omega)\mathbf{H}_{w,b}^T(\omega) \quad (5.2.46)$$

$$\mathbf{S}_{pp}(\omega) = \mathbf{H}_p^*(\omega)\mathbf{S}_{tbl}(\omega)\mathbf{H}_p^T(\omega) \quad (5.2.47)$$

Here, $\mathbf{S}_{tbl}(\omega)$ is the cross PSD of the turbulent force, calculated as Eq. (5.2.35). Eq. (5.2.45), Eq. (5.2.46) and Eq. (5.2.47) can be used to estimate outer panel (panel ‘a’) response, vibrating panel (panel ‘b’) response and the cavity pressure, respectively. The displacement PSD of the panel ‘a’, $\mathbf{S}_{ww,a}$ can be computed using Eq. (5.2.45) and transforming the same into velocity PSD, $\mathbf{S}_{vv,b}$ as, $\mathbf{S}_{vv,a} = \omega^2\mathbf{S}_{ww,a}$ (5.2.48)

Similarly, the velocity PSD, $\mathbf{S}_{vv,b}$ for panel ‘b’ can be obtained from Eq. (5.2.46) as,

$$\mathbf{S}_{vv,b} = \omega^2\mathbf{S}_{ww,b} \quad (5.2.49)$$

Once the complete velocity PSD matrix is estimated, velocity PSD value at any point or averaged over the plate surface can be easily determined. The cavity pressure PSD, \mathbf{S}_{pp} is computed using Eq. (5.2.47).

5.2.2.3 Panel-Cavity-Panel-Enclosure System; Four Equation Problem

This part of the mathematical description is an extension of the ‘panel-enclosure’ and ‘panel-gap-panel’ system, but with more complex fully coupled behaviour accounting the TBL excitation effect on an acoustic enclosure backed by double-walled panel system that are separated by a gap. A schematic of the problem is presented in Figure 5.2.3.

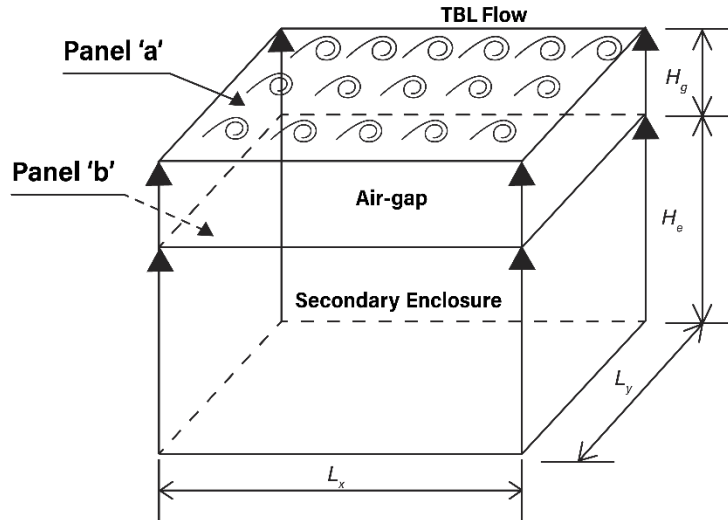


Figure 5.2.3: Schematic of a double wall panel configuration backed by an enclosed cavity

The structural panels and acoustic gap/enclosures are modelled as described in earlier sections. The induced response of the panel-gap-panel-enclosure system due to the external force can be expressed following as Eq. (5.2.28)

$$\text{where } \mathbf{H}(\omega) = \begin{bmatrix} \mathbf{H}_{11} & 0 & \mathbf{H}_{13} & 0 \\ 0 & \mathbf{H}_{22} & \mathbf{H}_{23} & \mathbf{H}_{24} \\ \mathbf{H}_{31} & \mathbf{H}_{32} & \mathbf{H}_{33} & 0 \\ 0 & \mathbf{H}_{42} & 0 & \mathbf{H}_{44} \end{bmatrix}^{-1} \quad (5.2.50)$$

Designation: 1-skin panel (panel ‘a’); 2-trim panel (panel ‘b’); 3-gap; 4-enclosure

The transfer functions (\mathbf{H}_{ij}) are derived from the dynamic equations of the two panels, gap and enclosure in modal domain, as detailed in Eq. (5.2.20), Eq. (5.2.21) and Eq. (5.2.27).

Subscripts, $i = j$ represent auto coupling, and $i \neq j$ represent cross-coupling. As there is no direct connection between a) the two panels, b) skin panel-enclosure, and c) gap-enclosure, $\mathbf{H}_{12} = \mathbf{H}_{21} = \mathbf{H}_{14} = \mathbf{H}_{41} = \mathbf{H}_{34} = \mathbf{H}_{43} = 0$. The TBL forces act on the skin panel only, and hence the force vector can be written as,

$$\mathbf{X}(\omega) = \begin{Bmatrix} \mathbf{F}_{tbl} \\ 0 \\ 0 \\ 0 \end{Bmatrix} \quad (5.2.51)$$

On putting Eq. (5.2.50) and Eq. (5.2.51) in Eq. (5.2.28) and rearranging, one can obtain the response function of the panels ($\mathbf{H}_{w,a}$ and $\mathbf{H}_{w,b}$) and the cavity (\mathbf{H}_p) for the fully coupled system. But, there are two challenges:-

a) Decoupling of the equations should be performed in such a way that initially only the coefficients of the \mathbf{H}_{ii} form is inverted, as the other coefficients are not necessarily square matrices to keep the generic fabric of the entire matrix system intact. As the solution proceeds, one can find combinations of matrix coefficients arranged together in square forms which can then be inverted.

b) Multiplication of matrix coefficients are to be done keeping their dimensions in mind. As all the four systems (two panels, two cavities) may have different number of modes accounted, violation of this rule otherwise will lead to further errors.

Finally, the solution developed in the present model takes the following form:

$$\mathbf{H}_{w,b} = -\left[\mathbf{H}_{22}^{-1} \mathbf{H}_{23} \mathbf{H}_{33}^{-1} \mathbf{H}_{32} - \left(\mathbf{I} - \mathbf{H}_{22}^{-1} \mathbf{H}_{24} \mathbf{H}_{44}^{-1} \mathbf{H}_{42} \right) \left(\mathbf{I} - \mathbf{H}_{33}^{-1} \mathbf{H}_{31} \mathbf{H}_{11}^{-1} \mathbf{H}_{13} \right) \right]^{-1} \mathbf{H}_{22}^{-1} \mathbf{H}_{23} \mathbf{H}_{33}^{-1} \mathbf{H}_{31} \mathbf{H}_{11}^{-1} \quad (5.2.52)$$

$$\mathbf{H}_g = \left(\mathbf{I} - \mathbf{H}_{33}^{-1} \mathbf{H}_{31} \mathbf{H}_{11}^{-1} \mathbf{H}_{13} \right)^{-1} \mathbf{H}_{33}^{-1} \left(\mathbf{H}_{31} \mathbf{H}_{11}^{-1} + \mathbf{H}_{32} \mathbf{H}_{w,b} \right) \quad (5.2.53)$$

$$\mathbf{H}_e = -\mathbf{H}_{44}^{-1} \mathbf{H}_{42} \mathbf{H}_{w,b} \quad (5.2.54)$$

$$\mathbf{H}_{w,a} = \mathbf{H}_{11}^{-1} \left(\mathbf{I} - \mathbf{H}_{13} \mathbf{H}_g \right) \quad (5.2.55)$$

The present formulation works perfectly all right when the number modes of panel ‘b’ and gap are equal. If these two are required to be different, the solution can be obtained by taking other possible mathematical rearrangements as well. In the coupled system, the panel displacement

PSDs ($\mathbf{S}_{ww,a}$ & $\mathbf{S}_{ww,b}$) and gap and enclosure pressure PSDs (\mathbf{S}_{gg} & \mathbf{S}_{ee} , respectively) can be calculated as,

$$\mathbf{S}_{ww,a}(\omega) = \mathbf{H}_{w,a}^*(\omega)\mathbf{S}_{tbl}(\omega)\mathbf{H}_{w,a}^T(\omega) \quad (5.2.56)$$

$$\mathbf{S}_{ww,b}(\omega) = \mathbf{H}_{w,b}^*(\omega)\mathbf{S}_{tbl}(\omega)\mathbf{H}_{w,b}^T(\omega) \quad (5.2.57)$$

$$\mathbf{S}_{gg}(\omega) = \mathbf{H}_g^*(\omega)\mathbf{S}_{tbl}(\omega)\mathbf{H}_g^T(\omega) \quad (5.2.58)$$

$$\mathbf{S}_{ee}(\omega) = \mathbf{H}_e^*(\omega)\mathbf{S}_{tbl}(\omega)\mathbf{H}_e^T(\omega) \quad (5.2.59)$$

The present work generates the gap and enclosure pressure PSD matrices, $\mathbf{S}_{gg}(\omega)$ and $\mathbf{S}_{ee}(\omega)$, which consists of pressure PSD at all the enclosure nodes. These, eventually, help in estimating the point pressure PSD at any point inside the gap/ enclosure and average gap/ enclosure pressure PSD.

Detailed expressions for the coefficients \mathbf{H}_{11} , \mathbf{H}_{12} , \mathbf{H}_{13} , ..., \mathbf{H}_{44} can be found in [APPENDIX B](#).

5.2.3 Structural Modelling: Tensioned Panel

Tension in aircraft panels is crucial for maintaining structural integrity and ensuring safe operation under high-speed conditions. Engineers carefully consider anticipated aerodynamic loads and structural requirements during the design phase to determine the appropriate levels of tension in panels. Tensioned panels are modelled to minimize deflections, mitigate fatigue issues and to have an enhanced ability to withstand external load.

In this present dissertation therefore, an attempt is made to understand the behaviour of tensioned panel subjected to TBL excitation and subsequently the sound transmission behaviour of the same. A brief mathematical description of the tensioned panel modelling is presented below. Analytical solution to estimate the natural frequencies of a simply supported tensioned plate can be found using Kirchhoff thin-plate theory, as given by

$$\omega_{mn}^2 = \frac{1}{\rho_s} \left\{ \frac{Eh^3}{12(1-\nu^2)} \left[\left(\frac{m\pi}{b} \right)^2 + \left(\frac{n\pi}{a} \right)^2 \right]^2 + N_m \left(\frac{m\pi}{b} \right)^2 + N_n \left(\frac{n\pi}{a} \right)^2 \right\} \quad (5.2.60)$$

where E is the Young's modulus

ν is the Poisson's ratio of the plate

ρ_s is the mass density of the structural panel

N_m is the lateral plate tension

N_n is the longitudinal plate tension

However, analytical formulas have their limitations for complex geometry, support conditions and even for non-isotropic material properties, where numerical approaches can be useful instead. In order to establish the accuracy of the FE modelling approach considered in this Chapter, a simply supported tensioned plate is modelled using FE approach, which can further be extended to any type of support conditions. The modal parameters obtained through the free-vibration analysis are used to estimate TBL-induced vibroacoustic response of that plate and compared with the existing analytical results.

The equilibrium equation for the tensioned panel can be derived using the principle of virtual work. Assuming small deformations and neglecting shear effects, the equation can be written as:

$$\nabla \cdot (D\nabla u) + f = 0 \quad (5.2.61)$$

where u is the displacement vector, D is the elastic modulus matrix, f represents the external force vector (due to tension).

In the context of modal analysis, the tensioning force can be introduced through the boundary conditions as a static preload on the plate. The tensioning force will induce a static deformation that modifies the stiffness matrix. The static tensioning force can be represented as a distributed load applied to the plate. For example, for longitudinal tension, one can apply a uniformly distributed force along the longitudinal direction of the plate. Let's denote the magnitude of this force as $F_{longitudinal}$. The static tensioning force will introduce an initial static displacement $U_{tension}$ in the plate due to the applied force. This displacement is the result of the tension force $F_{longitudinal}$ acting on the plate. The modified stiffness matrix $[K_{mod}]$ that accounts for the tensioning force can be expressed as follows:

$$[K_{mod}] = [K] + \frac{F_{longitudinal}}{U_{tension}} \quad (5.2.62)$$

where $U_{tension}$ is the static displacement induced by the tensioning force, $[K]$ is the stiffness matrix obtained from the non-tensioned panel model.

After establishing the tensioned panel model, one can proceed with the free vibration analysis to determine the natural frequencies and mode shapes of the panel.

The dynamic equation for free vibration can then be obtained by modifying the stiffness matrix with the modified stiffness matrix $[K_{mod}]$ wherein the effect of the tensioning forces has been taken care of as explained in Eq. (5.2.62) resulting in the governing equation as,

$$[M]\{\ddot{u}\} + [K_{mod}]\{u\} = 0 \quad (5.2.63)$$

Assuming harmonic solutions of the form $u(x, y, t) = \psi(x, y)e^{i\omega t}$, where ω represents the circular frequency, one can substitute this solution into the dynamic equation and simplify to obtain an eigenvalue problem:

$$[K_{mod}] \cdot \psi = \omega^2 [M] \cdot \psi \quad (5.2.64)$$

Here, M is the mass matrix, which can be derived by integrating the product of the shape functions and the material density over the element domain:

$$[M] = \int ([N]^T \cdot \rho \cdot [N])dA \quad (5.2.65)$$

Solving the eigenvalue problem yields a set of eigenvalues (ω^2) and corresponding Eigen vectors (ψ). The eigenvalues represent the square of the natural frequencies, and the eigenvectors represent the mode shapes of the panel. These modal parameters are further used in estimation of excited panel response.

In the present work, the eigen value analysis for the tensioned panel is performed in ANSYS where the tensioned panel is modelled using four-node isoparametric SHELL181 element. Necessary lateral and longitudinal tension are applied at the boundaries with suitable boundary conditions. In order to provide sufficient constraint a few strategic points are chosen in such a way that does not affect the overall solution. Initially, STATIC analysis is performed with keeping PSTRES ON. The solution of this initial static analysis is then transferred to the subsequent MODAL analysis.

The effect of tensioning in the panels on the free field sound radiation is investigated and presented later in this Chapter.

5.3 NUMERICAL METHODOLOGY

5.3.1 Sound Radiation into the Free Field

5.3.1.1 Radiated Sound Power Estimation using Cholesky Decomposed Pressure Spectra

In the previous Chapter the necessary mathematical steps to decompose the semi-empirical pressure spectrum using Cholesky decomposition and TBL-induced pressure fluctuation in the frequency domain is presented. This pressure fluctuation is used as the input forcing for the sound radiation study in the present Chapter. Using suitable modal transformation and converting the same into frequency domain, the structural response equation given in Eq. (4.2.21), Chapter 4 in the modal domain can be written as,

$$\{q(\omega)\} = [H(\omega)]\{F(\omega)\} \quad (5.3.1)$$

where $[H(\omega)]$ is the frequency response function defined by

$$H(\omega) = \frac{\varphi \varphi^T}{\bar{m}(-\omega^2 + 2\xi\omega_n\omega + \omega_n^2)} \quad (5.3.2)$$

with φ being the eigen vector (mode shape) and \bar{m} the modal mass.

Subsequently, the modal displacement $q(\omega)$ is transformed into the nodal domain using mode summation procedure and expressed as $d_s(\omega)$.

Once the vibration responses are obtained for all the points on the panel and the velocities in the frequency domain are calculated, one can invoke Eq. (5.3.3) to obtain the radiated sound pressure into the free field, where \dot{d}_s^* is the complex conjugate of the velocity.

$$\langle P_{rad} \rangle = \frac{1}{2} Re \int_A \dot{d}_s^*(\omega) p(\omega) dA \quad (5.3.3)$$

where $\langle P_{rad} \rangle$ is the sound power averaged over the radiating plate surface. p is the sound pressure radiated by the panel, obtained from the Eq. (5.2.5).

The estimation of the energy transmission behaviour of the vibrating plates due to TBL induced excitation is expressed as, Average Radiated Sound Power Level, $L_{p,rad}$.

$$L_{p,rad} = 10 \log(\langle P_{rad} \rangle / P_{ref}) \quad (5.3.4)$$

where reference sound power level P_{ref} is taken as 10^{-12} Watt.

In the present work the finite element modelling of the structural panel is carried out in ANSYS (V14.5) simulation package to obtain the structural modal parameters. The boundary element code used to model Eq. (5.2.3) is developed in-house using MATLAB (ver. R2013b) platform. The other necessary mathematical processes described are simulated using MATLAB. In the next section results are presented first to validate the developed technique. Subsequently, the vibration and acoustic responses for isotropic and orthotropic plates are obtained and are presented. The entire workflow is presented in Figure 4.3.1, Chapter 4.

5.3.1.2 Radiation Resistance Matrix (RRM) Approach

Vibroacoustic studies frequently employ the Radiation Resistance Matrix (RRM) method to estimate the radiated sound from vibrating surfaces, such as flexible panels. The fundamental idea of the RRM technique is to establish a connection between the structural vibration and the panel's acoustic emission. It measures the amount of vibrational energy that is transferred from the structure to the fluid around it in the form of acoustic energy. The RRM approach is advantageous as it enables the estimation of sound radiation without having to model the entire acoustic domain explicitly, which can be computationally expensive. However, it requires proper coupling between structural and acoustic models and careful consideration of the underlying assumptions. The flexible panel is discretized into finite elements, and the structural response for each element, such as surface velocity, are calculated from the dynamic analysis. The Radiation Resistance Matrix is constructed based on the radiation impedance and the interaction between different surface elements of the vibrating structure. It characterizes the coupling between the structural vibration and the acoustic radiation. The structural vibration information, obtained from the dynamic analysis of the panel, is combined with the Radiation Resistance Matrix to calculate the sound pressure in the surrounding acoustic field. With the sound pressure distribution known in the surrounding fluid, various acoustic parameters, such as sound power radiation, directivity, and frequency spectra, can be evaluated.

Using radiation resistance matrix (R) calculated as described in the Eq. (5.2.16), the radiated sound power (RSP) from the plate is estimated at each frequency step as,

$$RSP(\omega) = S_{vv}R \quad (5.3.5)$$

The results are obtained using in-house MATLAB codes and are presented in the 'Results and Discussion' section.

5.3.2 Sound Transmission into the Enclosed Cavity

The problem of sound transmission into an acoustic enclosure is dealt by modelling the structural panel using four-node isoparametric SHELL181 element, whereas the acoustic gap cavity or enclosure are modelled using eight-node FLUID30 element.

As can be seen in the Figure 5.2.2 the skin panel (panel 'a') directly gets excited by the external force due to TBL flow over the panel, which acts downward on the panel and the pressure developed inside the cavity acts upward on this panel. This is why in the Eq. 5.2.15 the TBL force,

F_{tbl} is positive, and gap pressure is considered as negative. In case of the trim panel (panel ‘b’) the gap pressure acts downward on the panel. Thus, as per the standard notation the gap pressure, P_g is taken as positive.

5.4 RESULTS AND DISCUSSION

5.4.1 Sound Radiation into the Free Field

5.4.1.1 *Frequency Domain Analysis: Cholesky Decomposition and Finite Element-Boundary Element (FE-BE) Approach*

[The results presented in this sub-section are from author’s ‘In Press’ article accepted in the Journal of Applied Mechanics and Technical Physics]

Prior to the main study a grid sensitivity study for the structural finite element is performed. Sensitivity of sound radiation from an aluminium plate to the various FE and BE grid resolution is studied and presented in Figure 5.4.1. The plate is simply supported on all the four sides and placed in an infinite baffle. A schematic of which is shown in Figure 4.2.1 in Chapter 4. The modulus of elasticity, density and damping ratio of the plate are taken as 70 GPa, 2700 kg/m³ and 0.0025, respectively. The length, L_x and the width, L_y of the plate is taken as 0.5 m and 0.35 m, respectively with the thickness taken as 2 mm. The wind flow speed is considered as 44.7 m/s. Three different FE grid resolution is studied, details of which are presented in Table 5.4.1. The BE grids are constructed based on the FE grids.

Table 5.4.1: Three different finite element grid systems for grid sensitivity study

Mesh quality	Grid resolution	Characteristic length (m)
Coarse	60 × 40	0.0085
Medium	80 × 65	0.0057
Fine	100 × 70	0.0049

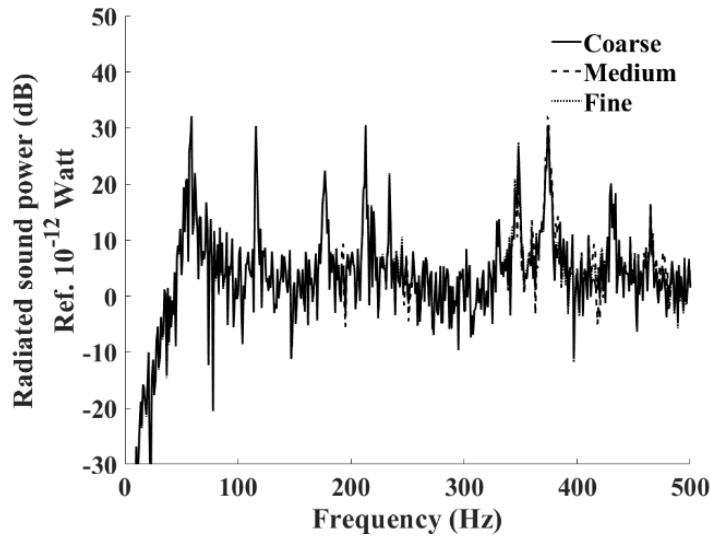


Figure 5.4.1: Sensitivity of average radiated SPL $L_{p,rad}$ (in dB) to grid resolution; simply supported Aluminium plate with $L_x = 0.5\text{m}$, $L_y = 0.35\text{m}$, thickness = 2mm; flow velocity of 44.7 m/s

The computation domain discretization using 60 x 40 mesh (coarse) is found to be sufficient in resolving the plate bending wave, as suggested by the sensitivity study.

In the next phase of the work, the developed model is used to obtain the radiated sound power for isotropic and antisymmetric orthotropic panels subjected to TBL excitation. Seven (7) different cases are considered for the analysis, and they are as follows –

- Case 1: Aluminum
- Case 2a: Carbon Fiber Reinforced (CFRP) Laminated composite with (0/90) lamination sequence;
- Case 2b: CFRP laminated composite with (0/90/0/90) lamination
- Case 3a: CFRP laminated composite with (30/-30) lamination
- Case 3b: CFRP laminated composite with (30/-30/30/-30) lamination
- Case 4a: CFRP laminated composite with (45/-45) lamination
- Case 4b: CFRP laminated composite with (45/-45/45/-45) lamination.

Material properties used to model the plates are as follows –

Young's modulus (E) = 70 GPa, Poisson's ratio = 0.3, Density (ρ) = 2700 kg/m³

CFRP laminates:

Young's modulus $E_{11} = 138 \text{ GPa}$, $E_{22} = E_{33} = 6.9 \text{ GPa}$

Shear modulus $G_{12} = G_{13} = 4.5 \text{ GPa}$, $G_{23} = 4.05 \text{ GPa}$

Poisson's ratio $\nu_{12} = 0.31$, $\nu_{23} = \nu_{13} = 0.3$

Density $\rho = 1570 \text{ kg/m}^3$

Primarily the structural frequencies and the mode shapes for the panels are obtained and they are listed in Table 5.4.2. The average radiated sound power level (SPL) in dB are then

obtained following Eq. 5.2.62. The average quadratic SPL for the aluminium panel is shown in Figure 5.4.2(a), and average quadratic SPL for the orthotropic laminated panels are shown in Figures 5.4.2 (b)-(d). The SPL in dB for the first few modes obtained for different cases are also listed in Table 5.4.3.

Table 5.4.2: Frequency (in Hz) and mode numbers for simply supported rectangular panels having dimensions 0.5 m x 0.35 m x 0.002 m

Case 1	Case 2a	Case 2b	Case 3a	Case 3b	Case 4a	Case 4b
58.43 (1,1)	52.96 (1,1)	58.55 (1,1)	50.11 (1,1)	60.78 (1,1)	55.57 (1,1)	69.75 (1,1)
116.11 (2,1)	87.08 (2,1)	111.13(2,1)	106.63 (2,1)	137.36 (1,2)	101.46 (2,1)	136.34 (2,1)
176.45 (1,2)	134.63 (1,2)	191.72 (1,2)	109.97 (1,2)	141.10 (2,1)	134.73 (1,2)	181.90 (1,2)
212.52 (3,1)	164.67 (3,1)	220.45 (3,1)	178.80 (2,2)	237.47 (2,2)	167.14 (3,1)	231.14 (3,1)
234.00 (2,2)	165.09 (2,2)	222.08 (2,2)	192.36 (3,1)	256.11 (1,3)	196.64 (2,2)	271.98 (2,2)
330.21 (3,2)	230.01 (3,2)	302.20 (3,2)	207.93 (1,3)	266.01 (3,1)	257.12 (4,1)	357.75 (4,1)
348.00 (4,1)	264.86 (4,1)	376.70 (4,1)	274.61 (3,2)	371.40 (2,3)	265.54 (1,3)	362.99 (1,3)
374.29 (1,3)	307.19 (1,3)	427.30 (1,3)	280.50 (2,3)	376.93 (3,2)	277.02 (3,2)	391.56 (3,2)
431.68 (2,3)	325.76 (4,2)	439.38 (4,2)	314.54 (4,1)	421.43 (1,4)	330.44 (2,3)	464.97 (2,3)
465.45 (4,2)	329.82 (2,3)	447.99 (2,3)	342.81 (1,4)	437.99 (4,1)	372.03 (5,1)	---

Table 5.4.3: Average radiated SPL (in dB) from rectangular simply supported 0.5 m x 0.35 m x 0.002 m panels placed in a baffle subjected to a flow velocity of 44.7 m/s

Case	Case I	Case II	Case III	Case IV	Case V	Case VI	Case VII
1 st mode	31.96	48.48	38.58	42.84	37.51	40.62	42.35
2 nd mode	30.36	25.52	28.98	26.68	30.09	20.77	31.92
3 rd mode	22.25	27.19	28.78	30.53	27.18	28.36	32.24

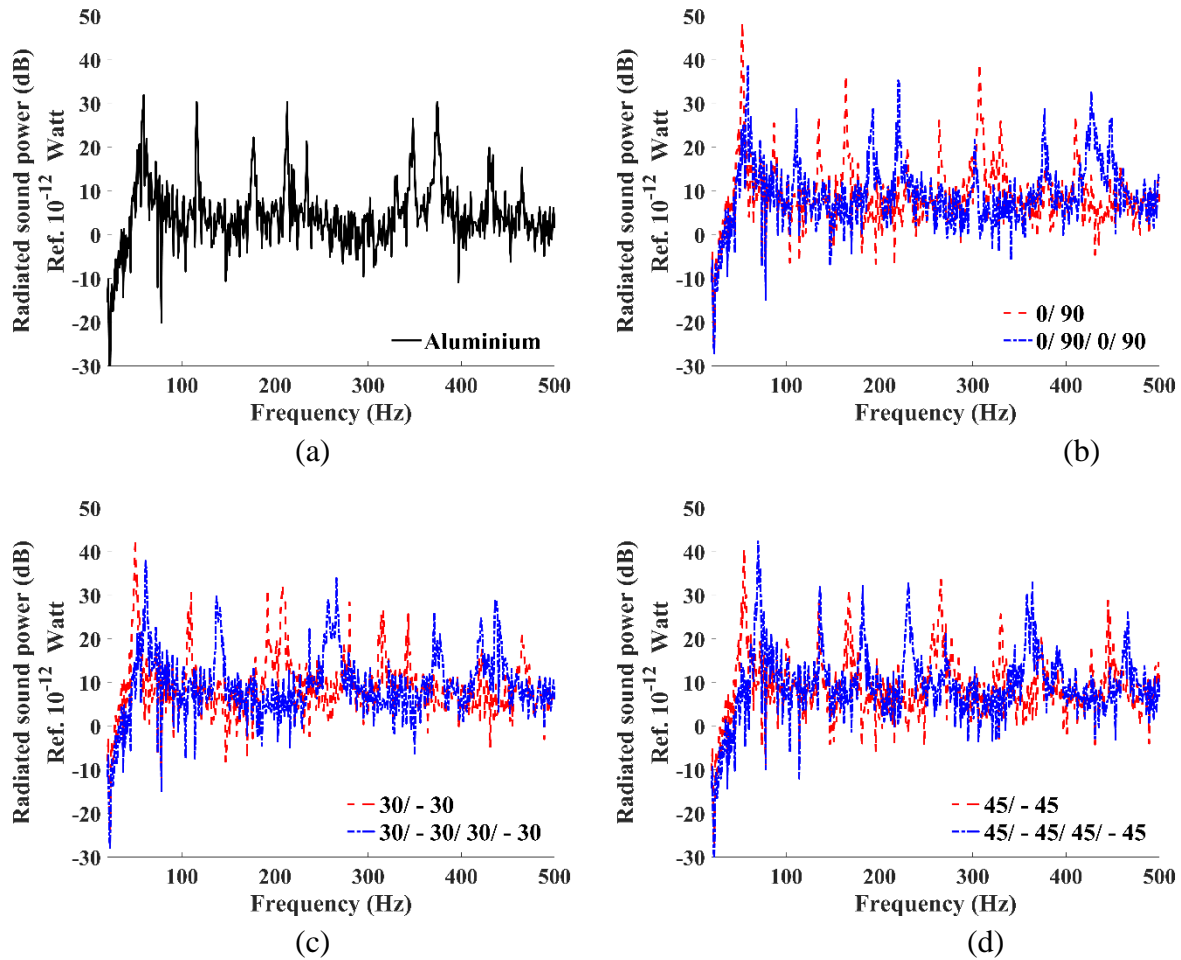


Figure 5.4.2: Average radiated SPL $L_{p,rad}$ (in dB) of simply supported plate with $L_x = 0.5\text{m}$, $L_y = 0.35\text{m}$, thickness = 2mm subjected to a TBL flow with flow velocity of 44.7 m/s (a) Case 1; Aluminium (b) Case 2a & 2b; orthotropic $(0/90)_n$ (c) Case 3a & 3b; orthotropic $(30/-30)_n$ (d) Case VI & VII; orthotropic $(45/-45)_n$

On comparing the results presented in Table 5.4.2 and Table 5.4.3 it is seen that the fundamental frequency of the aluminium panel is higher compared to those for 2-layer orthotropic lamina and as a consequence the average SPL is lower for the aluminium panel. This behaviour fully complies with the general understanding of mechanics where the response for a stiffer panel is lower. Whereas, for the 4-layer laminated panels the fundamental frequencies even though are higher compared to that of the aluminum panel, the average quadratic SPL for the orthotropic panels is also higher. This phenomenon suggests that the response for carbon fiber reinforced laminates is higher when compared with isotropic panels of the same size subjected to TBL loading.

It is further observed from the SPL results presented in Table 5.4.3 that the response in dB in the fundamental mode gets reduced when the number of layers are increased from 2 to 4 for $(0/90)_n$ and $(30/-30)_n$ lamina sequence. On the contrary for $(45/-45)_n$ lamina although the

fundamental frequency for 4-layer layup is significantly higher than 2-layer layup suggesting a stiffer laminate, the average quadratic SPL is slightly increased for the 4-layer layup panel.

Also, it is very interesting to note here that among the three configurations of 4-layer laminates considered for the present study, (45/-45/45/-45) laminate shows the maximum SPL values when subjected to TBL excitation. A static deflection study is also carried out for the $(\theta/-\theta/\theta/-\theta)$ angle ply laminates ($\theta = 30^\circ, 45^\circ$) and (0/90/0/90) lamina by applying a distributed 1 N transverse load over the panels and the central deflection of the panel is presented in the Table 4.4.5, Chapter 4. The central deflection for the lamination sequence with $\theta = 45^\circ$ is the least suggesting it to be the stiffest laminate, whereas the response for the same is the maximum. The extension–bending coupling provided by the antisymmetric laminate sequence along with the cross-spectrum phenomenon of the TBL model plays an important role in this not-so-normal behaviour in response of antisymmetric laminates subjected to TBL excitation.

5.4.1.2 Energy Domain Analysis: Radiation Resistance Matrix Approach

In this segment, simply supported aluminium and CFRP panels are considered for different case studies, and TBL-induced vibroacoustic responses are estimated in terms of averaged radiated sound power. The dimensions and CFRP lamina sequences considered are presented in the subsection 5.4.1.1. Finite element discretization is performed using a 60×40 mesh, and the damping ratio is considered as 0.0025 for all the cases. Free stream velocity is taken to be 44.7 m/s. The turbulent wall parameters are extracted and used in Smol'yakov and Tkachenko's single-point wall-pressure spectrum model [42].

Material properties used to model the plates are as follows –

Aluminium

Young's modulus (E) = 70 GPa, Poisson's ratio = 0.3, Density (ρ) = 2700 kg/m³

CFRP laminates:

Young's modulus $E_{11} = 138$ GPa, $E_{22} = E_{33} = 6.9$ GPa

Shear modulus $G_{12} = G_{13} = 4.5$ GPa, $G_{23} = 4.05$ GPa

Poisson's ratio $\nu_{12} = 0.31$, $\nu_{23} = \nu_{13} = 0.3$

Density $\rho = 1570$ kg/m³

The frequency and mode shape data for all these cases are already presented in Table 5.4.2. TBL induced averaged radiated sound power for all these cases are presented in Figure 5.4.3.

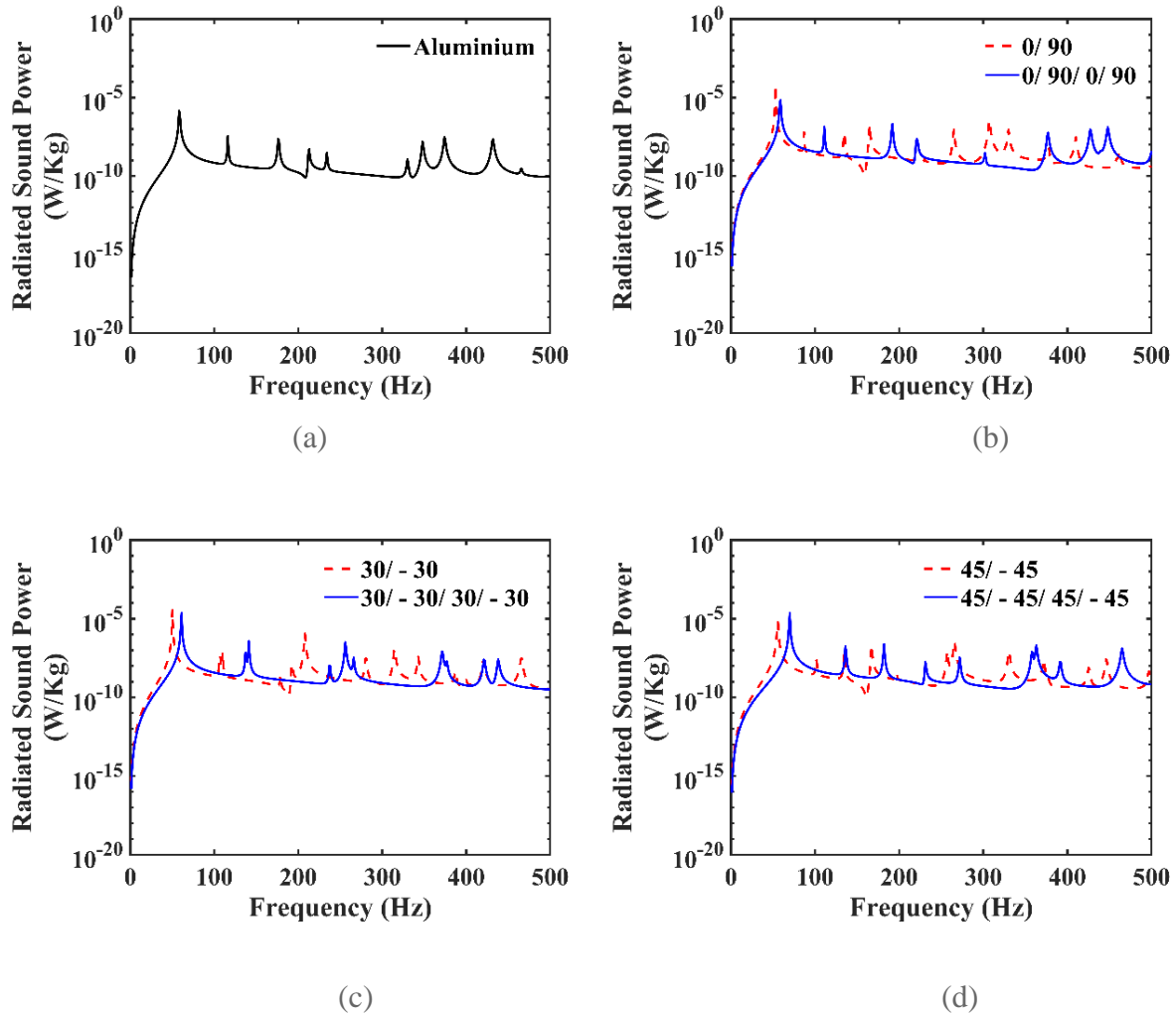


Figure 5.4.3: Radiated sound power from vibrating panels for flow speed 44.7 m/s, a) Case 1, b) Case 2a & 2b, c) Case 3a & 3b, d) Case 4a & 4b

The frequency-mode shape table (Table 5.4.2) suggests that the aluminium plate has a higher fundamental frequency than the two-layered laminates. Moreover, as the number of layers increases from two to four for a particular ply case (say, cross-ply Case 2a and Case 2b) the fundamental frequency increases due to increase in stiffness. This leads to decreased radiated sound power at the fundamental mode, making the results presented in Figure 5.4.3 consistent for Case 2 and Case 3. But for Case 4 as the number of layers increase radiated sound power increase. Antisymmetric laminate sequence-driven extension-twisting and shear-bending coupling (B_{16} and B_{26}), along with distributed TBL cross-spectrum may have played an important role here. In general, 4-layer laminates exhibit greater velocity and radiated sound power than that of the isotropic (aluminium) panel, though fundamental frequencies of the 4-layer laminates are higher. In general, antisymmetric laminates show greater response than that of the isotropic panels, and the antisymmetric sequence is responsible for this along with distribute TBL loading. This is

verified by considering a quasi-isotropic lamina sequence with 8-layers, which shows similar panel vibration with the isotropic one (refer Table 4.4.5, Chapter 4).

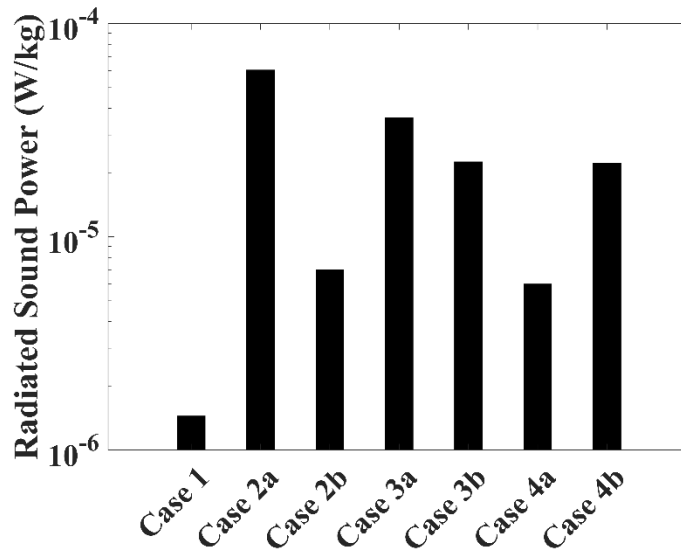


Figure 5.4.4: Comparison of first mode radiated sound power from vibrating isotropic and orthotropic laminated panels for flow speed 44.7 m/s

Some of the salient features as observed from the results can be listed as follows:

- 1) Radiated sound power (RSP) per unit mass of the Aluminium plate are the least among all the cases studied in the present work (Figure 5.4.4). For example, at the fundamental mode, the radiated sound power from the Aluminium plate is 1.441×10^{-6} W/Kg. All the laminated composite plates radiate greater sound power per unit weight than that of the Aluminium plate at their respective fundamental modes (Figure 5.4.4).
- 2) In general, the 4-ply laminates having a higher stiffness show lower radiated sound power as compared to 2-ply laminates with the exception of $(45/-45)_n$ lamina (Figure 5.4.4).
- 3) The sound power expressed in W/Kg for cross-ply laminates (Case 2a: 6.045×10^{-5} W/Kg; Case 2b: 6.989×10^{-6} W/Kg) is the highest as compared to the 30 degrees angle-ply laminates (Case 3a: 3.61×10^{-5} W/Kg; Case 3b: 2.242×10^{-5} W/Kg), whereas the $(45/-45)_n$ shows a completely different trend (Case 4a: 6.0×10^{-6} W/Kg; Case 4b: 2.211×10^{-5} W/Kg).

These features as is observed in the present study may help in the choice of the lamination sequence to be used for fuselage skin in vehicular structure at an early design stage, as far as the TBL induced panel response and resulting sound radiation in the free field is concerned.

5.4.1.3 Sound Radiation from Tensioned and Non-tensioned Panel: Validation

The developed FE-RRM model is validated with the analytical work reported by Maury *et al.* [53]. The physical and mechanical properties of the typical aircraft panel and the turbulent flow are given in Table 5.4.4. Here, the problem is defined as the external turbulent flow perturbing the

structural panel, and the structural vibration resulting in radiated sound power in the other half space of the structural panel. Therefore, two different set of properties are assigned to the external fluid (turbulence) and internal fluid (acoustic). Two types of panels are used, a) tensioned and b) non-tensioned. The tensioned panels are discretized with 30×25 elements, whereas non-tensioned panel is discretized with 50×35 elements, in stream-wise and span-wise directions, respectively. The in-vacuo free vibration analysis, performed using in-house MATLAB codes, yields the frequency and mode number data, which are presented in Table 5.4.5.

Table 5.4.4: Model properties for the validation study of TBL-induced sound radiation

Properties of the flow	
Free stream velocity [m/s]	225 m/s
Boundary layer thickness [m]	0.1
Sound speed	
External fluid [m/s]	300
Internal fluid [m/s]	340
Mass density	
External fluid [kg/m ³]	0.44
Air density [kg/m ³]	1.225
Properties of the structural panel	
Length [m]	0.414
Width [m]	0.314
Thickness [m]	0.001
Young's modulus [GPa]	72.4
Poisson ratio	0.33
Damping ratio	0.01, 0.05
Mass density [kg/m ³]	2800
Longitudinal tension [N-m]	29300
Lateral tension [N-m]	62100

Table 5.4.5: First *ten* frequencies (Hz) and mode numbers for tensioned and non-tensioned panels

Tensioned panel		Non-tensioned panel	
Predicted (present FE model)	Maury <i>et al.</i> , 2001	Predicted (present FE model)	Maury <i>et al.</i> , 2001
269	268	39	40
353	354	83	83
469	473	115	115
500	513	155	154
558	569	230	224
610	615	242	235
645	657	257	252
759	780	285	277
761	825	332	325
777		357	349

The TBL-induced radiated sound power (RSP) from the tensioned panels with structural damping ratio (ξ) of 0.01 and 0.05 are presented and compared in Figure 5.4.5. The RSP from the non-tensioned panel with a damping ratio of 0.01 is presented and compared in Figure 5.4.6. All three cases are found to be in very good agreement with the analytical results.

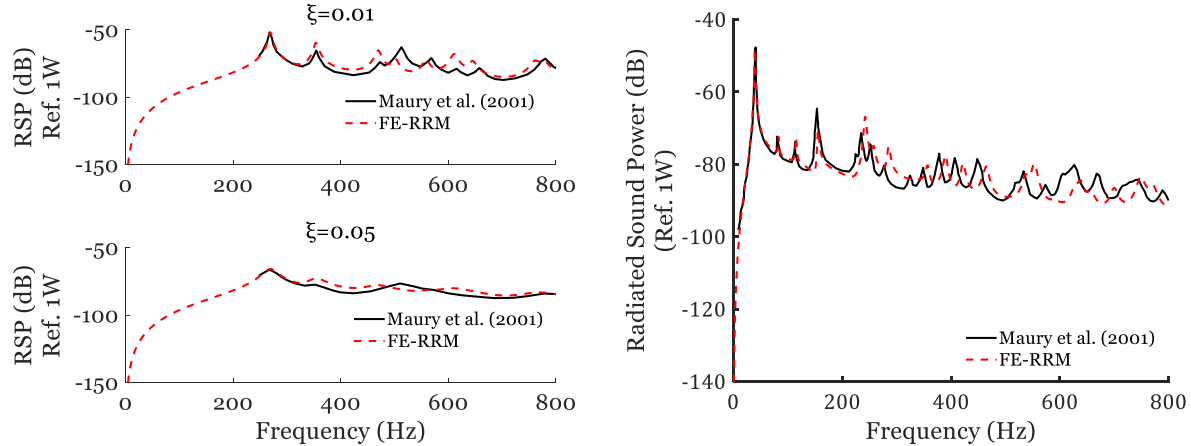


Figure 5.4.5: RSP from tensioned plate, with structural damping ratio 0.01 and 0.05 | Figure 5.4.6: RSP from non-tensioned plate (SS), with structural damping ratio 0.01

5.4.2 TBL-Induced Vibrational Energy Transfer through Stiffened Double Wall Panel

In this subsection parametric studies on TBL-excited double-wall systems are performed using simply supported aluminium plates both as the source panel (panel ‘a’) and the inner vibrating panel (panel ‘b’). Stiffeners, made of Aluminium are attached to the source panel in stiffened

panel case. The model parameters are presented in Table 5.4.6. Energy transmission is calculated in terms of averaged plate velocity PSDs (expressed in dB) and are presented for all the cases.

Table 5.4.6: Flow and structural properties for the double wall energy transmission case

Properties of the flow	
Free stream velocity [m/s]	35.8
Convective flow speed [m/s]	23.7
Displacement thickness [m]	0.0018
Kinematic viscosity [m ² /s]	1.46×10^{-5}
Friction velocity [m/s]	2.29
Air density [kg/m ³]	1.225
Properties of the structural panel	
Length [m]	0.5
Width [m]	0.35
Thickness [m]	0.002
Elastic modulus [GPa]	70
Poisson ratio	0.33
Mass density [kg/m ³]	2700
Damping ratio	0.0025

5.4.2.1 Case Study I: Cavity Thickness

Two different cavity thicknesses are studied keeping the thickness of the panel ‘b’ 2 mm, while considering two different thickness of panel ‘a’ as 2 mm and 3 mm. The effects of the cavity thicknesses along with plate thickness on the velocity PSD of panel ‘b’ are shown in the Figure 5.4.7 and Figure 5.4.8. Also, comparison is made between two situations where panel ‘b’ is either single and directly experiencing the turbulence (single panel case), or it is a part of the double wall system and acting as the inner vibrating panel. Double wall panel configuration with similar panel thickness even increases the energy transmission in the pumping mode due to resonating frequency. In general, it is observed that the narrower the cavity slightly greater is the energy transmission, as can be seen in Figure 5.4.7. However, in the case of panels with different wall thickness, in the absence of resonating panel modes, cavity modes play a significant role in energy transmission. In the presently studied frequency regime *three* cavity modes participate, i.e., rigid acoustic mode (0 Hz), and modes at 340 Hz and 485 Hz. As these modes span in the x and y directions, and not in the direction normal to the plate, it is seen that whatever may be the cavity thickness the effects on energy transmission is similar, and energy transfer is significant at or near the cavity modes (refer Figure 5.4.8). The panel velocity PSD for the double wall panel for both panel ‘a’ and panel ‘b’ is illustrated in Figure 5.4.9 and Figure 5.4.10 for two different panel configurations. It is observed that for the double wall panel system with different panel thickness

there is less energy being transmitted due to the shift in panel frequencies. However, increasing the panel thickness is not always a viable option as it increases the mass. Therefore, stiffeners are introduced, and the effects are discussed in the following section.

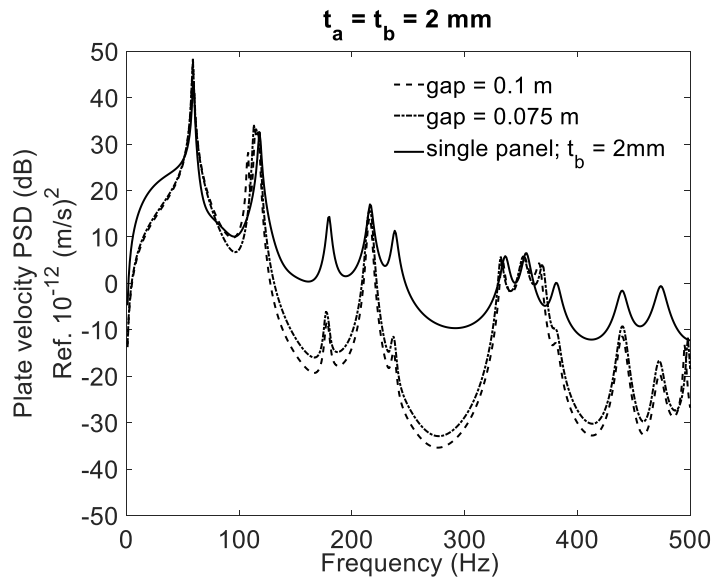


Figure 5.4.7: Effect of gap thickness on panel 'b' velocity; similar plate thickness; $U_\infty = 35.8$ m/s. Both panels are simply supported

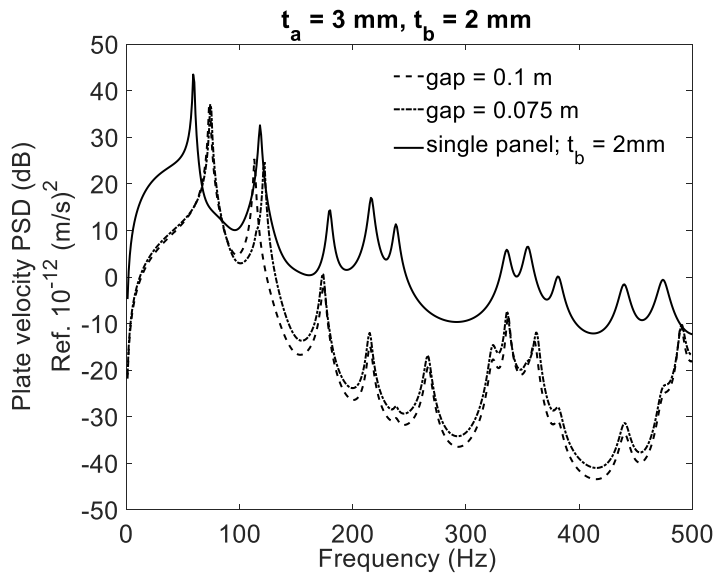


Figure 5.4.8: Effect of gap thickness on panel 'b' velocity; different plate thickness; $U_\infty = 35.8$ m/s. Both panels are simply supported

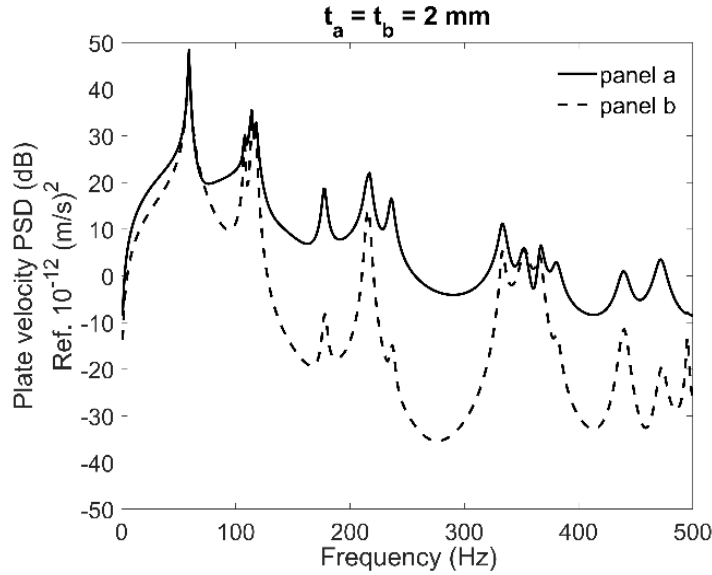


Figure 5.4.9: TBL-induced vibration of double wall configuration; similar plate thickness; gap = 0.1 m; $U_\infty = 35.8 \text{ m/s}$. Both panels are simply supported

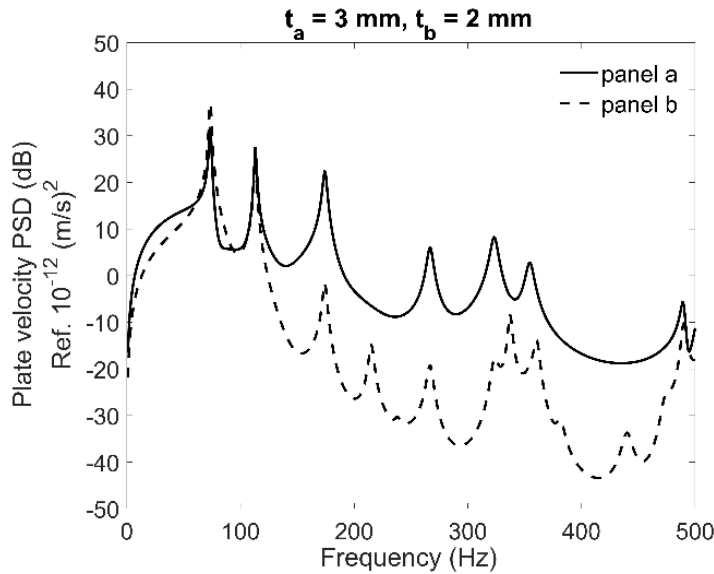


Figure 5.4.10 TBL-induced vibration of double wall configuration; different plate thickness; gap = 0.1 m; $U_\infty = 35.8 \text{ m/s}$. Both panels are simply supported

5.4.2.2 Case Study II: Stiffener Orientation

In the present study the source panel (panel ‘a’) is stiffened, and the inner vibrating panel (panel ‘b’) is considered unstiffened. Two different stiffener orientations are studied here - (i) Longitudinal stiffeners (2 in nos.) are placed along stream wise direction and (ii) Transverse stiffeners (2 in nos.) are placed along the crossflow direction. All the stiffener positions are equidistant from the edges (refer. Figure 5.4.11 and Figure 5.4.12). Depth and thickness of the stiffeners are 20 mm and 2 mm, respectively.

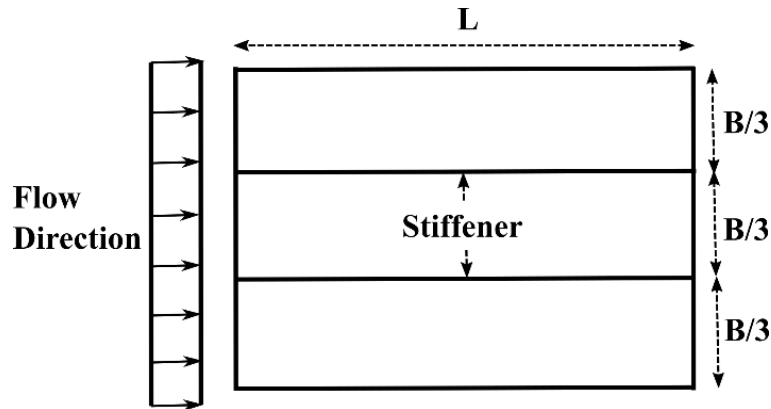


Figure 5.4.11: Schematic of the longitudinally stiffened panel

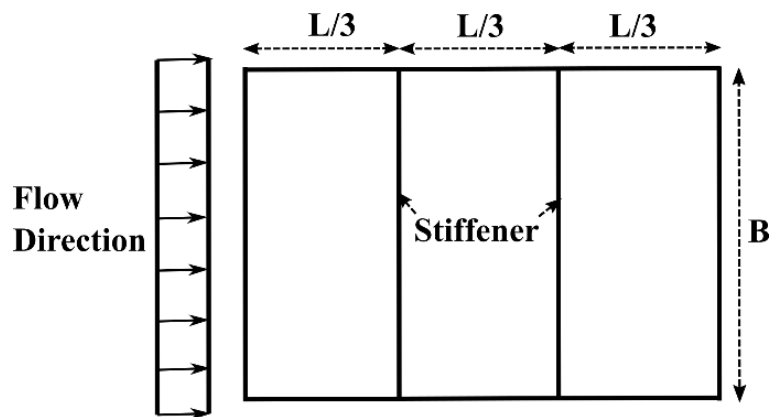


Figure 5.4.12: Schematic of the transverse stiffened panel

The effects of the stiffener orientation on the energy transmission behaviour are shown in the Figure 5.4.13 and Figure 5.4.14. In the present numerical study, it is observed that the transversely stiffened panels exhibit greater energy transmission than the longitudinally stiffened panels. This can be explained from the frequencies and mode shape patterns of the unstiffened plate, longitudinally and transversely stiffened plates. As in the case of double wall configuration wherever the frequencies and nature of mode shapes of the outer and inner panels come closer a higher energy transmission is observed due to the resonating phenomena. It is observed that the zero-frequency rigid acoustic mode strongly couples the vibration of panel ‘a’ with panel ‘b’ and thereby a shift in the coupled condition is observed (refer Table 5.4.7). Below 200 Hz the peak response is dominated by the panel ‘b’ modes, whereas above 200 Hz panel ‘a’ modes start affecting the response. Cavity frequencies 340 Hz and 485 Hz has got significant effect if there are uncoupled panel frequencies in the vicinity. There are few missing frequencies observed for the vibrating panel (panel ‘b’) in the coupled condition, ex. 179 Hz. In case of mechanical point excitation, the panel response is significant across the entire frequency regime (refer Figure 5.4.23) studied in this work, but in case of TBL loading the excitation of the higher modes are not that significant in comparison to the first fundamental mode (refer Figure 5.4.13 and Figure 5.4.14). The velocity PSD for the double wall panels with stiffened and unstiffened configurations are

shown in Figure 5.4.15. The effects of stiffening of panel 'a' on the vibration of panel 'b' are computed. Panels 'a' and 'b' are both deemed to be 2 mm thick. It has been found that stiffening one panel clearly lessens the transfer of vibrational energy for panels of identical thickness. This occurs as a result of the shift in frequency of the panels, which prevents resonance.

Plate velocity PSDs of the panels are computed and compared in order to comprehend the vibrational behaviour of both panels under coupled conditions and when the source panel (panel 'a') is stiffened (refer to Figure 5.4.16 and Figure 5.4.17). An intriguing finding is that, even though the source panel (panel 'a') is directly exposed to external TBL forcing, the vibrating panel's excitation level in pumping mode is higher than that of the source panel. This apparent increase in vibration level is a result of the rigid acoustic mode. Near the next acoustic mode (340 Hz), there is another increase in the vibration intensity of panel 'b'. Therefore, stiffening the source panel alone is not an effective technique to minimize the TBL-induced vibrational energy transfer in a double wall system. Instead, it is also necessary to reinforce the vibrating panel.

Table 5.4.7: Uncoupled and coupled frequency (Hz)

Uncoupled					
Unstiffened panel		Stiffened panel		Cavity	
t = 2 mm	t = 3 mm	Longitudinal	Transverse		
59	89	245	208	340	
118	117	291	249	485	
179	269	382	306		
216	324	434	330		
238	357	491	374		
336			452		
354					
381					
439					
474					

Coupled					
Panel 'a' unstiffened				Panel 'a' stiffened	
$t_a = t_b = 2$ mm		$t_a = 3$ mm, $t_b = 2$ mm		$t_a = t_b = 2$ mm, panel 'b'	
Panel 'a'	Panel 'b'	Panel 'a'	Panel 'b'	Longitudinal	Transverse
59#	59#	73#	73#	85**	86**
108	108	113#	113#	116**	116**
114	115	174**	175**	215**	208*
118#	117#	267*	215**	252*	214**
177#	178#	323*	267*	287*	244**
217#	216#	354*#	325*	332**	311*
236#	237#	489*#	337*#	358**	341*#
333#	333#		360*	381*	363**
352#	353#		440**	435*	441**
367*#	366*#			494#	474**
381#	381#				
439#	440#				
472#	473#				
	495*#				

*Panel 'a' dominated mode; **Panel 'b' dominated modes; #Coupled effect of panel 'a' and 'b'
 **#Coupled effect of panel 'a', panel 'b' and cavity

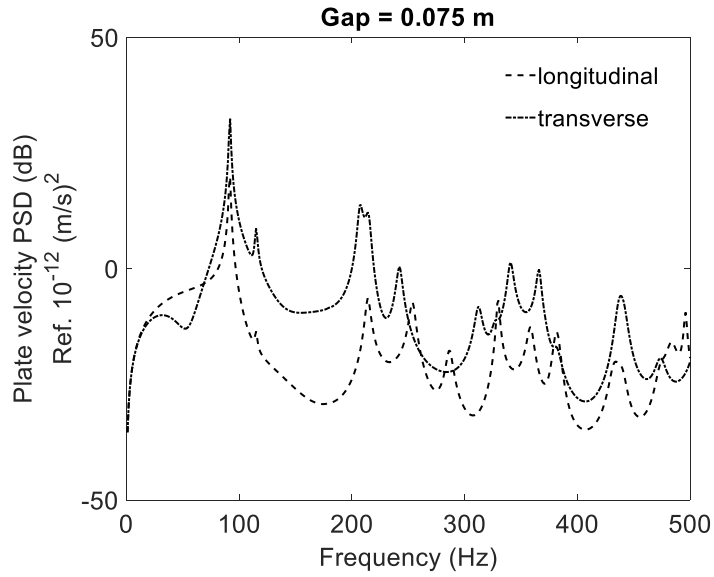


Figure 5.4.13: Effect of stiffener orientation; gap = 0.075 m

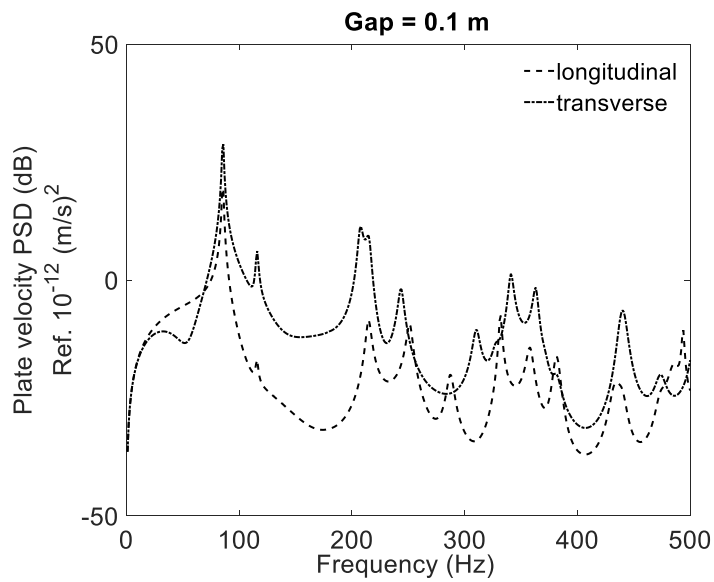


Figure 5.4.14: Effect of stiffener orientation; gap = 0.1 m

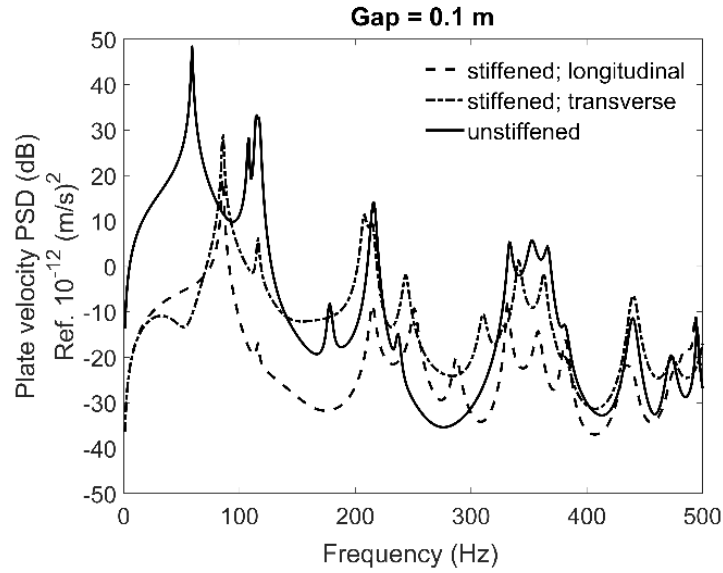


Figure 5.4.15: Effect of stiffening on vibration of panel ‘b’; $t_a = t_b = 2$ mm; gap = 0.1 m; $U_\infty = 35.8$ m/s. Both panels are simply supported

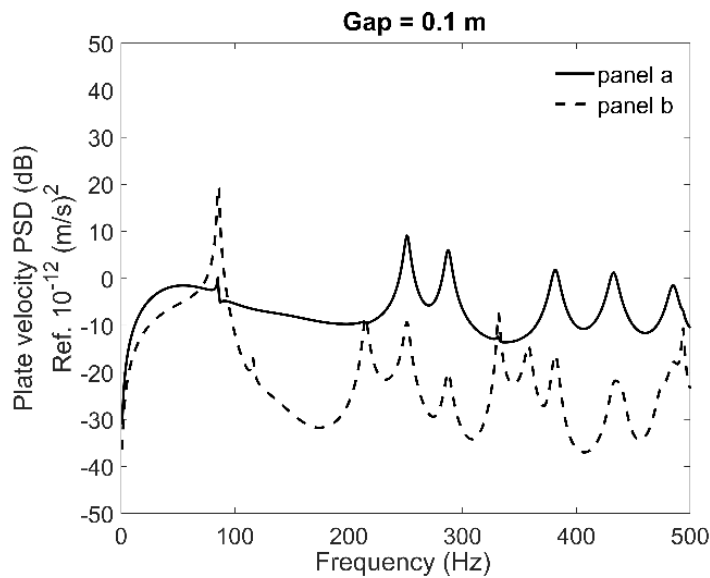


Figure 5.4.16: Comparison of vibration of panel ‘a’ and panel ‘b’; panel ‘a’ is longitudinally stiffened; gap = 0.1 m; $U_\infty = 35.8$ m/s. Both panels are simply supported

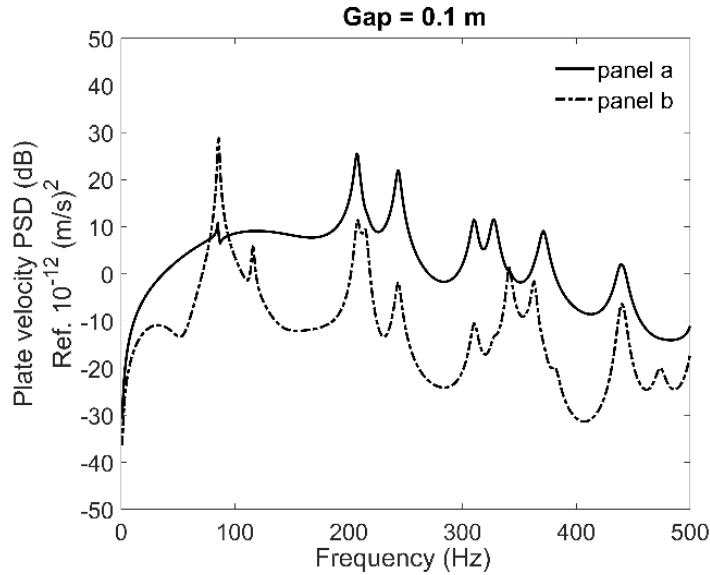


Figure 5.4.17: Comparison of vibration of panel ‘a’ and panel ‘b’; panel ‘a’ is transversely stiffened; gap = 0.1 m; $U_\infty = 35.8 \text{ m/s}$. Both panels are simply supported

5.4.2.3 Case Study III: Sound Radiation into the Free Field

The effect of different structural configuration on the radiating sound power level into the free field is studied and are presented in this section. First, a single aluminium panel which is similar to that of panel ‘b’ is considered. The TBL-induced panel velocity PSD is multiplied with the RRM, as described in Eq. (5.2.13), and the radiated sound power is estimated. Next, double wall configurations (panel-cavity-panel system) are considered, and the radiated sound power from the inner radiating panel (panel ‘b’) is estimated in the same way. Two different panel thicknesses for panel ‘a’ (t_a), 2 mm and 3 mm are studied for the double wall configuration. The thickness of panel ‘b’ is kept as 2 mm. Sound radiation into the free field is compared for a single panel and two double wall panel cases and presented in Figure 5.4.18. Gap thickness is kept as 0.1 m. The results obtained are perfectly in tune with the velocity behaviour of panel ‘b’ as reported earlier.

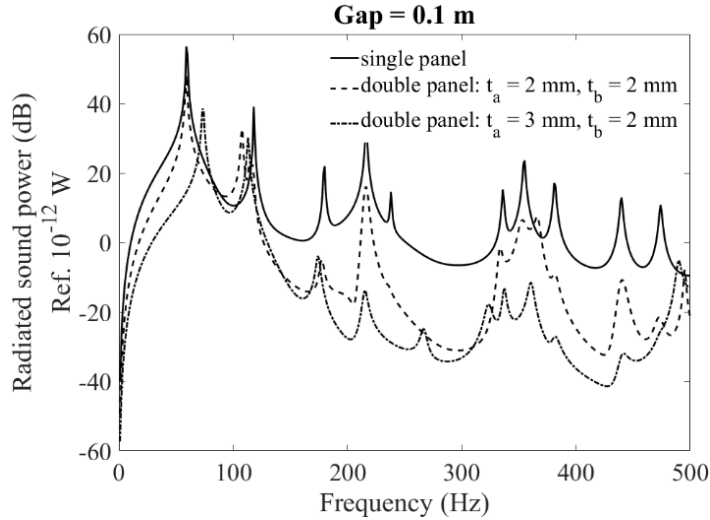


Figure 5.4.18: Radiated sound power for single and double panel configurations; gap = 0.1 m; $U_\infty = 35.8$ m/s. All panels are simply supported

5.4.2.4 Case Study IV: Sound Pressure inside the Cavity

It is essential to have an estimation of the sound pressure inside the gap, as this clearly indicates the energy transmission level through the acoustic path in a double-wall panel configuration. The sound pressure level inside the gap in terms of pressure PSD is estimated using Eq. (5.2.47). A Cloud-based Python-FE code is used for the computation. Two double wall configurations are considered, as previous, varying the thickness of the panel ‘a’ as 2 mm and 3 mm, keeping the thickness of the panel ‘b’ as 2 mm. The sound pressure PSD is estimated at the point $(L_x/3, L_y/3, -2L_z/3)$, where L_x , L_y and L_z are the panel length, panel width and the gap distance. The results are presented in Figure 5.4.19.

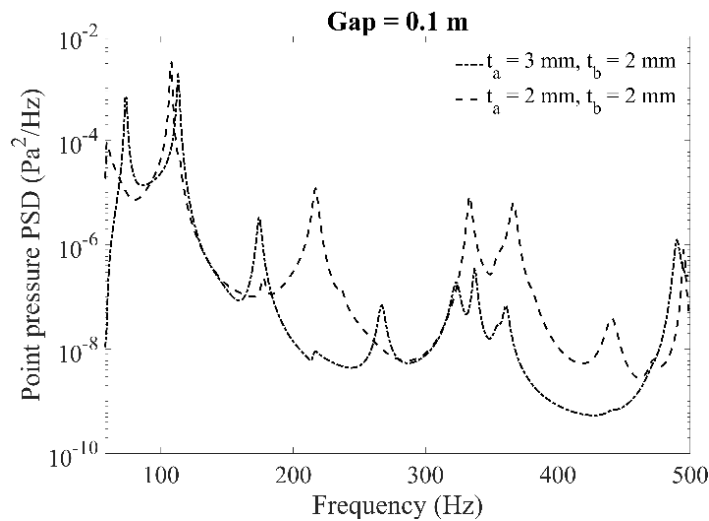


Figure 5.4.19: Pressure PSD inside the cavity measured at a point $(L_x/3, L_y/3, -2L_z/3)$; double panel configurations with varying source panel thickness; gap = 0.1 m; $U_\infty = 35.8$ m/s. Both panels are simply supported

It is clearly observed that with the thicker excited panel (panel ‘a’) being stiffer, the induced velocity in panel ‘a’ due to the TBL excitation is less as compared to the thinner excited panel. This in turn generates a lower pressure variation within the acoustic cavity.

5.4.2.5 Case Study V: Sound Transmission Loss Calculation through Single and Double Wall System

This is in continuation with the FE-RRM model presented and validated in the sub-section 5.4.1.3, the sound transmission loss (TL) is estimated from the RSP. Beside the single panel case described in sub-section 5.4.1.3, a double wall panel system is considered for RSP calculation using the developed mathematical formulation. In this case study two different configuration are considered, (i) thickness of Panel ‘a’, t_a is 1 mm, and Panel ‘b’, t_b is 1 mm, (ii) thickness of Panel ‘a’, t_a is 1.5 mm, and Panel ‘b’, t_b is 1 mm. Both the panels are considered as non-tensioned. Other physical and mechanical properties of the double wall case is kept being same as previous. The gap between two panels (cavity depth) is kept 0.1 m. Panels are discretized with 50×35 element mesh. The enclosed cavity is discretized with $50 \times 35 \times 10$ element mesh. A single stiffener is placed either in the stream wise (long-stiffened) or in the cross stream (cross-stiffened) direction at the mid-section and discretized with 50×1 and 35×1 elements, respectively. Structural panels are modelled with 4-node isoparametric SHELL181 elements, and the cavity is modelled using 8-node brick FLUID30 elements. In-vacuo analysis for the panels and rigid boundary analysis for the cavity are performed, using in-house MATLAB codes.

All the sound radiation results for single and double panel configuration are then converted into transmission loss (dB) using Eq. (5.4.1) and presented in Figure 5.4.20. Transmission loss is calculated in terms of incident power, Φ_{pp} , on the outer panel and the radiating power, RSP as

$$TL = 10\log_{10}\left(\frac{\Phi_{pp}S}{4\rho_{ext}c_{ext}RSP}\right) \quad (5.4.1)$$

where ρ_{ext} and c_{ext} are the mass density and sound speed for the external fluid.

It is worth noting that the fully coupled double wall system is solved in a rate of 4.5 s per Hz in a DELL Workstation with 8 cores and 32 GB RAM.

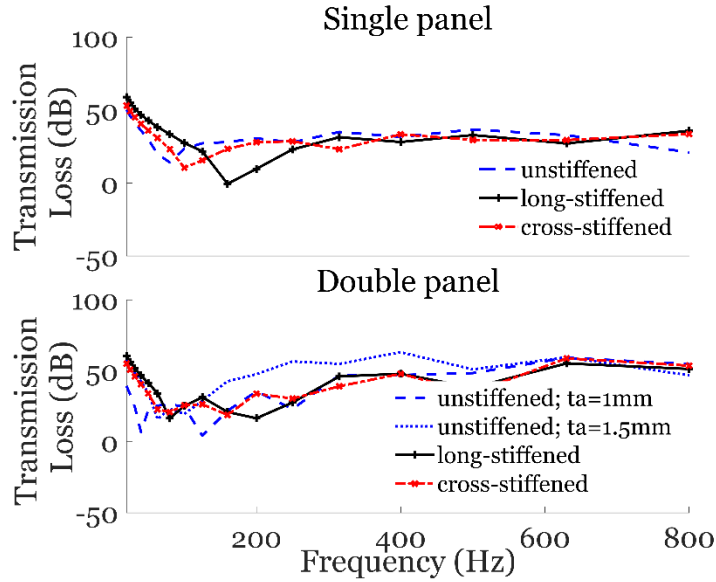


Figure 5.4.20: Transmission loss through different panel systems in $1/3^{\text{rd}}$ octave; skin panel is stiffened or unstiffened with thickness (t_a) 1 mm or 1.5 mm. Radiating panel is unstiffened with thickness 1 mm

It is observed that (i) single panel with longitudinal stiffening even exhibits negative TL at places, that means stiffening does not always works well for TL, (ii) beyond 400 Hz the effect of stiffening on both single and double wall panel is not significant, (iii) for doubled wall panel the best performance is for unstiffened panel with different panel thickness, (iv) all the cases of double wall panel it is found that the transmission loss factor deeps down at two varying frequencies corresponding to the frequency representing two panels of the coupled system.

5.4.3 Sound Transmission into the Enclosed Cavity

5.4.3.1 Double Wall-Backed Enclosure Response Due to TBL Loading: Validation

In this subsection a fully coupled panel-gap-panel-cavity system is modelled to estimate panel and cavity responses due to TBL excitation over the exposed panel. A schematic of the problem is presented in Figure 5.2.3. Goody model [41] is considered to generate the wall pressure spectrum. The presently developed model is validated by the analytical work reported by Caiazzo *et al.* [56]. The model properties of the panel-gap-panel-enclosure system is presented in Table 5.4.8. The thickness of Panel ‘a’ is considered as 2 mm and that for panel ‘b’ is considered as 3 mm. FE meshing for the flexible panels is adopted as to keep the element size well below the wavelength ($\Delta x < \lambda/3$) of the plate bending wave, in order to account for the convective part of the pressure fluctuations [130]. The in-vacuo free vibration analysis for structural panels, and rigid boundary free vibration analysis for the gap and enclosure are performed using in-house Python codes. These yields the frequency and mode number data, for all the systems, which are presented in Table 5.4.9.

Table 5.4.8: Model properties for the double wall backed acoustic enclosure

Properties of the external flow	
Free stream velocity [m/s]	240
Boundary layer thickness [m]	0.08
Displacement thickness [m]	0.0018
Kinematic viscosity [m ² /s]	3.3553×10^{-5}
Friction velocity [m/s]	6.75
External sound speed [m/s]	300
External air density [kg/m ³]	0.44
Empirical parameters α_x, α_y	0.10, 0.77
Properties of the structural panel	
Length [m]	0.4
Width [m]	0.3
Thickness [m]	0.002, 0.003
Young's modulus [GPa]	100
Poisson ratio	0.33
Mass density [kg/m ³]	2380
Damping ratio	0.01
Properties of the acoustic enclosures	
Internal sound speed [m/s]	343
Internal air density [kg/m ³]	1.19
Length [m]	0.4
Width [m]	0.3
Height of gap [m]	0.038
Height of enclosure [m]	0.4
Damping ratio	0.05

Table 5.4.9: First *eight* frequencies (Hz) upto 1000Hz

Structural Panel		Cavity		Coupled
Panel 'a'	Panel 'b'	Gap	Enclosure	
108	162	429	429	134
225	337	572	431	202
317	474	715	572	322
421	630	858	608	419
433	649		715	444
628	941		716	592
667	999		834	632
696			858	698

In order to perform robust calculations solving all the matrix equations in FE framework, cloud-based Python environment is deployed. 24 modes for panel ‘a’, 20 modes for panel ‘b’ and gap, and 48 modes for enclosure are considered for validation and all the subsequent calculations. The TBL-excited enclosure pressure PSD at a given point, referring Figure 19 of Caiazzo *et al.*, 2018 [57], is estimated using the developed FE model, and presented in Figure 5.4.21. The estimated result is found to be in excellent agreement with the analytical result reported [57].

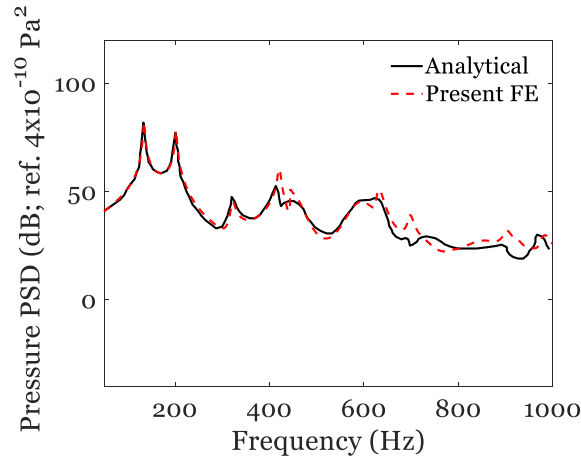


Figure 5.4.21: Enclosure pressure PSD at $(L_x/3, L_y/3, -2L_z/3)$

5.4.3.2 Case Study: Enclosure Pressure with Variable Gap Distance

Once the FE model is validated, next the enclosure pressure PSD at the same location is estimated keeping all the conditions as previous. The only variable is the gap distance between the two panels. Results are obtained for three different gap distances, 0.019m, 0.038m and 0.076m, and presented in Figure 5.4.22.

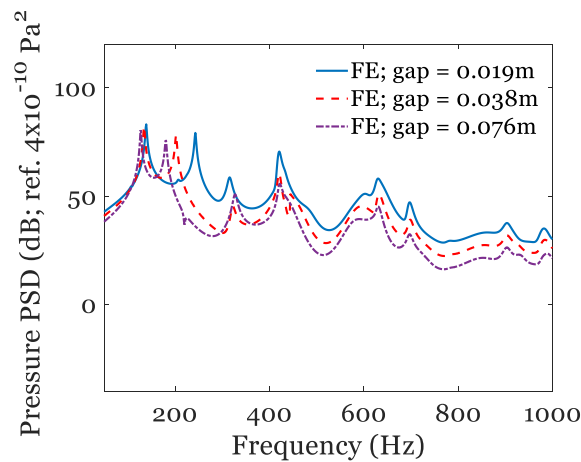


Figure 5.4.22: Pressure PSD at $(L_x/3, L_y/3, -2L_z/3)$ for different gap distance

It is observed that,

- (1) the lowest gap distance (0.019 m) produces maximum point pressure into the enclosure, and in case of highest gap distance (0.076 m) the transmitted pressure into enclosure is minimum.
- (2) with the increase in the gap distance from 0.038 m to 0.076 m the enclosure pressure is generally reducing, but in the 0-400Hz region, this is not always true, especially in the 300-450Hz range. 3rd (322Hz) and 4th (422Hz) coupled modes may be responsible for this changed behaviour.
- (3) there is a frequency shift in the coupled system, but the 2nd fundamental frequency shift for lowest gap (0.019 m) is quite significant. This is due to reduction in gap the 2nd fundamental mode of panel ‘a’ is dominating the system.

5.4.3.3 Double Wall System Response Due to Mechanical Loading: Validation

The energy transmission through a double-wall panel system is examined for the model described by Cheng *et al.* [188]. The effect of the enclosure backing the double-wall panel system can be considered insignificant in comparison to the effect of the gap cavity between the two panels [Cheng *et al.* [188], page 2745]. As per the model, panel ‘a’ is excited by a mechanical point load and the energy is transmitted to the panel ‘b’, and the average quadratic velocities of the panels are shown in Figure 5.4.23. The gap thickness is 0.11 m. The present modelling of energy transmission through a double-wall system is found to be in excellent agreement with the analytical results. Therefore, this model is further used to estimate for TBL excitation and for stiffened panel.

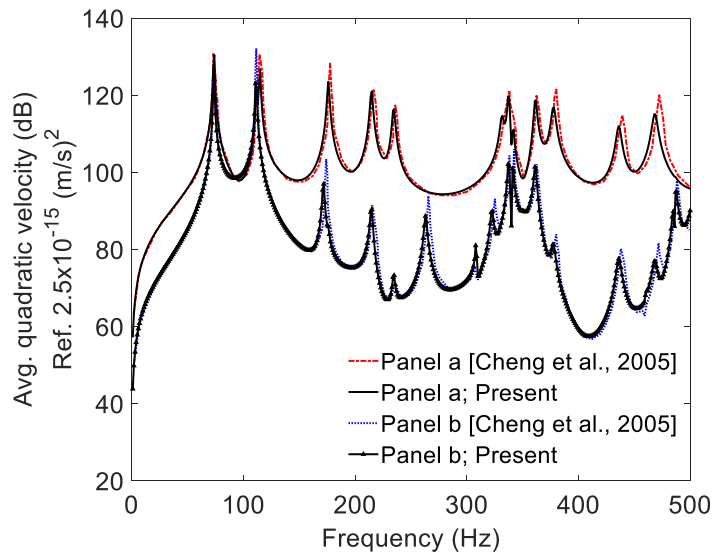


Figure 5.4.23: Numerical and analytical plate response prediction of a double-wall system

5.5 CONCLUSION

The study of TBL-induced sound radiation into a free field and sound transmission into an enclosed cavity has provided valuable insights into the complex dynamics of acoustic energy propagation and control. These investigations are crucial in various industries, including aerospace,

automotive, and architectural engineering, where minimizing noise transmission and optimizing acoustic performance are essential goals.

The analysis of double wall panels has revealed the significance of energy transmission across coupled structures. By considering the interaction between the panels and the cavity, researchers have devised methods to mitigate sound transmission effectively. Stiffened panels have been found to enhance the structural and acoustic characteristics of such systems, demonstrating the importance of combining mechanical and acoustical considerations for optimal design.

The application of advanced numerical techniques such as Cholesky decomposition, Boundary Element Method (BEM), and the Radiation Resistance Matrix (RRM) method has enabled a detailed understanding of acoustic behaviour. These methods provide efficient and accurate ways to model complex systems, allowing researchers to simulate and predict sound radiation and transmission with a high degree of fidelity.

The integration of a fully coupled system, accounting for interactions between the panels, cavity, and surrounding medium, has resulted in a more comprehensive representation of real-world scenarios. The gap distance between panels has been identified as a critical parameter influencing the acoustic performance of double wall systems. Optimizing this parameter can lead to substantial reductions in sound transmission and improved overall acoustic insulation.

Moreover, the investigation of orthotropic laminated composites has demonstrated the potential of using advanced materials to tailor acoustic properties. These materials allow for greater control over stiffness and damping characteristics, contributing to the overall sound insulation effectiveness of the system.

The important conclusions derived from the present studies are listed below:

5.5.1 Sound Radiation into the Free Field

1. Two different approaches; finite element-boundary element (FE-BE) and finite element-radiation resistance matrix (FE-RRM) approaches are providing similar trends so far as TBL-induced sound radiation is concerned.
2. In case of orthotropic laminates, as the number of layers increase from *two* to *four* radiated sound power decrease as a result of increased frequency due to greater stiffness. However, this behaviour gets completely reversed in case of 45° laminates.
3. In general, all the orthotropic laminates radiate more sound power per unit weight of the panel than that of the isotropic (aluminium) panel.

5.5.2 TBL-Induced Vibrational Energy Transfer through Stiffened Double Wall Panel

1. Double-wall panel configuration with similar panel thickness is not recommended due to its higher energy transmission at the resonating pumping mode.

1. Greater the cavity thickness, greater the reduction in forward energy transmission. The rigid acoustic mode is having significant contribution in shifting the frequency of the coupled system.
2. Change in stiffener orientation alters the energy transmission behaviour, both in terms of peak frequency, and the magnitude, transverse stiffener orientation being at the upper side.
3. For the present configuration, longitudinally stiffened panels are found to be better attenuator of the energy transmission. Coupling between uncoupled panel modes and the nearby cavity modes exhibits higher energy transmission.

5.5.3 Sound Transmission into the Enclosed Cavity

1. The fully coupled panel-gap-panel-enclosure modelling and enclosure pressure prediction through present cloud-based Python-FE model is found to be excellent.
2. Subsequently, a case study is performed with variable gap distance. It is observed that 0.019m gap distance is transmitting highest level of energy of all the cases. Increasing the gap distance from 0.038m to 0.076m is not exhibiting transmission reduction in the 0-400Hz, as was expected.
3. The present model can incorporate complex structural geometry and boundary conditions for the panels made of isotropic or orthotropic laminates.
4. This present model can incorporate active structural acoustic control (ASAC) strategy using the flexible FE modelling framework.

CHAPTER 6: CONCLUSIONS

6.1 INTRODUCTION

The present dissertation focuses on the turbulent boundary layer (TBL) excited structural vibration and resulting noise radiation and transmission studies following the motivation presented in Chapter 1. In order to address such a complex mechanism coupled fluid-structure-acoustic models are developed along with an extensive turbulence modelling. Turbulence-structure interaction and resulting noise radiation/transmission is an active research area and only a very few works are found in open literature addressing the entire coupled model capable of dealing generic geometry and boundary conditions.

A thorough review is conducted and reported in Chapter 2 based on the rationale for the current dissertation, which is highlighted in Chapter 1. After a critical evaluation of earlier works, the current dissertation's goal is stated as

- numerical modelling of TBL wall pressure fluctuations, feeding the wall parameters into the semi-analytical pressure spectrum models, and predicting the best turbulence model-spectrum model for accurate estimation of the wall pressure
- development of the numerical turbulence-structure interaction model to estimate the vibration of flexible structural panels
- development of a fully coupled structure-acoustic numerical model to estimate sound radiation in the free field and sound transmission into an enclosed cavity

Following the defined objective, the research questions are formulated as to

- identify the best predicting configuration of turbulence model and spectrum model
- develop a fluid-structure interaction model
- develop a flow-excited vibroacoustic model

To address these fundamental research questions, a few different aspects are considered, such as turbulent boundary layer modelling through semi-analytical and numerical technique, formulation or development of a structural model, an acoustic model and the development of a one-way fluid-structure coupling model, and a two-way structure-acoustic coupling model. Chapter 3 focuses on the estimation of TBL wall pressure using semi-analytical models and the Cholesky decomposition technique. The study identifies the sensitivity of mean square pressure to CFD-RANS turbulence model parameters, which is crucial in early design stages. The LES technique powered by artificial inflow turbulence is used to obtain real-time wall-pressure fluctuations. The obtained pressure is then used in Chapter 4 as the forcing function to excite the flexible panel beneath the TBL. Numerical TBL-structure coupled modelling is developed in the FE environment, with the structural panel being modelled using four-node linear quadrilateral isoparametric finite element. The dynamic analysis estimates the FRF of the structural panel, which is coupled with the TBL cross-PSD to estimate panel vibration. The results are validated with the experimental results for both point and surface averaged velocity PSD. Chapter 5

discusses the sound radiation and transmission problems due to the TBL-excited vibrating structural panel. Free-field sound radiation problem is detailed with governing equations, numerical modelling, and the implementation of the radiation resistance matrix (RRM). Numerically estimated radiated sound power is validated with established analytical results. A fully coupled structure-acoustic model is developed to capture the mechanism of sound transmission into an enclosed cavity due to TBL-excited flexible panel vibration. The work is extended for a panel-gap-panel-cavity system and validated with previously reported analytical results.

To provide a meaningful conclusion for the current study, the significant contributions and research findings are highlighted in this chapter together with the basic summary of the dissertation. Here, a critical evaluation of the current dissertation is done and provided. The potential directions for future research are briefly discussed, and the importance of the current research is underlined in the conclusion.

6.2 WALL PRESSURE ESTIMATION USING CFD

Combined RANS-Semi-Analytical Model Approach

The investigation on the sensitivity of the zero-pressure gradient flat plate turbulent boundary layer wall-pressure spectrum for flow over flat plates is presented in Chapter 3. The approximations of pressure spectrum models and the variation in mean square pressure fluctuations due to change in model parameters is examined. The study numerically replicates wind tunnel and in-flight test results using different RANS configurations. The findings suggest that the Smol'yakov-Tkachenko model and Rackl-Weston model are suitable for wind tunnel experiments and in-flight tests, respectively. The $k - \omega$ family of models is the best predictor of mean square pressure with good convergence, while the $k - \epsilon$ family is recommended for near wall studies. The study bridges the gap in selecting suitable RANS turbulence closure models for wall pressure parameters.

Large Eddy Simulation (LES)

In the later part of Chapter 3 large eddy simulation (LES) to estimate TBL wall pressure fluctuation, using artificial inflow turbulence at the inlet to continuously perturb flow is presented. This method is found to be more effective than the current spectral synthesiser method in ANSYS Fluent. The estimated pressure fluctuations are Fourier transformed, and the power spectra are obtained. The LES-predicted wall pressure spectra match well with the established semi-analytical spectra, with low-Re flow spectra matching the Smol'yakov-Tkachenko model, and high-Re flow spectra matching the Efimtsov and Goody models.

6.3 COUPLED VIBROACOUSTIC MODELLING IN ENERGY DOMAIN

Coupled TBL-Structure Interaction Modelling

In Chapter 4 the dynamic behaviour of flexible panels with longitudinal and transverse stiffeners, revealing the complex interactions between turbulence, boundary layer effects, and the presence of stiffeners is explored. Stiffeners significantly influence structural integrity and performance, altering vibrational response and influencing design and performance. Panels with transverse stiffeners transmit more vibrational energy than those with longitudinal stiffeners due to changes in overall stiffness. These panels also have a higher panel response when subjected to TBL-excitation, with more modes being excited due to turbulent excitation in the low frequency regime (0-500 Hz). Orthotropic laminated composite panels show significantly higher panel velocity response compared to isotropic panels. For antisymmetric lamination sequence both for cross and angle ply the panel response due to the TBL is higher compared to that of isotropic panels. In general, it is observed that with the increase in number of layers the panel response decreases as is normal because of the increase in the stiffness. However, for $(45/-45)_n$ the results obtained are counter-intuitive as with the increase in number of layers the response is also increased due to TBL excitation.

Coupled FE-RRM Technique

In Chapter 5 coupled FE-RRM technique is developed to estimate sound power radiated from a TBL-excited flexible panel. The RRM is formulated using the elemental radiator approach. As a natural process it is observed in this study that the sound power radiated from orthotropic laminates decreases with the increase in the number of layers due to increased stiffness for all angle and cross ply laminates (0/90 and $\theta/-\theta$), but shows a counter-intuitive result for $45^\circ/-45^\circ$ lamination sequence. Generally, orthotropic laminates radiate more sound power per unit weight of the panel than isotropic (aluminium) panels.

Vibrational Energy Transfer through Stiffened Double Wall Configuration

Double wall panel configurations with both the walls having same thickness are not recommended due to higher energy transmission in resonating pumping mode. With the increase in cavity thickness the forward energy transmission reduces, and also it is found the rigid acoustic mode (0 Hz) significantly affects the transfer of energy in the first few modes. As observed for the panel studied in the present work the energy transmission through the double wall panel with transverse stiffener is higher compared to longitudinal stiffener. The results suggest that the acoustic mode having frequency closure to the uncoupled mode of panels enhances sound transmission through the double wall panel.

Fully Coupled Modelling for Sound Transmission into an Enclosed Cavity

The cloud-based Python-FE model developed for panel-gap-panel-enclosure modelling and enclosure pressure prediction is found to be excellent. A case study reveals that as the gap distance decreases the energy transmission increases. The model can handle complex structural geometry and boundary conditions for isotropic or orthotropic laminate panels and has the potential to incorporate active structural acoustic control (ASAC) strategy using the flexible FE modelling framework.

6.4 COUPLED VIBROACOUSTIC MODELLING IN FREQUENCY DOMAIN

Cholesky's Decomposition and Structural Vibration

Chapter 4 also deals with the decomposition of wall pressure spectrum and estimation of wall pressure fluctuation in normal frequency domain. The TBL forcing function thus obtained is then used for calculation of complex panel vibration in the frequency domain.

It is found from the study that the average quadratic plate velocity of the aluminium plate is the least among all the cases studied. 4-ply laminates with higher stiffness show lower averaged plate velocity PSD compared to 2-ply laminates, except for $(45/-45)_n$ lamina. These features may help in choosing the lamination sequence for fuselage skin in vehicular structures at an early design stage, considering TBL induced panel response and sound radiation in the free field.

Coupled FE-BE Technique

The two approaches, presented in Chapter 5, finite element-boundary element (FE-BE) and finite element-radiation resistance matrix (FE-RRM), show similar trends in TBL-induced sound radiation. Orthotropic laminates show a decrease in radiated sound power as the number of layers increases but reverses for 45° laminates. Generally, orthotropic laminates radiate more sound power per unit weight than isotropic (aluminium) panels.

6.5 CONCLUSIONS

Some of the salient developments and findings of the present research work are listed below:

- A two-fold sensitivity study is performed to identify best predicting turbulence model for 'TBL over flat plate' problem. The $k - \omega$ family of models is found to be best serving the purpose, along with Spalart-Allmaras one equation model. The $k - \epsilon$ family of models is not recommended to address this type of problems. The results are presented in Figure 3.5.7 to Figure 3.5.10 in Chapter 3.
- The large eddy simulation (LES) technique powered by artificial inflow turbulence generated through in-house user defined function (UDF) in ANSYS Fluent is observed to

be satisfactorily capturing near-wall pressure fluctuations, as presented in Figure 3.5.18 and Figure 3.5.19 in Chapter 3. This is a marked improvement over the existing ‘spectral synthesizer’ method available in ANSYS Fluent library.

- An investigation is done in Chapter 3 to recognize the best predicting wall pressure spectrum model. As revealed in Figure 3.5.1(a), the Goody, Smol’yakov and Smol’yakov Tkachenko models are seen to be very close to the wind tunnel experimental spectrum. Whereas Figure 3.5.1(b) depicts that the Efimtsov and Rackl-Weston models best capture the in-flight test data.
- The wall pressure spectrum is decomposed using Cholesky’s technique to obtain frequency-dependent pressure fluctuations, which in turn used as input forcing to the flexible panel system, the average quadratic panel velocity is estimated, and presented in Figure 4.4.11 in Chapter 4. This is probably the first time this technique is implemented for TBL-induced vibration analysis.
- The Cholesky-decomposed wall pressure fluctuation is used in an FE-BE approach to calculate free field sound radiation, the results of which can be found in Figure 5.4.2 in Chapter 5.
- An elemental radiator-based FE-RRM technique is also used to estimate the radiated sound power in the spectral domain into the free field and presented in Figure 5.4.3 in Chapter 5.
- A detailed modelling of stiffened panel-gap-panel configuration excited by TBL pressure fluctuation is performed using FE-FE technique, and the vibroacoustic response are calculated for both the panels and the cavity. The results are presented in the sub section 5.4.2 in Chapter 5.
- Finally, an exhaustive fully coupled FE model is prepared to address TBL-excited panel-gap-panel-enclosure system, simulated in cloud-based Python environment. The FRF of individual domain, i.e., panels or cavities have been separated out which enables this model to estimate panel response in terms of displacement, velocity or acceleration PSD, and gap cavity/ enclosure cavity response in terms of pressure PSD at any required point in the entire domain. This kind of approach in the FE literature has not been encountered by the present researcher.

Based on the conclusive findings obtained through the present research, the scope for future research is identified and stated in the following section.

6.6 SCOPE FOR FUTURE RESEARCH

- This work can be extended to investigate combined RANS-Semi-Analytical approach for different velocity range and over curved surface.
- Implementing Cholesky’s technique to decompose semi-analytical wall pressure spectra over any curved surface can be undertaken.
- If computational resources, this work can easily be extended to TBL wall pressure estimation using *three*-dimensional (3D) large eddy simulation (LES).

- Experimental validation of the presently developed coupled vibroacoustic model to estimate energy transfer through single/double wall configuration into the enclosed acoustic cavity can be done.
- Extension of the vibroacoustic model for curved panel with enclosure with arbitrary geometry can be identified as a future work.
- In future one can include experimental damping as a parameter in the developed model.
- The model presented in this dissertation can act as the base model to development passive (absorbent layer) and/or active (linear quadratic regulator, LQR) control strategy for the TBL-excited vibroacoustic model.

6.7 STATEMENT OF CONTRIBUTION

The unique features of the present thesis work are as follows:

- An extensive study is performed to evaluate the sensitivity of TBL wall pressure to the different turbulence model parameters and semi-analytical spectrum models.
- An in-house code for artificial inflow turbulence generation is developed and augmented in the commercial flow solver to estimate wall pressure more accurately.
- Semi-analytical pressure spectrum is decomposed using Cholesky's technique to produce frequency-dependent wall pressure fluctuation.
- A coupled FE-RRM based generalized numerical model is developed in the MATLAB platform to estimate the free field sound radiation from a flexible panel.
- A FE-FE based numerical model based on Green's modal coupling approach is developed in cloud-based Python environment to perform interior vibroacoustic analysis.

APPENDIX A

The detailed results of sensitivity of MSP for wind tunnel experiment to the RANS turbulence models mentioned in Chapter 3 are given in Table 3.A.1 and 3.A.2. Table 3.A.1 details the error of the MSP as obtained from experimentally and numerically at Point 1. Table 3.A.2 details the same at Point 2.

Table 3.A.1: Experimental and numerical parameters; Point 1; $U_\infty = 30$ m/s

Model	Solver	y^+	U_τ	δ	δ^*	θ	\bar{p}^2 (ST)	\bar{p}^2 (RW)
Experimental values			1.18	29.54	4.04	3.14	28.955	29.59
SA	O.FOAM	1	1.15	24.5	3	2.1	25.6123	23.34
		30	1.17	24.8	3.3	2.2	27.7158	25.9
		100	1.16	26.5	3.4	2.2	27.11	25.83
	Fluent	1	1.22	29.83	2.9	2.2	33.2	34.58
		30	1.17	30.99	3.4	2.1	27.54	29.21
		100	1.17	30	3.8	2	27.63	28.71
$k - \omega$	O.FOAM	1	1.14	21.3	3	2.1	25.2628	24.66
		30	1.19	23.8	3.4	2.3	29.8032	30.54
		100	1.183	25.75	3.5	2.3	29.1847	29.45
	Fluent	1	1.19	28.14	3	2.2	30.1158	29.95
		30	1.19	29.21	3.5	2.2	29.7268	30.56
		100	1.19	28.75	4	2.1	29.7522	30.3
$k - \omega$ SST	O.FOAM	1	1.12	22.3	3	2.1	23.6346	20.03
		30	1.16	23	3.3	2.2	26.7371	23.9
		100	1.154	21.75	3.3	2.1	26.4095	22.62
	Fluent	1	1.17	21.6	3.1	2.2	27.504	23.99
		30	1.14	23.99	3.5	2.1	25.0066	22.6
		100	1.14	22.5	4.1	2.1	25.4995	21.81
$k - \epsilon$	O.FOAM	1	1.53	33.5	5.2	3.6	81.6805	101.6
		30	1.19	23.8	3.3	2.2	30.2481	27.35
		100	1.183	22.8	3.3	2.1	29.1794	26
	Fluent	1	1.12	22.3	3	2.1	23.6346	20.03
		30	1.16	23	3.3	2.2	26.7371	23.9
		100	1.154	21.75	3.3	2.1	26.4095	22.62
R $k - \epsilon$	O.FOAM	1	1.4	30.8	3.9	2.3	57.3563	64.32
		30	1.1	28.75	3.3	2.2	21.7601	21.22
		100	1.14	40	3.4	2.1	25.1857	29.67
	Fluent	1	1.39	29.83	4.4	3.1	55.4239	62.26
		30	1.14	23.99	3.5	2.1	24.9943	22.6
		100	1.14	25	3.9	2.1	25.4154	23.12

Table 3.A.2: Experimental and numerical parameters; Point 1; $U_\infty = 50$ m/s

Model	Solver	y^+	U_τ	δ	δ^*	θ	\bar{p}^2 (ST)	\bar{p}^2 (RW)
Experimental values			1.89	23	3.37	2.58	188.8705	263.33
SA	O.FOAM	1	1.87	23	2.8	2	180.0016	204.76
		30	1.86	23.8	3	2	176.5348	203.56
		100	1.86	25.25	3.2	2	175.4397	209.91
	Fluent	1	1.95	30.5	2.7	2.1	214.35	284.76
		30	1.87	29.7	3	2	180.91	233.53
		100	1.87	31.3	3.6	1.9	180.62	239.75
$k - \omega$	O.FOAM	1	1.83	21.3	2.8	2	163.8959	222.69
		30	1.89	22.8	3.1	2.1	189.0555	261.77
		100	1.89	23	3.3	2.1	187.4897	259.41
	Fluent	1	1.95	27.73	2.7	2.1	214.3511	271.43
		30	1.9	30.4	3	2	193.0304	253.5
		100	1.9	30	3.7	2	193.662	251.82
$k - \omega$ SST	O.FOAM	1	1.79	24.8	2.7	1.9	152.0452	175.38
		30	2.08	34.5	2.4	1.7	276.8019	401.82
		100	1.84	25	3	1.9	169.9854	199.05
	Fluent	1	1.87	20.82	2.8	2.1	179.0819	194.24
		30	1.82	20.9	3	2	162.8651	172.55
		100	1.84	21.3	3.8	2	168.5817	182.98
$k - \epsilon$	O.FOAM	1	2.42	31.5	4.7	3.3	511.9758	740.91
		30	1.89	22.3	3	2	188.9635	211.19
		100	1.884	21.5	3.1	2	186.0652	204.24
	Fluent	1	2.36	32.49	4.4	3.1	463.3937	675.29
		30	1.87	24.82	3	2	179.6693	213.13
		100	1.86	25	3.7	2	178.6657	208.83
$k - \epsilon$ R	O.FOAM	1	2.31	32.75	3.5	2.9	421.818	618.19
		30	1.79	28	3.1	2.1	153.2422	193
		100	1.83	36.25	3.1	1.9	165.6821	234.27
	Fluent	1	2.21	27.73	4	2.8	352.8618	469.76
		30	1.82	20.85	3	2	162.7226	172.32
		100	1.84	22.5	3.7	1.9	168.165	188.38

SA = Spalart Allmaras, ST = Smol'yakov and Tkachenko, RW = Rackl and Weston

The typical error analysis of MSP estimation using different y^+ values are presented in Table 3.A.3 to Table 3.A.6.

Table 3.A.3: Error in \bar{p}^2 estimation (in %); point 1; Smol'yakov-Tkachenko model

Model	y^+	30 m/s		50 m/s	
		Open FOAM	Fluent	Open FOAM	Fluent
	1	15.72	15.72	9.25	11.15
$k - \omega$	30	8.84	7.31	5.83	5.72
	100	7.31	0.49	1.01	-4.40

Table 3.A.4: Error in \bar{p}^2 estimation (in %); point 2; Smol'yakov-Tkachenko model

Model	y^+	30 m/s		50 m/s	
		Open FOAM	Fluent	Open FOAM	Fluent
	1	12.12	13.88	10.91	12.77
$k - \omega$	30	5.83	5.83	4.27	7.44
	100	4.42	-0.72	0.79	-2.57

Table 3.A.5: Error in \bar{p}^2 estimation (in %); point 1; Rackl-Weston Model

Model	y^+	30 m/s		50 m/s	
		Open FOAM	Fluent	Open FOAM	Fluent
	1	-16.68	1.23	-15.43	3.08
$k - \omega$	30	3.22	3.27	-0.59	-3.73
	100	-0.48	2.40	-1.49	-4.37

Table 3.A.6: Error in \bar{p}^2 estimation (in %); point 2; Rackl-Weston Model

Model	y^+	30 m/s		50 m/s	
		Open FOAM	Fluent	Open FOAM	Fluent
	1	-18.67	2.81	-16.20	8.14
$k - \omega$	30	5.67	5.66	2.78	-3.66
	100	2.01	3.03	0.56	-2.77

APPENDIX B

Calculation of the modal dynamic stiffness of the structural panels, gap cavity and their coupling (Cheng *et al.* [188])

$$H_{11} = M_a + K_m \phi_a^T(x_m, y_m) \phi_a(x_m, y_m),$$

$$M_a = \begin{bmatrix} \ddots & & \square & & \square \\ \square & m_{a,ij}(\omega_{a,ij}^2 + 2i\zeta_{a,ij}\omega_{a,ij}\omega - \omega^2) & & & \square \\ & & \square & & \\ \square & & & & \ddots \\ \square & & & & \end{bmatrix}_{MN \times MN},$$

$$\phi_a(x_m, y_m) = [\varphi_{a,11}(x_m, y_m), \varphi_{a,12}(x_m, y_m), \dots, \varphi_{a,MN}(x_m, y_m)],$$

$$H_{12} = -K_m \phi_a^T(x_m, y_m) \phi_b(x_m, y_m), H_{21} = H_{12}^T,$$

$$H_{22} = M_b + K_m \phi_b^T(x_m, y_m) \phi_b(x_m, y_m),$$

$$M_b = \begin{bmatrix} \ddots & & \square & & \square \\ \square & m_{b,ij}(\omega_{b,ij}^2 + 2i\zeta_{b,ij}\omega_{b,ij}\omega - \omega^2) & & & \square \\ & & \square & & \\ \square & & & & \ddots \\ \square & & & & \end{bmatrix}_{MN \times MN},$$

$$H_{13}^T = A_a \begin{bmatrix} L_{1,11}^{ag} & \dots & L_{1,MN}^{ag} \\ \dots & \dots & \dots \\ L_{n_g,11}^{ag} & \dots & L_{n_g,MN}^{ag} \end{bmatrix},$$

$$H_{23}^T = -A_b \begin{bmatrix} L_{1,11}^{bg} & \dots & L_{1,MN}^{bg} \\ \dots & \dots & \dots \\ L_{n_g,11}^{bg} & \dots & L_{n_g,MN}^{bg} \end{bmatrix},$$

$$H_{24}^T = A_b \begin{bmatrix} L_{1,11}^{be} & \dots & L_{1,MN}^{be} \\ \dots & \dots & \dots \\ L_{n_e,11}^{be} & \dots & L_{n_e,MN}^{be} \end{bmatrix},$$

$$H_{31} = \frac{\rho c_0^2 A_a \omega^2}{V_g} \begin{bmatrix} \frac{1}{m_{g,11}} [L_{1,11}^{ag} \dots L_{1,MN}^{ag}] \\ \dots \\ \frac{1}{m_{g,n_g n_g}} [L_{n_g,11}^{ag} \dots L_{n_g,MN}^{ag}] \end{bmatrix},$$

$$H_{32} = -\frac{\rho c_0^2 A_b \omega^2}{V_g} \begin{bmatrix} \frac{1}{m_{g,11}} [L_{1,11}^{bg} \dots L_{1,MN}^{bg}] \\ \dots \\ \frac{1}{m_{g,n_g n_g}} [L_{n_g,11}^{bg} \dots L_{n_g,MN}^{bg}] \end{bmatrix},$$

$$H_{33} = \begin{bmatrix} \ddots & & \square & & \square \\ \square & -\omega^2 + 2i\zeta_{g,j}\omega_{g,j}\omega + \omega_{g,j}^2 & & & \square \\ & & \square & & \\ \square & & & & \ddots \\ \square & & & & \end{bmatrix}_{n_g \times n_g},$$

$$H_{42} = \frac{\rho c_0^2 A_a \omega^2}{V_e} \begin{bmatrix} \frac{1}{m_{e,11}} [L_{1,11}^{be} \dots L_{1,MN}^{be}] \\ \dots \\ \frac{1}{m_{g,n_g n_g}} [L_{n_e,11}^{be} \dots L_{n_e,MN}^{be}] \end{bmatrix},$$

$$H_{44} = \begin{bmatrix} \ddots & \square & \square \\ \square & -\omega^2 + 2i\zeta_{e,j}\omega_{e,j}\omega + \omega_{e,j}^2 & \square \\ \square & \square & \ddots \end{bmatrix}_{n_e \times n_e}.$$

BIBLIOGRAPHY

- [1] J. Araújo Alves, F. Neto Paiva, L. Torres Silva, and P. Remoaldo, “Low-Frequency Noise and Its Main Effects on Human Health—A Review of the Literature between 2016 and 2019,” *Applied Sciences*, vol. 10, no. 15, p. 5205, Jul. 2020, doi: 10.3390/app10155205.
- [2] A.-M. O. Mohamed, E. K. Paleologos, and F. M. Howari, “Noise pollution and its impact on human health and the environment,” in *Pollution Assessment for Sustainable Practices in Applied Sciences and Engineering*, Elsevier, 2021, pp. 975–1026. doi: 10.1016/B978-0-12-809582-9.00019-0.
- [3] G. Firdaus and A. Ahmad, “Noise Pollution and Human Health: A Case Study of Municipal Corporation of Delhi,” *Indoor and Built Environment*, vol. 19, no. 6, pp. 648–656, Dec. 2010, doi: 10.1177/1420326X10370532.
- [4] J. F. Wilby, “Aircraft interior noise,” *J Sound Vib*, vol. 190, no. 3, pp. 545–564, Feb. 1996, doi: 10.1006/jsvi.1996.0078.
- [5] V. Mellert, I. Baumann, N. Freese, and R. Weber, “Impact of sound and vibration on health, travel comfort and performance of flight attendants and pilots,” *Aerosp Sci Technol*, vol. 12, no. 1, pp. 18–25, Jan. 2008, doi: 10.1016/j.ast.2007.10.009.
- [6] Z. Wu, J. Liang, M. Fu, G. Fang, and Z. Zhou, “Study of random fatigue behavior of C/SiC composite thin-wall plates,” *Int J Fatigue*, vol. 116, pp. 553–561, Nov. 2018, doi: 10.1016/j.ijfatigue.2018.07.001.
- [7] J. Wang, F. Zhao, Y. Sha, and S. Gu, “Fatigue life research and experimental verification of superalloy thin-walled structures subjected to thermal-acoustic loads,” *Chinese Journal of Aeronautics*, vol. 33, no. 2, pp. 598–608, Feb. 2020, doi: 10.1016/j.cja.2019.09.012.
- [8] W. W. Willmarth and C. E. Wooldridge, “Measurements of the fluctuating pressure at the wall beneath a thick turbulent boundary layer,” *J Fluid Mech*, vol. 14, no. 2, pp. 187–210, Oct. 1962, doi: 10.1017/S0022112062001160.
- [9] V. Blitterswyk and J. Corey, “Experimental characterization of turbulent motions using wall-pressure measurements in low Reynolds number turbulent boundary layers,” Carleton University, 2016.
- [10] M. ~K. Bull, “On the form of the wall-pressure spectrum in a turbulent boundary layer in relation to noise generation by boundary layer-surface interactions,” in *Mechanics of Sound Generation in Flows*, Jan. 1979, pp. 210–216.
- [11] J. Van Blitterswyk and J. Rocha, “An experimental study of the wall-pressure fluctuations beneath low Reynolds number turbulent boundary layers,” *J Acoust Soc Am*, vol. 141, no. 2, pp. 1257–1268, Feb. 2017, doi: 10.1121/1.4976341.
- [12] N. Thomson and J. Rocha, “Comparison of Semi-Empirical Single Point Wall Pressure Spectrum Models with Experimental Data,” *Fluids*, vol. 6, no. 8, p. 270, Jul. 2021, doi: 10.3390/fluids6080270.

- [13] E. Salze, C. Bailly, O. Marsden, E. Jondeau, and D. Juve, “An experimental characterisation of wall pressure wavevector-frequency spectra in the presence of pressure gradients,” in *20th AIAA/CEAS Aeroacoustics Conference*, Reston, Virginia: American Institute of Aeronautics and Astronautics, Jun. 2014. doi: 10.2514/6.2014-2909.
- [14] M. C. Goody and R. L. Simpson, “Surface Pressure Fluctuations Beneath Two- and Three-Dimensional Turbulent Boundary Layers,” *AIAA Journal*, vol. 38, no. 10, pp. 1822–1831, Oct. 2000, doi: 10.2514/2.863.
- [15] T. S. Miller, J. M. Gallman, and M. J. Moeller, “Review of Turbulent Boundary Layer Models for Acoustic Analysis,” *J Aircr*, vol. 49, no. 6, pp. 1739–1754, Nov. 2012, doi: 10.2514/1.C031405.
- [16] R. Rackl and A. Weston, “Modeling of Turbulent Boundary Layer Surface Pressure Fluctuation Auto and Cross Spectra-Verification and Adjustments Based on TU-144LL Data,” 2005. [Online]. Available: <http://www.sti.nasa.gov>
- [17] S. A. Rizzi, R. G. Rackl, and E. V Andrianov, “Flight test measurements from the Tu-144LL structure/cabin noise follow-on experiment,” 2000.
- [18] J. Rocha and D. Palumbo, “On the sensitivity of sound power radiated by aircraft panels to turbulent boundary layer parameters,” *J Sound Vib*, vol. 331, no. 21, pp. 4785–4806, Oct. 2012, doi: 10.1016/j.jsv.2012.05.030.
- [19] B. E. Launder and B. I. Sharma, “Application of the energy-dissipation model of turbulence to the calculation of flow near a spinning disc,” *Letters in Heat and Mass Transfer*, vol. 1, no. 2, pp. 131–137, Nov. 1974, doi: 10.1016/0094-4548(74)90150-7.
- [20] D. C. Wilcox, “Reassessment of the scale-determining equation for advanced turbulence models,” *AIAA Journal*, vol. 26, no. 11, pp. 1299–1310, Nov. 1988, doi: 10.2514/3.10041.
- [21] F. R. Menter, “Two-equation eddy-viscosity turbulence models for engineering applications,” *AIAA Journal*, vol. 32, no. 8, pp. 1598–1605, Aug. 1994, doi: 10.2514/3.12149.
- [22] F. R. Menter, M. Kuntz, and R. Langtry, “Ten years of industrial experience with the SST turbulence model,” *Turbulence, heat and mass transfer*, vol. 4, no. 1, pp. 625–632, 2003.
- [23] P. Spalart and S. Allmaras, “A one-equation turbulence model for aerodynamic flows,” in *30th Aerospace Sciences Meeting and Exhibit*, Reston, Virginia: American Institute of Aeronautics and Astronautics, Jan. 1992. doi: 10.2514/6.1992-439.
- [24] T.-H. Shih, W. W. Liou, A. Shabbir, Z. Yang, and J. Zhu, “A new k-epsilon eddy viscosity model for high Reynolds number turbulent flows: Model development and validation,” 1994.
- [25] F. R. Menter, “Influence of freestream values on k-omega turbulence model predictions,” *AIAA Journal*, vol. 30, no. 6, pp. 1657–1659, Jun. 1992, doi: 10.2514/3.11115.
- [26] J. Smagorinsky, “General circulation experiments with the primitive equations,” *Mon Weather Rev*, vol. 91, no. 3, pp. 99–164, Mar. 1963, doi: 10.1175/1520-0493(1963)091<0099:GCEWTP>2.3.CO;2.

- [27] D. K. Lilly, "The representation of small-scale turbulence in numerical simulation experiments," *IBM Form*, pp. 195–210, 1967.
- [28] J. W. Deardorff, "A numerical study of three-dimensional turbulent channel flow at large Reynolds numbers," *J Fluid Mech*, vol. 41, no. 2, pp. 453–480, Apr. 1970, doi: 10.1017/S0022112070000691.
- [29] B. M. Efimtsov, "Characteristics of the field of turbulent wall pressure-fluctuations at large Reynolds-numbers," *Soviet Physics Acoustics-USSR*, vol. 28, no. 4, pp. 289–292, 1982.
- [30] D. M. Chase, "Modeling the wavevector-frequency spectrum of turbulent boundary layer wall pressure," *J Sound Vib*, vol. 70, no. 1, pp. 29–67, 1980.
- [31] B. M. Efimtsov, "The prediction of the pressure fluctuation field characteristics of the TBL," *Contract No. BTRC-101F, Document No. BTRC101F-5*, vol. 95, 1995.
- [32] B. M. Efimtsov, "Similarity criteria for the spectra of wall pressure fluctuations in a turbulent boundary layer," *Soviet Physics Acoustics*, vol. 30, pp. 33–35, 1984.
- [33] B. Efimtsov, N. Kozlov, S. Kravchenko, and A. Andersson, "Wall pressure-fluctuation spectra at small forward-facing steps," in *5th AIAA/CEAS Aeroacoustics Conference and Exhibit*, Reston, Virginia: American Institute of Aeronautics and Astronautics, May 1999. doi: 10.2514/6.1999-1964.
- [34] M. S. Howe, *Acoustics of fluid-structure interactions*. Cambridge university press, 1998.
- [35] T. M. Farabee and M. J. Casarella, "Spectral features of wall pressure fluctuations beneath turbulent boundary layers," *Physics of Fluids A: Fluid Dynamics*, vol. 3, no. 10, pp. 2410–2420, Oct. 1991, doi: 10.1063/1.858179.
- [36] A. V. Smol'yakov, "Calculation of the spectra of pseudosound wall-pressure fluctuations in turbulent boundary layers," *Acoust Phys*, vol. 46, no. 3, pp. 342–347, May 2000, doi: 10.1134/1.29890.
- [37] A. L. Laganelli and H. F. Wolfe, "Prediction of fluctuating pressure in attached and separated turbulent boundary-layer flow," *J Aircr*, vol. 30, no. 6, pp. 962–970, Nov. 1993, doi: 10.2514/3.46440.
- [38] J. E. Robertson, "Prediction of in flight fluctuating pressure environments including protuberance induced flow," 1971.
- [39] M. V Lowson, "Prediction of boundary layer pressure fluctuations," 1968.
- [40] M. V Lowson, "Pressure fluctuations in turbulent boundary layers National Aeronautics and Space Administration -W A."
- [41] M. Goody, "Empirical Spectral Model of Surface Pressure Fluctuations," *AIAA Journal*, vol. 42, no. 9, pp. 1788–1794, Sep. 2004, doi: 10.2514/1.9433.
- [42] A. V Smol'Yakov, V. M. Tkachenko, and J. S. Wood, "Model of a field of pseudosonic turbulent wall pressures and experimental data," *Soviet physics. Acoustics*, vol. 37, no. 6, pp. 627–631, 1991.
- [43] P. Welch, "The use of fast Fourier transform for the estimation of power spectra: A method based on time averaging over short, modified periodograms," *IEEE Transactions on Audio*

- and *Electroacoustics*, vol. 15, no. 2, pp. 70–73, Jun. 1967, doi: 10.1109/TAU.1967.1161901.
- [44] G. M. Corcos, “Resolution of Pressure in Turbulence,” *J Acoust Soc Am*, vol. 35, no. 2, pp. 192–199, Feb. 1963, doi: 10.1121/1.1918431.
- [45] G. M. Corcos, “The resolution of turbulent pressures at the wall of a boundary layer,” *J Sound Vib*, vol. 6, no. 1, pp. 59–70, Jul. 1967, doi: 10.1016/0022-460X(67)90158-7.
- [46] Y.-K. Lin, *Probabilistic theory of structural dynamics*. McGraw-Hill, 1967.
- [47] J. S. Bendat and A. G. Piersol, *Random Data*. Wiley, 2010. doi: 10.1002/9781118032428.
- [48] Y. F. Hwang and G. Maidanik, “A wavenumber analysis of the coupling of a structural mode and flow turbulence,” *J Sound Vib*, vol. 142, no. 1, pp. 135–152, Oct. 1990, doi: 10.1016/0022-460X(90)90587-P.
- [49] Y. F. Hwang, “A Discrete Model of Turbulence Loading Function for Computation of Flow-Induced Vibration and Noise,” in *Noise Control and Acoustics*, American Society of Mechanical Engineers, Nov. 1998, pp. 389–395. doi: 10.1115/IMECE1998-0534.
- [50] S. Hambric, Y. F. Hwang, O. America, and others, “Vibrations of flat plates excited by low Mach number turbulent boundary layers,” in *Proc INTERNOISE*, 2000, pp. 3257–3264.
- [51] S. A. Hambric, Y. F. Hwang, and W. K. Bonness, “Vibrations of plates with clamped and free edges excited by low-speed turbulent boundary layer flow,” *J Fluids Struct*, vol. 19, no. 1, pp. 93–110, Jan. 2004, doi: 10.1016/j.jfluidstructs.2003.09.002.
- [52] J. Rocha, A. Suleman, and F. Lau, “Prediction of turbulent boundary layer induced noise in the cabin of a BWB aircraft,” *Shock and Vibration*, vol. 19, no. 4, pp. 693–705, 2012, doi: 10.3233/SAV-2011-0660.
- [53] C. Maury, P. Gardonio, and S. J. Elliott, “Active Control of the Flow-Induced Noise Transmitted Through a Panel,” *AIAA Journal*, vol. 39, no. 10, pp. 1860–1867, Oct. 2001, doi: 10.2514/2.1200.
- [54] C. Maury, P. Gardonio, and S. J. Elliott, “A wavenumber approach to modelling the response of a randomly excited panel, part i: general theory,” *J Sound Vib*, vol. 252, no. 1, pp. 83–113, Apr. 2002, doi: 10.1006/jsvi.2001.4028.
- [55] C. Maury, P. Gardonio, and S. J. Elliott, “A wavenumber approach to modelling the response of a randomly excited panel, part ii: application to aircraft panels excited by a turbulent boundary layer,” *J Sound Vib*, vol. 252, no. 1, pp. 115–139, Apr. 2002, doi: 10.1006/jsvi.2001.4029.
- [56] A. Caiazzo, R. D’Amico, and W. Desmet, “A Generalized Corcos model for modelling turbulent boundary layer wall pressure fluctuations,” *J Sound Vib*, vol. 372, pp. 192–210, Jun. 2016, doi: 10.1016/j.jsv.2016.02.036.
- [57] A. Caiazzo, N. Alujević, B. Pluymers, and W. Desmet, “Active control of turbulent boundary layer-induced sound transmission through the cavity-backed double panels,” *J Sound Vib*, vol. 422, pp. 161–188, May 2018, doi: 10.1016/j.jsv.2018.02.027.

- [58] R. H. Kraichnan, "Pressure Fluctuations in Turbulent Flow over a Flat Plate," *J Acoust Soc Am*, vol. 28, no. 3, pp. 378–390, May 1956, doi: 10.1121/1.1908336.
- [59] G. M. Lilley and T. H. Hodgson, "On surface pressure fluctuations in turbulent boundary layers," 1960.
- [60] J. E. Ffowcs Williams and R. H. Lyon, "The sound radiated from turbulent flows near flexible boundaries," 1963.
- [61] G. M. Corcos, "The structure of the turbulent pressure field in boundary-layer flows," *J Fluid Mech*, vol. 18, no. 03, p. 353, Mar. 1964, doi: 10.1017/S002211206400026X.
- [62] W. W. Willmarth and F. W. Roos, "Resolution and structure of the wall pressure field beneath a turbulent boundary layer," *J Fluid Mech*, vol. 22, no. 01, p. 81, May 1965, doi: 10.1017/S0022112065000599.
- [63] J. E. F. Williams, "Surface-pressure fluctuations induced by boundary-layer flow at finite Mach number," *J Fluid Mech*, vol. 22, no. 3, pp. 507–519, Jul. 1965, doi: 10.1017/S0022112065000939.
- [64] D. M. Chase, "Turbulent-Boundary-Layer Pressure Fluctuations and Wavenumber Filtering by Nonuniform Spatial Averaging," *J Acoust Soc Am*, vol. 46, no. 5B, pp. 1350–1365, Nov. 1969, doi: 10.1121/1.1911860.
- [65] R. H. Mellen, "On wave-vector filter analysis of turbulent flow," *J Acoust Soc Am*, vol. 89, no. 4B, pp. 1955–1955, Apr. 1991, doi: 10.1121/1.2029662.
- [66] R. H. Mellen, "Wave-vector filter analysis of turbulent flow," *J Acoust Soc Am*, vol. 95, no. 3, pp. 1671–1673, Mar. 1994, doi: 10.1121/1.408556.
- [67] G. Schewe, "On the structure and resolution of wall-pressure fluctuations associated with turbulent boundary-layer flow," *J Fluid Mech*, vol. 134, no. 1, p. 311, Sep. 1983, doi: 10.1017/S0022112083003389.
- [68] B. E. McGrath and R. L. Simpson, "Some features of surface pressure fluctuations in turbulent boundary layers with zero and favorable pressure gradients," 1987.
- [69] K. L. Chandiramani, "Response of underwater structures to convective component of flow noise," *J Acoust Soc Am*, vol. 67, no. S1, pp. S2–S2, Apr. 1980, doi: 10.1121/1.2018149.
- [70] K. L. Chandiramani, "Response of underwater structures to convective component of flow noise," *J Acoust Soc Am*, vol. 73, no. 3, pp. 835–839, Mar. 1983, doi: 10.1121/1.389025.
- [71] R. H. Mellen, "On modeling convective turbulence," *J Acoust Soc Am*, vol. 88, no. 6, pp. 2891–2893, Dec. 1990, doi: 10.1121/1.399695.
- [72] H. Choi and P. Moin, "On the space-time characteristics of wall-pressure fluctuations," *Physics of Fluids A: Fluid Dynamics*, vol. 2, no. 8, pp. 1450–1460, Aug. 1990, doi: 10.1063/1.857593.
- [73] D. M. Chase, "The wave-vector-frequency spectrum of pressure on a smooth plane in turbulent boundary-layer flow at low Mach number," *J Acoust Soc Am*, vol. 90, no. 2, pp. 1032–1040, Aug. 1991, doi: 10.1121/1.402291.

- [74] W. L. Keith, D. A. Hurdis, and B. M. Abraham, "A Comparison of Turbulent Boundary Layer Wall-Pressure Spectra," *J Fluids Eng*, vol. 114, no. 3, pp. 338–347, Sep. 1992, doi: 10.1115/1.2910035.
- [75] R. M. Lueptow, "Transducer resolution and the turbulent wall pressure spectrum," *J Acoust Soc Am*, vol. 97, no. 1, pp. 370–378, Jan. 1995, doi: 10.1121/1.412322.
- [76] E. Manoha, "The wavenumber-frequency spectrum of the wall pressure fluctuations beneath a turbulent boundary layer," in *Aeroacoustics Conference*, Reston, Virginia: American Institute of Aeronautics and Astronautics, May 1996. doi: 10.2514/6.1996-1758.
- [77] M. K. Bull, "Wall-pressure fluctuations beneath turbulent boundary layers: some reflections on forty years of research," *J Sound Vib*, vol. 190, no. 3, pp. 299–315, Feb. 1996, doi: 10.1006/jsvi.1996.0066.
- [78] H. Sawada, T. Kohno, and T. Kunimasu, "Pressure fluctuation measurements in the NAL 0.2-m supersonic wind tunnel," in *36th AIAA Aerospace Sciences Meeting and Exhibit*, Reston, Virginia: American Institute of Aeronautics and Astronautics, Jan. 1998. doi: 10.2514/6.1998-636.
- [79] B. M. Abraham and W. L. Keith, "Direct Measurements of Turbulent Boundary Layer Wall Pressure Wavenumber-Frequency Spectra," *J Fluids Eng*, vol. 120, no. 1, pp. 29–39, Mar. 1998, doi: 10.1115/1.2819657.
- [80] S. P. Gravante, A. M. Naguib, C. E. Wark, and H. M. Nagib, "Characterization of the Pressure Fluctuations Under a Fully Developed Turbulent Boundary Layer," *AIAA Journal*, vol. 36, no. 10, pp. 1808–1816, Oct. 1998, doi: 10.2514/2.296.
- [81] A. V. Smol'yakov, "Calculation of the spectra of pseudosound wall-pressure fluctuations in turbulent boundary layers," *Acoust Phys*, vol. 46, no. 3, pp. 342–347, May 2000, doi: 10.1134/1.29890.
- [82] V. M. Tkachenko, "Conditions of similarity of the cross-spectra of pseudosound pressures in turbulence," *Acoust Phys*, vol. 46, no. 3, pp. 348–356, 2000.
- [83] M. Wang, "Dynamic-wall modelling for LES of complex turbulent flows," *Annu. Rev Res. Briefs*, pp. 241–250, 1999.
- [84] A. V. Smol'yakov, "Noise of a turbulent boundary layer flow over smooth and rough plates at low mach numbers," *Acoust Phys*, vol. 47, no. 2, pp. 218–225, 2001.
- [85] B. Efimtsov, A. Golubev, S. Rizzi, A. Andersson, R. Rackl, and E. Andrianov, "Influence of Small Steps on Wall Pressure Fluctuation Spectra Measured on Tu-144LL Flying Laboratory," in *8th AIAA/CEAS Aeroacoustics Conference & Exhibit*, Reston, Virginia: American Institute of Aeronautics and Astronautics, Jun. 2002. doi: 10.2514/6.2002-2605.
- [86] B. Efimtsov, N. Kozlov, and A. Andersson, "Wall Pressure Fluctuations in a Local Supersonic Region," in *9th AIAA/CEAS Aeroacoustics Conference and Exhibit*, Reston, Virginia: American Institute of Aeronautics and Astronautics, May 2003. doi: 10.2514/6.2003-3221.

- [87] B. M. Efimtsov, V. V Zosimov, A. V Romashov, and S. A. Rybak, “Correlation of pressure fluctuations with tangential stresses in a turbulent boundary layer,” *Acoust Phys*, vol. 49, no. 1, pp. 113–115, 2003.
- [88] J. Rocha and D. Palumbo, “On the sensitivity of sound power radiated by aircraft panels to turbulent boundary layer parameters,” *J Sound Vib*, vol. 331, no. 21, pp. 4785–4806, Oct. 2012, doi: 10.1016/j.jsv.2012.05.030.
- [89] V. Blitterswyk and J. Corey, “Experimental characterization of turbulent motions using wall-pressure measurements in low Reynolds number turbulent boundary layers,” Carleton University, 2016.
- [90] H. Shahmohamadi and M. M. Rashidi, “Experimental investigation and a novel analytical solution of turbulent boundary layer flow over a flat plate in a wind tunnel,” *Int J Mech Sci*, vol. 133, pp. 121–128, Nov. 2017, doi: 10.1016/j.ijmecsci.2017.08.043.
- [91] N. Thomson and J. Rocha, “Semi-empirical wall pressure spectral modeling for zero and favorable pressure gradient flows,” *J Acoust Soc Am*, vol. 152, no. 1, pp. 80–98, Jul. 2022, doi: 10.1121/10.0012188.
- [92] R. Leneveu, M. Rissman, and A. A. Pinar, “Validation with experimental data of an heterogeneous turbulent wall pressure fluctuation model in a FEM structural context,” in *25th AIAA/CEAS Aeroacoustics Conference*, Reston, Virginia: American Institute of Aeronautics and Astronautics, May 2019. doi: 10.2514/6.2019-2751.
- [93] E. Salze, E. Jondeau, A. Pereira, S. L. Prigent, and C. Bailly, “A new MEMS microphone array for the wavenumber analysis of wall-pressure fluctuations: application to the modal investigation of a ducted low-Mach number stage,” in *25th AIAA/CEAS Aeroacoustics Conference*, Reston, Virginia: American Institute of Aeronautics and Astronautics, May 2019. doi: 10.2514/6.2019-2574.
- [94] A. N. Kolmogorov, “Equations of turbulent motion of an incompressible fluid, *Izv. Acad. Sci., USSR*,” *Physics (College Park Md)*, vol. 6, no. 1, p. 2, 1942.
- [95] W. P. Jones and B. E. Launder, “The prediction of laminarization with a two-equation model of turbulence,” *Int J Heat Mass Transf*, vol. 15, no. 2, pp. 301–314, Feb. 1972, doi: 10.1016/0017-9310(72)90076-2.
- [96] W. P. Jones and B. E. Launder, “The calculation of low-Reynolds-number phenomena with a two-equation model of turbulence,” *Int J Heat Mass Transf*, vol. 16, no. 6, pp. 1119–1130, Jun. 1973, doi: 10.1016/0017-9310(73)90125-7.
- [97] K. Hanjalić and B. E. Launder, “A Reynolds stress model of turbulence and its application to thin shear flows,” *J Fluid Mech*, vol. 52, no. 4, pp. 609–638, Apr. 1972, doi: 10.1017/S002211207200268X.
- [98] B. E. Launder and D. B. Spalding, “The numerical computation of turbulent flows,” *Comput Methods Appl Mech Eng*, vol. 3, no. 2, pp. 269–289, Mar. 1974, doi: 10.1016/0045-7825(74)90029-2.

- [99] B. E. Launder and B. I. Sharma, “Application of the energy-dissipation model of turbulence to the calculation of flow near a spinning disc,” *Letters in Heat and Mass Transfer*, vol. 1, no. 2, pp. 131–137, Nov. 1974, doi: 10.1016/0094-4548(74)90150-7.
- [100] D. C. Wilcox, “Reassessment of the scale-determining equation for advanced turbulence models,” *AIAA Journal*, vol. 26, no. 11, pp. 1299–1310, Nov. 1988, doi: 10.2514/3.10041.
- [101] J. C. Kok, “Resolving the dependence on free-stream values for the kx turbulence model—NLR-TP-99295,” 1999.
- [102] F. R. Menter, “Influence of freestream values on k-omega turbulence model predictions,” *AIAA Journal*, vol. 30, no. 6, pp. 1657–1659, Jun. 1992, doi: 10.2514/3.11115.
- [103] D. C. Wilcox, “Formulation of the k-w Turbulence Model Revisited,” *AIAA Journal*, vol. 46, no. 11, pp. 2823–2838, Nov. 2008, doi: 10.2514/1.36541.
- [104] T.-H. Shih, W. W. Liou, A. Shabbir, Z. Yang, and J. Zhu, “A new k-epsilon eddy viscosity model for high Reynolds number turbulent flows: Model development and validation,” 1994.
- [105] M. Leschziner, *Statistical Turbulence Modelling for Fluid Dynamics — Demystified*. Imperial College Press, 2015. doi: 10.1142/p997.
- [106] S. B. Pope, *Turbulent Flows*. Cambridge University Press, 2000. doi: 10.1017/CBO9780511840531.
- [107] T. J. Craft, B. E. Launder, and K. Suga, “Development and application of a cubic eddy-viscosity model of turbulence,” *Int J Heat Fluid Flow*, vol. 17, no. 2, pp. 108–115, Apr. 1996, doi: 10.1016/0142-727X(95)00079-6.
- [108] J. W. Deardorff, “A numerical study of three-dimensional turbulent channel flow at large Reynolds numbers,” *J Fluid Mech*, vol. 41, no. 2, pp. 453–480, 1970.
- [109] M. Germano, U. Piomelli, P. Moin, and W. H. Cabot, “A dynamic subgrid-scale eddy viscosity model,” *Physics of Fluids A: Fluid Dynamics*, vol. 3, no. 7, pp. 1760–1765, Jul. 1991, doi: 10.1063/1.857955.
- [110] P. Moin, W. C. Reynolds, and J. H. Ferziger, “Large eddy simulation of incompressible turbulent channel flow,” 1978.
- [111] P. P. Sullivan, J. C. McWilliams, and C.-H. Moeng, “A grid nesting method for large-eddy simulation of planetary boundary-layer flows,” *Boundary Layer Meteorol*, vol. 80, no. 1–2, pp. 167–202, Jul. 1996, doi: 10.1007/BF00119016.
- [112] B. Koren and C. Beets, “Large-eddy simulation with accurate implicit subgrid-scale diffusion,” *Department of Numerical Mathematics [NM]*, no. R 9601, 1996.
- [113] N. Okong’o and D. Knight, “Compressible large eddy simulation using unstructured grids - Channel and boundary layer flows,” in *34th AIAA/ASME/SAE/ASEE Joint Propulsion Conference and Exhibit*, Reston, Virginia: American Institute of Aeronautics and Astronautics, Jul. 1998. doi: 10.2514/6.1998-3315.

- [114] K. Mahesh, G. Constantinescu, and P. Moin, “A numerical method for large-eddy simulation in complex geometries,” in *Computational Fluid and Solid Mechanics 2003*, Elsevier, 2003, pp. 23–30. doi: 10.1016/B978-008044046-0.50009-9.
- [115] K. Mahesh, G. Constantinescu, and P. Moin, “A numerical method for large-eddy simulation in complex geometries,” *J Comput Phys*, vol. 197, no. 1, pp. 215–240, Jun. 2004, doi: 10.1016/j.jcp.2003.11.031.
- [116] E. Balaras, “Modeling complex boundaries using an external force field on fixed Cartesian grids in large-eddy simulations,” *Comput Fluids*, vol. 33, no. 3, pp. 375–404, Mar. 2004, doi: 10.1016/S0045-7930(03)00058-6.
- [117] J. A. Templeton, G. Medic, and G. Kalitzin, “An eddy-viscosity based near-wall treatment for coarse grid large-eddy simulation,” *Physics of Fluids*, vol. 17, no. 10, p. 105101, 2005, doi: 10.1063/1.2084228.
- [118] J. Fröhlich, J. A. Denev, C. Hinterberger, and H. Bockhorn, “On the Impact of Tangential Grid Refinement on Subgrid-Scale Modelling in Large Eddy Simulation,” in *Numerical Methods and Applications*, Berlin, Heidelberg: Springer Berlin Heidelberg, pp. 550–557. doi: 10.1007/978-3-540-70942-8_66.
- [119] K. Sengupta, F. Mashayek, and G. B. Jacobs, “Large Eddy Simulation Using a High-Order Nodal Discontinuous Galerkin Method on Unstructured Grids,” in *Fluids Engineering*, ASME/ED, Jan. 2006, pp. 409–413. doi: 10.1115/IMECE2006-16050.
- [120] S. T. Bose, P. Moin, and D. You, “Grid-independent large-eddy simulation using explicit filtering,” *Physics of Fluids*, vol. 22, no. 10, p. 105103, Oct. 2010, doi: 10.1063/1.3485774.
- [121] D. Drikakis, M. Hahn, A. Mosedale, and B. Thornber, “Large eddy simulation using high-resolution and high-order methods,” *Philosophical Transactions of the Royal Society A: Mathematical, Physical and Engineering Sciences*, vol. 367, no. 1899, pp. 2985–2997, Jul. 2009, doi: 10.1098/rsta.2008.0312.
- [122] H. Choi and P. Moin, “Grid-point requirements for large eddy simulation: Chapman’s estimates revisited,” *Physics of Fluids*, vol. 24, no. 1, p. 011702, Jan. 2012, doi: 10.1063/1.3676783.
- [123] D. R. Chapman, “Computational Aerodynamics Development and Outlook,” *AIAA Journal*, vol. 17, no. 12, pp. 1293–1313, Dec. 1979, doi: 10.2514/3.61311.
- [124] C. Maury, P. Gardonio, and S. J. Elliott, “Model for the control of the sound radiation by an aircraft panel excited by a turbulent boundary layer,” 2000.
- [125] W. R. Graham, “Boundary layer induced noise in aircraft, part i: the flat plate model,” *J Sound Vib*, vol. 192, no. 1, pp. 101–120, Apr. 1996, doi: 10.1006/jsvi.1996.0178.
- [126] W. R. Graham, “A comparison of models for the wavenumber–frequency spectrum of turbulent boundary layer pressures,” *J Sound Vib*, vol. 206, no. 4, pp. 541–565, Oct. 1997, doi: 10.1006/jsvi.1997.1114.

- [127] W. R. Graham, “High-frequency vibration and acoustic radiation of fluid-loaded plates,” *Philosophical Transactions of the Royal Society of London. Series A: Physical and Engineering Sciences*, vol. 352, no. 1698, pp. 1–43, Jul. 1995, doi: 10.1098/rsta.1995.0057.
- [128] W. R. Graham, “Boundary layer induced noise in aircraft,” *Unknown*, 1992.
- [129] J. S. Bendat and A. G. Piersol, “Random data: Analysis and measurement procedures 2nd Edition A Wiley-Interscience Publication,” *New York*, 1986.
- [130] F. Han, R. J. Bernhard, and L. G. Mongeau, “prediction of flow-induced structural vibration and sound radiation using energy flow analysis,” *J Sound Vib*, vol. 227, no. 4, pp. 685–709, Nov. 1999, doi: 10.1006/jsvi.1998.3013.
- [131] F. Han, L. G. Mongeau, and R. J. Bernhard, “A model for the vibro-acoustic response of plates excited by complex flows,” *J Sound Vib*, vol. 246, no. 5, pp. 901–926, Oct. 2001, doi: 10.1006/jsvi.2001.3699.
- [132] F. Birgersson, S. Finnveden, and G. Robert, “Modelling turbulence-induced vibration of pipes with a spectral finite element method,” *J Sound Vib*, vol. 278, no. 4–5, pp. 749–772, Dec. 2004, doi: 10.1016/j.jsv.2003.10.024.
- [133] D. Fritze, S. Marburg, and H.-J. Hardtke, “Estimation of Radiated Sound Power: A Case Study on Common Approximation Methods,” *Acta Acustica united with Acustica*, vol. 95, no. 5, pp. 833–842, Sep. 2009, doi: 10.3813/AAA.918214.
- [134] J. Rocha, “Sound Radiation and Vibration of Composite Panels Excited by Turbulent Flow: Analytical Prediction and Analysis,” *Shock and Vibration*, vol. 2014, pp. 1–18, 2014, doi: 10.1155/2014/316481.
- [135] L. Maxit and V. Denis, “Prediction of flow induced sound and vibration of periodically stiffened plates,” *J Acoust Soc Am*, vol. 133, no. 1, pp. 146–160, Jan. 2013, doi: 10.1121/1.4768875.
- [136] M. Berton, L. Maxit, D. Juvé, and C. Audoly, “Prediction of flow-induced sound and vibration: on different methods for introducing the TBL excitation in the vibroacoustic model,” in *Acoustics 2013*, 2013, p. p–1281.
- [137] N. Hu and M. Misol, “Effects of riblet surfaces on boundary-layer-induced surface pressure fluctuations and surface vibration,” *Dtsch. Jahrestagung Fur Akust. Deutsche Gesellschaft Fur Akust*, pp. 1–4, 2015.
- [138] E. Ciappi, S. De Rosa, F. Franco, P. Vitiello, and M. Miozzi, “On the dynamic behavior of composite panels under turbulent boundary layer excitations,” *J Sound Vib*, vol. 364, pp. 77–109, Mar. 2016, doi: 10.1016/j.jsv.2015.11.024.
- [139] A. Purohit, A. K. Darpe, and S. P. Singh, “Experimental investigations on flow induced vibration of an externally excited flexible plate,” *J Sound Vib*, vol. 371, pp. 237–251, Jun. 2016, doi: 10.1016/j.jsv.2016.02.039.
- [140] P. Jeyaraj, C. Padmanabhan, and N. Ganesan, “Vibration and Acoustic Response of an Isotropic Plate in a Thermal Environment,” *J Vib Acoust*, vol. 130, no. 5, Oct. 2008, doi: 10.1115/1.2948387.

- [141] P. Jeyaraj, N. Ganesan, and C. Padmanabhan, “Vibration and acoustic response of a composite plate with inherent material damping in a thermal environment,” *J Sound Vib*, vol. 320, no. 1–2, pp. 322–338, Feb. 2009, doi: 10.1016/j.jsv.2008.08.013.
- [142] X. Zhao, Q. Geng, and Y. Li, “Vibration and acoustic response of an orthotropic composite laminated plate in a hygroscopic environment,” *J Acoust Soc Am*, vol. 133, no. 3, pp. 1433–1442, Mar. 2013, doi: 10.1121/1.4790353.
- [143] X. Zhao, B. Zhang, and Y. Li, “Vibration and acoustic radiation of an orthotropic composite cylindrical shell in a hygroscopic environment,” *Journal of Vibration and Control*, vol. 23, no. 4, pp. 673–692, Mar. 2017, doi: 10.1177/1077546315581943.
- [144] K. A. Mulholland and H. D. Parbrook, “The measurement of sound transmission loss of panels with small transmission loss,” *J Sound Vib*, vol. 2, no. 4, pp. 502–509, Oct. 1965, doi: 10.1016/0022-460X(65)90126-4.
- [145] B. M. Efimtsov and L. A. Lazarev, “Sound Transmission Loss of Panels with Resonant Elements,” *Acoust Phys*, vol. 47, no. 3, pp. 291–296, May 2001, doi: 10.1007/BF03353582.
- [146] B. M. Efimtsov and L. A. Lazarev, “Analysis of the sound transmission loss of panels with resonant systems on the basis of equivalent representations,” *Acoust Phys*, vol. 51, no. 3, pp. 300–305, Jun. 2005, doi: 10.1134/1.1922543.
- [147] S. Xie and S. Liu, “Sound transmission loss characteristics of single corrugated panel,” in *Proceedings of the 2010 Symposium on Piezoelectricity, Acoustic Waves and Device Applications*, IEEE, Dec. 2010, pp. 166–170. doi: 10.1109/SPAWDA.2010.5744296.
- [148] J. Zhou, A. Bhaskar, and X. Zhang, “Optimization for sound transmission through a double-wall panel,” *Applied Acoustics*, vol. 74, no. 12, pp. 1422–1428, Dec. 2013, doi: 10.1016/j.apacoust.2013.06.002.
- [149] M. P. Arunkumar, M. Jagadeesh, J. Pitchaimani, K. V. Gangadharan, and M. C. L. Babu, “Sound radiation and transmission loss characteristics of a honeycomb sandwich panel with composite facings: Effect of inherent material damping,” *J Sound Vib*, vol. 383, pp. 221–232, Nov. 2016, doi: 10.1016/j.jsv.2016.07.028.
- [150] A. Santoni, P. Bonfiglio, P. Fausti, and S. Schoenwald, “Predicting sound radiation efficiency and sound transmission loss of orthotropic cross-laminated timber panels,” 2017, p. 015013. doi: 10.1121/2.0000626.
- [151] S. Ehsan Moosavimehr and A. Srikantha Phani, “Sound transmission loss characteristics of sandwich panels with a truss lattice core,” *J Acoust Soc Am*, vol. 141, no. 4, pp. 2921–2932, Apr. 2017, doi: 10.1121/1.4979934.
- [152] Y. Zhang, D. Thompson, G. Squicciarini, J. Ryue, X. Xiao, and Z. Wen, “Sound transmission loss properties of truss core extruded panels,” *Applied Acoustics*, vol. 131, pp. 134–153, Feb. 2018, doi: 10.1016/j.apacoust.2017.10.021.
- [153] W. Li, Y. He, Z. Xu, and Z. Zhang, “Sound transmission loss characteristics of four-side simply supported sandwich panels,” *Journal of Sandwich Structures & Materials*, vol. 21, no. 2, pp. 707–726, Feb. 2019, doi: 10.1177/1099636217698394.

- [154] C. Droz, O. Robin, M. Ichchou, and N. Atalla, “Improving sound transmission loss at ring frequency of a curved panel using tunable 3D-printed small-scale resonators,” *J Acoust Soc Am*, vol. 145, no. 1, pp. EL72–EL78, Jan. 2019, doi: 10.1121/1.5088036.
- [155] F. Errico, G. Tufano, O. Robin, N. Guenfoud, M. Ichchou, and N. Atalla, “Simulating the sound transmission loss of complex curved panels with attached noise control materials using periodic cell wavemodes,” *Applied Acoustics*, vol. 156, pp. 21–28, Dec. 2019, doi: 10.1016/j.apacoust.2019.06.027.
- [156] Z.-H. Wen, D.-W. Wang, and L. Ma, “Sound transmission loss of sandwich panel with closed octahedral core,” *Journal of Sandwich Structures & Materials*, vol. 23, no. 1, pp. 174–193, Jan. 2021, doi: 10.1177/1099636219829369.
- [157] P. G. Bremner and M. Zhu, “Recent Progress using SEA and CFD to Predict Interior Wind Noise,” May 2003. doi: 10.4271/2003-01-1705.
- [158] W. J. de Lima, N. Vlahopoulos, R. Sbragio, and J. He, “Interior Aircraft Noise Computations due to TBL Excitation using the Energy Finite Element Analysis,” May 2009. doi: 10.4271/2009-01-2248.
- [159] J. Da Rocha, A. Suleman, and F. Lau, “Prediction of flow-induced noise in transport vehicles: development and validation of a coupled structural-acoustic analytical framework,” *Canadian Acoustics*, vol. 37, no. 4, pp. 13–29, 2009.
- [160] J. Du, Y. Liu, Y. Wang, and G. Wang, “Vibro-acoustic analysis of an elastically restrained plate duct silencer backed by irregular acoustical cavity,” *Applied Acoustics*, vol. 138, pp. 60–71, Sep. 2018, doi: 10.1016/j.apacoust.2018.03.004.
- [161] W. K. Blake, “Turbulent boundary-layer wall-pressure fluctuations on smooth and rough walls,” *J Fluid Mech*, vol. 44, no. 04, p. 637, Dec. 1970, doi: 10.1017/S0022112070002069.
- [162] G. Schewe, “On the structure and resolution of wall-pressure fluctuations associated with turbulent boundary-layer flow,” *J Fluid Mech*, vol. 134, no. 1, p. 311, Sep. 1983, doi: 10.1017/S0022112083003389.
- [163] G. C. Lauchle and M. A. Daniels, “Wall-pressure fluctuations in turbulent pipe flow,” *Physics of Fluids*, vol. 30, no. 10, p. 3019, 1987, doi: 10.1063/1.866080.
- [164] M. S. Howe, “On the structure of the turbulent boundary-layer wall pressure spectrum in the vicinity of the acoustic wavenumber,” *Proceedings of the Royal Society of London. A. Mathematical and Physical Sciences*, vol. 412, no. 1843, pp. 389–401, Aug. 1987, doi: 10.1098/rspa.1987.0093.
- [165] Y. Rozenberg, G. Robert, and S. Moreau, “Wall-Pressure Spectral Model Including the Adverse Pressure Gradient Effects,” *AIAA Journal*, vol. 50, no. 10, pp. 2168–2179, Oct. 2012, doi: 10.2514/1.J051500.
- [166] S. Lakshmi pathy and S. S. Girimaji, “Extension of Boussinesq turbulence constitutive relation for bridging methods,” *Journal of Turbulence*, vol. 8, p. N31, Jan. 2007, doi: 10.1080/14685240701420478.

- [167] B. E. Launder and D. B. Spalding, “The numerical computation of turbulent flows,” *Comput Methods Appl Mech Eng*, vol. 3, no. 2, pp. 269–289, Mar. 1974, doi: 10.1016/0045-7825(74)90029-2.
- [168] D. C. Wilcox, “The Wilcox k-omega Turbulence Model,” <https://turbmodels.larc.nasa.gov/wilcox.html>, Aug. 2013.
- [169] F. R. Menter, “Improved two-equation k-omega turbulence models for aerodynamic flows,” 1992.
- [170] F. R. Menter, “The Menter Shear Stress Transport Turbulence Model,” <https://turbmodels.larc.nasa.gov/sst.html>, Jul. 2013.
- [171] F. R. Menter, “Two-equation eddy-viscosity turbulence models for engineering applications,” *AIAA Journal*, vol. 32, no. 8, pp. 1598–1605, Aug. 1994, doi: 10.2514/3.12149.
- [172] P. Spalart and S. Allmaras, “A one-equation turbulence model for aerodynamic flows,” in *30th Aerospace Sciences Meeting and Exhibit*, Reston, Virginia: American Institute of Aeronautics and Astronautics, Jan. 1992. doi: 10.2514/6.1992-439.
- [173] G. Kalitzin, G. Medic, G. Iaccarino, and P. Durbin, “Near-wall behavior of RANS turbulence models and implications for wall functions,” *J Comput Phys*, vol. 204, no. 1, pp. 265–291, Mar. 2005, doi: 10.1016/j.jcp.2004.10.018.
- [174] D. K. Lilly, “On the application of eddy viscosity concept in the inertial sub-range of turbulence,” *NCAR manuscript*, vol. 123, 1966.
- [175] S. B. Pope, *Turbulent flows*. Cambridge university press, 2000.
- [176] J. Smagorinsky, “General circulation experiments with the primitive equations: I. The basic experiment,” *Mon Weather Rev*, vol. 91, no. 3, pp. 99–164, 1963.
- [177] I. B. Celik, U. Ghia, P. J. Roache, and C. J. Freitas, “Procedure for Estimation and Reporting of Uncertainty Due to Discretization in CFD Applications,” *J Fluids Eng*, vol. 130, no. 7, p. 078001, 2008, doi: 10.1115/1.2960953.
- [178] X. Gloerfelt and T. Le Garrec, “Generation of inflow turbulence for aeroacoustic applications,” in *14th AIAA/CEAS Aeroacoustics Conference (29th AIAA Aeroacoustics Conference)*, Reston, Virginia: American Institute of Aeronautics and Astronautics, May 2008. doi: 10.2514/6.2008-2926.
- [179] H. Y. Hafeez and C. E. Ndikilar, “Boundary layer equations in fluid dynamics,” in *Applications of Heat, Mass and Fluid Boundary Layers*, Elsevier, 2020, pp. 67–94. doi: 10.1016/B978-0-12-817949-9.00012-8.
- [180] N. Mahmoudnejad and K. A. Hoffmann, “A hybrid scheme for the numerical simulation of shock/discontinuity problems,” *Int J Comput Fluid Dyn*, vol. 25, no. 9, pp. 469–486, Oct. 2011, doi: 10.1080/10618562.2011.632371.
- [181] B. R. Adhikary, A. Majumdar, A. Sahu, and P. Bhattacharya, “Sensitivity of TBL Wall-Pressure over the Flat Plate on Numerical Turbulence Model Parameter Variations,” *CFD Letters*, vol. 15, no. 7, pp. 148–174, May 2023, doi: 10.37934/cfdl.15.7.148174.

- [182] K.-J. Bathe, *Finite element procedures*, 1st ed., vol. 1037. New Jersey: PRENTICE HALL, 1996.
- [183] C. E. Wallace, “Radiation Resistance of a Rectangular Panel,” *J Acoust Soc Am*, vol. 51, no. 3B, pp. 946–952, Mar. 1972, doi: 10.1121/1.1912943.
- [184] L. E. Wittig and A. K. Sinha, “Simulation of multicorrelated random processes using the FFT algorithm,” *J Acoust Soc Am*, vol. 58, no. 3, pp. 630–634, Sep. 1975, doi: 10.1121/1.380702.
- [185] F. J. Fahy, *Sound and structural vibration: radiation, transmission and response*. Elsevier, 2007.
- [186] S. Ghosh and P. Bhattacharya, “Energy transmission through a double-wall curved stiffened panel using Green’s theorem,” *J Sound Vib*, vol. 342, pp. 218–240, Apr. 2015, doi: 10.1016/j.jsv.2014.12.041.
- [187] Z. Zhou, Z. Mei, D. Wu, and G. Chen, “Vibroacoustic behavior of submerged stiffened composite plates excited by a turbulent boundary layer,” *J Sound Vib*, vol. 528, p. 116894, Jun. 2022, doi: 10.1016/j.jsv.2022.116894.
- [188] L. Cheng, Y. Y. Li, and J. X. Gao, “Energy transmission in a mechanically-linked double-wall structure coupled to an acoustic enclosure,” *J Acoust Soc Am*, vol. 117, no. 5, pp. 2742–2751, May 2005, doi: 10.1121/1.1886525.

VITA

Mr. Biplab Ranjan Adhikary was born in 1986 in Uttarpara, India. He received the Bachelor of Engineering in Civil Engineering from Jadavpur University, Kolkata, India in 2009 and the Master of Technology with the specialization in Ocean Engineering and Naval Architecture in 2011 from Indian Institute of Technology Kharagpur. He secured an All India Rank 63 in the prestigious pan-India based examination Graduate Aptitude Test in Engineering (GATE) in his pre-final year of undergraduate course. He served Mazagon Dock Limited, Mumbai, a premier defence shipyard, under the Ministry of Defence, Govt. of India. He worked as Assistant Professor in two degree level engineering colleges in Kolkata. Later he started his own institute GATEit, to mentor Civil Engineering GATE aspirants and Applied Mathematics enthusiasts. He worked on two consecutive projects as Research Associate and Senior Research Fellow funded by AR&DB (DRDO), Govt. of India and DST, Govt. of West Bengal, respectively. During his Ph.D. research work on Vibroacoustic Response Due to Turbulent Boundary Layer Over Plate Structures, he has completed courses on Computational Fluid Dynamics for Professionals and Structural Dynamics. He has few publications in journals of international repute and presented his research findings in well-known international conferences. His research interests are in finite element analysis, computational fluid dynamics, fluid-structure interactions and vibroacoustics. Presently, he is working as Structural Engineer and Automation Lead, McDermott and contributing in the field of Advanced Finite Element Analysis and in-house Digital Twin program.

